



Universiteit
Leiden

The Netherlands

Methodology matters: characterization of glioma through advanced MR imaging

Schmitz Abecassis, B.

Citation

Schmitz Abecassis, B. (2025, September 10). *Methodology matters: characterization of glioma through advanced MR imaging*. Retrieved from <https://hdl.handle.net/1887/4260526>

Version: Publisher's Version

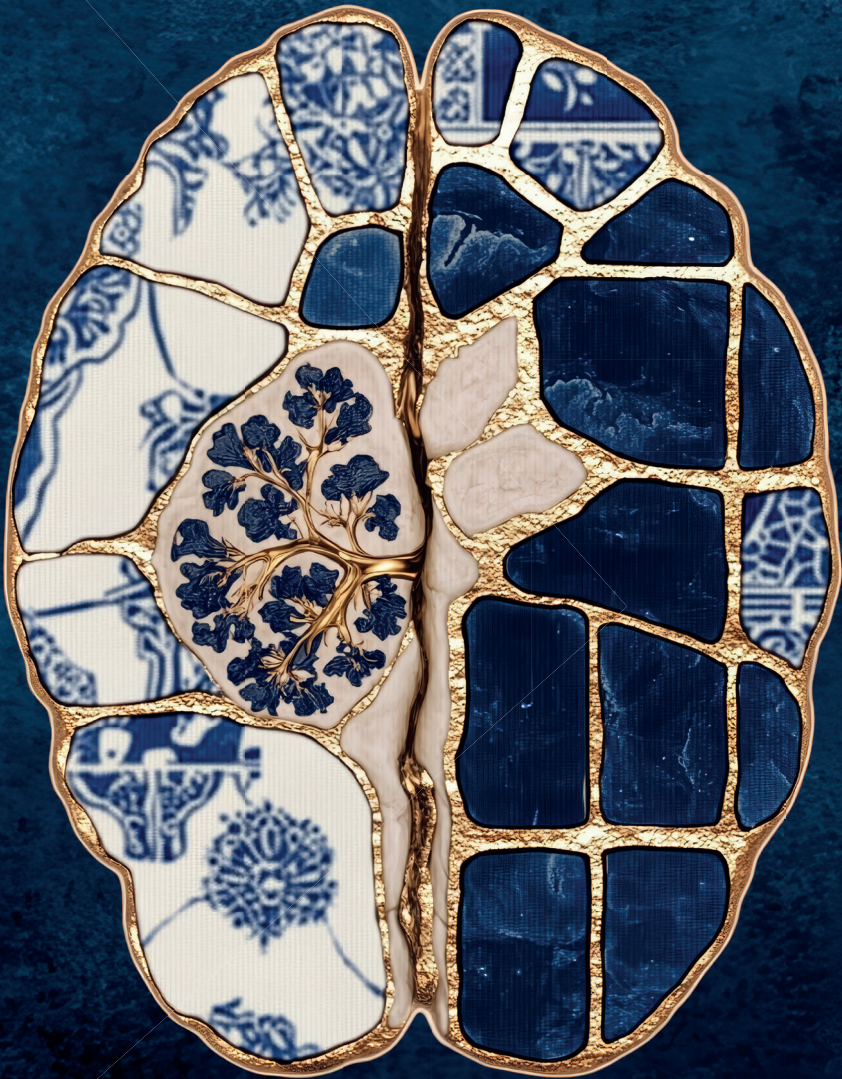
License: [Licence agreement concerning inclusion of doctoral thesis in the Institutional Repository of the University of Leiden](#)

Downloaded from: <https://hdl.handle.net/1887/4260526>

Note: To cite this publication please use the final published version (if applicable).

METHODOLOGY MATTERS

Characterization of Glioma through Advanced MR Imaging



Bárbara Schmitz Abecassis

Stellingen behorende bij het proefschrift getiteld:

Methodology Matters: Characterization of Glioma through Advanced MR Imaging

1. To bring CEST closer to clinical use, future research should focus not only on developing robust processing methods but also on ensuring these methods remain scientifically sound, while also practically feasible for clinical application. *(this thesis)*
2. The most effective way to introduce ultra-high field imaging into clinical care, is to integrate it as a complementary tool alongside routine clinical MR protocols. *(this thesis)*
3. Machine learning is better suited for pathologies with very well-defined imaging characteristics, unlike glioma. *(this thesis)*
4. To consider the implementation of new MR techniques, such as CEST, into clinical practice, not only substantial validation is needed, but also a careful consideration of practical aspects such as standardization, accessibility and costs. *(this thesis)*
5. Machine learning algorithms need to be continuously trained and updated to remain relevant.
6. Ultra-high field MR imaging would make the most sense for advanced imaging techniques, as they would exponentially benefit from the increased signal-to-noise ratio (SNR).
7. More intense collaboration between research groups and MRI vendors will speed up the implementation of advanced MR techniques into clinical practice.
8. While a healthy lifestyle, including regular exercise, cannot cure brain tumors like gliomas, it can significantly improve patients' quality of life.
9. Science cannot exist without continuous scrutiny; it is a process not an ideal.
10. The journey to earning a PhD is much like training for a marathon.

Cover artwork

Front cover keywords

Illustrations generated with Midjourney

CT scan-inspired transverse cross-section of a human brain with a tumor with intricate detailing. The brain should be displayed from the top-down and not a side view. The brain structure is designed using the ornate patterns incorporating traditional Japanese motifs (including Seigaiha, Asanoha, sayagata) golden kintsugi lines. Include Dutch and Portuguese tile patterns. High contrast, intricate textures, and a refined minimalist composition.

Back cover keywords

A refined and intricate background for a chapter page, featuring a deep midnight blue base. Seamlessly integrate with traditional Japanese motifs such as Seigaiha (wave patterns), Asanoha (hemp leaf), and Sayagata (linked geometric designs). The composition should be highly detailed yet well-balanced, creating a sophisticated interplay of textures and patterns. Minimalist aesthetic with an elegant and timeless feel.

Layout

Luc van Loon

Printing

Ridder Print, www.ridderprint.nl

ISBN

978-94-6522-478-7

This work was performed in the framework of the Medical Delta program Cancer Diagnostics 3.0: Big Data Science of in & ex vivo Imaging. Medical Delta is gratefully acknowledged for financial support for the printing costs of this thesis.

© **Bárbara Schmitz Abecassis, 2025.**

All right reserved. No part of this thesis may be reproduced, stored or transmitted in any form or by any means without prior permission of the author or the copyright-owning journals for previously published chapters.

Methodology Matters:
Characterization of Glioma through Advanced MR Imaging

Proefschrift

ter verkrijging van
de graad van doctor aan de Universiteit Leiden,
op gezag van rector magnificus prof. dr. ir. H. Bijl,
volgens besluit van het college voor promoties
te verdedigen op woensdag 10 september 2025
klokke 16:00 uur

door

Bárbara Schmitz Abecassis
geboren te Lissabon, Portugal
in 1995

Promotors

Prof. Dr. Ir. M.J.P. van Osch

Prof. Dr. M.J.B. Taphoorn

Copromotor

Dr. J.A.F. Koekkoek

Promotiecommissie

Prof. Dr. A.G. Webb

Prof. Dr. M. Broekman

Dr. Ir. E. Warnert

Erasmus Medical Center

Dr. Ir. E. Wiegers

University Medical Center Utrecht

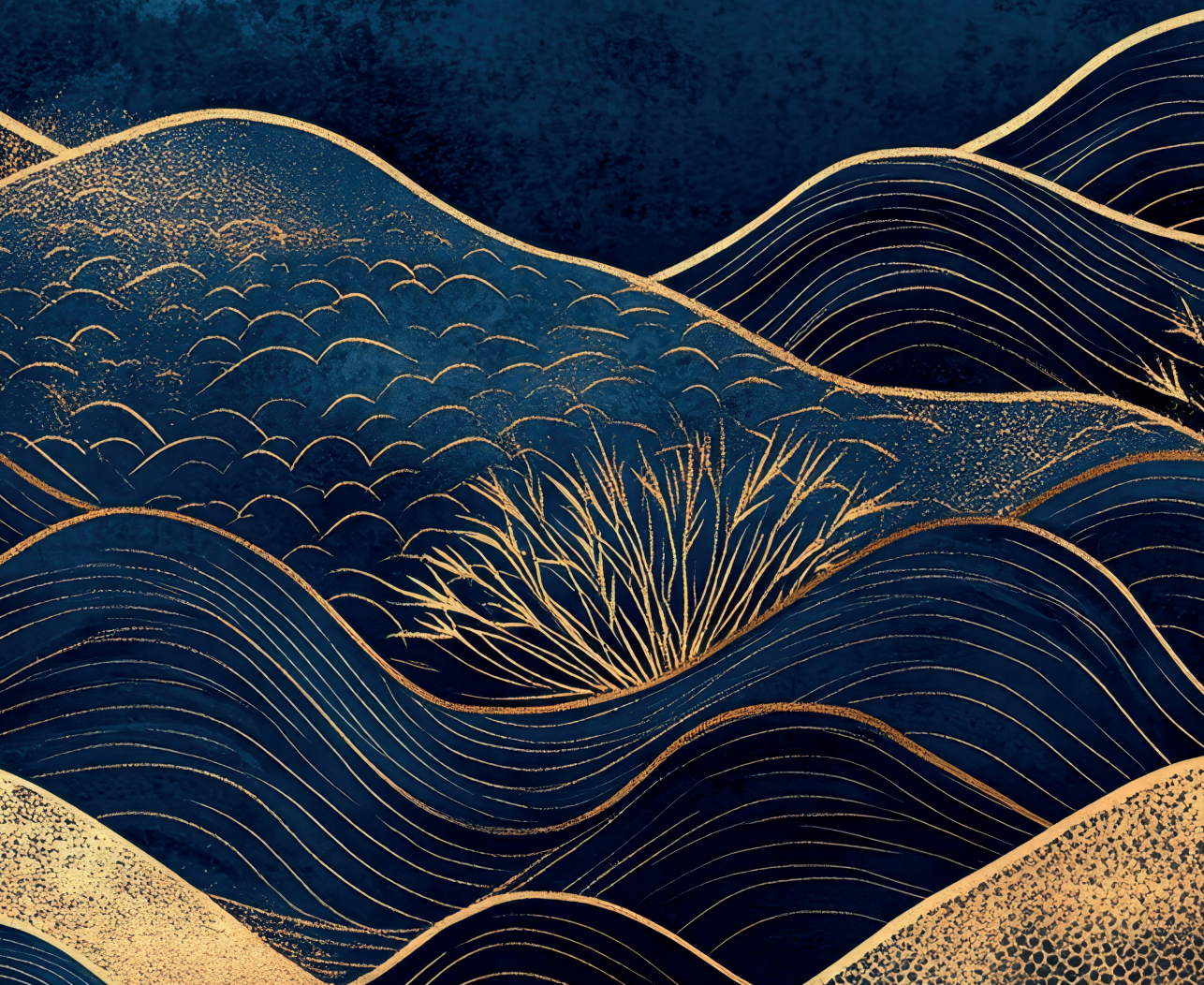
“ Virtue is knowledge. ”

Socrates in Plato's Meno

Contents

Chapter 1	9	Introduction
Chapter 2	15	Chemical Exchange Saturation Transfer for Preoperative Glioma Characterization
Chapter 3	21	The use of variable delay multipulse chemical exchange saturation transfer for separately assessing different CEST pools in the human brain at 7T
Chapter 4	45	Investigation of metabolite correlates of CEST in the human brain at 7T
Chapter 5	71	Insights into CEST contrast at 2 ppm in enhancing and non-enhancing lesions from glioma patients scanned at 7T
Chapter 6	91	Extension of T_2 hyperintense areas in patients with a glioma: a comparison between high-quality 7T MRI and clinical scans
Chapter 7	111	MRI phenotypes of glioblastomas early after treatment are suggestive of overall patient survival
Chapter 8	139	Discussion
Chapter 9	148	Summary in English
	150	Summary in Dutch
	152	Summary in Portuguese
Chapter 10	155	References
Chapter 11	170	List of publications
	171	First author presentations at international conferences
	173	Acknowledgments
	175	Curriculum Vitae

1 Introduction



1.1 Glioma disease background

Gliomas are the most common form of adult primary brain tumors, accounting for approximately 25% of the total of primary brain tumors and 81% of all adult malignant brain tumors¹. Gliomas originate from glial cells, which provide physical and chemical support to neurons, including astrocytes, oligodendrocytes, microglia and ependymal cells²⁻⁴. Despite being relatively rare, gliomas still pose one of the biggest challenges in neuro-oncology. Due to their infiltrative growth these tumors tend to recur after antitumor treatment and prognosis is generally poor, particularly for the higher grade gliomas. Currently, despite extensive treatment, patients with glioblastoma (the most malignant and most commonly occurring glioma) have a median overall survival between 12 and 15 months⁵. Lower-grade gliomas have a slower growth rate and have a 5-year overall survival rate between 70% and 97%⁶. The cause of gliomas is still poorly understood, and identifying the triggers for the onset of these tumors could help in its prevention. However, as of today, only a few risk factors have been confirmed and are widely accepted¹. For instance, a family history of glioma is a known risk factor, although it accounts for only a small percentage (5-10%) of cases⁷. Another risk factor is the exposure to ionizing radiation. A few studies have investigated the relationship between intensity of radiation obtained during childhood and the development of central nervous system tumors. These studies found a sevenfold increased risk to develop a glioma after exposure to radiation^{8,9}.

The diagnosis of a glioma typically involves a combination of clinical (symptom) assessment, lesion visualization by means of imaging methods, and importantly, pathological and genetic/molecular tissue examination¹⁰. Tissue collection through surgery is performed by means of a resection or a biopsy¹¹. Tumor resection is usually aimed at the maximal safe removal of the tumor, while a biopsy is performed when surgery is contraindicated. Contraindications include situations where a substantial part of the tumor is located in or near brain regions where tumor resection could significantly impair the patient's neurological functions.

Following surgery and determining the integrated tissue diagnosis including both histopathological and molecular-genetic characteristics, patients typically undergo radiotherapy, chemotherapy with temozolomide or PCV (procarbazine, CCNU, and lomustine), or targeted therapy. In case of tumor recurrence, similar antitumor treatment options can be weighed against each other, depending on the efficacy of previous treatment, performance score, and the availability of experimental treatments¹².

1.2 MR imaging in the clinical workflow of gliomas

Magnetic resonance imaging (MRI) is the most commonly used imaging method to diagnose and follow-up gliomas. Advantages of MR imaging for gliomas include its good soft tissue contrast, detailed visualization through high-resolution images, its non-invasiveness and lack of any ionizing radiation. Different modalities are available, allowing to characterize, for example, tumor vascularity and metabolism, as well as to perform functional imaging to assess

brain activity to support surgical planning. Standard MRI protocol recommendations have been outlined by the European Organization for Research and Treatment of Cancer (EORTC) and the United States National Brain Tumor Society (NBTS)¹³. These include anatomical images such as 3D T_1 -weighted imaging (pre-contrast), which suppresses any signal from water (like edema) while maintaining fat tissue contrast. Moreover, T_2 fluid-attenuated inversion recovery (FLAIR) suppresses free fluid, such as edema, while maintaining a hyperintense appearance from the solid tumor tissue. On T_2 -weighted imaging, the solid component of the tumor also appears hyperintense, most likely due to its protons' longer relaxation times, which also make any water component appear brighter, in contrast to T_2 -FLAIR images. Other modalities, such as diffusion-weighted imaging, are also recommended due to their ability to non-invasively estimate tumor cellularity and grade¹⁴. Lastly, post-contrast 3D T_1 -weighted images are recommended, most commonly using gadolinium-based contrast agents. The contrast agent travels to the newly developed capillaries surrounding the tumor, which tend to be leakier than regular blood vessels, leading to extravasation of contrast agent into the extracellular space. This causes a shortening of the longitudinal proton relaxation time (T_1), resulting in a hyperintense signal. The resulting hyperintensity can indicate malignancy due to the neovascularity fueling tumor cells.

Conventional imaging allows visualization of different tumor components, such as the necrotic core, edema, and gadolinium contrast enhancing and non-enhancing lesions. However, conventional imaging has a few disadvantages. For example, it can be challenging to differentiate between edema and the non-enhancing component of the tumor, as both appear hyperintense on T_2 MR images. Another current challenge is delineating tumor borders. Gliomas tend to be diffuse and in most cases their lesion is not clear and well differentiated due to their infiltrative growth. This in turn makes it extremely difficult to define a clear-cut boundary. In the monitoring of response after antitumor treatment, it can be hard to differentiate between tumor recurrence and treatment-related effects, often referred to as progression and pseudo-progression, respectively. Another challenge includes differentiating between pseudo-progression and radiation necrosis. The former mimics tumor progression through treatment induced inflammation, whereas the latter is caused by radiation damage to the brain and blood vessels. However, on conventional MRI such as T_2 weighted images, both appear hyperintense.

Advanced imaging techniques provide an opportunity to aid in differentiating between true tumor progression, pseudo-progression and radiation necrosis. For example, it could allow to visualize tumor specific metabolic and perfusion changes. The further refinement of imaging techniques might contribute to better decision-making and subsequently a better prognosis for patients⁵⁶.

1.3 Advanced MR imaging for gliomas

The advancement of MR imaging techniques has brought new opportunities to non-invasively characterize gliomas and surrounding tissue¹⁵. Capturing more detailed tumor characteristics could aid in a more complete diagnostic understanding of the different glioma molecular

subtypes recently established by the WHO¹⁰. For treatment it could mean establishing a more targeted treatment plan based on the tumor's genetic and molecular makeup. For treatment follow-up more accurately distinguishing true tumor progression, pseudo-progression and radiation necrosis is of the highest importance. The opportunities for advanced MR imaging techniques in improving glioma standard of care are well recognized. This is why extensive research has also been carried out on trying to image pathophysiological characteristics of gliomas: increased vascular needs and abnormal metabolism¹⁶⁻¹⁹.

One of the hallmarks of cancer includes neo-angiogenesis where new blood vessels are formed to provide enough oxygen and nutrients for tumor growth²⁰. Perfusion imaging is one of the advanced MR imaging techniques that seeks to measure the blood flow to tumors. This indirect measure of tumor vascularity has shown to be valuable for characterizing gliomas using modalities such as dynamic susceptibility contrast (DSC) and arterial spin labeling (ASL) MRI.

DSC is based on monitoring the first passage (or more precisely approximately the first 1-2 minutes after injection) of contrast agent through tissue. From DSC it is possible to estimate the relative cerebral blood volume (rCBV), and the ratio with contralateral tissue has been shown to help predict tumor-grades and stratify patients based on their survival prognosis^{21,22}, as well as identifying differences regarding IDH1 mutation and MGMT status²³. An interesting case report has also shown through histopathology that aggressive recurrent tumor tissue exhibits high rCBV, while low rCBV corresponded to non-tumorous tissue²⁴. Lastly, DSC has shown to have one of the highest diagnostic accuracies for differentiating between true- and pseudo-progression in high-grade gliomas, and the highest specificity (0.88 [0.70 – 0.96])²⁵.

ASL allows to non-invasively quantify cerebral blood flow (CBF) by using the blood as endogenous tracer. ASL-based perfusion maps are generally found to show increased signal-intensities in gliomas compared to the healthy appearing brain²⁶. Studies have demonstrated the ability to differentiate between tumor grades based on maximum signal intensity in the tumors region compared to contralateral healthy tissue. It is known that glioblastomas have an increase in metabolic demands and therefore perfusion, compared to lower grade tumors which typically have a lower blood flow^{27,28}. ASL has also been shown to be useful to predict IDH1 mutation and MGMT promoter status, which are relevant concerning survival prognosis and treatment response, respectively²⁹. Although deemed valuable and already applied in some clinical centra, these advanced perfusion modalities are not yet widely available, partly due to technical constraints and lack of standardization^{16,18}. ASL has also shown to increase sensitivity and specificity to distinguish between true- and pseudo progression, especially when combined with DSC²⁵. One study has even concluded that ASL has sufficient diagnostic accuracy to potentially replace DSC-MRI and in this way avoid higher doses of contrast agent³⁰.

Another hallmark of cancer is deregulated cellular metabolism, where the metabolic needs and byproducts differ from those of healthy cells²⁰. Consequently, advanced MR imaging can be valuable for capturing the abnormal metabolic behavior of gliomas. Proton magnetic resonance

spectroscopy (1H-MRS) is an MR modality that can non-invasively measure metabolites in gliomas. It is useful, for instance, in differentiating between glioblastoma and lower-grade gliomas³¹. Additionally, the oncometabolite 2-hydroxyglutarate (2-HG), which accumulates due to the IDH mutation, has recently gained attention for its significant diagnostic performance when measured with 1H-MRS³².

A more recent technique, chemical exchange saturation transfer (CEST), is another modality which allows to indirectly measure metabolites³³. In Chapter 2 this technique is introduced in more detail, including its methodology and value in glioma imaging.

1.4 Ultra-high field imaging

Another advancement in glioma imaging has been the utilization of ultra-high field (UHF) MR. UHF systems operate at magnetic field strengths of 7 Tesla and above³⁴. With stronger MRI systems, it is possible to obtain images with higher spatial resolution, larger spectral resolution and increased sensitivity³⁴. These advantages stem from improvements in signal-to-noise ratio (SNR), which scale super-linearly with the magnetic field (B_0)³⁴.

The benefits of UHF MR imaging for gliomas have been recently outlined³⁵. The main findings indicate that 7T MR imaging enhances the visualization of microbleeds, allows for quantification and characterization of blood vessels in glioblastomas, improves contrast between gray and white matter, and can refine radiotherapy planning^{36–38}. The latter was investigated by comparing the ability to delineate radiotherapy targeted volumes between clinical MRI scans and 7T T₂-FLAIR. The 7T image allowed to significantly reduce the targeted volume leading to the idea that healthy tissue can in this way be spared during treatment³⁷.

Additionally, advanced MR imaging modalities, such as CEST, can also benefit from the increased magnetic field strength due to enhanced spectral resolution, specificity to protons with high exchange rates, and longer water T₁, which amplifies the CEST effect³⁹. These characteristics can improve the specificity to the proton group of interest when acquiring CEST images. Few clinical studies have explored these advantages for glioma endogenous CEST contrasts at 7T^{40–47}. Nuclear Overhauser effect (NOE)-mediated and amide protein transfer (APT) CEST contrasts were found to be higher in the tumor areas and overlapped with gadolinium weighted T₁ tumor lesions, respectively^{40,41}. Moreover, NOE-CEST contrast at 7T has been found to aid in differentiating between high and low-grade gliomas⁴³. Conversely, NOE-suppressed APT-CEST at 7T has shown potential in predicting Isocitrate Dehydrogenase (IDH) mutation status and differentiating between high and low-grade gliomas, although it did not predict MGMT promoter methylation status^{42,44}. Interestingly, APT-CEST was found to provide higher contrast in gliomas located in the right hemisphere compared to the left. Finally, NOE-suppressed APT-CEST contrast at 7T appears to significantly differ according to patient's response to treatment⁴⁶. Recently, glutamate-CEST at 7T was shown to be significantly associated with recent epileptic seizure and drug-refractory epilepsy, suggesting glutamate's role in glioma-associated seizures⁴⁵.

1.5 Goals and outline of this thesis

The overarching goal of this thesis is to explore the value of advanced MRI modalities for imaging gliomas. The first goal is to evaluate the use of CEST at ultra-high-field at 7T to characterize these brain tumors. The second goal is to investigate how ultra-high-field imaging at 7T can aid in answering current clinical challenges in the assessment of gliomas.

This thesis starts with a Chapter introducing CEST imaging, reviewing recent literature and contextualizing its clinical relevance for gliomas (Chapter 2). This Chapter is part of an extensive literature overview on advanced MRI techniques for preoperative glioma characterization.

Hereafter the thesis dives into the methodology of CEST, where the feasibility of a novel and advanced image analysis technique, variable delay multi pulse (VDMP) is investigated to separately assess the different CEST pools in the human brain (Chapter 3). The goal of Chapter 4 was to determine what the most optimal image acquisition protocol parameters would be to image the CEST amines pools. Initially simulations and phantom work were performed. From these *in vitro* findings, the acquisition parameters were then applied for image acquisition *in vivo*. Together with MRS the metabolite contributor to the amines CEST contrast observed was determined. The final chapter (Chapter 5) on CEST consisted of investigating the use of 2 ppm CEST pool contrast to non-invasively differentiate between the enhancing and non-enhancing (parts of) glioma lesions.

The second part of the thesis aimed at exploring novel modalities to respond to current clinical challenges, namely treatment planning and the differentiation between true- and pseudo-tumor progression. Chapter 6 addresses the comparison between high-quality 7T MR imaging and clinical MRI in assessing tumor extension, volume and shape characteristics of the hyperintense component of gliomas. In Chapter 7 a clustering analysis method was applied based on radiological perfusion characteristics retrieved from clinical DSC and ASL imaging to identify different phenotypes of gliomas. Ultimately the goal was to form groups on the basis of these phenotypes which would share similar clinical outcome.

2 Chemical Exchange Saturation Transfer for Preoperative Glioma Characterization

Bárbara Schmitz-Abecassis
Ece Ercan
Mina Kim
Laura Mancini

This chapter is part of the CEST subsection of the following article:
Advanced MR Techniques for Preoperative Glioma Characterization: Part 2.
Journal of Magnetic Resonance Imaging (2023). DOI:10.1002/jmri.28663

2.1 Overview

CEST imaging enables the acquisition of information from proteins, peptides, and small molecules, which are not detectable with conventional MRI due to their low concentration in tissue. Specifically, CEST selectively saturates the magnetization of solute molecules with exchangeable protons that resonate at a frequency different from water³³. This saturation results in a decrease in water magnetization, creating a new contrast associated with the solute pool⁴⁸. By exploiting the chemical exchange of exchangeable protons, CEST obtains indirect high-resolution images from the solute pool⁴⁹. In a typical CEST sequence, a saturation period is followed by data acquisition⁴⁸, and the whole module is repeated while varying the saturation frequencies. Results are usually shown using a Z-spectrum, which presents the measured normalized water intensity as a function of saturation frequency⁴⁸.

Amide Proton Transfer (APT)-CEST imaging is the most studied CEST technique and refers to effects observed around 3.5 ppm downfield from water³³. APT-CEST is attributed to the slow-exchanging amides in proteins and correlates strongly with pH³³. The nuclear Overhauser effect (NOE) is another CEST effect that arises from mobile macromolecules, observed at around -3.5ppm⁴⁹.

Amine protons at 2 and 3 ppm from water that exchange at intermediate and fast rates, respectively, are found in important molecules, such as creatine, glutamate, and proteins. The detection of these exchanging pools has potential practical applications in the brain (tumors and associated epilepsy), muscle, and heart, motivating the development of appropriate CEST methods⁵⁰.

Glucose CEST (glucoCEST) relies on the injection of exogenous D-glucose to study tissue perfusion parameters, such as blood volume, blood–brain barrier (BBB) permeability, as well as tumor malignancy, without the need for a GBCA injection. This method provides more reliable results at 7T than at 3T⁵¹.

Isolating CEST contrast *in vivo* while controlling for multiple confounding effects requires advanced post-processing. A range of techniques is available, resulting in several potential metrics with which to describe the CEST effect. Asymmetry analysis (MTRasym) is an inherently simple approach, and its efficiency and ease of use have made this method popular in patient studies. However, different methods have been developed in response to the challenges encountered with MTRasym. These challenges include a macromolecular contribution due to the asymmetry of magnetization transfer effects and the contribution of NOE effects. Although a detailed description of these methods is beyond the scope of this paper, it is important to mention the most promising ones: water saturation shift referencing (WASSR); the three-offset method (APT*); MTRREX; the apparent relaxation due to exchange (AREX); the apparent APT ratio (APTR*); and Z-spectrum modulation as a combination of direct water saturation and solute pools of interest⁴⁹.

2.2 Clinical application

Because of its ability to reflect molecular changes, APT-CEST is used to study tumor microenvironment and metabolism *in vivo*⁴⁹, as demonstrated in Figure 1.

Cancer cells often exhibit structural, physiologic, and molecular changes and have an altered metabolic profile compared to healthy cells. Especially in high-grade gliomas, the level of peptides and mobile proteins is substantially increased compared to surrounding tissue⁵². An elevated protein content entails increased chemical exchange between the solute and bulk water. A good correlation has been demonstrated between endogenous protein profiles and APT-weighted signals in gliomas⁵³. Studies that have assessed APT-CEST have shown a sensitivity to differentiate tumor grades, with increased contrast in higher grades, and the ability to detect tumor aggressiveness⁵⁴. However, different studies have also shown that suppressing NOE contrast, often decreased in glioma compared to healthy-appearing brain tissue, allowed more reliable characterization of the enhancing lesions of glioblastomas and differentiation between glioma grades, considering the IDH mutations and MGMT methylation status⁵⁵. Investigating CEST contrast in relation to molecular and genetic markers is in line with the most recent 2021 WHO classification¹⁰.

The potential usefulness of APT-CEST for presurgical applications relies, in particular, on early detection and, consequently, propagation of more targeted treatment strategies, especially in the group of patients who do not show typical contrast enhancement on conventional T_1 -weighted imaging, although they harbor HGGs⁵⁶. Recent work by Warnert et al. aimed to use APT contrast to image non-enhancing gliomas and to more accurately distinguish tumorous from healthy tissue, based on tumor heterogeneity⁵⁷. Heterogeneous APT-CEST contrast was detected within these tumors, with a greater effect size of APT-CEST⁵⁷. Understanding the cause for the intra-tumoral contrast differences could include retrieving biopsies from APT-hyperintense lesions to correlate with histopathological observations and improve overall diagnosis⁵⁸.

Given the popularity and large body of work performed around this technique, recently published work has attempted to homogenize the application of APT-CEST in available clinical systems⁵⁹.

2.3 GlucoCEST

Since tumor cells utilize a glycolytic metabolic pathway, there will be an increase in glucose consumption. As such, glucoCEST imaging has been suggested to depict the saturation exchange between glucose-hydroxyl protons and water between 1.2 and 3 ppm⁶¹. Recent studies in glioma patients showed that the glucoCEST signal from dynamic glucose injection may reflect local blood flow, vascular permeability, and volume of the extracellular space, somewhat similar to what DCE T_1 -weighted MR does although the correlation between DCE and dynamic glucoCEST cannot be fully understood at the moment⁶⁰.

2.4 Amine CEST

Together with the glycolytic metabolism, the hypoxic microenvironment that is considered one of the major driving forces of tumorigenesis leads to intra- and extracellular acidosis in solid tumors, and these intracellular pH changes (pHi) may be evaluated using amine-CEST⁶¹. In addition, it has also been shown that increased levels of amine protons can be detected in regions of an active tumor where mobile glutamine (Gln) and other neutral amino acids are a major source of fuel for malignant tumors, and transport systems are often amplified to increase Gln consumption⁶².

Specifically, the amine CEST contrast at 2 ppm has been shown to correlate with Cr distribution in brain tumors, which is an essential metabolite in the process of converting adenosine diphosphate (ADP) to adenosine triphosphate (ATP)⁶³. A decrease in Cr CEST contrast was correlated with increased aggressiveness, and significant differences between the tumor and healthy brain regions have been observed, which most probably reflects the abnormal metabolism of gliomas in different malignancy states⁶⁴.

It has also been suggested that the amine and amide concentration-independent detection (AACID) signal from the ratio of the CEST effects generated by amide and amine protons from endogenous tissue proteins may be used to evaluate intracellular pH changes (pHi) in stroke⁶¹.

Moreover, the amines of glutamate (Glu) resonating at around 3 ppm have been shown to also play a role in CEST contrasts of gliomas. Neal et al. have shown that an increase in Glu concentration in the peritumoral area of diffuse gliomas is a result of altered Glu homeostasis⁴⁵. Altered Glu concentrations were associated with higher glioma aggressiveness, described by the enhancement on contrast-enhanced scans⁴⁵.

2.5 Validation

CEST, including APT, has not yet been widely implemented in clinical settings for glioma imaging. However, in a recent consensus publication, updated implementation guidelines have been defined. There has also been an effort from the industry to develop a clinical sequence, which has resulted in a commercially available APT-CEST product for clinical use. Yet, cross-vendor reproducibility has not been widely investigated. Most studies have, so far, focused on technical validation and, to some extent, have included clinical validation; however, a sizable multi-site comparison is still missing. Another challenge includes the lack of standardized diagnostic cut-off criteria, which would be essential for wide clinical use. Last, implementation, including data analysis and post-processing, would require special training and expertise. Once these translational challenges are tackled, CEST could be an interesting technique to adopt in glioma imaging.

2.6 Summary

In conclusion, CEST has shown potential as a novel technique that can provide unique endogenous contrast. APT-CEST yields the most promising results, evidenced by its popularity and high research output. Other CEST-based contrasts that derive from amine and glucose still need to demonstrate their value in larger cohorts. Overall, CEST is still in need of multi-site, multi-vendor clinical validation before it can be adopted for widespread glioma imaging in clinical practice.

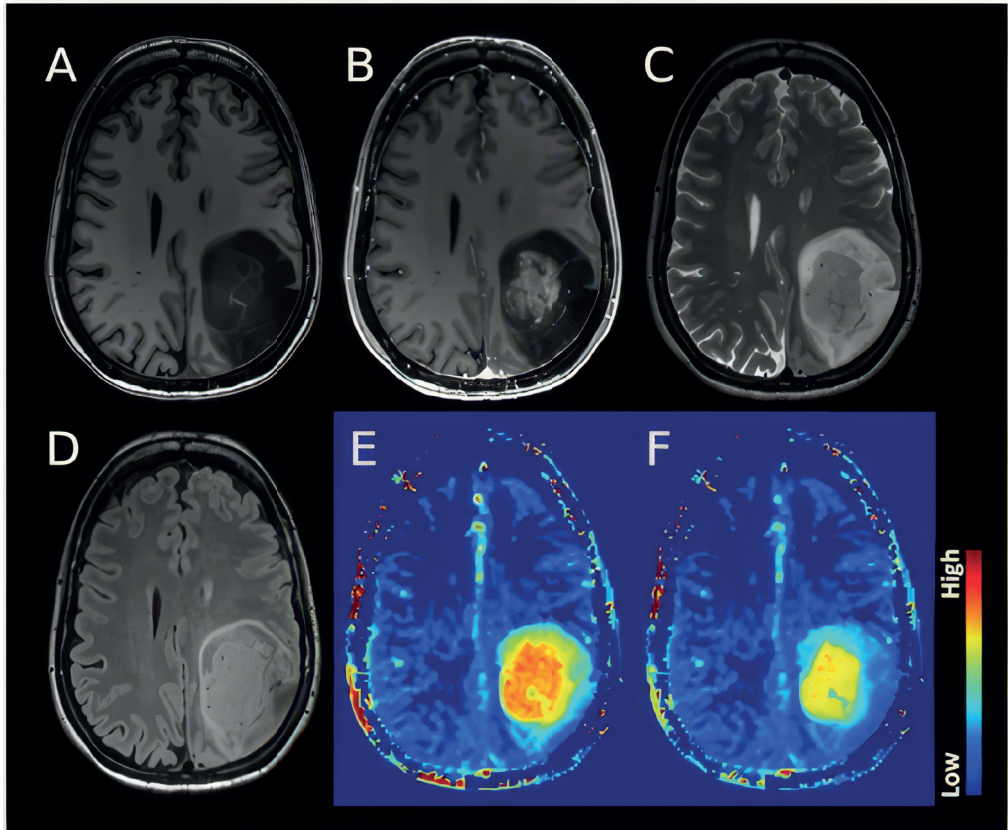


Figure 1. Example of an astrocytoma, IDH-mutant, 1p/19q retained, CNS WHO grade 4. The structural images (A: T_1w , B: T_1w post-Gd, C: T_2w , D: FLAIR) demonstrate a heterogeneous lesion with a rather solid central and well-enhancing part and a peripheral compartment demonstrating some T_2 /FLAIR mismatch without overt enhancement. The APT-weighted maps (E: standard APT CEST, F: fluid-suppressed APT CEST (Casagrande S et al. ISMRM 29th An Meet 2021)) show significantly elevated signal in the enhancing tumor, suggesting clearly high-grade features. Notably, the rim zone of the lesion shows variable degrees of APTw signal elevation in the fluid-suppressed images, thus suggesting that this compartment features mixed solid and cystic parts. Interestingly, the anterior rim zone, along with a halo surrounding the enhancing area, demonstrate a mildly elevated APTw signal that indicates likely high-grade metabolic tumor characteristics. The data were acquired on a Siemens 3T Prisma scanner. APTw protocol included $DC=91\%$, $B_1rms=2\mu T$, $Tsat=2s$, and WASAB1 for B_0 correction. WASAB1 and APTw data were processed in Olea Sphere 3.0 software (Olea Medical, La Ciotat, France).

3 The use of variable delay multipulse chemical exchange saturation transfer for separately assessing different CEST pools in the human brain at 7T

Bárbara Schmitz-Abecassis
Elena Vinogradov
Jannie P. Wijnen
Thijs van Harten
Evita Wieggers
Hans Hoogduin
Matthias J. P. van Osch
Ece Ercan

Magnetic Resonance in Medicine (2022). DOI: 10.1002/mrm.29005

3.1 Abstract

Current challenges of *in vivo* chemical exchange saturation transfer (CEST) imaging include overlapping signals from different pools. The overlap arises from closely resonating pools and/or the broad magnetization transfer contrast (MTC) from macromolecules. This study aimed to evaluate the feasibility of variable delay multi-pulse (VDMP) CEST to separately assess solute pools with different chemical exchange rates in the human brain *in vivo* while mitigating the Magnetization Transfer Contrast (MTC).

VDMP saturation build-up curves were simulated for amines, amides and relayed Nuclear Overhauser Effect. VDMP data was acquired from glutamate and BSA phantoms, and from 5 healthy volunteers at 7T. For the *in vivo* data, MTC removal was performed via a 3-pool Lorentzian-fitting. Different B_1 amplitudes and mixing times were used to evaluate CEST pools with different exchange rates.

Our results show the importance of removing MTC when applying VDMP *in vivo* and the influence of B_1 for distinguishing different pools. Finally, we report the optimal B_1 and mixing times to effectively saturate slow- and fast-exchanging components. Slow-exchanging amides and rNOE components could be distinguished when using $B_1 = 1\mu\text{T}$ and $t_{\text{mix}} = 10\text{ ms}$ and 40 ms , respectively. Fast exchanging components reached the highest saturation when using a $B_1 = 2.8\mu\text{T}$ and $t_{\text{mix}} = 0\text{ ms}$.

VDMP is a powerful CEST-editing tool, exploiting chemical exchange rate differences. After MTC removal, it allows to separately assess slow- and fast-exchanging solute pools in *in vivo* human brain.

3.2 Introduction

CEST has received increased attention in recent years given its ability to noninvasively image solutes such as proteins, peptides, and metabolites *in vivo*^{48,65}. Even with advantages as high spatial resolution and SNR, a crucial challenge of CEST is the quantification of CEST effects from different solutes in the human brain. This is mainly caused by an overlapping signal from different pools (eg, amide protons and amines, as well as the broad magnetization transfer contrast [MTC] effect), resulting in a lack of specificity to differentiate the CEST effect from different pools⁶⁶. Exploiting the differences in the exchange rates and using high or low B_1 amplitude to target a specific CEST pool of interest could improve the specificity in the observation of a certain CEST pool⁶⁶. However, the use of higher B_1 amplitudes results in a more pronounced MT effect and more direct saturation of water; thus it creates a stronger overlap with the semisolid macromolecular pool. Magnetization transfer ratio asymmetry analysis, a quantification method based on the subtraction of signals obtained with positive and negative offset with respect to the water frequency, has been widely used for eliminating MTC and quantifying the CEST effect from the solute pool of interest^{67,68}. Nevertheless, the lack of symmetry in the MT effect and the pronounced relayed nuclear Overhauser effect (rNOE) at 7T complicate the use of magnetization transfer ratio asymmetry analysis, especially at higher field strengths.

A relatively novel CEST method called variable- delay multipulse CEST (VDMP-CEST), was introduced to address this challenge⁶⁹. VDMP-CEST uses the interpulse delay (mixing times) of the pulsed CEST sequences as an exchange filter to exploit exchange rate differences of different CEST pools. Varying the mixing time allows the observation of differences in the saturation buildup depending on the intrinsic exchange rate properties of the solute pool of interest. For instance, amines, such as glutamate (Glu) and creatine, are fast-exchanging molecules with exchange rates of 700 Hz and higher, whereas amide and rNOE effects can originate from slow-exchanging molecules with exchange rates of 10 to 30 Hz^{70,71}. Amide effects with higher exchange rates (eg, 162 Hz and 365 Hz), but still lower than those of amines, were also reported in the literature⁷². Because of the difference in the exchange rate, it will take a longer time for the saturation to build-up for amides compared with amines. This is reflected in the buildup curves that show the change in Z magnetization as a function of mixing time. Therefore, amines are expected to have a rather quick saturation buildup profile compared with that of rNOE and amide pools, which would require a longer time to build-up saturation. To date, all VDMP-CEST applications but one were performed on phantoms and in *in vivo*

mouse models^{68,73,74}. Only one study showed the feasibility of VDMP-CEST in the human brain⁶⁸. In this study, only one B_1 amplitude was used and the buildup curves from different CEST pools in the human brain were not investigated. The use of different B_1 amplitudes, in addition to changing the mixing times, could further help separately evaluate the CEST effect from various CEST pools in the human brain. Moreover, VDMP does not account for MTC from macromolecules, hindering an accurate quantification of the CEST effect. A previous study

used subtraction of two different mixing times to suppress MTC in the human brain white matter (WM)⁶⁸. Because MTC varies in different tissue types, it is difficult to eliminate MTC in all brain regions through subtraction⁷⁵. Moreover, the use of different B_1 amplitudes will result in different levels of MTC contribution, and thus requires a more sophisticated method than subtraction to eliminate the MTC. In this study, we aimed to evaluate the potential utility of VDMP-CEST for exchange rate sensitive imaging and thereby to separately assess CEST effects from amide, amine, and rNOE pools. Our secondary goal was to evaluate VDMP-CEST in combination with MTC removal in *in vivo* human brain. These aims are achieved by simulations, phantom scans, and *in vivo* experiments of the human brain. First, we simulated the VDMP buildup curves of amide, amine, and rNOE pools. Second, for confirmation of the VDMP effects in the case of two pools, we used phantom experiments. Finally, we applied VDMP-CEST in the human brain at 7T using various B_1 amplitudes and removing the MTC via a three-pool Lorentzian model. We generated VDMP buildup curves from amide, amine, and rNOE pools after the MTC removal and investigated the evolution of VDMP buildup curves from these pools for different B_1 amplitudes.

3.3 Methods

3.3.1 Simulations

VDMP saturation buildup curves from CEST pools with different exchange rates in the human brain were simulated similar to that in a previous study⁷⁴. A two- pool model (water + one solute pool) was used to simulate two conditions: slow exchange and fast exchange. For slow- exchanging molecules, two cases were considered: amides (frequency offset $[\Delta] = 3.5$ ppm, exchange rate $[k_{sw}] = 30$ Hz) and rNOE ($\Delta = -3.5$ ppm, $k_{sw} = 16$ Hz). To represent fast-exchanging molecules, amines (Glu, $\Delta = 3$ ppm, $k_{sw} = 5500$ Hz) were simulated. Additionally, a three- pool model (water + two solute pools) was employed to simulate the overlap of amide and amine pools at 3 ppm (amide + amine). The details on simulations can be found in the Supporting Information.

3.3.2 Phantom preparation

One phantom consisting of three vials of 60 mL was prepared and assembled into one glass recipient filled with fomblin. To mimic the amine and amide proton exchangeable groups separately and in combination, the vials contained (1) a 50 mM solution of Glu, (2) 10% bovine serum albumin (BSA), and (3) a mixture solution of 10% BSA and 50 mM Glu. Details of phantom preparation are explained in the Supporting Information.

3.3.3 Human subjects

Six healthy female volunteers (Mean age: 28 years; SD = 4) were included in the study. Written informed consent was obtained from the volunteers. The study adhered to the local institutional review board guidelines and approval.

3.3.4 MRI scans

MRI acquisitions were performed on a whole-body 7T Achieva Philips MRI scanner (Philips Healthcare) equipped with a dual- transmit and a 32-channel receiver head coil (Nova Medical Inc.).

The scan protocol for the phantom and *in vivo* acquisitions consisted of a short survey scan, a SENSE reference scan, acquisition of a B_0 map to be used to perform third-order B_0 shimming, acquisition of a B_1 map using the dual refocusing echo acquisition mode (DREAM) sequence⁷⁶, and VDMP-CEST scans. The B_1 maps for each volunteer can be found in Supporting Information Figure S1. For *in vivo* scans, a MPRAGE sequence was additionally used to obtain 3D T_1 -weighted images to assess gray matter (GM) and WM tissue probabilities per voxel. Imaging parameters can be found in Table 1. For VDMP-CEST scans, a pulsed 3D CEST preparation was followed by a gradient echo readout with FLASH. Shim parameters obtained by third-order shimming were

used to improve B_0 inhomogeneities. CEST preparation employed 20 sinc-Gauss pulses of 20 ms duration. The VDMP-CEST pulse sequence is illustrated in Figure 1. A total of 29 frequencies with a step size of 107 Hz were acquired between -1500 and 1500 Hz. For normalization, an M_0 image was acquired at 500,000 Hz (around 1678 ppm). Seven mixing times (t_{mix}) were used (0, 10, 15, 20, 40, 60, 100 ms). For phantom scans, two different B_1 amplitudes were used: 2 μT and 3 μT . For *in vivo* scans, four different B_1 amplitudes were used (one per subject): 0.99 μT , 1.99 μT , 2.81 μT , and 3.26 μT . The B_1 amplitudes used and the corresponding B_1 average power for each mixing time are listed in Supporting Information Table S1. B_1 average power was defined as $B_1 \text{ avg power} = \sqrt{\frac{1}{\text{PTR}} \int_0^{\text{PTR}} B_1^2 dt}$, where B_1 is the B_1 amplitude of the pulse and pulse repetition time (PTR) is the sum of the pulse widths (t_p) and interpulse delays (t_{mix}), $\text{PTR} = t_p + t_{\text{mix}}$ ⁷⁷.

To investigate the role of B_1 average power during the whole saturation duration on the buildup curves, VDMP-CEST experiment was conducted on a fifth volunteer, while keeping a fixed B_1 average power (1.55 μT) and using the previously listed mixing times. To keep the B_1 average power the same for all mixing times, the B_1 amplitude was increased while increasing the t_{mix} . To investigate the reliability of Lorentzian fitting parameters, a sixth volunteer was scanned with a CEST sequence with B_1 amplitude of 0.99 μT , t_{mix} of 10 ms, and a larger frequency span between -75 000 and 75 000 Hz. More information on this acquisition is described in the Supporting Information.

Table 1. Image acquisition parameters represented for both phantom and *in vivo* experiments.

Imaging parameters	Phantom VDMP-CEST	<i>In vivo</i> VDMP-CEST	3D T_1 -weighted images	DREAM B_1 map
TR/TE/TI, ms	3.7 / 2	3.7 / 2	4.2 / 1.85	8.0 / 1.97
FA, degrees	5	5	7	10
FOV, mm ³	246 x 246 x 21	246 x 246 x 21	246 x 246 x 246	246 x 246 x 21
Voxel size, mm ³	1.5 x 1.5 x 3	1.5 x 1.5 x 3	0.9 x 0.9 x 0.9	1.5 x 1.5 x 1.5
TFE Factor	75	75	352	164
SENSE factor (RL/AP/ FH)	2/1/1	2/1/1	2.5/2/1	-
B_1 amplitude	2 μT & 3 μT	0.99 μT , 1.99 μT , 2.81 μT , 3.26 μT	-	-
Mixing times, ms	0, 10, 20, 40, 60, 80, 100	0, 10, 15, 20, 40, 60, 100	-	-
Total scan time, min	~ 42 min per B_1	~ 40 min per B_1	02:21 min	00:09 min

Abbreviations:

AP: anterior-posterior

FA: flip angle

FH: foot-head

RL: right-left

TFE: turb field echo

VDMP: variable delay multipluse

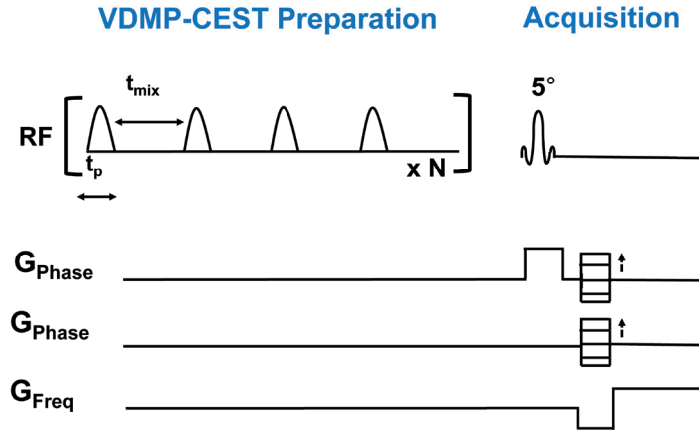


Figure 1. VDMP pulse sequence preparation, where the mixing time (t_{mix}) is illustrated as the interpulse delay. The total preparation time will also depend on the pulse duration (t_p) and the number of radio frequency (RF) pulses (N).

3.3.5 Image processing of the *in vivo* data

Probability maps of the GM and WM were retrieved from the 3D T_1 -weighted image using FMRIB (Functional Magnetic Resonance Imaging of the Brain) Software Library (FSL) v6.0.15. Segmentations were performed on the original 3D T_1 -weighted image. For this purpose, the skull was removed using the Brain Extraction Tool (BET) in FSL⁷⁸. Extracted brain images were segmented using fMRIB's automated segmentation tool (FAST)⁷⁹. The spatial volume estimation maps were registered to the CEST space using a resampler contained in the FreeSurfer package⁸⁰. A voxel was regarded as GM or WM if the partial volume estimation exceeded the threshold of 0.7.

3.3.6 Data analysis

Custom-written MATLAB scripts were used for data analysis. Corrections for B_0 field inhomogeneities were performed by spline interpolation followed by shifting of the Z-spectra based on the minimum Z determination. The reference scan acquired at a far offset (M_0 image) was used to normalize all CEST images. ROI-based assessment of the Z magnetization was done for both phantom and *in vivo* data over the frequency ranges by calculating the average of all voxels. For the phantom data, ROIs were manually drawn on each vial on the midslice (Supporting Information Figure S2) and VDMP saturation buildup curves for different pools were calculated for each ROI for all mixing times. For the human brain, the WM and GM buildup curves were evaluated within the midslice by masking the CEST data with the previously obtained GM and WM masks. For MT contrast removal in the *in vivo* data, $(1 - S/S_0)$ was calculated for each frequency of the Z-spectra from each mixing time. A three-pool Lorentzian model was fitted for each t_{mix} using the Levenberg–Marquardt algorithm⁸¹. The model used consisted of water, MT, and rNOE pools at fixed chemical shift values (0 ppm, 0 ppm, -3.5 ppm,

respectively). The initial point for the MT pool amplitude was defined as the signal amplitude of $(1 - S/S_0)$ at 5 ppm. The initial points, upper and lower boundaries of all fit parameters, are listed in the Supporting Information Table S2. The fitted MT pool was subsequently removed (subtracted) from $(1 - S/S_0)$. The MT- removed Z-spectra were used to assess the CEST signal at the frequency of interest (3.5 ppm for amides, 2 ppm for amines, and -3.5 ppm for rNOE) for each mixing time. VDMP saturation buildup curves were generated as a function of the ratio between the change in saturation $(S - S_0)$ and S_0 , for all the mixing times (t_{mix}). The VDMP curves were then normalized to the first mixing time ($t_{\text{mix}} = 0$ ms). The image processing and analysis pipeline for the *in vivo* data are shown in Figure 2. Based on VDMP buildup curves, the optimal B_1 and mixing time combinations were determined for amide, amine, and rNOE pools. Finally, voxel-based VDMP- CEST maps were generated by removing the MTC per voxel through the three-pool Lorentzian fittings as described above. The B_1 inhomogeneities were linearly corrected per voxel by using the B_1 map obtained from the same subject. The contrast of amide, amine, and rNOE pools was evaluated. The contrast observed corresponds to $(1 - S/S_0)$ after the MTC removal.

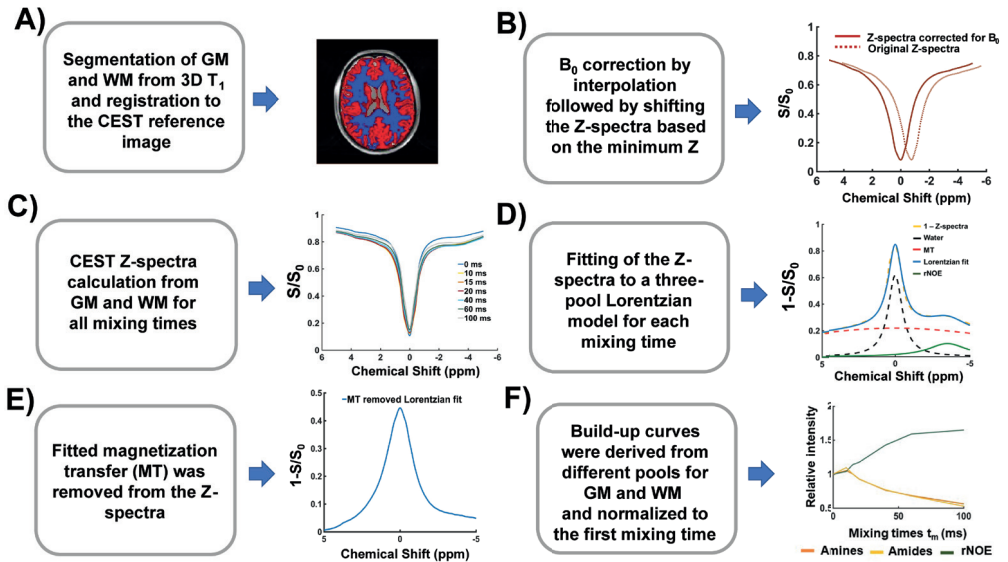


Figure 2. Image processing & analysis. A) gray matter (GM) and white matter (WM) were segmented from the 3D T_1 and registered to CEST space. B) B_0 field inhomogeneities corrections were performed by interpolation and shifting of the Z-spectra based on the minimum Z. C) Z-spectra were plotted for each mixing time from the average signal taken from the voxels in the GM and WM. D) Z-spectra from all mixing times were fitted to a three-pool Lorentzian model, for GM and WM. E) The MTC pool fitted in step (D) was subtracted from the Z-spectra. F) VDMP build-up curves were generated for GM and WM, for each B_1 amplitude, and normalized to the first mixing time.

3.4 Results

3.4.1 Simulations

Figure 3A shows the buildup curves that are simulated for amides, rNOE, and amines (Glu) using a two-pool model. Slow-exchanging pools (amides and rNOE) show a gradual saturation buildup, whereas a fast decay without a buildup is observed for the fast-exchanging amines. In Figure 3B, the buildup curve for the mixture of amide and amines (Glu) at 3 ppm, that is simulated using a three-pool model, is shown with the orange line. In this case, the buildup trend follows a similar trend to that from the amine-only pool, suggesting that the very fast-exchanging nature of amines dominates the overall signal. In Figure 3B, a similar graph is also displayed for a mixture of amide and amine (Glu) concentrations at 3 ppm using the Glu concentration in the human GM and WM. The dotted line represents the buildup curve of amines in the GM, where Glu concentrations are higher than in the WM.

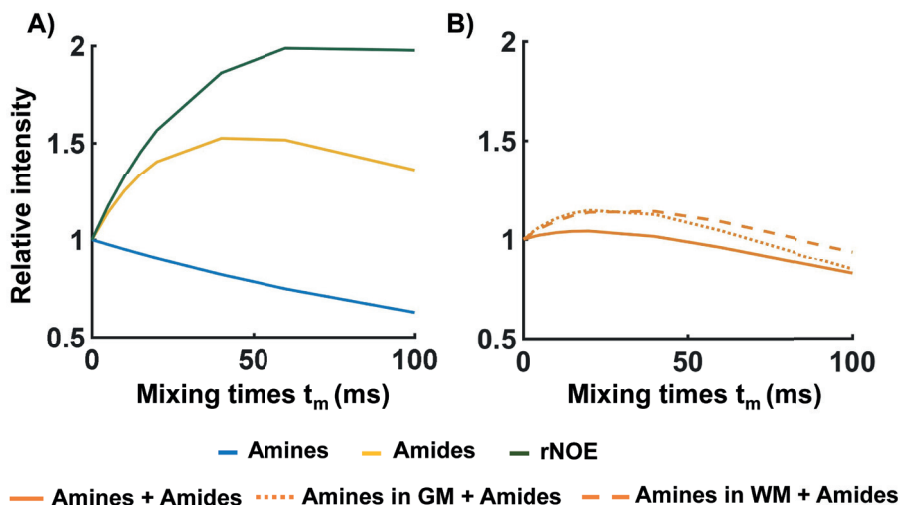


Figure 3. Simulated and normalized VDMP saturation build-up curves when A) a 2-pool (water + one solute) model was used for Amine, Amide and NOE pools individually. In B) a 3-pool model (water + amide + amine) was used to simulate the normalized build-up curves for a combination of amides and amines: when maintaining the same water T_1 value and solute pool fractions of amides and amines those used as in A (full orange line), and when the combination included Amine (glutamate) pool fractions and water T_1 values that are representative of the conditions found in the human brain gray (GM) (dotted orange line) and white matter (WM) (dashed orange line).

3.4.2 Phantom studies

Figure 4A illustrates the saturation buildup trend for the amide and rNOE pools in dotted and dashed lines, respectively, when a B_1 of 2 μ T is used. Both in the mixture phantom as well as in the 10% BSA phantom, both amide and rNOE slow-exchanging pools exhibit a slow buildup of saturation. A similar trend is seen in Figure 4B for a B_1 of 3 μ T. Whereas from the fast-exchanging

Glu pool, it is not possible to observe at which time point it reaches its saturation peak. Because the VDMP curves are normalized to the first mixing time, there is a continuous decrease in saturation across the mixing times as a result of T_1 relaxation⁶⁹. For a B_1 of 2 μT (Figure 4A), the signal from Glu (light-blue line) is not observable for $t_{\text{mix}} > 0$. However, a B_1 of 3 μT is sufficient to observe a more efficient saturation of Glu (Figure 4B). For both cases, the mixture phantom follows the same buildup trend at 3 ppm (dark-blue solid line) and at 3.5 ppm (yellow dotted line), similar to the trend of amides from a BSA- only phantom (green dotted line).

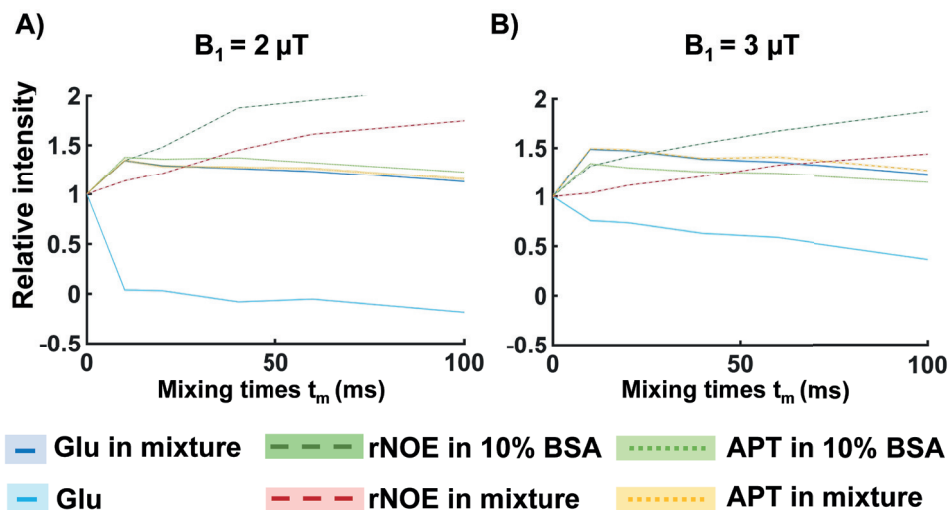


Figure 4. VDMP saturation build-up curves from the phantom experiment (normalized to the first t_{mix}). The signal from individual phantoms and from the mixture phantom were presented with separate lines. NOE (dashed lines) and amide (dotted lines) are retrieved from the 10% BSA and mixture (50 mM glutamate and 10% BSA) phantom. Full light and dark blue lines represent glutamate from the single and mixture phantom, respectively. B_1 amplitude per pulse unit was 2 μT for (A) and 3 μT for (B).

3.4.3 Human studies

In Figure 5A, B, the Z-spectra obtained using a B_1 of 0.99 μT are shown for all t_{mix} from the GM and WM, respectively. When using a lower B_1 , a more evident rNOE contrast is observed at -3.5 ppm. This holds especially in the WM (Figure 5B). Independently of the mixing times, a broadening of the Z- spectra is observed with a higher B_1 value ($B_1 = 3.26 \mu\text{T}$). (Figure 5C,D), in line with a MTC increase at higher B_1 ⁴⁹. A trend of increased broadening with increasing B_1 was observed also for $B_1 = 1.99 \mu\text{T}$ and $B_1 = 2.81 \mu\text{T}$ (data not shown). The presence of MTC in *in vivo* human brain is notorious in VDMP-CEST buildup curves because all CEST pools buildup trends are similar to the one of the MT when MT removal is not applied (Figure 6A). Upon removing the MTC, a gradual buildup trend was observed for the slow-exchanging molecules (rNOE and amides), whereas a faster decay could be observed for fast-exchanging ones (amines), similar to the simulation and phantom results (Figure 6B). A rNOE curve displays significantly different

behavior than amide and amine pools, both in terms of buildup and the level-off, reflecting the slower and different (relayed) nature of the processes involved. The reliability of Lorentzian fittings was investigated based on the acquisition with a larger frequency span. Histograms of the fitting parameters are shown in the Supporting Information Figure S3. Except for the full-width half-maximum (FWHM) of NOE, which was restricted by the upper boundary for some WM voxels, none of the fit parameters were restricted by fit borders when all frequencies were used. A discrepancy was observed between the larger frequency span and a smaller subset of 27 frequency offsets for FWHM of MT and amplitude of rNOE. To investigate the influence of the B_1 on the saturation buildup trends of CEST pools in the human brain, MTC- removed VDMP build curves are plotted for different B_1 amplitudes (Figure 7, Supporting Information Figure S4). After MTC removal, rNOE follows a slow and gradual buildup of saturation, independently of the B_1 amplitude applied. The amide pool, although also slow exchanging, displays a more characteristic buildup in saturation when applying a B_1 of 0.99 μT and 1.99 μT (Figure 7A- D; respectively). Differences in saturation buildup curves of amides and amines were more evident with a B_1 of 3.26 μT /2.81 μT , where for the GM a fast decay trend from the amine pool is evident (similar to simulation and phantom results). Regardless of inherent concentration differences between GM and WM, B_1 of 0.99 μT and 2.81 μT /3.26 μT , are observed to be sensitive for separately assessing the saturation buildup of slow- and fast- exchanging components, respectively. Instead of keeping the B_1 amplitude per pulse the same, when a fixed B_1 average power was used for all mixing times, the VDMP curves were also dominated by the MTC (Supporting Information Figures S5 and S6). After removing MTC, the saturation of the pools could be observed, especially for the amide pool. However, the rNOE pool showed a less efficient saturation and a reduced buildup when a fixed B_1 average power of 1.55 μT was used for each mixing time. Because of the SAR restrictions, a B_1 average power scheme higher than 1.55 μT could not be used to acquire and observe buildup trends.

Based on VDMP buildup curves, the optimal B_1 and mixing time combinations were determined to be 0.99 μT and a t_{mix} of 10 ms and 40 ms for amide and rNOE pools, respectively. The optimal B_1 amplitude and mixing time to effectively saturate fast- exchanging amine pools were 2.81 μT /3.26 μT and 10/0 ms. Voxel-based VDMP maps corresponding to these B_1 and mixing times are shown in Figure 8. For the B_1 of 0.99 μT , the CEST effect from amides follows the same trend on the VDMP map (Supporting Information Figure S7) as the one observed in the buildup curves (Figure 7A): a higher CEST effect at $t_{\text{mix}} = 10$ ms followed by a decreasing CEST effect at t_{mix} of 40 ms and 100 ms. Similarly for the rNOE pool, the highest CEST effect is at $t_{\text{mix}} = 40$ ms with a B_1 of 0.99 μT , in line with the VDMP buildup curves. For the fast exchanging amines, the highest CEST effect is found at $t_{\text{mix}} = 10$ ms and 0 ms for a B_1 of 2.81 and 3.26 μT , respectively, as expected from the peak in saturation observed in the saturation buildup curves (Figure 8 and Supporting Information Figure S8). The mean signal intensity values ($1 - S/S_0$) for all the GM and WM voxels are reported in Supporting Information Table S3.

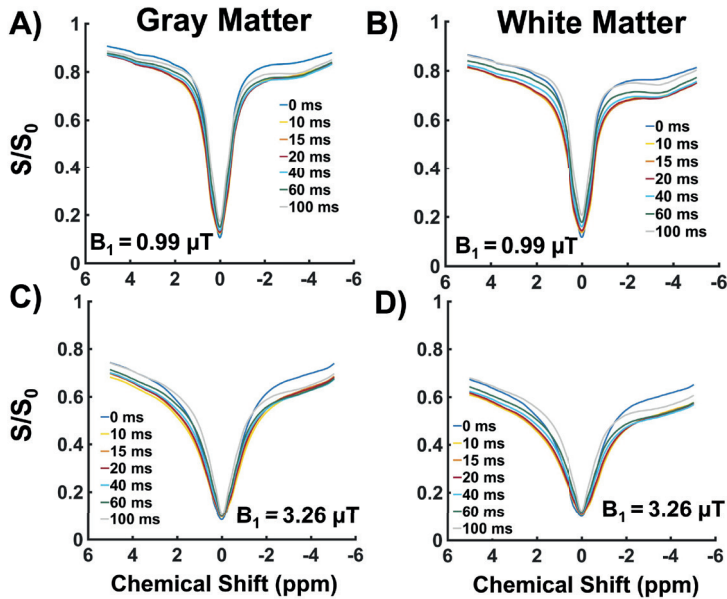


Figure 5. The B_0 corrected Z-spectra from the gray matter (GM) and white matter (WM) for the different mixing times before removing the MTC. In A) and B) the Z-spectra are displayed when having applied a B_1 amplitude of $0.99 \mu\text{T}$. In C) and D) the Z-spectra are shown when having adopted a higher B_1 amplitude of $3.26 \mu\text{T}$.

Gray Matter

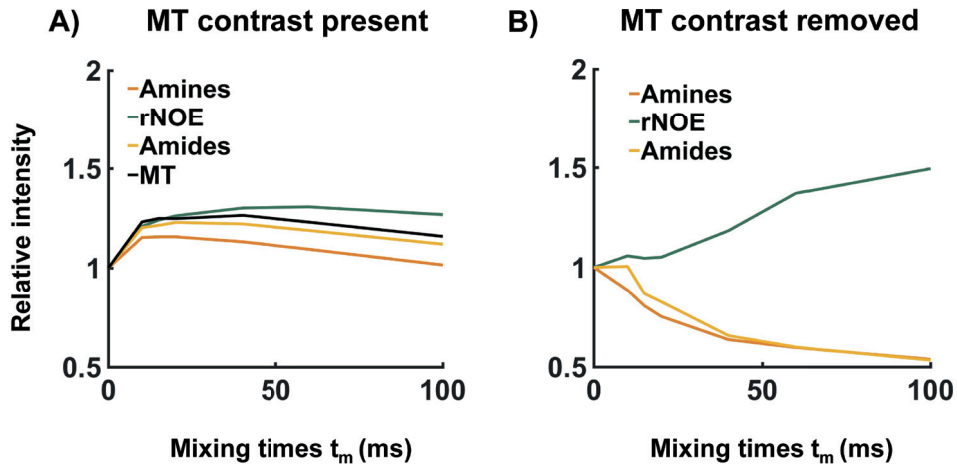


Figure 6. A typical example of the effect of MTC on the VDMP build-up curves from the human WM for $B_1 = 3.26 \mu\text{T}$. In A) the saturation build-up of the different CEST pools is plotted together with the MT contrast. In B) the MTC has been removed and the trend of the VDMP build-up curves from the CEST pools with different exchange rates can be distinguished.

3.5 Discussion

The aim of this study was to evaluate the potential of VDMP-CEST to assess *in vivo* proteins and metabolites in the human brain at 7T. The most salient finding of this study is the importance of removing MTC for *in vivo* VDMP applications in the human brain. By mitigating the MTC, the saturation buildup curves from amide, rNOE, and amine pools were shown for the first time from the human brain. Additionally, the influence of B_1 amplitude on the saturation efficiency was shown for different pools, suggesting the necessity to choose an optimal B_1 to separately evaluate slow- from fast-exchanging pools based on their VDMP saturation buildup curves. Finally, the optimal mixing time and B_1 combinations were reported for amide, rNOE, and amine pools in the human GM and WM.

Although VDMP-CEST is selective for fast- and slow-exchanging pools, the application *in vivo* suffers from an evident contribution from MTC (Figure 6)⁴⁹. Mitigating the MTC through Lorentzian fittings revealed the importance of MT removal when applying VDMP-CEST in the human brain. A previous study, aimed to suppress MT contrast, employed the subtraction of two images obtained with different mixing times⁸². An advantage of this subtraction method is that it is easily implemented. However, because of differences in molecular composition between different tissue compartments, different levels of MTC are expected for different voxels. Moreover, in diseased tissue, pathological processes yield to changes in MTC⁴⁹. This makes it difficult — if not impossible — to choose the two mixing times that would, after subtraction, eliminate the MT effect effectively within the whole image⁸³. A more recent study in mouse brain has used a model to fit VDMP buildup curves to extract the slow- and fast-exchanging MTC components. Because relatively high B_1 peak values (6 and 12 μ T) and large frequency offset ranges were used in this study, translating this approach into *in vivo* human studies would be complicated based on SAR constraints. Moreover, fitting slow-exchanging pool from VDMP curves makes it difficult to distinguish the slow MTC component from the other slow- exchanging pools such as amide and rNOE. Therefore, we proposed an alternative method, using a three-pool Lorentzian fit, which mitigates the MTC in the human GM and WM for each mixing time separately. This method was also extended to eliminate MTC on a voxel-by-voxel basis (Figure 8). Our results, in Figures 6 and 7, show that MTC removal with this method has a considerable impact on the VDMP buildup curve trends, making it possible to observe distinguishable buildup curves from amide, rNOE, and amine pools. Besides contributing to the MTC effect in the human brain, the B_1 amplitude of the applied RF pulses also has an impact on the saturation efficiency of the CEST pool of interest⁴⁹. To determine the ideal B_1 amplitude and saturation duration, Khlebnikov et al used Bloch- McConnell equation simulations and showed that slow- exchanging (16-30 Hz) amides required a lower B_1 (<1.5 μ T) and a longer saturation duration (>2.5 s).5 Fast-exchanging amines, such as Glu (exchange rate of ~5500 Hz), required higher B_1 (~6 μ T) and shorter saturation duration (<1 s) to achieve the maximum CEST effect⁶⁸. Translating these parameters to the human *in vivo* situation is challenging given the maximum allowed power and SAR limitations of human MRI scanners. We investigated the optimum B_1 for most efficiently detecting amide, rNOE, and amine. When studying the B_1

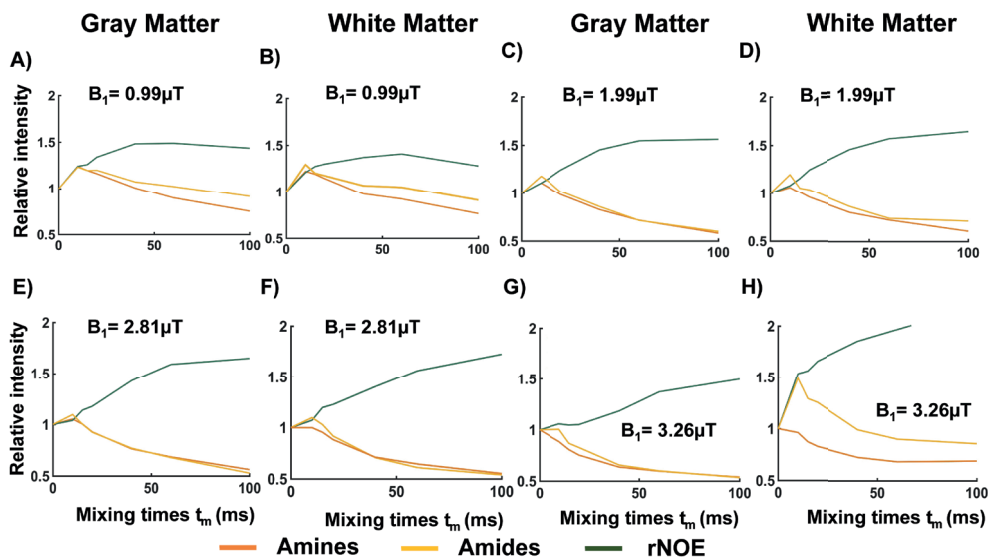


Figure 7. Normalized and MT removed VDMP saturation build-up curves for different mixing times, when the B_1 amplitude applied was 0.99 μT (A and B), 1.99 μT (C and D), 2.81 μT (E and F), and 3.26 μT (G and H), from gray (GM) and white matter (WM), respectively.

effect in controlled phantom experiments (Figure 4), we could observe that slower exchanging components (amides and rNOE) are more efficiently saturated when a lower B_1 is applied and hence leading to clear buildup trends for these pools without the contribution from fast-exchanging ones. In contrast, the fast-exchanging (amine CEST) pools could be observed mainly when using a higher B_1 (3 μT). Given the presence of protein amine CEST contrast in BSA, the exchanging components in this phantom cannot be exclusively attributed to rNOE and amide proton transfer. Rather, these are thought to be derived from amide CEST, aromatic NOE, and protein amine CEST⁸⁴. In our results from the human brain (Figures 7 and 8), we could observe that for both in the GM and WM, amides and rNOE were more efficiently saturated with a B_1 amplitude of 1 μT , similar to previous simulations results⁶⁶. This is also in line with previous *in vivo* CEST studies that focused on the slow-exchanging pools such as amide and rNOE in the human brain and brain tumors at 7T^{85–87}. For rNOE, an efficient saturation was achieved independently of the B_1 amplitude used. However, with a B_1 amplitude of 1 μT , the buildup trend reached a maximum value relatively earlier before the decay starts, eliminating the need to use very long mixing times, whereas amines were more efficiently saturated with a higher B_1 amplitude of around 2.81 μT /3.26 μT ⁸⁸. In heterogeneous tissue, where multiple solute pools are overlapping on their resonance frequency, the effect of the interpulse delay and B_1 amplitude could be used together to modulate the effect from different pools. We evaluated the optimal combination of B_1 amplitude and t_{mix} to achieve the most sensitive saturation buildup for different CEST pools present in the human brain. Our results (Figures 7 and 8) suggest that B_1 amplitude of 1 μT and t_{mix} of 10 ms and 40 ms are optimal to achieve the highest signal from amides and rNOE, respectively. This is in line with the slower exchanging nature of these

pools. Contrary to slow-exchanging components, which need a low B_1 amplitude and longer interpulse delays, high B_1 amplitude in combination with a short interpulse delay is needed to detect signal from fast-exchanging components because of their rapid saturation. The highest signal from amines were found using a B_1 amplitude of 2.81 μT /3.26 μT and with a combination of a very short ($t_{\text{mix}} = 10$ ms) or no interpulse delay ($t_{\text{mix}} = 0$ ms). The short time necessary to achieve maximum saturation highlights the fast-exchanging nature of amines, which is in accordance with previous studies from the human brain⁸⁸. A previous study explored VDMP for quantification of fast-exchanging metabolites⁷³. In agreement with our results, it was shown that Glu's signal in a phantom predominantly decayed for increasing mixing times⁷³. By using these optimal values, the CEST contrast observed on the voxel-based VDMP maps from amides, rNOE, and amines (Figure 8) were in accordance with the GM/WM distribution of the corresponding solutes, as well as the CEST effects observed from these molecules in GM and WM in previous work^{85,89–91}. Based on the voxel-based maps (data not shown), it is, however, not possible to specifically distinguish Glu that resonates at around 3 ppm from other possible amine groups (that resonate at around 2 ppm). For instance, creatine (amine group at 2 ppm) has a slightly slower exchange rate (810 Hz) than that of Glu (5500 Hz). However, the overlap of both pools in the frequency spectra makes separation too challenging⁹², whereas the saturation buildup curves of amines overlapped with those of amides at 3.5 ppm at lower B_1 amplitudes (<2.81 μT), contrary to what is observed at higher amplitudes ($B_1 = 2.81$ μT and 3.26 μT ; Figure 7). This suggests that fast-exchanging molecules were simply not observable at these lower B_1 amplitudes. Thus, when applying VDMP, the choice of B_1 can help in differentiating slow- and fast-exchanging pools. Slight differences between the voxel-based maps and the VDMP-curves might be explained by the fact that the later results from the average signal observed in the GM and WM. The simulations and phantom results (Figures 3 and 4) aimed to illustrate how VDMP buildup curves would display the saturation buildup of the CEST pools of interest in ideal conditions. In the present investigation, we could show how our *in vivo* data are — to a certain extent — in line with these results (Figures 3 and 4 vs Figures 6 and 7). Different factors derived from the heterogeneous nature of human brain tissue such as T_1 relaxation, MTC, and the eventual interplay between different compounds, play a role in the underlying CEST signal observed in our *in vivo* results.

Our study has some limitations. Our VDMP simulations did not consider the B_1 amplitude of the RF pulse. Therefore, simulation results are limited to show the effect of the number of VDMP pulses and duration, as well as the saturation buildup of the CEST pools of interest. Moreover, when calculating the Z-magnetization as an average of the imaged voxels, the quality of calculated CEST signal can be affected by the number of voxels included. Voxel-based VDMP maps were therefore investigated and corroborated the findings from the ROI-based results. Additionally, the number of VDMP pulses and their duration were kept constant for this study. Xu et al have shown through simulations that for a B_1 of 4 μT , the most efficient saturation buildup could be reached when using 16 to 32 pulses⁶⁹. Therefore, the number and amplitude of RF pulses were chosen accordingly to achieve a sufficient saturation within SAR limits and a feasible scanning time on a human 7T MRI scanner. It would be interesting to

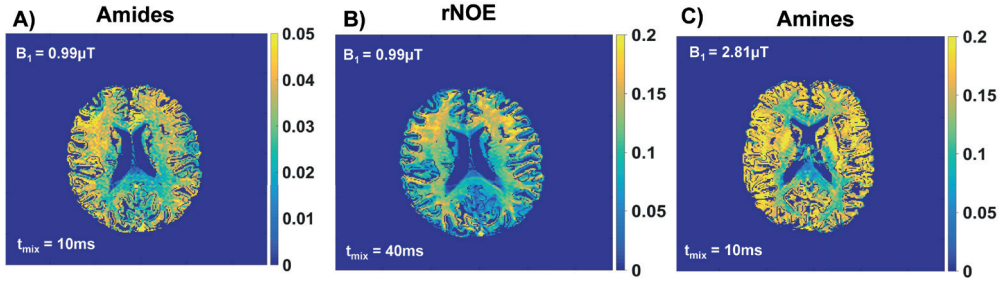


Figure 8. Voxel-based VDMP maps obtained using the optimal B₁ amplitude and mixing time (t_{mix}) where the most CEST effect is observed according to the saturation build-up curves, specifically for A) amides at 3.5ppm, B) rNOE -3.5 ppm and C) amines at 2 ppm.

investigate the relationship between the pulse duration and number, as well as B₁ amplitude, to better target specific CEST pools *in vivo* of the human brain at 7T. We also maintained the B₁ amplitude constant for each pulse, which results in a decrease of the B₁ average power with an increased interpulse delay. In one volunteer (Supporting Information Figures S5 and S6), we kept the B₁ average power constant for the entire saturation duration to investigate the effect of fixed B₁ average power. With the fixed B₁ average power, we observed a similar VDMP buildup trend for amines and amides, impairing pool differentiation (possibly caused by the use of low B₁ amplitude for shorter t_{mix}). This suggests that for overall saturation efficiency it is more valuable to fix the B₁ amplitude per pulse, independently from the mixing time. The T₂ of the evaluated pools were mostly longer than the pulse duration used (amide 100 ms, amine 200 ms, and rNOE 5 ms).²⁰ Therefore, the T₂ relaxation during the pulse is not expected to affect water protons for amide and amine pools, also in line with the previous explanation on how the VDMP pulses could serve as a T₂ filter⁶⁹. rNOE effects, however, are more complex and of a relayed nature. Further work is needed to investigate the influence of T₁ and the T₂ relaxation on the VDMP saturation buildup trends for these pools, as well as quantifying the contribution of slow- and fast-exchanging components, including multiple existent exchange rates per CEST pool. For instance, amine protons were also reported to be present in proteins, and were shown to contribute to amineCEST contrast in the rat brain⁹². In our study, we were not able to differentiate between the amineCEST contrast deriving from metabolites such as Glu and the ones from proteins. Finally, model-based fitting with predefined boundary values is a limitation, especially when a short frequency-offset range is used. The fittings were adequate for MTC removal; however, additional work is necessary to verify this method further *in vivo* and in pathology.

VDMP-CEST relies on the inherent differences in exchange rates of slow- and fast-exchanging solute pools. We have proposed a new method to mitigate the MTC effect in VDMP-CEST. By mitigating the MTC through Lorentzian fittings and using the mixing time as an exchange filter, we obtained the saturation buildup curves from amide, rNOE, and amine pools for the first time from the human brain. The MTC removal is essential to distinguish solute pools with

different exchange rates from the human brain *in vivo*. Moreover, the mixing time and maximum RF amplitude (B_1) should be carefully chosen to increase the specificity to the solute pool of interest. Our results suggest that VDMP has potential to mitigate the challenge to separately evaluate fast- and slow-exchanging CEST-pools in the human brain *in vivo*.

3.6 Acknowledgments

This study is part of the project “Non-Invasive Characterization of Active Multiple Sclerosis Lesions Through Chemical Exchange Saturation Transfer (CEST) Imaging” (project no. 16862) financed by the Dutch Research Council (NWO) Talent Programme Veni. This work was also funded by the Medical Delta Cancer Diagnostics 3.0 program.

3.7 Supporting information

3.7.1 Simulations

Using a two pool-model (water + one solute pool), we separately simulated the saturation build-up of relayed Nuclear Overhauser (rNOE), amide, and amine pools. The concentrations used to simulate rNOE (frequency offset (Δ) = - 3.5 ppm, exchange rate (k_{sw}) = 16 Hz), amides (Δ = 3.5 ppm, exchange rate (k_{sw}) = 30Hz), and amines in glutamate (Δ = 3 ppm, k_{sw} = 5500 Hz) were 0.1 M, 0.072 M, and 0.02 M respectively⁴⁹. The corresponding pool fractions were 0.00091 for rNOE, 0.00066 for amides, and 0.00055 for amines (glutamate). T_1 relaxation of water was assumed to be 2 s for the build-up curve simulations. Other parameters used for the simulations were the following: number of pulses: 20, pulse width: 0.02 s and mixing times: 0, 5, 10, 15, 20, 40, 60 and 100 ms.

In addition to these conditions, we used a three-pool model (water + two solute pools) to simulate the condition for a mixture of amine and amides. First, we considered the condition when the pool fractions of amides and amines were the ones described above (0.00066 for amides and 0.00055 for amines) and when T_1 relaxation of water was assumed to be 2 s⁴⁸. Additionally, we simulated the condition when the amide concentration is kept the same (as 0.072 M but the amine concentration (glutamate at 3 ppm) is set equal to the glutamate concentrations found in the human brain. We separately simulated glutamate concentrations typically found in the GM and WM, i.e. respectively 0.0115 M and 0.0066 M⁶⁶. The corresponding pool fractions for amines (glutamate) were 0.00031 in GM and 0.00018 in WM. For simulating amines in GM and WM, T_1 relaxation of water was adapted to 1.8 and 1.2 s, respectively⁶⁶. Other parameters used for these simulations were the following: number of pulses: 20, pulse width: 0.02 s and mixing times: 0, 5, 10, 15, 20, 40, 60 and 100 ms.

3.7.2 Phantom preparation

The mixture solution was made with the aim of observing combined CEST effect when both amide and amine groups are present in a solution. All solutions were prepared in deionized water and titrated to achieve a physiological pH of 7.3 (\pm 0.05). To scan the phantoms at a temperature closer to physiological conditions, a water-circulating blanket was placed around the phantom beaker and connected to a Blanketrol III hyper-hypothermia system (Cincinnati Sub-Zero, Cincinnati, OH, USA). Phantom temperature was monitored using a temperature probe that was placed inside the fomblin medium. The same heating set-up was kept during data acquisition. The temperature of the medium was 34°C during the CEST acquisitions.

Supporting Information Table S1. B_1 amplitudes used to acquire *in vivo* human brain VDMP-CEST images and the corresponding B_1 average power values for different mixing times.

Mixing times (ms)	0	10	15	20	40	60	100
B_1 amplitude (μ T)	$B_{1\text{ avg power}}$ (μ T)	$B_{1\text{ avg power}}$ (μ T)	$B_{1\text{ avg power}}$ (μ T)	$B_{1\text{ avg power}}$ (μ T)	$B_{1\text{ avg power}}$ (μ T)	$B_{1\text{ avg power}}$ (μ T)	$B_{1\text{ avg power}}$ (μ T)
0.99	1.17	0.96	0.89	0.83	0.68	0.59	0.48
1.99	2.35	1.92	1.77	1.66	1.36	1.17	0.96
2.81	3.31	2.70	2.50	2.34	1.91	1.66	1.35
3.26	3.85	3.14	2.91	2.72	2.22	1.92	1.57

3.7.3 Acquisition to investigate Lorentzian Fittings

To investigate the reliability of Lorentzian fitting parameters, a CEST sequence with a B_1 amplitude of 0.99 μ T and t_{mix} of 10 ms and a larger frequency span was employed. A total of 57 frequencies were acquired between -75000 and 75000 Hz with the following values: 75000, 60000, 45000, 33000, 24000, 18000, 13500, 10500, 8400, 6600, 5100, 3900, 3000, 2250, 1800, 1500, 1350, 1200,1050, 900, 750, 600, 450, 360, 270, 210, 150, 90, 0, -90, -150, -210, -270, -360, -450, -600, -750, -900, -1050, -1200, -1350, -1500, -1800, -2250, -3000, -3900, -5100, -6600, -8400, -10500, -13500, -18000, -24000, -33000, -45000, -60000, -75000. CEST preparation employed 20 sinc-gauss pulses of 20 ms duration. For normalization, an M_0 image was acquired at 80000 Hz. Histograms were made of fitting parameters when all 57 frequencies and when a subset of 27 frequencies between -1500 Hz and 1500 Hz are used.

Supporting Information Table S2. Parameters used for Lorentzian fittings.

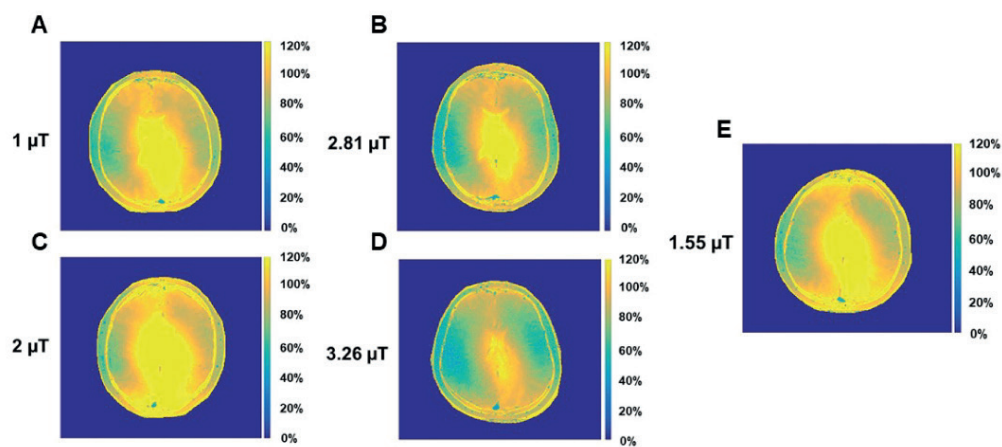
Parameter	Start	Lower Boundary	Upper Boundary
A_{water}	0.8	0.05	1
$\text{FWHM}_{\text{water}}$	1.4	0.3	10
A_{MT}	*	0.01	1
FWHM_{MT}	15	10	120
A_{NOE}	0.02	0.0	0.4
FWHM_{NOE}	3	1	5

A is the amplitude, FWHM is the full width at half maximum

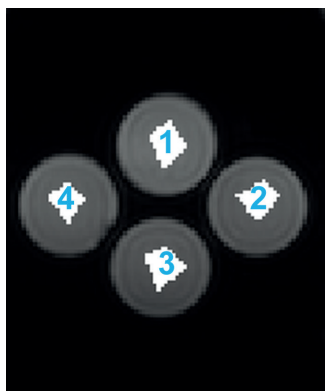
* The starting value of the MT pool was determined to be equal to the $(1-S/S_0)$ at 5 ppm for each spectra.

Supporting Information Table S3. Mean $1-S/S_0$ values from the gray matter and white matter voxels are reported for amide, rNOE and amines pool when using the most optimal B_1 and mixing time for each CEST pool detection.

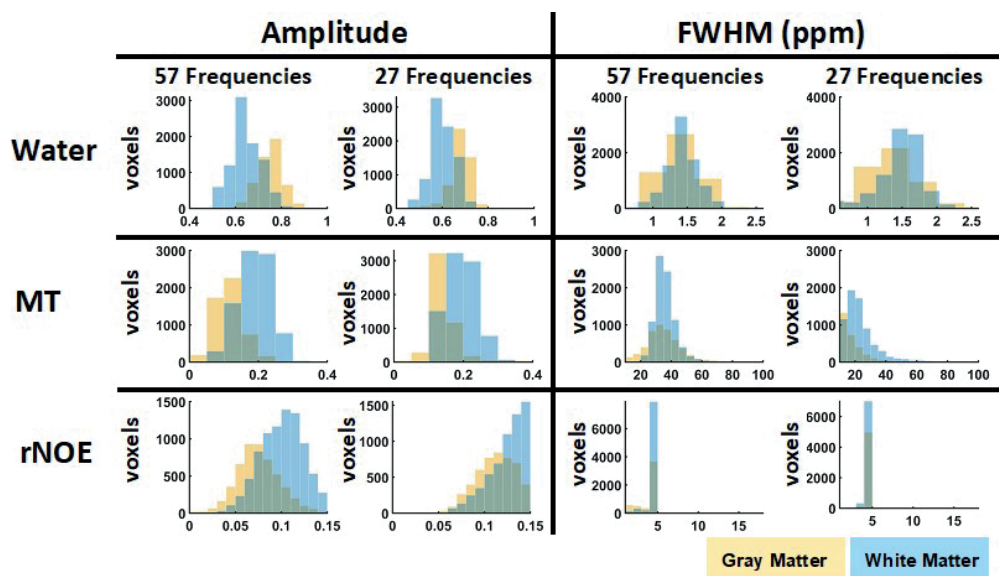
VDMP-CEST parameters / CEST pools	Gray matter			White matter		
	Amides	rNOE	Amines	Amides	rNOE	Amines
$B_1 = 2.81\mu\text{T}$ and $t_{\text{mix}} = 10\text{ ms}$	6%	7%	16%	5%	7%	14%
$B_1 = 0.99\mu\text{T}$ and $t_{\text{mix}} = 10\text{ ms}$	4%	8%	8%	3%	10%	8%
$B_1 = 0.99\mu\text{T}$ and $t_{\text{mix}} = 40\text{ ms}$	3%	9%	7%	3%	12%	6%



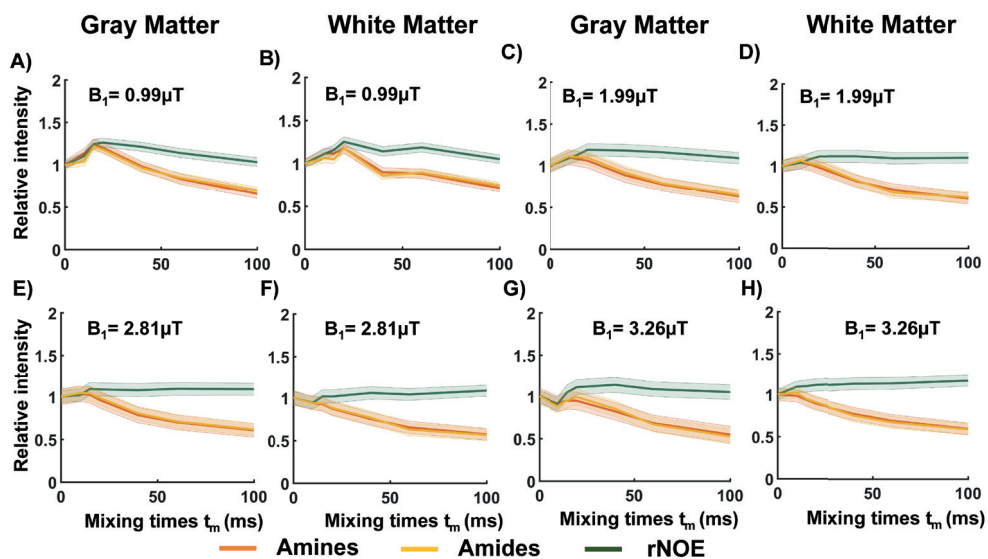
Supporting Information Figure S1. B_1 maps from the human brain, corresponding to volunteers scanned with different B_1 amplitudes: using a B_1 amplitude of 0.99 μT (A), 2.81 μT (B), 1.99 μT (C), 3.26 μT (D) and a fixed B_1 average power of 1.55 μT (E).



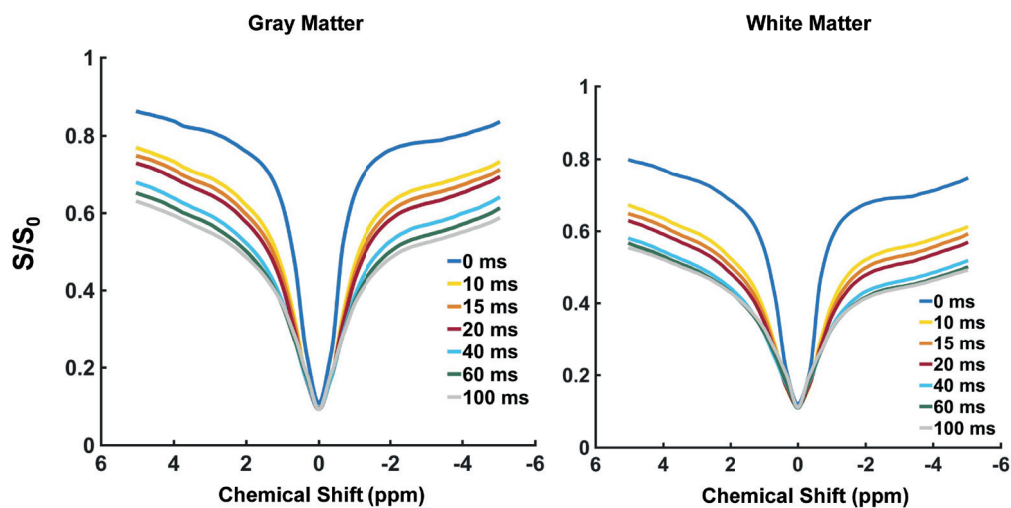
Supporting Information Figure S2. Region of interest (in white) overlaid on the CEST image from the phantom, for all different vials: 1) Glutamate, 2) Egg White (data not shown), 3) Mixture of glutamate and BSA 10% and 4) BSA 10%.



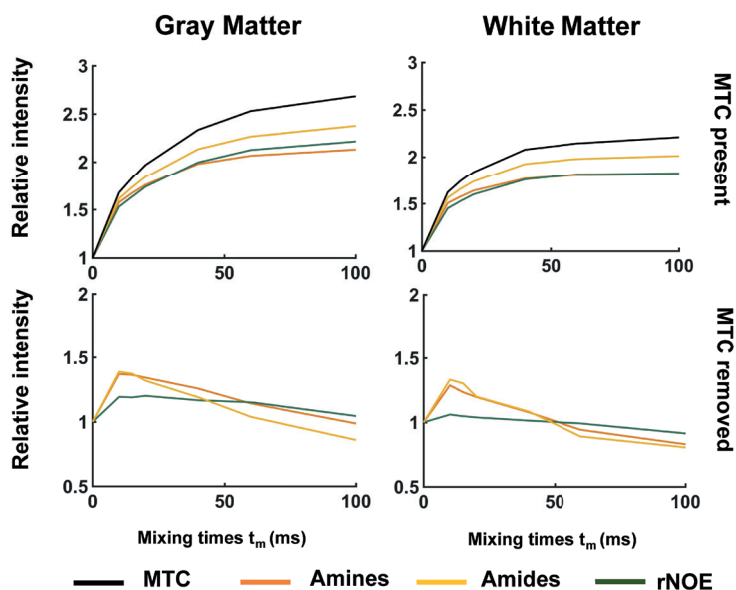
Supporting Information Figure S3. Histograms of the fitting parameters and corresponding number of voxels for gray and white matter respectively. The fitting parameters obtained using a larger frequency offset range (-75000 Hz to 750000 Hz) is compared with those obtained with a shorter frequency range (-1500 Hz to 1500 Hz).



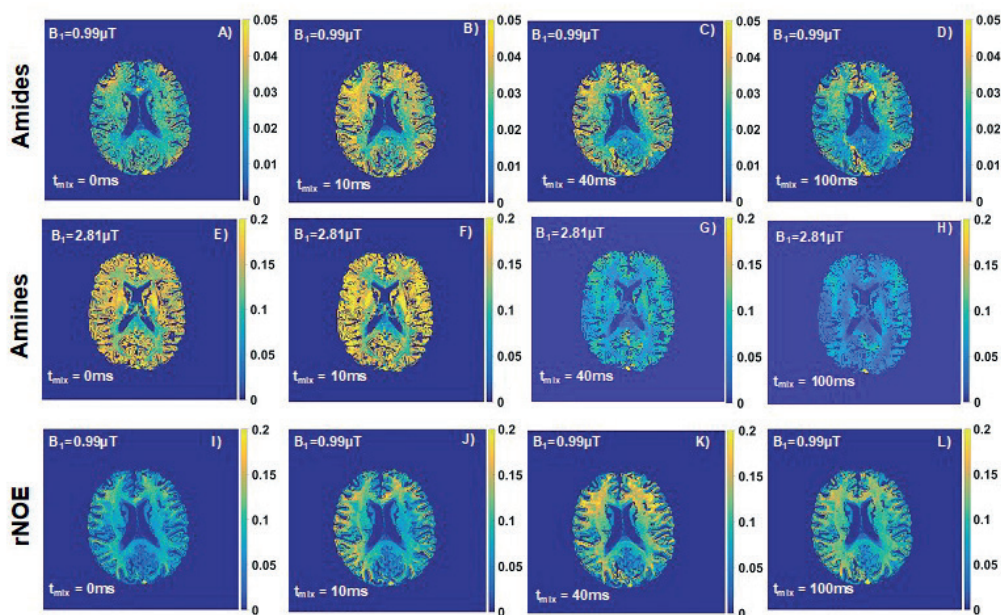
Supporting Information Figure S4. Average VDMP saturation build-up curves from all voxels included, and corresponding standard deviation, for different mixing times, when the B_1 amplitude applied was $0.99 \mu T$ (A and B), $1.99 \mu T$ (C and D), $2.81 \mu T$ (E and F), and $3.26 \mu T$ (G and H), from gray (GM) and white matter (WM), respectively.



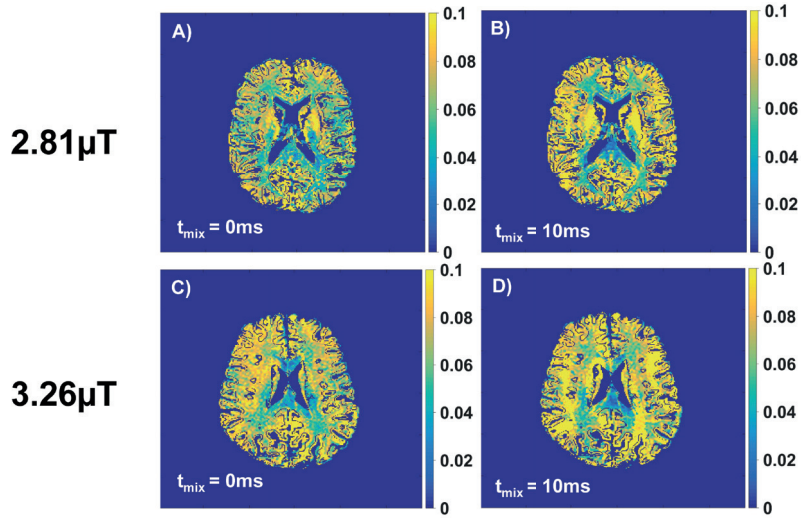
Supporting Information Figure S5. Z-spectra from *in vivo* human gray and white matter when scanning with a fixed B_1 average power of $1.55 \mu T$.



Supporting Information Figure S6. VDMP build-curves from *in vivo* human gray and white matter when scanning with a fixed B_1 average power of $1.55 \mu\text{T}$. In the upper row the magnetization transfer contrast is still present and in the lower row it has been removed.



Supporting Information Figure S7. B_1 corrected VDMP-CEST maps of the *in vivo* human gray and white matter from four different mixing times (t_{mix}) and acquired with the optimal B_1 amplitude, which results in the most efficient saturation for the CEST pool of interest.



Supporting Information Figure S8. B_1 corrected VDMP-CEST maps of amines contrast in the *in vivo* human gray and white matter of mixing times (t_{mix}) 10 ms at: A) $B_1 = 2.81 \mu\text{T}$ and mixing times (t_{mix}) 0ms, B) $B_1 = 2.81 \mu\text{T}$ and $t_{\text{mix}} = 10\text{ms}$, C) $B_1 = 3.26 \mu\text{T}$ and $t_{\text{mix}} = 0\text{ms}$ & D) $B_1 = 3.26 \mu\text{T}$ and $t_{\text{mix}} = 10\text{ms}$.

4 Investigation of metabolite correlates of CEST in the human brain at 7T

Bárbara Schmitz-Abecassis
Chloé Najac
Jaimy Plugge
Matthias J. P. van Osch
Ece Ercan

NMR in Biomedicine (2024). DOI: 10.1002/nbm.5104

4.1 Abstract

Metabolite-weighted chemical exchange saturation transfer MRI can be used to indirectly image metabolites such as creatine and glutamate. This study aims to further explore the contrast of CEST at 2 ppm in the human brain at 7T and investigate the metabolite correlates of CEST at 2 ppm via correlations with magnetic resonance spectroscopy (MRS).

Simulations were performed to establish the optimal acquisition parameters, such as total saturation time (t_{sat}) and B_1 root mean squared ($B_{1,\text{rms}}$) for CEST at 2 ppm in the human brain. Parameters were validated via *in vitro* phantom studies at 7T using concentrations, pH and temperature comparable to what is found in the human brain. Finally, 10 healthy volunteers were scanned at 7T for comparison with MRS.

Our results show that the optimal parameters to acquire CEST at 2 ppm images are: $B_{1,\text{rms}} = 2.14 \mu\text{T}$ & $t_{\text{sat}} = 1500 \text{ ms}$, respectively. Comparison with MRS showed no significant correlation between CEST at 2 ppm and total Creatine measured by MRS ($R = 0.19$; $p\text{-value} = 0.273$). However, a significant correlation was found between CEST at 2 ppm and Glu ($R = 0.39$; $p\text{-value} = 0.033$), indicating the broad Glutamate-weighted CEST as the main measurable contributor to CEST at 2 ppm.

We identified and confirmed optimal CEST at 2 ppm sequence parameters and validated CEST at 2 ppm measurements in a controlled *in vitro* environment. Our findings suggest that glutamate is a substantial contributor to the CEST at 2 ppm contrast observed in the human brain, whereas the creatine contribution to CEST at 2 ppm in the brain did not show a measurable contribution.

4.2 Introduction

Chemical exchange saturation transfer (CEST) MRI is an emerging technique which allows to non-invasively image endogenous metabolites and proteins *in vivo*⁴⁸. CEST is derived from the exchange of protons between the bulk water pool and the solute pool of interest. CEST contrast is achieved by applying a train of frequency specific RF pulses with a certain B_1 power to saturate the pool of interest and by measuring the decrease in the signal from the water pool due to chemical exchange. CEST is a very sensitive technique for *in vivo* metabolic imaging and highly benefits from ultra-high field (UHF) (e.g. 7T, 9.4T MRI), exploiting the advantage of higher SNR and higher spectral resolution at UHF.

Fast and intermediate exchanging CEST pools of guanidium and amine protons, resonating at approximately 2 and 3 ppm from the water signal, respectively, have gained recent interest given the presence of these protons in metabolites such as creatine (Cr) and glutamate (Glu)⁴⁹. The most popular examples of metabolite-weighted CEST include glutamate-weighted (CEST at 3 ppm) CEST for the brain and creatine-weighted (CEST at 2 ppm) CEST for brain and muscle^{90,93–95}. The alteration of CEST at 3 ppm contrast from amine protons has also been investigated in the scope of brain pathologies. Especially in epilepsy, CEST at 3 ppm has shown promise in identifying epileptic foci in patients⁹⁶. Similarly, in brain tumors, Neal et al. have shown increased CEST at 3 ppm in glioma associated epilepsy, specifically in the peritumoral area⁴⁵. CEST at 2 ppm, on the other hand, has mostly been explored for muscle imaging⁹⁴. Preclinical work by Cai et al. has been able to correlate the concentration of Cr and CEST at 2 ppm contrast as an indicator of brain tumor aggressiveness⁹⁷.

Differentiating between CEST at 2 ppm and CEST at 3 ppm pools in the brain can be challenging because of the proximity of their resonance spectra. While the exchange rates for CEST at 3 ppm and CEST at 2 ppm, and thus the optimal acquisition parameters for achieving maximum contrast, differ, other factors such as temperature and pH influence the resulting CEST effect^{66,98}. The origins of CEST at 3 ppm is for the most part well established, despite a recent study suggesting that CEST at 3 ppm in the rat brain is originating from amines in proteins⁹². Previous work has shown and validated the substantial contribution of glutamate to CEST at 3 ppm contrast in the brain of a similar animal model and of three healthy volunteers⁸⁸. However, limited work is available validating CEST at 2 ppm of the human brain *in vivo* at 7T. The optimal acquisition parameters and metabolite correlates of CEST at 2 ppm in the human brain at 7T is also yet to be established. Although Harris et al. have already investigated the feasibility of CEST at 2 ppm imaging in phantoms, this was not performed in the human brain at 7T. Singh et al. have carried out the phantom experiments at 7T, evaluating the feasibility of CEST at 2 ppm imaging using Z-spectral fittings as well as in a small group of four volunteers. However, phantom experiments did not include T_1 and T_2 corrections to match those of the brain, and the *in vivo* experiments did not include MR spectroscopy (MRS) validation to confirm the origins of CEST at 2 ppm or correlate the CEST at 2 ppm contrast with Cr concentration⁸⁹.

The aim of this study is to further explore CEST at 2 ppm contrast of the human brain and

to investigate the metabolite correlates of CEST at 2 ppm through comparison with MRS measurements at 7T. First, we simulated the CEST effect based on Bloch-McConnell equations to determine ideal B_1 and saturation time settings. Hereafter, we imaged phantoms made of Cr solutions to validate the optimized CEST acquisition parameters *in vitro*. Since CEST contrast is influenced by temperature, we also scanned a phantom at both room and body temperatures to determine to what extent this variation could influence the contrast obtained. Finally, we investigated metabolite correlates of CEST at 2 ppm of the human brain *in vivo* via comparison with magnetic resonance spectroscopy (MRS). To achieve this goal, we scanned 10 healthy volunteers using a 7T human MRI system and examined the correlation between tCr obtained from MRS and CEST at 2 ppm. Differently from previous studies^{66,88,92,99}, we also assessed if Glu has a contribution to the CEST at 2 ppm contrast, given the broad effect of the CEST at 2 ppm pool, and the closely resonating CEST at 3 ppm pool. We further computed for the apparent exchange-dependent relaxation (AREX) employing a multi-pool Lorentzian fitting of the *in vivo* data. This approach aimed to correct for competing CEST effects and T_1 scaling. The goal was to see if statistical results differed from those obtained using the conventional MTR asymmetry metric.

4.3 Methods

4.3.1 Simulations

CEST from Cr in the human brain was simulated via Bloch-McConnell equations, using a five-pool model, including Cr, Glu, NOE, water and magnetization transfer (MT) pools. The goal was to simulate the CEST MTR asymmetry when using different total saturation time (t_{sat}) and B_1 rms values, such that we could assess which parameter combination would yield maximum signal intensity. For each pool, we considered literature values of exchange rate constants, for spontaneous (k_o) and base (k_b) catalysis, respectively (Cr: $k_o = 0$ Hz and $k_b = 7.81 \cdot 10^9$ Hz; Glu: $k_o = 2.79 \cdot 10^3$ Hz and $k_b = 4.5 \cdot 10^{10}$ Hz; NOE: $k_o = 0$ Hz and $k_b = 16 \cdot 10^7$ Hz) as well as T_2 values at 7T (Cr: 7.1 ms and Glu: 6.9 ms). Both metabolite concentrations were kept at 10 mM to mimic the approximate conditions in the human brain. For water, T_1 and T_2 were 1.6 s 62 ms respectively. Lastly, MT was simulated as a semi-solid pool given the very short T_2 times (± 10 -5 s), thus we only considered its Z-magnetization¹⁰⁰.

4.3.2 Phantom preparation

Firstly, a phantom was prepared consisting of 10 vials of 60 ml each, which were placed in a glass container with Electronic Liquid FC-3283 (Fluorinert™, 3M™) embedding the tubes: (1) deionized water only, (2) a mixture of Cr (10 mM) and Glu (10 mM), (3-10) Cr or Glu with a range of concentration from 5 to 40 mM. Cr and Glu phantoms were made with N-Amidinosarcosine and L-Glutamic acid, respectively. Our objective was to establish a gradient of concentrations for the two metabolites, incorporating levels that closely approximate *in vivo* concentrations in the brain. Additionally, higher concentrations were included to evaluate the correlation between CEST and metabolites' concentration. Ultimately, the phantom was scanned at room temperature (21.5°C), at approximately 28°C, and finally at 36°C. The goal was to create a temperature gradient to observe how the CEST contrast would change as a function of temperature. Secondly, we prepared an additional phantom with 4 vials of 50 ml each. The goal was to match the metabolite concentration and correct for T_1 and T_2 relaxation times found in the human brain. These vials contained (1) deionized water, (2) 10 mM Cr and 10 mM Glu (3) 10 mM Cr and (4) 10 mM Glu, a range of concentration similar to previous studies⁷⁰. A total 0.5 mM of CuSO_4 and 1% agarose were added for T_1 and T_2 adjustments¹⁰¹. Initial optimization of CuSO_4 and 1% agarose concentrations showed no significant contributions of these compounds to the Z-Spectra, except for an expected slight MT effect (Supplementary Figure S4). All vials were titrated to achieve a physiological pH of approximately 7.3 (± 0.05). Both phantoms were first heated up at the desired temperature on a hot plate, whereafter transferred into the scanner once the desired temperature was reached. To maintain the temperature constant while scanning, a water-circulating blanket was placed around the phantom container and connected to a Blanketrol III hyper-hypothermia system (Cincinnati Sub-Zero, Cincinnati, OH, USA). The temperature was monitored during image acquisition with an MRI compatible thermometer probe immersed in the Electronic Liquid FC-3283 or Fomblin® perfluoropolyether (PFPE)

medium surrounding the phantom tubes.

4.3.3 *In vivo* data collection

We included 10 healthy volunteers (8 Females, 2 Males; 31.7 ± 16 years). The study adhered to the local Institutional Review Board guidelines and approval. All participants gave written informed consent.

MRI scans were acquired using a whole body 7T Philips Achieva MRI scanner (Philips Healthcare, Best, The Netherlands) equipped with a dual-transmit and a 32-channel receiver head coil (Nova Medical Inc, Wilmington, MA, USA).

The acquisition protocol included a short survey scan, a sensitivity encoding (SENSE) reference scan, a B_0 map for third order B_0 shimming, a dual refocusing echo acquisition mode (DREAM) B_1 map to assess B_1 distribution and a water saturation shift reference (WASSR) scan for post-processing B_0 correction¹⁰². For B_1 inhomogeneity mitigation, we placed two dielectric pads on the right and left side of the head. The dielectric pads were custom made as previously described by Teeuwisse et al 2012^{103,104}.

4.3.3.1 CEST

The CEST imaging acquisition protocol was based on the outcome of the simulation and phantom studies and consisted of two CEST scans. Firstly, to achieve an optimal CEST at 2 ppm contrast, a pulsed CEST preparation of 20 sinc-gauss pulses of 50 ms with 25 ms interpulse delay (t_{sat} of 1500 ms) and a B_1 rms of 2.14 μT was applied. Secondly, a pulsed CEST preparation of 20 sinc-gauss pulses of 40 ms with no interpulse delay (t_{sat} of 800 ms) and a B_1 rms of 3.3 μT was used to achieve an optimal CEST at 3 ppm contrast. Differently from previous Glu-CEST experiments that were all performed with the same human 7T platform of a different vendor and predominantly on one site, the interpulse delays used in our work were required to adhere SAR and RF amplifier requirements of the scanner used in our study. A total of 22 frequencies were acquired with a step size of 136.4 Hz between -1500 Hz and 1500 Hz. CEST acquisition details regarding the scans initially performed in phantoms for optimization can be found in the Supplementary Table S1.

4.3.3.2 MR Spectroscopy

The MRS acquisition protocol consisted of a short semi-LASER scan with a TE of 34 ms and TR of 6000 ms, 32 single acquisitions and a B_1 amplitude of 18 μT . Water suppression was achieved using the variable pulse power and optimization relaxation delays (VAPOR) sequence. Frequency offset corrected inversion (FOCI) refocusing pulses were used to minimize in-plane chemical shift displacement errors. In total, four voxels-of-interest (VOIs) were acquired with

the following dimensions: 30 mm x 15 mm x 25 mm. VOIs were placed (1) in the frontal and posterior-cingulate cortex (PCC) to maximize gray matter (GM) content and (2) in the left and right parietal white matter (WM) to maximize WM content, with the effort to minimize partial volume effect. A visual representation of the VOIs planning can be found in Figure 3. For each VOI, a separate water reference scan was acquired (same acquisition parameters, 2 single acquisitions).

4.3.4 Data analysis

4.3.4.1 Anatomical images

3D T_1 -weighted images were segmented into probabilistic tissue maps for WM, GM and cerebrospinal fluid (CSF) using FSL (Brain extraction Tool and FAST algorithm in the FMRIB Software Library)^{78,79}. A custom-build MATLAB routine was then used to create binary tissue maps (values are either 0 or 1, with 1 given to the tissue with highest probabilistic value) and quantify the volume of each tissue type within each MRS VOI. Maps were also used to mask CEST images to account only for voxels with GM and WM content above 70% (and thus limit partial volume effect).

4.3.4.2 CEST

The WASSR data was used for B_0 inhomogeneity correction. B_1 corrections were done according to the method previously described¹⁰⁵. The normalized, B_0 and B_1 corrected CEST images were then used to separately calculate the MTR asymmetry for 2 and 3 ppm CEST pools: $MTR_{asym} = \frac{Z(-x \text{ ppm}) - Z(+x \text{ ppm})}{Z(-x \text{ ppm})}$. We also fitted the data voxel wise to a five-pool Lorentzian model using the Levenberg-Marquardt algorithm⁸¹. More details can be found in the Supplementary Material. AREX was calculated per voxel as described in a previous publication¹⁰⁶.

The VOIs used for MRS acquisitions were used as masks to retrieve the CEST MTR asymmetry values.

4.3.4.3 MR Spectroscopy

Water-suppressed MRS spectra were corrected for eddy-currents and individual phase- and frequency-drift using a custom-built MATLAB routine and fitted with LCModel¹⁰⁷. A basis-set was generated using the FID-A toolbox¹⁰⁸. Non-water-suppressed data from same VOI were used for quantification. Water signal was corrected for GM, WM and cerebral spinal fluid (CSF) tissue fractions. Literature values for T_1 and T_2 relaxation time values of water in GM, WM and CSF as well as T_1 and T_2 relaxation time values of neurometabolites were used for correction¹⁰⁹. Cramer-rao lower bounds (CRLBs) for total creatine ($tCr = Cr + PCr$) and Glu were obtained

from LCModel output. Individual water acquisitions were inspected for any large phase or amplitude drop (which could be explained with subject movement). For one dataset in the PCC we observed a large phase change in one of the single acquisitions and excluded it before averaging all other single acquisitions.

4.3.5 Statistical analysis

To evaluate the *in vivo* correlation between CEST and MRS results, we employed linear correlation, calculating the Pearson's correlation coefficient for both the CEST MTR asymmetry and AREX values, along with the metabolite concentrations obtained through MRS. For significance inspection we performed a student's t-test, setting the significance threshold at $p < 0.05$. Statistics were performed in R version 4.1.2 (R Core Team (2021)).

4.4 Results

4.4.1 Simulations

Figure 1 illustrates the results of five-pool model simulations from CEST at 2 ppm for concentrations similar to those found in the human brain (10 mM) while taking the hardware limitations into account. The simulations showed that maximum CEST at 2 ppm value can be obtained with a t_{sat} of 1.5 s and a $B_1\text{rms}$ of 2.5 μT or a t_{sat} of 1 s and a $B_1\text{rms}$ of 3 μT . The areas in white on the right side of each map represent the acquisition parameter combinations that are not possible to achieve due to SAR and hardware limitations when imaging *in vivo*. In the Supplementary Figure S1A we show that as a comparison to CEST at 2 ppm, CEST at 3 ppm requires the maximum $B_1\text{rms}$ possible, which was approximately 3.5 μT , and a somewhat shorter t_{sat} of 1 s.

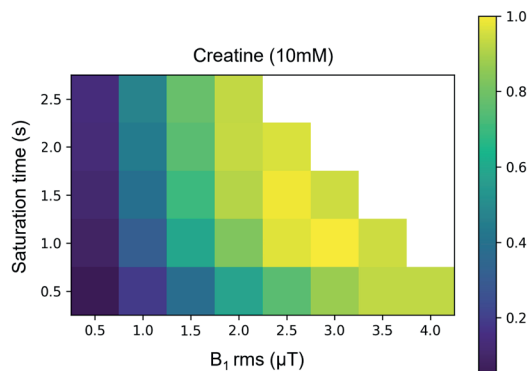


Figure 1. Normalized five-pool model simulation results. CEST MTR asymmetry was investigated as a function of varying $B_1\text{rms}$ and t_{sat} to find the optimal acquisition values for CEST at 2 ppm CEST, corresponding to the CEST pools at 2 ppm. The areas on the right side in white of each figure, represent the parameter combinations which were not experimented due to SAR limitations *in vivo*.

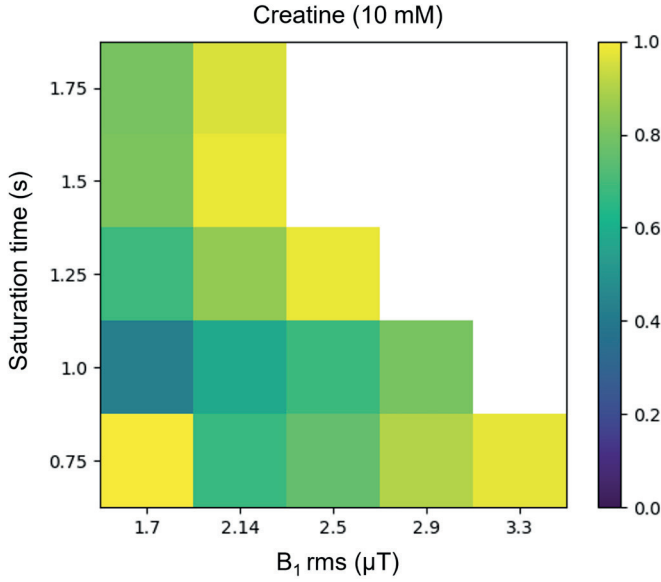


Figure 2. Phantom results normalized to the highest MTR asymmetry value. Maps illustrating how CEST at 2 ppm CEST changes as a function of total saturation time (s) and B_1 rms (μ T). The data shown corresponds to measurements of phantoms with a concentration of 10mM of creatine scanned at $\pm 36^\circ\text{C}$.

4.4.2 Phantoms

Figure 2 illustrates how CEST at 2 ppm changes *in vitro* at 36°C as a function of t_{sat} and B_1 rms. Results at other temperatures can be found in Supplementary Figure S3. We wanted to specifically assess the optimal parameters to achieve maximum CEST contrast in an ideal experimental setting before applying it *in vivo*. Our results confirm that maximum CEST at 2 ppm was reached when using a $t_{\text{sat}} = 1500$ ms and a B_1 rms of $2.14 \mu\text{T}$. Unexpectedly, a t_{sat} of 750 ms and a B_1 rms of $1.7 \mu\text{T}$ also yielded maximum CEST at 2 ppm. For CEST at 3 ppm, similarly to the literature, we found a t_{sat} of 750 ms and a B_1 rms of $3.3 \mu\text{T}$ yielded the maximum MTR asymmetry (Supplementary Figure S1B). Additionally, we found temperature to have a linear relation with CEST at 2 ppm MTR asymmetry, where a physiological temperature yielded higher CEST contrast than at room temperature (Supplementary Figure S3A). Interestingly, for CEST at 3 ppm MTR asymmetry we observed the opposite, an inverse relation between temperature and MTR asymmetry (Supplementary Figure S3B).

4.4.3 Healthy volunteers

Figure 3 shows a representative example of how the MRS VOIs were planned in the GM and WM. The corresponding MR spectra are displayed for each VOI alongside the fitted signals of interest: tCr and Glu. Both metabolites could be measured and the results presented here represent reflect the average findings from all included subjects: a similar concentration of tCr

in WM (VOI1: 6.6 mM \pm 0.4; VOI2: 6.6 mM \pm 0.3) and GM (VOI3: 6.6 \pm 0.7; VOI4: 6.6 mM \pm 0.5), and a higher concentration of Glu in the GM (VOI3: 8.7 mM \pm 0.7; VOI4: 8.3 mM \pm 0.6) compared to the WM (VOI1: 6.5 mM \pm 0.3; VOI2: 6.4 mM \pm 0.6).

Figure 4 shows the average Z-Spectra and MTR asymmetry of CEST at 2 ppm of the voxels within the MRS VOI1 and VOI2 in the WM and VOI3 and VOI4 in the GM. The MTR asymmetry peak appears to be more evident in the GM voxels, whereas in the WM, there seems to be a greater contribution from NOE.

CEST maps at 2 ppm are displayed in Figure 5 for two representative subjects, with respective B_0 and B_1 maps. CEST at 2 ppm maps generally exhibit high values, especially in the GM, whereas susceptibility to B_1 inhomogeneity resulted in a loss of contrast in the anatomical right side of the brain. This phenomenon appears consistent across different subjects (Figures 5A and 5B). In contrast, we observed a more homogeneous B_1 distribution in the CEST at 3 ppm maps (Supplementary Figures S5A and S5B). Supplementary Figures S7A and S7B show AREX maps from CEST at 2 ppm, where higher values can be observed in the WM compared to the GM, as AREX represents an inverse metric of steady-state Z-spectra.

For both MTR asymmetry and AREX, CEST at 2 ppm value distributions from all 10 subjects are displayed for the VOIs placed in the WM and in the GM in Figures 6A and 6B and Supplementary Figure S8, respectively. CEST at 2 ppm MTR asymmetry values are broadly distributed, mostly between 0-20% in both GM and WM VOIs whereas the AREX values range between 0-80%. CEST at 3 ppm MTR asymmetry is mostly distributed between -10 and 5% in the WM and tends towards higher values in the GM (-10% to 10%) (Figures 6C and 6D). Intra-tissue distribution variability (i.e. VOI1 vs VOI2 or VOI3 vs VOI4) is observed for both CEST pools, for both CEST at 2 ppm and CEST at 3 ppm distributions in the GM and WM, with slightly less variation for CEST at 3 ppm contrast in the WM Figure 6C).

Figures 7A and 7B demonstrate the correlation between metabolite concentrations measured in the GM and WM and the corresponding CEST at 2 ppm MTR asymmetry values. Figure 7A shows a non-significant correlation between tCr and CEST at 2 ppm contrast ($R = 0.19$; p -value = 0.273). However, in Figure 7B, a significant correlation was found between CEST at 2 ppm and Glu concentration ($R = 0.39$; p -value = 0.033). We conducted similar comparisons for the AREX, an inverse metric of the Z-spectra, which also accounts for MT and T_1 . In Figure 7C and 7D, similar to MTR asymmetry results, we found no correlation of AREX at 2 ppm and tCr ($R = 0.003$; p -value = 0.98) but an inverse significant correlation between AREX at 2 ppm and Glu ($R = 0.6$; p -value = 0.002). For internal validation, we also confirmed the significant correlation between the CEST at 3 ppm MTR asymmetry and Glu concentration ($R = 0.66$; p -value < 0.001) and did not find a significant correlation between CEST at 3 ppm MTR asymmetry and tCr ($R = 0.07$; $p = 0.681$) (Supplementary Figures 6SB and 6SA, respectively). Similarly, no correlation between CEST at 3 ppm and tCr was obtained using the AREX metric; however, also in this case, an inverse significant correlation between AREX at 3 ppm and Glu was obtained ($p = 0.010$; $R = 0.47$) (Supplementary Figures 6SC and 6SD).

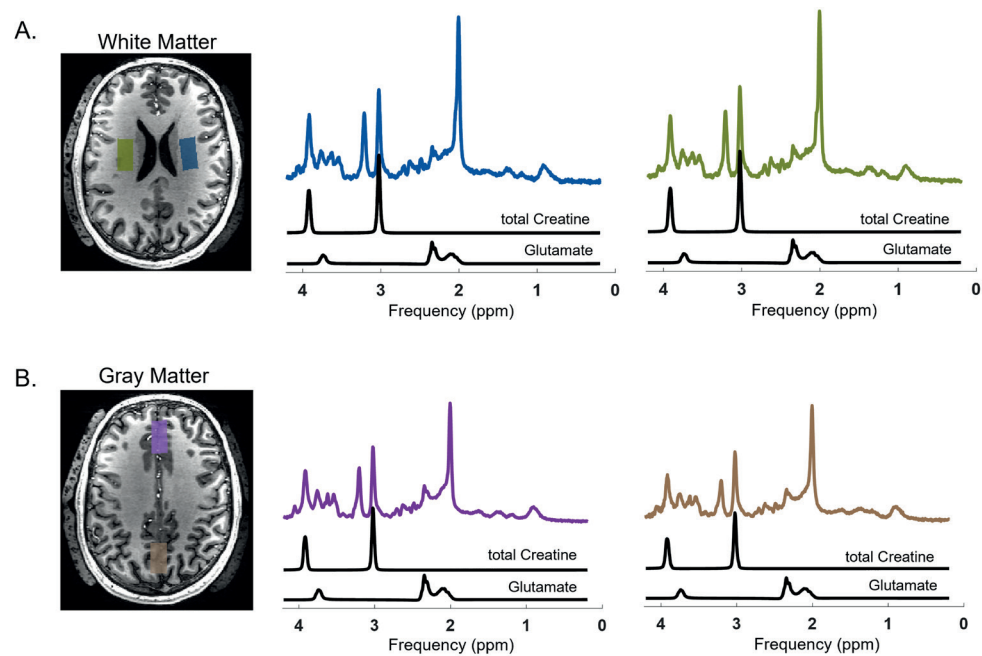


Figure 3. An example of how the MRS VOIs were planned and typical MRS results showing tCr and Glu fits from the WM (A) and from the GM (B). Outside of the skull area the dielectric pads can be seen.

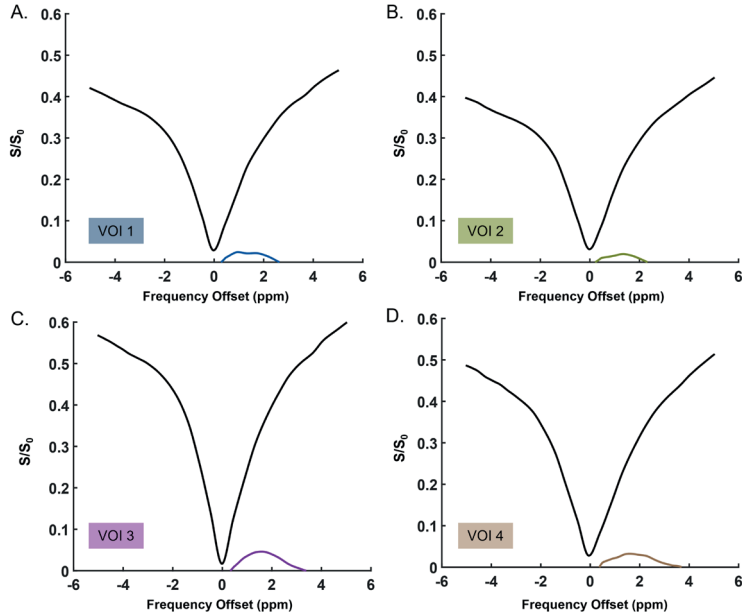


Figure 4. Average Z-Spectra and MTR asymmetry of the voxels in two VOIs in the White Matter (A & B) and Gray Matter (C & D). These results are from 1 representative volunteer.

4.5 Discussion and conclusions

The primary objective of our study was to further investigate CEST at 2 ppm in the human brain at 7T. Additionally, we conducted an internal validation of CEST at 3 ppm on a different 7T human MR platform than that predominantly used in previous studies in the literature. First, we identified optimal CEST at 2 ppm acquisition parameters in the human brain at 7T through simulations and confirmed them in phantoms *in vitro*. Subsequently, we evaluated the performance of the optimized sequences in the *in vivo* human brain using MRS as ground truth measurements of tCr and Glu concentrations. Our findings revealed a significant correlation between CEST at 2 ppm MTR asymmetry and Glu as measured by MRS, suggesting that glutamate is a substantial contributor to the observed CEST at 2 ppm contrast in the human brain. However, we did not observe a significant correlation between CEST at 2 ppm and Cr concentration in the brain.

Glutamate-weighted CEST imaging in the brain is gaining attention given its abundance and physiological role, supported by its visibility due to the presence of amine protons⁸⁸. Because of the involvement of Glu in pathologies such as epilepsy, the use of CEST for Glu imaging at 7T has been explored in at least three previous studies^{110–112}. Similarly, Cr is well known for playing an important role in tissue bioenergetics and is present in both muscles and brain aiding in adenosine triphosphate synthesis for cell energy requirements¹¹³. Cr, with its amine and guanidinium protons, is an interesting CEST contrast to be explored in *in vivo* human brain, especially considering its observed concentration changes in brain tumors¹¹⁴. Although both metabolites have amine protons, amines found in Glu resonate around 3 ppm from water with an exchange rate of approximately 5500 ± 500 Hz⁸⁸, while amines in Cr resonate around 2 ppm with an intermediate exchange rate of around 950 ± 100 Hz⁷⁰. Their neighboring frequencies and the overlap between these two pools creates a challenge of specificity to each pool. Nevertheless, by taking advantage of the inherent differences in the exchange rates of amines in Glu and Cr, we determined via simulations the optimal saturation length and power to achieve maximum saturation efficiency for both metabolites separately, while accounting for SAR and hardware limitations of human MRI scanners. Consistent with a previous study, our simulation results (Figure 1) showed that an intermediate B_1 rms with a long t_{sat} is essential to achieve maximum CEST at 2 ppm MTR asymmetry contrast. In the case of CEST at 3 ppm, our results corroborated previous findings on a human 7T system from a different vendor, emphasizing the need for a high B_1 rms with a shorter t_{sat} is needed to achieve high CEST at 3 ppm contrast^{66,99,115}.

Via *in vitro* experiments, we validated the simulation results and determined the optimal RF power (B_1 rms) and t_{sat} length to be: 2.14 μT & 1500 ms and 3.3 μT & 1000 ms, for CEST at 2 ppm and CEST at 3 ppm, respectively (Figure 2 and Supplementary Figure S1B, respectively). While one might argue, based on MTR asymmetry results (Figure 1), that choosing a higher B_1 rms would be beneficial for CEST at 2 ppm, our assessment with the presence of glutamate, as expected in the human brain, revealed that a B_1 rms of 2.5 μT and a t_{sat} of 1500 ms, would noticeably increase the contribution of CEST at 3 ppm (Supplementary Figure S2A). Interestingly,

a considerably high CEST MTR asymmetry was found in our phantoms with a low t_{sat} and B_1 rms (750 ms and a B_1 rms of 2.5 μT) (Figure 2). This observation, which is not supported by our simulations, could be attributed to field inhomogeneities, possibly induced by the movement of water within the heating blanket used during our measurements. Interestingly, a previous study which looked at CEST at 2 ppm fittings in the human brain showed a somewhat lower B_1 rms of 1.45 μT and a slightly longer saturation duration of 2 s to be more beneficial for CEST at 2 ppm imaging⁹⁹. However, the same study indicated that a B_1 rms of 2 μT and total saturation of 2 s yielded comparable CEST at 2 ppm contrast to their suggested parameters (approximately 5% in the GM). Our simulation results did initially show the benefit of aiming for a slightly higher B_1 rms of 2.5 μT or 3 μT , with t_{sat} set at either 1 s or 1.5 s, respectively. This is different from what we observed in phantoms, where the most optimal acquisition parameters were firstly a B_1 rms of 2.14 μT with a t_{sat} of 1.5 s, and secondly a B_1 rms of 2.5 μT with a t_{sat} of 1.25 s. The latter B_1 rms is in line with what has been also recently shown to be optimal for CrCEST imaging in the mouse brain⁹⁹. As for CEST at 3 ppm, the highest B_1 rms of 3.3 μT with a t_{sat} of 1000 ms could not be reached within the SAR limitations. Consequently, for phantom experiments, we chose to reduce t_{sat} to 750ms and found the highest t_{sat} possible to be 750 ms while accommodating a B_1 rms of 3.3 μT . *In vitro* studies in our work showed that the CEST contrast at 2 ppm and 3 ppm both increased with an increase in concentration (Supplementary Figure S3). Phantom experiments to validate metabolite-weighted contrast have been previously performed by Khlebnikov et al. 2019⁶⁶. Differently from this work, our conclusions are also based on *in vivo* experiments. Our results indicate that hardware limitations need to be taken into account when developing and optimizing acquisition parameters, and emphasize the importance of choosing a concentration representative of physiological conditions to accurately mimic *in vivo* situations.

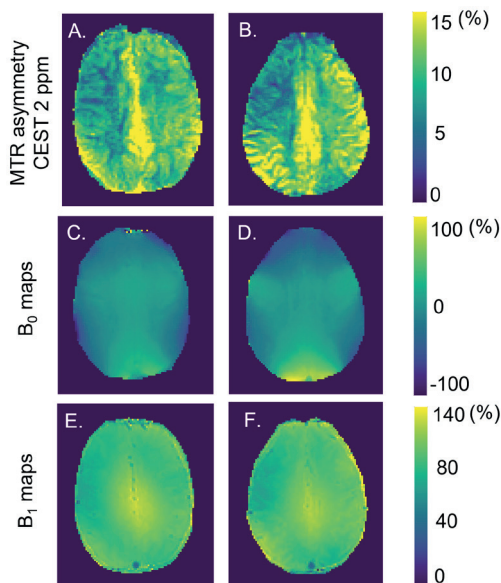


Figure 5. (A) & (B) CEST at 2 ppm MTR asymmetry maps of two representative subjects. (C) & (D) and (E) & (F) the corresponding B_0 and B_1 maps, respectively.

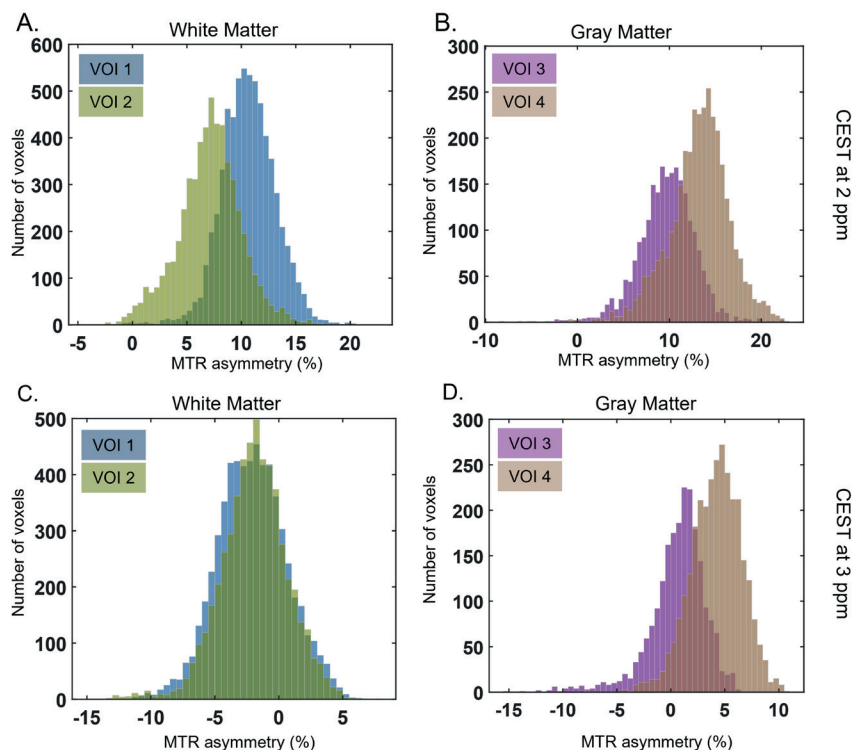


Figure 6. Histograms of the CEST MTR asymmetry contrast distribution from (A, B) CEST at 2 ppm and (C, D) CEST at 3 ppm in the VOIs placed in WM and GM, respectively. For each ROI the histogram reflects the average contrast across all 8 imaging slices from the 10 subjects combined.

To study the metabolite-weighted CEST contrast in the human brain, we applied CEST measurements using the optimized acquisition parameters and validated them against MRS. While many prior studies have applied specific CEST sequences to capture CEST at 3 ppm contrast, we have also included MRS for validation of CEST at 2 ppm in the GM and WM of multiple subjects, additionally to what has been previously done⁸⁹. As expected, our results showed a significant correlation between Glu concentrations and CEST at 3 ppm MTR asymmetry (Supplementary Figure S6B). Surprisingly, we observed a significant correlation between CEST at 2 ppm and Glu concentrations, whereas no correlation was found between CEST at 2 ppm and tCr concentrations. The lack of correlation for CEST at 2 ppm could be attributed to different reasons. Firstly, the well-known similarity in Cr concentrations in the GM and WM limits the range over which the correlation could be assessed¹¹⁶. A potential future approach could include measurements in physiological conditions, such as during muscle exercise, where more pronounced tCr concentration changes are expected. Additionally, MRS measures tCr, therefore the phosphocreatine also contributes to the MRS measurements. The CEST contrast at 2 ppm is known to have PCr contribution around 80% in the rat brain with a saturation of $2 \mu\text{T}$ ^{117,118}. Although we know that the concentrations of Cr and PCr are comparable

in magnitude in the human brain, we do not know to in which proportions we are capturing the signal from Cr and/or PCr¹¹⁹. Differences in relative sensitivity to Cr and PCr could potentially play a role in correlating results from these two methodologies. Finally, the CEST contribution at 2 ppm can also include contrast from other proteins/peptides, from which some guanidinium protons contribution can arise as previously shown by Zhang et al³⁶. On the other hand, the correlation of the CEST at 2 ppm pool with Glu concentrations could be due to contamination from the CEST at 3 ppm pool. It is known that this CEST pool can have a broad effect, especially in physiological temperatures. Moreover, Glu concentrations in the brain are higher than tCr, making it relatively easier to be more sensitive to the proton pool at 3 ppm. These results seem to suggest that the CEST MTR asymmetry contrast at 2 ppm is significantly influenced by Glu. On the other hand, when quantifying CEST with AREX, thus correcting for T_1 and MT effects, we found similar results for both CEST at 2 ppm and CEST at 3 ppm compared to MTR asymmetry (Figure 8 and Supplementary Figure S6). The observed inverse correlations were expected, as the AREX calculates the inverse Lorentzian difference⁸⁵. The inverse CEST effect can also be seen in Supplementary Material Figure S7, where the WM appears more hyperintense than the GM, contrary to what we observed in MTR asymmetry maps (Figure 6A and 6B).

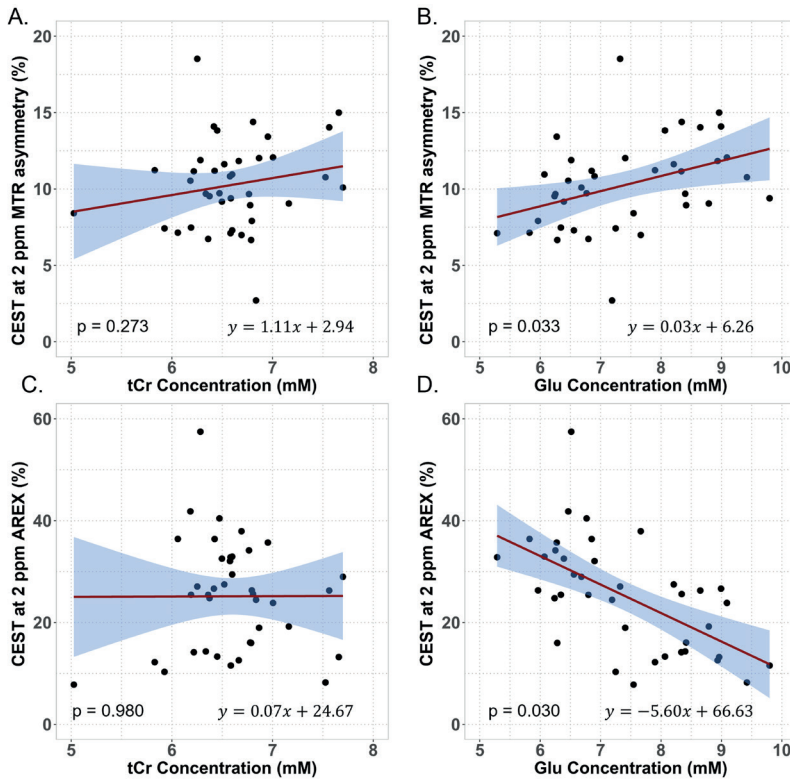


Figure 7. *In vivo* correlation results from data acquired with B_1 rms = 2.14 μ T. Correlations of the (A,B) MTR asymmetry ($p = 0.273$, $p = 0.033$) and (C,D) AREX ($p = 0.980$, $p = 0.030$) of CEST at 2 ppm with tCr and Glu concentrations measured with MRS, respectively. The data plotted corresponds to 39 VOIs both in GM and WM as measured in 10 subjects.

Previous studies have shown the feasibility of CEST at 3 ppm imaging in the human brain at 7T^{88,120}. Through simulations, *in vitro* experiments and measurements in healthy volunteers, we confirmed that the previously employed acquisition parameters also work on a different 7T platform than that used predominantly in the literature from a single center. By correlating the CEST at 3 ppm MTR asymmetry values with Glu concentrations, we can confirm that Glu is a substantial contributor to the CEST at 3 ppm contrast. Interestingly, a recent study has challenged the origins of the CEST contrast at 3 ppm, suggesting that it arises mainly from proteins rather than Glu in the rat brain⁹². Despite the difference in species, it is important to note that the data were acquired at a higher field strength than typically used in studies involving human subjects. Notably, the employed B_1 power was similar to our settings at 7T (3.6 μ T), whereas previous simulations have shown that to achieve sensitivity to Glu at 9.4T a B_1 of around 7.5 μ T would be optimal⁶⁶. Additionally, simulations suggest that the CEST peak at 3 ppm becomes wider with increased B_0 ⁴⁹. Consequently, the CEST contrast of proteins, which is typically observed around 3.5 ppm at 3T and 7T, might have also contributed to the observed effects around 3 ppm in that particular study.

When comparing the CEST contrast distributions within the two VOIs representing WM or GM for CEST at 2 ppm (Figures 6A and 6B), or even for CEST at 3 ppm (Figures 6C and 6D), the interregional spread is evident. These differences might be attributed to discrepancies in B_1 distribution within the brain illustrated in figures 5E and 5F (or Supplementary Figures S5E and S5F), even though for the vast majority of VOIs, the B_1 was above 80% (Supplementary Table S3). The B_1 differences predominantly appear as the systematic right-left variation, which reflect intraregional MTR asymmetry distribution in the WM VOIs (Figure 6A and 6C). We attempted to mitigate B_1 inhomogeneity effects by using dielectric pads during data acquisition and by applying a quadratic B_1 correction method¹⁰⁵. The fact that the B_1 correction approach was originally developed for CEST at 3 ppm, which in principle uses a higher B_1 power value, might explain why it did not perform as effectively for the CEST at 2 ppm data. Furthermore, the uneven histogram distribution and negative values in WM could also be explained by contribution of other CEST effects such as magnetization transfer (MT) and nuclear Overhauser effect (NOE) to the MTR asymmetry. We would expect for the most part less contamination, especially when acquiring images with higher B_1 rms (ie. filtering out other competing effects from slower exchanging pools such as NOE and amide protons). However, imperfect saturation and B_1 homogeneity distribution *in vivo* might have led to contamination to some extent throughout data acquisition, becoming more noticeable when combining data from all volunteers. Other analysis methods such as Lorentzian fittings could be considered as a good alternative for filtering out prominent competing effects *in vivo*^{121,122}. After performing these fits, we computed the AREX metric accounting for T_1 and MT, but still observed an uneven distribution of the CEST contrast (Supplementary Material Figure S8). This could perhaps be due to field inhomogeneities, or challenges arising from fitting broad CEST pools. Consequently, contamination by neighboring pools may result in the interference of undesired CEST effects, as exemplified in one volunteer in Supplementary Material Figure S7. Our results in Supplementary Material Figure S9 show how broad the CEST at 2 ppm and CEST at 3 ppm

fittings are within the frequency spectrum, in line with a previous observation that the CEST contrast from fast exchanging components does not follow Lorentzian line shapes¹²³. This has also been previously described in literature suggesting^{41,42} that, because of the rather wide CEST at 3 ppm effect at physiological pH, fitting Lorentzians is particularly challenging because of the very wide peak¹²⁴. Xu et al. discuss that the specificity of performing Lorentzian fittings improves CEST at 2 ppm quantification and that Cr and PCr pools could be extracted from animal muscle¹¹⁸. However, the concentration of these metabolites in muscle is higher than in the brain, and studies supporting this claim have been conducted at 11.7T, allowing for a higher spectral resolution than at 7T^{125–127}.

In addition to the B_1 inhomogeneities, our study has a few other limitations. An interesting cofounder affecting *in vitro* experiments for CEST at 3 ppm contrast seems to be temperature. We observed CEST at 2 ppm and CEST at 3 ppm contrasts to have a linear and inverse relation with temperature, respectively (Supplementary Figure S3B), as also shown in a zebrafish model for CEST at 3 ppm¹²⁸. Lastly, since this investigation primarily served as a proof of principle for CEST at 2 ppm, our conclusions are limited by the relatively small sample size of 10 subjects, all of whom were healthy. However, the subjects spanned a relatively wide age range, which might have helped to study the CEST contrasts over different metabolite concentrations, since it is known that metabolite concentration in the brain changes with age¹²⁹.

In conclusion, we investigated optimal acquisition parameters for metabolite CEST imaging through simulations and validated these concepts in a controlled *in vitro* environment. We confirmed the significant contribution of Glu to the CEST at 3 ppm MTR asymmetry *in vivo*. Contrary to expectations, we observed that the CEST at 2 ppm pool is significantly correlated with Glu concentrations, indicating that the contrast is likely weighted by Glu. Our findings suggest that Glu is a substantial contributor to the CEST at 2 ppm contrast observed in the human brain, whereas the Cr contribution to CEST at 2 ppm in the brain did not exhibit a significant impact. A potentially interesting future step could involve applying a similar protocol in muscle imaging to assess whether CEST at 2 ppm can be validated in the presence of a larger concentration of Cr protons. Furthermore, it would be valuable to verify these sequences in pathologies such as brain tumors, expanding on the work of Cai et al.⁶³. This way, the specificity of metabolite-weighted CEST could be reliably validated for future clinical applications.

4.6 Acknowledgments

This study is part of the project “Non-Invasive Characterization of Active Multiple Sclerosis Lesions Through Chemical Exchange Saturation Transfer (CEST) Imaging” (project no. 16862) financed by the Dutch Research Council (NWO) Talent Programme Veni. This work was also funded by the Medical Delta Cancer Diagnostics 3.0 program.

We would like to thank Wyger Brink for making the dielectric pads we used and supporting us while tackling B_1 constraints during protocol optimization. We would also like to thank Emiel

C.A. Roefs with the support while finetuning the analysis pipeline and with adjusting the T_1 and T_2 of the phantoms.

4.7 Conflict of interest

Ece Ercan is a full-time employee at Philips Healthcare, Best, The Netherlands.

4.8 Supplementary material

In vivo data analysis to calculate AREX:

For each voxel, Z-spectra was fitted to a five-pool Lorentzian model using the Levenberg-Marquardt algorithm. The model included the water, MT, relayed nuclear Overhauser effect (rNOE), amines at 2 ppm and amines at 3 ppm¹³⁰. The fitting parameters can be found in the supplementary material under Table S2. Hereafter the relaxation compensated (AREX) contrast was calculated per voxel, also correcting for direct water saturation, MT and T_1 : $AREX = \frac{\frac{1}{Z_{lab}} - \frac{1}{Z_{ref}}}{T_1}$, where Z_{lab} is the yielded label Z-spectrum and Z_{ref} is a reference spectrum given by $Z_{ref} = Z_{lab} + L_{pool}$, where L_{pool} is the Lorentzian dedicated to a specific pool at a certain resonance frequency (in ppm).

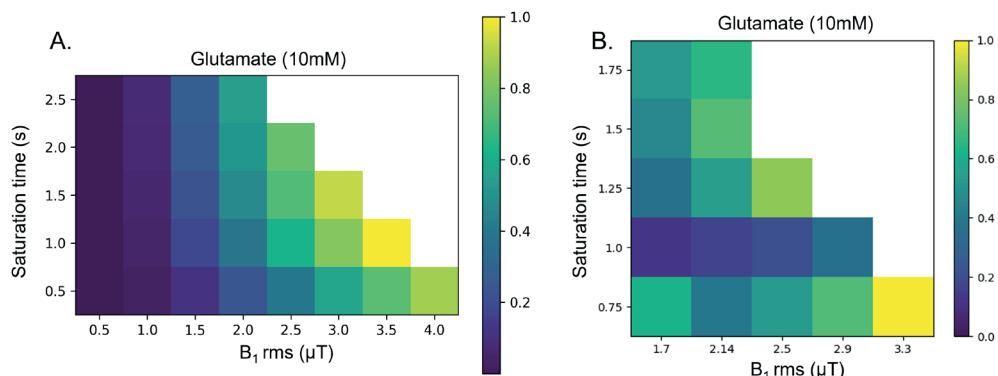
Supplementary Table S1. Acquisition parameters from phantom scans acquired during protocol optimization.

	Phantom image acquisition parameters
Shot TR/TR/TE (s)	5 / 3.3 / 1.82
Field of view (FOV (mm ³))	246 x 246 x32
Voxel size (mm ³)	2 x 2 x 4
Radiofrequency (RF) pulses	Sinc gauss
Frequency steps (Hz)	22 steps of 136.4
Frequency offset (Hz)	-1500Hz to 1500
Frequencies (ppm)	5, 4.54, 4.08, 3.62, 3.16, 2.7, 2.24, 1.78, 1.32, 0.86, 0.46, 0, -0.46, -0.86, -1.32, -1.78, -2.24, -2.7, -3.16, -3.62, -4.54, -5
B ₁ rms (μT)	1.7, 2.1, 2.5, 2.9, 3.3
RF pulse duration/interval/repetition	50ms/25ms/10 50ms/0ms/20 75ms/50ms/10 50ms/25ms/20 100ms/75ms/10
RF total saturation duration (ms)	750 / 1000 / 1250 / 1500 / 1750

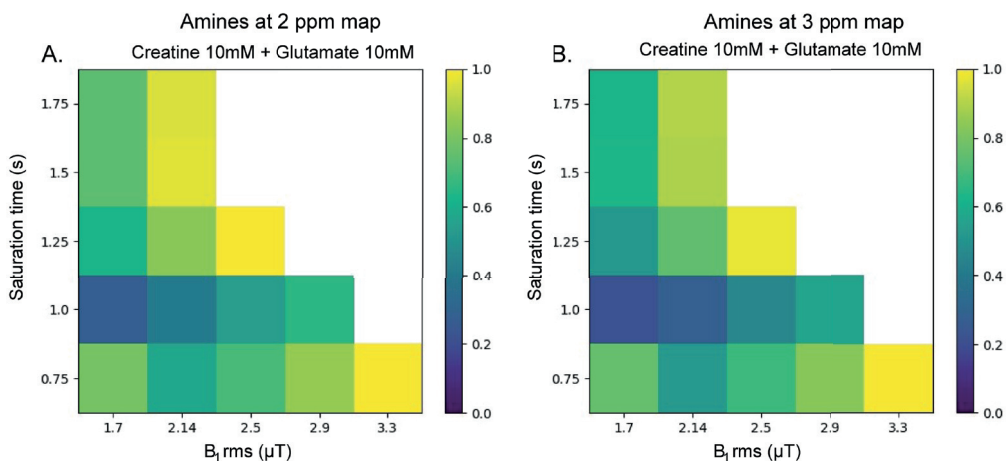
Supplementary Table S2. Table showing the actual average (Act avg) B₁ measured in each VOI for CEST at 2 ppm MTR asymmetry (Act avg B₁ 2 ppm) and for CEST at 3 ppm MTR asymmetry (Act avg B₁ 3 ppm), the MTR asymmetry values for both CEST contrasts and corresponding metabolite concentrations measured with MRS. For volunteer 9 the metabolites in VOI3 could not be measured (CRLB > 10%).

VOI	VOI1					VOI2						
Measurements	CEST measurements				MRS measurements		CEST measurements			MRS measurements		
Volunteers	Act avg B ₁ CEST at 2 ppm (μT)	CEST at 2 ppm MTRasym (%)	Act avg B ₁ CEST at 3 ppm (μT)	CEST at 3 ppm MTRasym (%)	Total creatine (mM)	Glutamate (mM)	Act avg B ₁ CEST at 2 ppm (μT)	CEST at 2 ppm MTRasym (%)	Act avg B ₁ CEST at 3 ppm (μT)	CEST at 3 ppm MTRasym (%)	Total creatine (mM)	Glutamate (mM)
Volunteer 1	1.9	10.1	3.5	-2.2	7.7	6.7	1.8	7.5	3.3	-1.0	6.2	6.3
Volunteer 2	1.9	10.5	3.3	-2.2	6.2	6.5	1.7	7.0	3.0	-1.0	6.7	7.7
Volunteer 3	2.4	11.9	3.7	-1.2	6.3	6.5	2.7	7.9	3.5	-0.2	6.8	6.0
Volunteer 4	2.0	9.5	3.4	-1.1	6.4	6.2	1.8	6.7	3.0	-3.5	6.8	6.3
Volunteer 5	2.1	11.0	3.5	-3.6	6.6	6.1	1.9	7.3	3.2	-0.2	6.6	6.6
Volunteer 6	2.2	13.4	3.7	-0.1	7.0	6.3	1.9	9.7	3.3	-0.5	6.8	6.3
Volunteer 7	2.1	10.8	3.6	-1.8	6.6	6.9	1.8	6.7	3.1	-1.0	6.4	6.8
Volunteer 8	2.2	9.7	3.3	-2.7	6.5	6.8	1.7	2.7	2.6	-4.5	6.8	7.2
Volunteer 9	2.0	11.2	3.4	0.0	6.4	6.9	1.9	7.1	3.2	-1.8	6.1	5.8
Volunteer 10	1.9	9.2	3.0	-2.8	6.5	6.4	1.8	7.1	2.8	-2.9	6.6	5.3

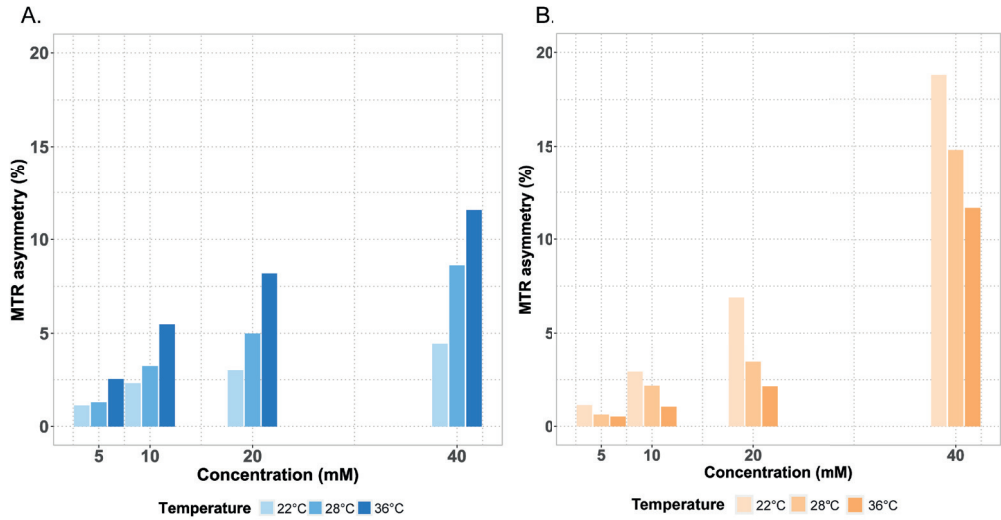
VOI	VOI3						VOI4					
Measurements	CEST measurements						CEST measurements			MRS measurements		
	Act avg B ₁ CEST at 2 ppm (μT)	CEST at 2 ppm MTRasym (%)	Act avg B ₁ CEST at 3 ppm (μT)	CEST at 3 ppm MTRasym (%)	Total creatine (mM)	Glutamate (mM)	Act avg B ₁ CEST at 2 ppm (μT)	CEST at 2 ppm MTRasym (%)	Act avg B ₁ CEST at 3 ppm (μT)	CEST at 3 ppm MTRasym (%)	Total creatine (mM)	Glutamate (mM)
Volunteer 1	1.8	11.8	3.3	1.7	6.7	8.9	2.0	13.8	3.6	3.4	6.5	8.1
Volunteer 2	1.8	8.9	3.1	0.6	6.8	8.4	2.0	14.1	3.6	3.5	6.4	9.0
Volunteer 3	2.2	11.2	3.4	0.2	6.2	8.3	2.4	12.1	3.7	3.3	7.0	9.1
Volunteer 4	1.8	8.4	3.0	-1.0	5.0	7.5	2.1	11.2	3.4	2.4	5.8	7.9
Volunteer 5	2.1	9.0	3.5	1.0	7.2	8.8	2.1	12.0	3.6	1.2	6.9	7.4
Volunteer 6	2.0	11.6	3.5	1.1	6.5	8.2	2.2	18.5	3.8	4.1	6.3	7.3
Volunteer 7	1.7	10.8	2.9	0.4	7.5	9.4	2.1	15.0	3.6	1.3	7.7	9.0
Volunteer 8	2.0	9.4	3.1	0.3	6.6	9.8	1.9	9.7	3.0	0.5	6.3	8.4
Volunteer 9	1.7	9.2	2.9	-0.5			2.2	14.4	3.7	3.2	6.8	8.3
Volunteer 10	1.8	7.4	2.9	0.2	5.9	7.2	2.1	14.0	3.4	2.2	7.6	8.6



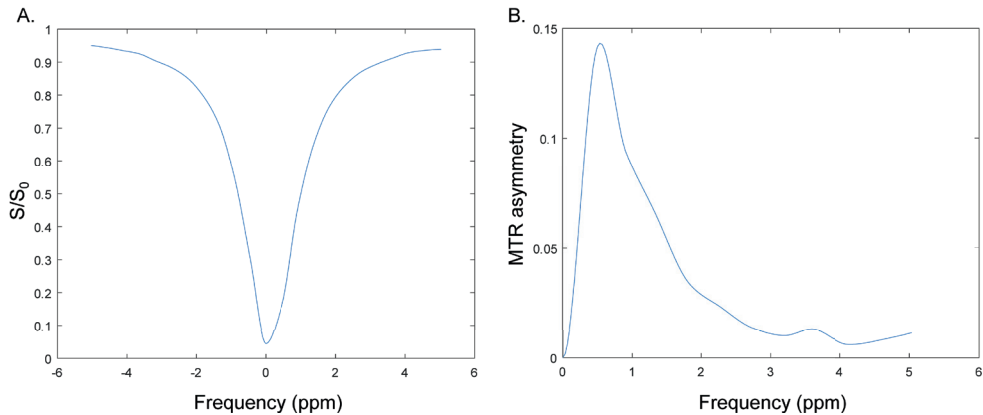
Supplementary Figure S1. (A) Normalized five-pool model simulation results normalized to the maximum CEST at 3 ppm MTR asymmetry value, investigated as a function of varying B_1 rms and t_{sat} values. The areas on the right side in white of each figure, represent the parameter combinations which were not measured due to SAR limitations *in vivo*. (B) Phantom results normalized to the highest CEST at 3 ppm MTR asymmetry value, illustrating how CEST at 3 ppm CEST changes as a function of total saturation time (s) and B_1 rms (μ T). The data shown corresponds to measurements of phantoms with a concentration of 10mM of glutamate scanned at $\pm 36^\circ\text{C}$.



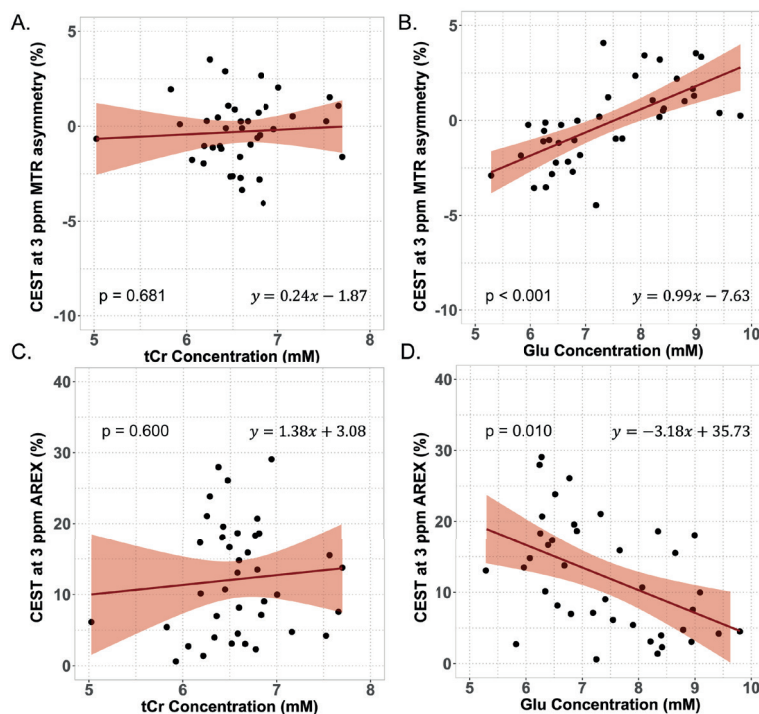
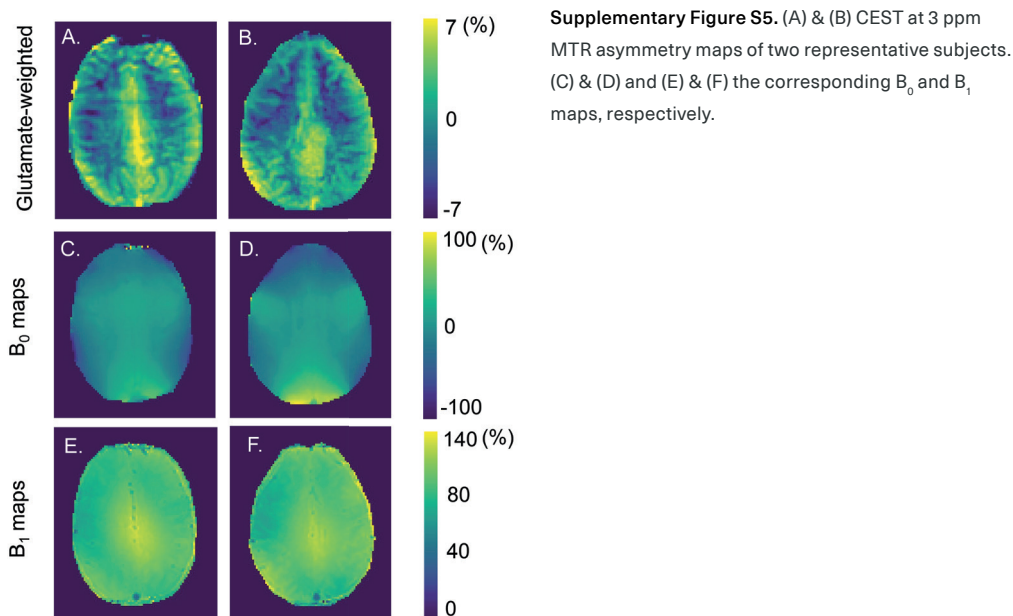
Supplementary Figure S2. Normalized phantom results to the maximum MTR asymmetry value. CEST MTR asymmetry was investigated as a function of varying B_1 rms and t_{sat} values for (A) CEST at 2 ppm and (B) CEST at 3 ppm in a phantom, when in the presence of both creatine and glutamate. The areas on the right side in white of each figure, represent the parameter combinations which were not experimented due to SAR limitations *in vivo*.



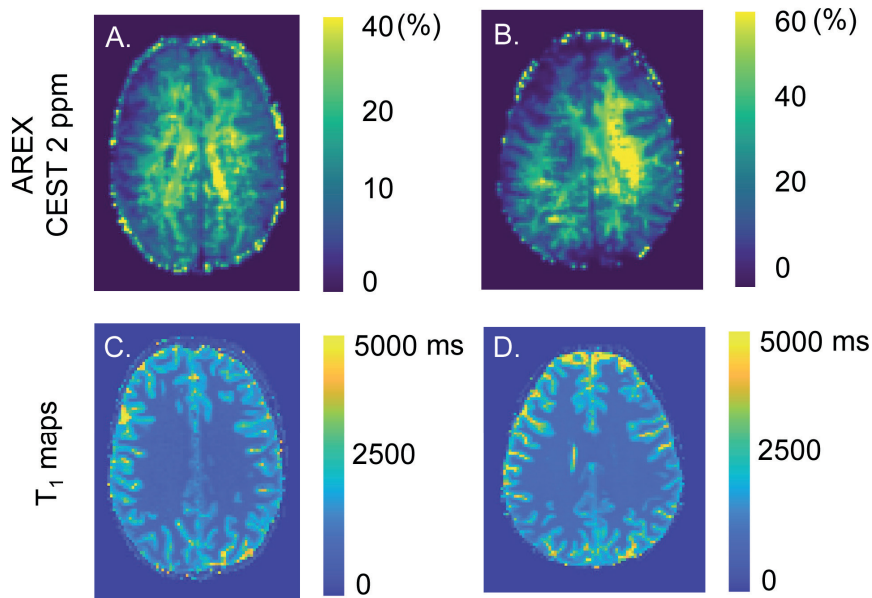
Supplementary Figure S3. Bar graph illustrating how the MTR asymmetry of (A) CEST at 2 ppm and (B) CEST at 3 ppm phantoms changed between three different temperature conditions. These scans were acquired with the parameters determined to be most optimal for 2 ppm and 3 ppm, respectively. It is evident that the CEST signal increases with temperature for CEST at 2 ppm and decreases for CEST at 3 ppm.



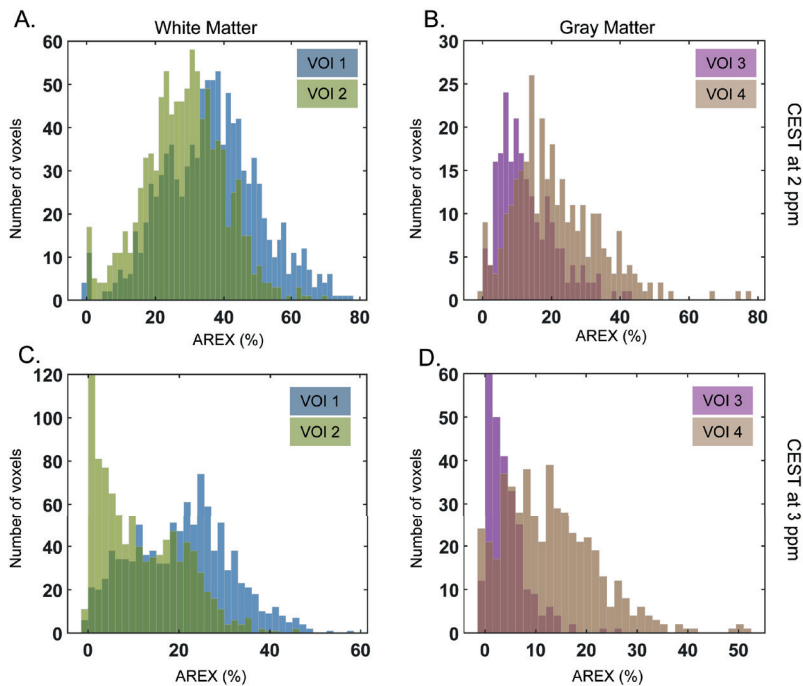
Supplementary Figure S4. (A) Z-Spectra and (B) MTR asymmetry from an ROI placed over a phantom with 0.5mM CuSO_4 and 1% agarose. This experiment was part of the initial optimization performed to determine the optimal concentrations to reach T_1 and T_2 relaxation times similar to those found in the human brain. The graphs shows that, except for MT effect, there are no heavy contributions of the compounds used to the Z-Spectra and MTR asymmetry.



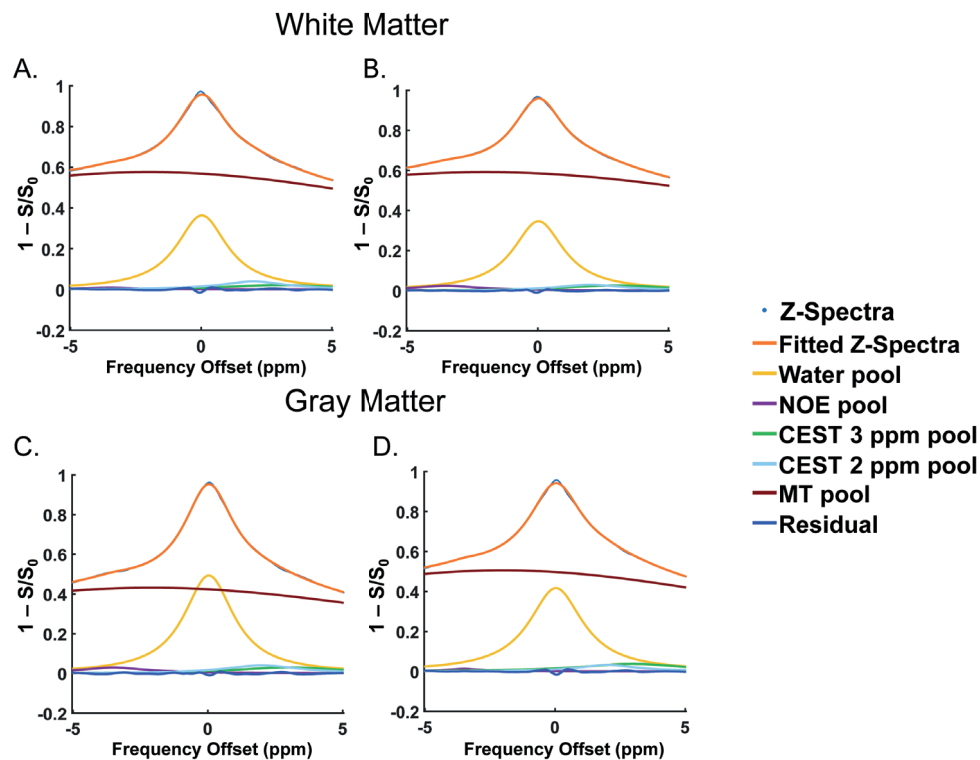
Supplementary Figure S6. *In vivo* correlation results from data acquired with $B_{1,rms} = 3.3\mu T$. Correlations of the (A,B) MTR asymmetry ($p = 0.681$, $p < 0.001$) and (C,D) AREX ($p = 0.600$, $p = 0.010$) of CEST at 3 ppm with tCr and Glu concentrations measured with MRS, respectively. The data plotted corresponds to 39 VOIs both in GM and WM as measured in 10 subjects.



Supplementary Figure S7. (A) & (B) AREX maps of CEST at 2 ppm of two representative subjects. (C) & (D) the respective T₁ maps.



Supplementary Figure S8. Histograms of the CEST AREX contrast distribution from (A, B) CEST at 2 ppm and (C, D) CEST at 3 ppm in the VOIs placed in WM and GM, respectively. For each ROI the histogram reflects the average signal across all 8 imaging slices from the 10 subjects combined.



Supplementary Figure S9. Z-Spectra and five CEST pools fitted with Lorentzian line shapes from two VOIs in the WM (A & B) and GM (C & D). These results are from 1 representative volunteer.

5 Insights into CEST contrast at 2 ppm in enhancing and non-enhancing lesions from glioma patients scanned at 7T

Bárbara Schmitz-Abecassis

Jeroen de Bresser

Linda Dirven

Martin J. B. Taphoorn

Matthias J. P. van Osch

Johan A. F. Koekkoek

Ece Ercan

Submitted to NMR in Biomedicine (2025)

5.1 Abstract

Chemical exchange saturation transfer (CEST) has been demonstrated to provide a non-invasive opportunity to image gliomas. Pre-clinical ultra-high field MRI studies have shown the value of the 2 ppm pool, however *in vivo* studies in glioma patients are currently lacking. This study aimed to explore the 7T MRI CEST contrast of the 2 ppm in gliomas and the tumor's different components.

Twenty-one glioma patients treated at two tertiary referral centers for brain tumors in the Netherlands were scanned. Regions of interest were defined as contrast enhancing (CE-lesion), and non-enhancing (NE-lesion) tumor, and the contralateral normal-appearing white matter (CL NAWM). Magnetization transfer ratio asymmetry (MTRasym), Lorentzian difference (LD), spillover and magnetization transfer corrected inverse difference (REX) and relaxation-compensated (AREX) were calculated for all regions of interest.

The 2 ppm CEST pool signal between tumor regions and normal-appearing tissue were found to be significantly different for all four CEST quantification methods (MTRasym $p = 0.001$; LD $p < 0.001$; REX $p = 0.008$; AREX $p = 0.001$). The CE and NE lesions showed significantly different 2 ppm pool CEST MTRasym ($p = 0.034$) and LD ($p = 0.052$). Significantly different 2 ppm CEST REX ($p = 0.005$) and AREX ($p = 0.001$) were found between the CL NAWM and the NE lesions.

CEST 2 ppm pool contrast was distinctive between normal appearing white matter, enhancing and non-enhancing tumor lesions, independently of the metric used. These findings suggest that the CEST pool at 2 ppm provides a valuable non-invasive contrast for imaging gliomas.

5.2 Introduction

Chemical exchange saturation transfer (CEST) is an MR modality that has been increasingly used to characterize brain tumors non-invasively. The majority of previous CEST work on brain tumors focused on the amide proton transfer (APT) pool at 3.5 ppm and Nuclear Overhauser (NOE) effects, and showed an increase in APT and decrease in NOE from brain tumors compared to normal-appearing tissue, respectively^{40,41,131,132}. On the other hand, only a few studies focused on the CEST pool at 2 ppm although they showed its relevance for tumor differentiation. For example, pre-clinical work has shown that the CEST effect at 2 ppm is reduced in tumor compared to normal tissue⁶³. This was especially observed upon tumor progression and increased aggressiveness⁶⁴. The distribution of the 2 ppm CEST effect was also shown to correlate with creatine distribution in brain tumors⁶³. Moreover, in clinical research, the CEST pool at 2 ppm, among others, was shown to help risk-stratification of glioma patients based on tumor grade and molecular status⁵⁶. An increased contrast of CEST at 2 ppm was found in the tumor compared to normal brain tissue⁵⁶. The ratio of amides and amines has also shown to be useful to help determine the tumor grade without the need for contrast agent enhanced imaging¹³³. These examples illustrate how the 2 ppm CEST pool can be used to non-invasively characterize glioma, based on endogenous contrast. Such an opportunity could also be interesting as a future alternative to current invasive imaging techniques relying on exogenous contrast agents.

The use of gadolinium-based contrast agents (GBCAs) for the acquisition of enhanced T_1 -weighted images are currently the standard procedure for glioma patients, reflecting an increase in blood-brain barrier permeability¹³⁴. However, some patients are allergic to such agents, making procedures more complicated. Moreover, there are concerns about gadolinium deposition in the brain especially for patients undergoing extensive follow-up imaging¹³⁵. Since glioma patients need frequent radiological monitoring of potential tumor recurrence or progression, it becomes highly desirable to develop/use an endogenous imaging contrast, especially for patients with lower grade glioma who have a more prolonged survival. Finally, there is also a group of patients without tumor enhancement on their post-contrast T_1 weighted (T_{1w}) scans¹³⁶. This includes not only patients with lower grade gliomas, such as isocitrate dehydrogenase (IDH) mutant astrocytoma, but also patients with higher grade glioma, such as glioblastoma, IDH wild type^{10,137}. For these reasons it becomes clinically relevant to explore different contrasts to non-invasively characterize glioma.

A few *in vivo* patient studies on the 2 ppm CEST pool have been performed on clinical systems, whereas most CEST studies on glioma patients have primarily focused on APT-CEST. No clinical study has yet investigated how the CEST contrast at 2 ppm obtained using 7T MRI differs between different tumor components (ie. non-enhancing and enhancing lesions). Moreover, the quantification of the 2 ppm CEST pool is most often performed using MTR asymmetry. An evaluation of other quantification metrics such as Lorentzian Difference (LD), the spillover and magnetization transfer corrected inverse difference (REX), and apparent

exchange-dependent relaxation (AREX) which have been previously used in APT-CEST studies is lacking. Given the higher spectral resolution at 7T, we hypothesize to be more specific to the pool resonating at 2 ppm. In this study, we aimed to investigate the CEST effects at 2ppm in enhancing and non-enhancing lesions from glioma patients using several CEST quantification metrics (MTR Asymmetry, LD, REX and AREX). Understanding how the contrast differs in these lesions compared to normal appearing white matter, could possibly aid in the future with: 1) the assessment of non-enhancing tumors, since these can also have poor prognosis. 2) understand if this CEST contrast, additionally to the already established APT and NOE, could add value as a future alternative to the use of gadolinium-based contrast agents (GBCA).

5.3 Methods

5.3.1 Patient inclusion

For this study we prospectively included 21 patients from Leiden University Medical Center and Haaglanden Medical Center, The Netherlands, between March 2021 and May 2023. Adult patients with a histopathologically confirmed or highly suspected glioma, a Karnofsky Performance Status (KPS) score ≥ 70 and no contraindications for MRI were eligible for inclusion. Patient characteristics are outlined in Table 1. The study adhered to the local Institutional Review Board guidelines and approval. All patients gave written informed consent.

5.3.2 Imaging data acquisition

5.3.2.1 Clinical imaging

Clinical data was retrospectively collected from the hospital archives for all included patients. Patients were either scanned on a 3T MR scanner (Philips Ingenia or Achieva, Philips Healthcare, Best, The Netherlands) or on a Siemens MAGNETOM Avanto 1.5T scanner (Siemens, Erlangen, German). At 3T, the 3D T_1 post-contrast gadolinium enhanced scan was acquired with a 3D-gradient-echo readout and the following acquisition parameters: TR = 9.91 ms, TE = 4.67 ms, voxel size = $1 \times 1 \times 1 \text{ mm}^3$, field of view (FOV) = $220 \times 175 \times 156 \text{ mm}^3$, 0.3 ml per kg bodyweight of gadolinium-based contrast agent (gadoterate meglumine) and a total acquisition time of 2:57 minutes; the T_2 -FLAIR was acquired with the following parameters: TR = 11000 ms, TE = 125 ms, resolution = $0.4 \times 0.4 \times 5.5 \text{ mm}^3$, FOV = $220 \times 175 \text{ mm}$ and a total acquisition time of 2:12 minutes. At 1.5T the 3D T_1 -post contrast gadolinium enhanced scan was acquired with the following acquisition parameters: TR = 9ms, TE = 2.38ms, resolution = $0.9 \times 0.9 \times 0.9 \text{ mm}^3$, FOV = $240 \times 240 \times 176 \text{ mm}$ and 0.1ml/kg of prebolus and 20ml of contrast agent (Dotarem 0.5mmol/ml); the T_2 -FLAIR was acquired with the following parameters: TR = 7500ms, TE = 105ms, voxel size = $0.4 \times 0.4 \times 5 \text{ mm}^3$ and FOV = $230 \times 230 \times 144 \text{ mm}^3$ and a total acquisition time of 2:08 minutes.

Table 1. Clinical characteristics of the participating glioma patients (n = 21).

Patient demographics		Intervention	
Age, mean ± standard deviation	57.9 ± 13.7	No intervention	4 (19%)
Female	11 (52%)	Surgery	17 (81%)
Male	10 (48%)	Partial resection	10 (48%)
Diagnosis		Biopsy	7 (33%)
Glioblastoma, IDH-wildtype	15 (71%)	Radiotherapy	13 (62%)
Diffuse Astrocytoma, IDH mutant	2 (10%)	Photon therapy	12 (57%)
Anaplastic Astrocytoma, IDH-mutant	2 (10%)	Proton therapy	1 (5%)
Oligodendroglioma, IDH-mutant and 1p/19q codeleted	2 (10%)	Total dose 30 Gy	2 (10%)
MGMT status		40 Gy	1 (5%)
Methylated	7 (33%)	60 Gy	8 (38%)
Unmethylated	8 (38%)	Adjuvant chemotherapy	15 (71%)
Unknown	6 (29%)	Temozolomide	31 (62%)
		Temozolomide and lomustine	1 (5%)
		PCV (Procarbazine, CCNU (Lomustine), Vincristine)	1 (5%)
		Total daily use of dexamethasone	
		1 mg	4 (19%)
		2 mg	1 (5%)
		4 mg	1 (5%)
		6 mg	1 (5%)

5.3.2.2 CEST imaging

CEST data was prospectively acquired at a whole-body 7T MRI scanner, Achieva Philips MRI scanner (Philips Healthcare, Best, the Netherlands) equipped with a dual-transmit and a 32-channel receiver head coil (Nova Medical Inc, Wilmington, MA, USA). The maximum achievable gradient strength and slew rate of the scanner are 40 mT/m and 200 T/m/s respectively.

The acquisition protocol consisted of a short survey scan, a sensitivity encoding (SENSE) reference scan, a B₀ map to be used to perform third order B₀ shimming, a DREAM B₁ map to correct for B₁ inhomogeneities (TR = 8.0ms, TE = 1.97 ms, FOV = 246 x 246 x 32 mm³ and a voxel size = 2 x 2 x 4 mm³, acquisition time: 08 seconds), a water saturation shift reference (WASSR) B₀ map (TR = 3.3 ms, TE = 1.83 ms, FOV = 246 x 246 x 32 mm³ and a voxel size = 2 x 2 x 4 mm, acquisition time: 25 seconds) for post-processing corrections and the CEST scan. A pulsed CEST preparation of 10 sinc-gauss pulses of 50 ms duration and 50 ms interval (total saturation: 1000 ms), was followed by a gradient echo sequence with turbo field echo readout (TR = 3.3

ms, TE = 1.82 ms, FOV = 246 x 246 x 32 mm³ and a voxel size = 2 x 2 x 4 mm³, acquisition time: 05:06 minutes). The B₁ rms per pulse unit was 2.94 μT. In total 22 frequencies were acquired with a step size of 136.4 Hz between -1500 Hz and 1500 Hz. Each volume took approximately 14 seconds. Finally, five scans were acquired with variable flip angles (2, 5, 7, 10 and 15 degrees) which we used to estimate the T₁ values for each patient (TR = 7.0 ms, TE = 1.3 ms, FOV = 246 x 246 x 32 mm and a voxel size = 2 x 2 x 4 mm, acquisition time: 2 seconds for each scan). The total acquisition time was 5:38 minutes.

5.3.3 Data analysis

5.3.3.1 CEST analysis

Corrections for B₀ inhomogeneities were performed using the WASSR scan according to the method described elsewhere¹⁰². The DREAM B₁ map was used for correcting the AREX maps. The reference scan (M₀ image) was acquired at a further offset of approximately 102 kHz to normalize the CEST images. The Z magnetization acquired was assessed over the frequency offsets for all voxels. In turn 1-S/S₀ spectra were fitted to a 5-pool Lorentzian model using the Levenberg–Marquardt algorithm. Fitting parameters can be found in the Supplementary Material in Supplementary Table S1. From the fitted data we proceeded to calculate the Lorentzian Difference, REX and the AREX metric as previously described¹³⁸. The magnetization transfer ratio (MTR) asymmetry was calculated according to the following formula: $MTR_{asym} = \frac{Z(-x \text{ ppm}) - Z(+x \text{ ppm})}{Z(-x \text{ ppm})}$ for the 2 ppm and 3.5 ppm pools.

5.3.3.2 Defining tumor areas of interest

To compare the CEST contrast within the different tumor compartments we delineated regions of interest (ROI) within the gadolinium contrast-enhancing tumor lesion (Gd CE lesion) and non-enhancing lesions (NE lesion), as well as an area in the contralateral normal-appearing white matter (CL NAWM) for within patient comparison. The enhancing lesion segmentations were delineated on the post-contrast gadolinium enhanced T₁w images and only voxels that did not exhibit partial volume effects were considered. Therefore, we only included the Gd CE lesions of patients who had a tumor of at least 10 mm measured in the transverse plane (in the largest diameter), hence lesions had to have at least 5 CEST voxels of 2 mm to be included. The NE lesions were delineated on the T₂-FLAIR, including the T₂ hyperintense areas, which had to have a clear and solid T₂ hyperintense area. We excluded the area of the Gd CE lesion and necrosis from the NE lesion segmentation. Lastly, a ROI within the CL NAWM was segmented within a region where the B₁ was at least 85% of the maximum B₁ to avoid having the issue with B₁ inhomogeneities for comparison.

5.3.3.3 Statistical analysis

To compare the CEST values between tumor lesions within each metric, a Kruskal Wallis test was used, given the non-normally distributed data. A post-hoc test was then applied to assess which groups were significantly different between each other. The significance threshold was set at $p \leq 0.05$. Statistical analysis was done using R version 4.1.2 (R Core Team 2021).

5.3.4 Data availability

Data will be made available upon reasonable request.

5.4 Results

Figure 1 presents the average and standard deviation of CEST metric values calculated from the voxels of the CL NAWM, the NE lesion, and the Gd CE lesion. This data encompasses all 21 patients; however, in one case, no NE lesion was present, and in twelve cases, no Gd CE lesions were observed. All quantification results can be found in the Supplementary Table S2.

MTR asymmetry of the 2 ppm CEST pool differed significantly between the different tumor lesions ($p = 0.001$). More specifically, the Gd CE lesions (6.6 ± 2.5) exhibited on average a significantly higher 2 ppm CEST contrast percentage values compared to the CL NAWM (2.6 ± 1.9 , $p = 0.002$) and the NE lesion (3.6 ± 1.7 , $p = 0.034$). Similarly, the LD also showed to be overall significantly different between lesions ($p < 0.001$), and having significantly higher 2 ppm LD values on the Gd CE lesion (8.1 ± 1.4), significantly higher than the CL NAWM (5.2 ± 1.8 , $p < 0.001$), and the NE lesion (6.6 ± 1.2 , $p = 0.052$). The latter two lesions also showed significantly different LD values ($p = 0.004$).

In figure 1C, the REX measured at 2 ppm was overall significantly different between lesions ($p = 0.008$). This was specifically observed between the (CL NAWM = 50.0 ± 20.2) and the NE lesion (31.9 ± 13.0) ($p = 0.005$). The 2 ppm CEST contrast in the Gd CE lesion (39.5 ± 15.6) was on average lower than the CL NAWM and higher than the NE lesion, but not significantly different. For T_1 corrected AREX in figure 1D, similar significant results were observed ($p = 0.001$). The CL NAWM (37.8 ± 17.5) had significantly higher 2 ppm CEST contrast compared to the NE lesion (20.1 ± 11.4) ($p = 0.001$). Contrarily, this was not the case for the Gd CE lesion (25.9 ± 14.3), which on average had a higher 2 ppm CEST contrast than the NE lesion, but not significantly.

Figure 2 illustrates an example of a patient with glioblastoma, IDH wild type, World Health Organization (WHO) grade 4, displaying CEST maps generated from the different calculated CEST metrics from the CEST pool at 2 ppm. The respective T_2 -FLAIR and post-contrast Gd T_1w anatomical images are shown in figure 2C and figure 2F. It can be observed that the whole tumor area appears as hyperintense areas on the MTR asymmetry (figure 2A) and Lorentzian difference (figure 2B) maps. Conversely, the REX (figure 2D) and AREX (figure 2E) metrics

display the tumor area as hypointense lesions.

Figure 3 presents an example of a patient with an anaplastic astrocytoma, IDH mutant, WHO grade 3, displaying the CEST maps for the CEST pool at 2 ppm. Although this tumor lacks an enhancing component (figure 3F), a small hyperintense region (figure 3C) is visible in the tumor area on the MTR asymmetry (figure 3A) and Lorentzian difference (figure 3B) maps. Conversely, the REX (figure 3D) and AREX (figure 3E) maps show a very hypointense tumor lesion, which corresponds well with the tumor area depicted in the anatomical images.

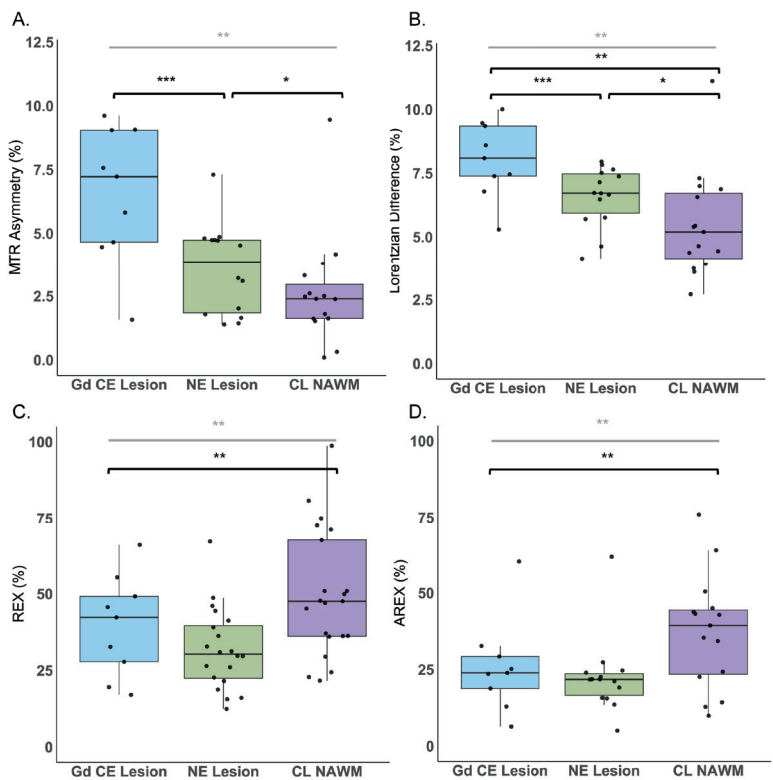


Figure 1. Scatter and box plots showing the amines 2 ppm values for each patient and respective mean and standard deviations of the calculated A. MTR asymmetry, B. Lorentzian difference, C. REX and D. AREX of the voxels included in the contralateral normal appearing white matter (CL NAWM), non-enhancing lesion (NE lesion) and gadolinium contrast enhanced lesion (Gd CE lesion) regions of interest. The significantly different results are illustrated with *, **, and *** for ≤ 0.05 , ≤ 0.01 and ≤ 0.001 , respectively.

Figure 4 presents an example of a patient with astrocytoma, IDH mutant, WHO grade 2 with a non-enhancing tumor. The MTR asymmetry CEST map (figure 4A) reveals a slight hyperintense area that aligns with the hyperintense tumor region on the T₂-FLAIR image (figure 4C). This lesion also appears slightly hyperintense on the Lorentzian difference CEST map (figure 4B). In contrast, the REX (figure 4D) and AREX (figure 4E) CEST maps display the same tumor lesion as hypointense.

Figure 5 displays a representative contrast-enhancing tumor in the upper row and a non-enhancing tumor in the lower row. The enhancing tumor is a classic example of a glioblastoma, where the enhancing rim is clearly distinguished, surrounded by a non-enhancing area (figures 5A-5B). On both the CEST REX and AREX maps (figures 5E-5F), the enhancing rim appears as a hyperintense region encircling the necrotic core of the tumor, which shows up as hypointense. Conversely on the MTR asymmetry and Lorentzian difference maps (figures 5C-5D), a hyperintense area is seen on the regions where the enhancing and necrotic areas are present. The surrounding non-enhancing areas are less hyperintense, which is in line with our results in figure 1A and 1B. In contrast, the non-enhancing tumor in the lower row (figures 5G-5H) represents a lower-grade tumor (anaplastic astrocytoma, IDH mutant, WHO grade 3) with a hypointense tumor area on the CEST REX and AREX maps (figures 5K-5L). The MTR asymmetry and Lorentzian difference maps show slightly higher 2 ppm CEST contrast in the tumor area (figures 5I-5J). The hypointense area on the REX and AREX maps in figures 1K and 1L correspond with the non-enhancing region seen on the T_2 -FLAIR image and the surgical resection cavity, less evident on figures 1I and 1J.

Lastly, Figure 6 presents the Lorentzian fittings obtained from the average Z-spectra of voxels within the Gd CE (figure 6A), NE (figures 6B-6D), and CL NAWM (figures 5C-5E) segmentations. These fittings correspond to two representative tumors: an enhancing tumor in the upper row and a non-enhancing tumor in the lower row. As quantitatively demonstrated in Figure 1, the 2 ppm CEST pool values are higher in the CE and NE regions compared to the CL NAWM. Moreover, the broad Z-spectra from the CL NAWM could be due to magnetization transfer (MT) effects.

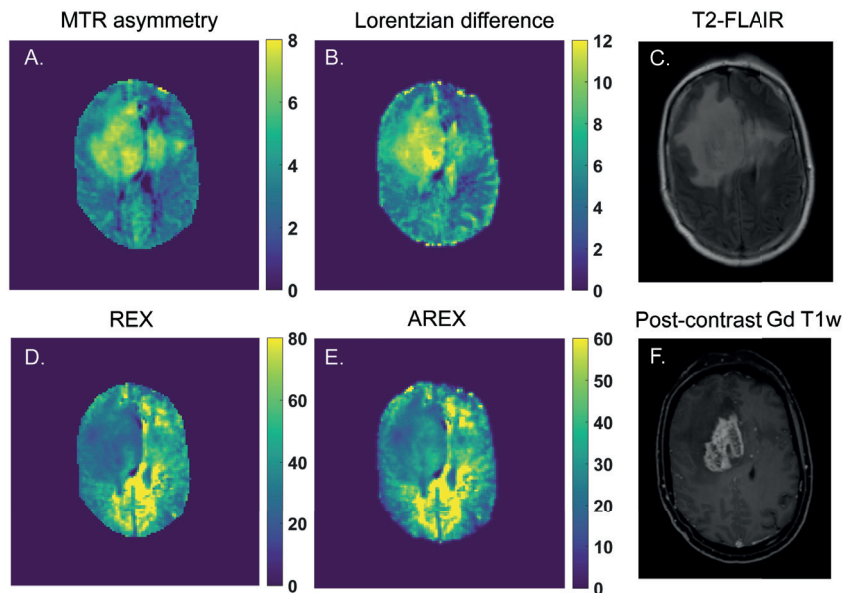


Figure 2. An example of a glioblastoma patient and the calculated 2 ppm pool CEST maps from A. MTR asymmetry (%), B. Lorentzian difference (%), D. REX (%) and E. AREX (%). In C. and F. the anatomical T_2 -FLAIR and post-contrast Gd enhanced T_1w are shown, respectively, illustrating where the tumor lesion can be found.

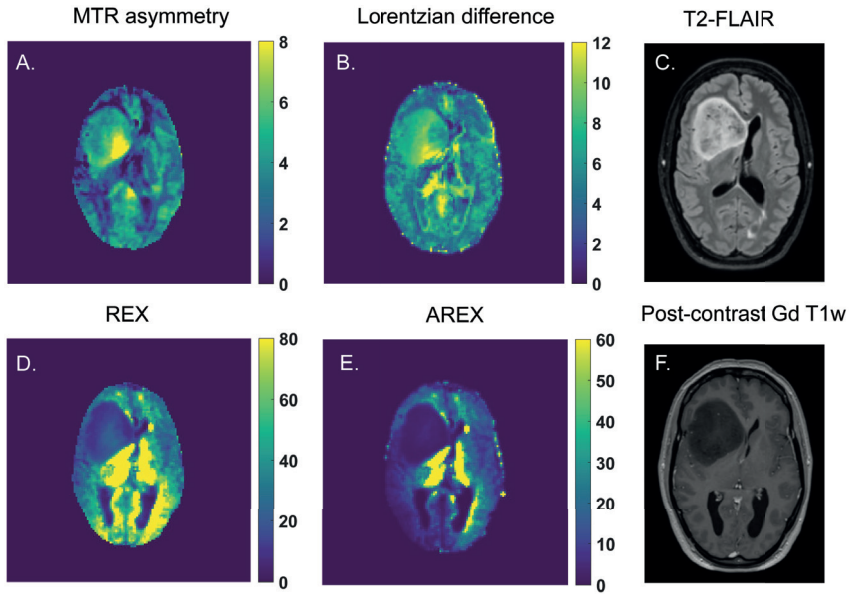


Figure 3. An example of an anaplastic astrocytoma (IDH mutant) and the calculated 2 ppm pool CEST maps from A. MTR asymmetry (%), B. Lorentzian difference (%), D. REX (%) and E. AREX (%). In C. and F. the anatomical T_2 -FLAIR and post-contrast Gd enhanced T_1w are shown, respectively, illustrating where the tumor lesion can be found.

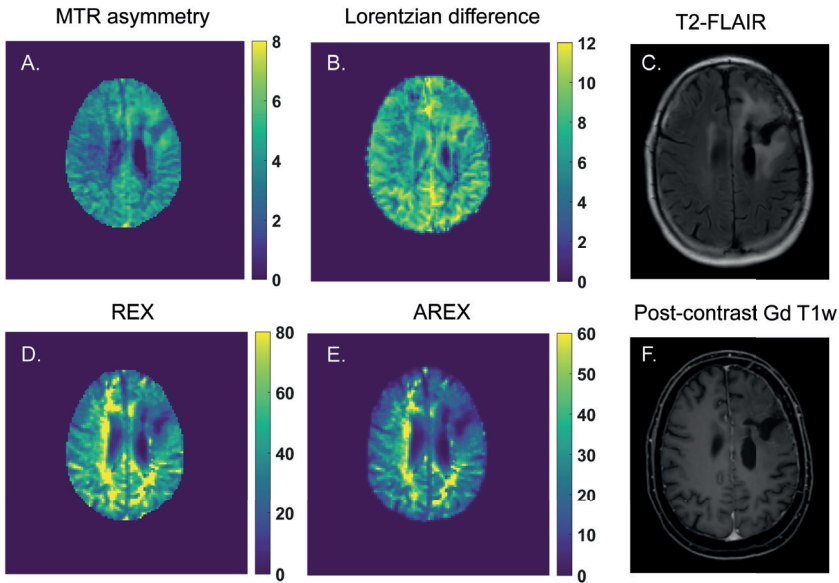


Figure 4. An example of a diffuse astrocytoma (IDH mutant) patient and the calculated 2 ppm pool CEST maps from A. MTR asymmetry (%), B. Lorentzian difference (%), D. REX (%) and E. AREX (%). In C. and F. the anatomical T_2 -FLAIR and post-contrast Gd enhanced T_1w are shown, respectively, illustrating where the tumor lesion can be found.

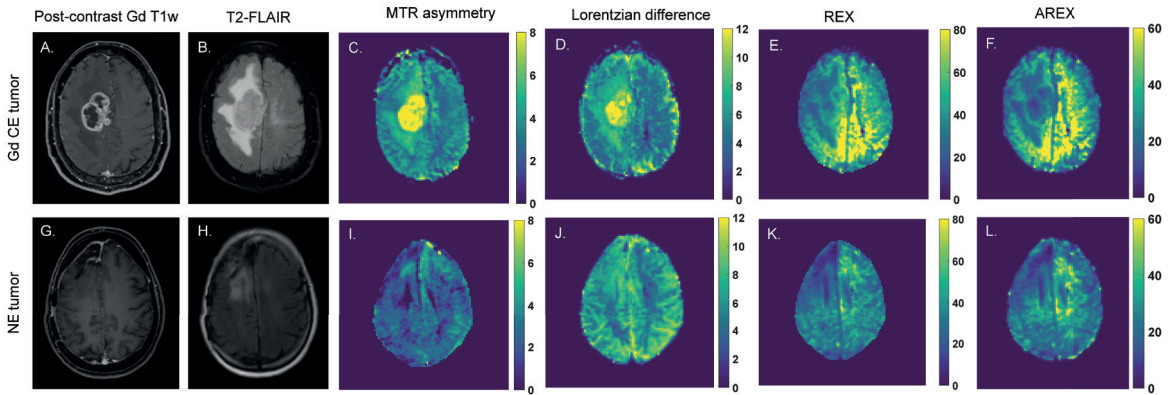


Figure 5. Two examples of enhancing and non-enhancing tumors on the upper and lower rows, respectively. A, D and G, H illustrate where the tumor lesions can be found on the post-contrast Gd T_1w and T_2 -FLAIR images, respectively. C – F and I – L shows the resulting MTR asymmetry (%), Lorentzian difference, REX (%) and AREX (%) CEST map of the 2 ppm pool for both cases.

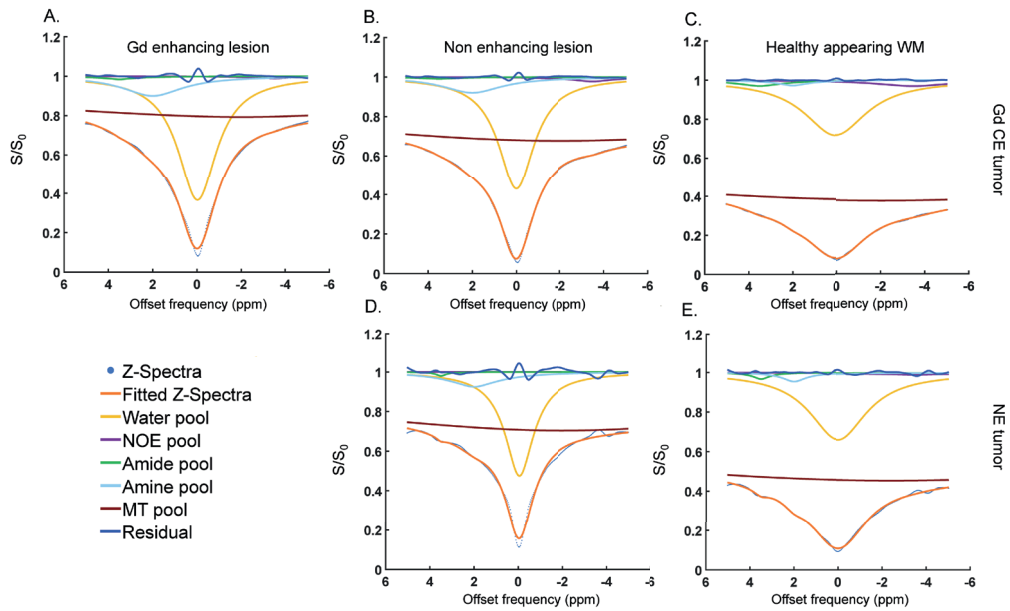


Figure 6. Two examples of 5-pool Lorentzian fittings from a enhancing tumor (upper row) and non-enhancing tumor (lower row). These graphs represent the average fittings of the voxels present in the A. gadolinium enhanced lesion, B., D. non-enhancing lesions and C., E. and contralateral healthy appearing white matter.

5.5 Discussion

The goal of this study was to investigate the CEST contrast at 2 ppm in the different tumor areas of gliomas. To this end, we acquired the CEST images at 7T MRI with a high B_1 rms accounting for the intermediate exchange rate of the CEST pool at 2 ppm^{66,139}. Hereafter we applied a manual segmentation process to define the different tumor regions of interest. Finally, we quantified the CEST contrast utilizing different metrics already in use for glioma CEST imaging⁵⁹. Our results showed that the 2 ppm CEST contrast differed between CE and NE lesions and CL NAWM depending on the metric used.

In this study we evaluated for the first time the 7T MRI CEST contrast of the 2 ppm CEST pool in the contrast enhancing and non-enhancing regions of gliomas. Although we did not investigate the source of this 2 ppm CEST contrast, one can speculate about its origins. Guanidinium protons resonating at this frequency can be found in metabolites such as creatine¹¹⁸. Creatine is known to be crucial for cellular metabolism. It provides phosphate from phospho-creatine to synthesize adenosine triphosphate within the cells. Previous work has shown that oxygen consumption increases in the presence of creatine, illustrating why it is crucial for maintaining adequate cell energy production through aerobic metabolism¹¹³. Healthy cells rely mostly on oxygen for ATP production, however tumors such as gliomas, often experience a metabolic shift towards anaerobic metabolism¹⁴⁰.

We observed overall increased 2 ppm CEST signal in CE and NE lesions compared to the CL NAWM. Previous animal work has shown similar results to ours, where the CEST contrast at 2 ppm when fitting the Z-spectra was found to be significantly different in the tumor compared to the normal-appearing tissue⁶³. Our results in figure 1 shows that the contrast enhancing, non-enhancing and normal-appearing regions 2 ppm CEST contrast significantly differed between each other. However, we could only find significant differences between all 3 regions while measuring the 2 ppm contrast with the Lorentzian difference. Although our MTR asymmetry results show a similar trend, most likely an increased standard deviation of the MTR asymmetry values in the non-enhancing lesions could have contributed to the fact that no significant difference was found between the CL NAWM and the NE lesion. Additionally, MTR asymmetry is sensitive to non-symmetric contaminants from neighboring pools, non-specific MT effects and direct water saturation. These factors could have influenced the MTR asymmetry quantification, whereas their impact is less pronounced when calculating the Lorentzian difference. A similar explanation could explain the fact that for the REX and AREX results we could only find a significant difference between the NE lesion and the CL NAWM. Figures 1C and 1D show a high standard deviation in all lesions, including a few outliers. When analyzing only the high-grade patients, we found a significant overall difference between the MTR asymmetry and Lorentzian difference metrics. Although we cannot rule out potential differences between tumor grades, the limited statistical power arising from the limited sample size restricted us from evaluating sub-groups with different tumor grades. In addition to the original analysis, when only the high-grade patients were included, we found no significant differences between tumor regions for

either REX or AREX. This is likely due to the relatively smaller effect sizes combined with the relatively large standard deviations (Supplementary Figure S1).

The fact that we do observe for at least one metric significant difference in the 2 ppm CEST contrast between the enhancing and non-enhancing components in glioma is not surprising. These two lesions have been suggested to be metabolically distinct. For example, one study found that enhancing lesions have an elevated lactate and pyruvate level compared to the non-enhancing lesion, reflecting the glycolytic metabolic preference and can correlate with the tumor's malignancy grade¹⁴¹. Another possible explanation relies on the fact that enhancing areas, typically representing higher-grade tumor activity, are metabolically more active. The increased energy requirements in order to meet cell proliferation demands could result in an increase in the presence of creatine in the cells. Non-enhancing lesions have less aggressive and infiltrative characteristics and could thus have relatively more preservation of creatine levels, since the cells are metabolically less intense.

To support this, a previous study looked at the total creatine in WHO grade 2 gliomas. The authors found that normalized total creatine levels were a significant predictor for tumor progression and malignant transformation in lower-grade gliomas¹⁴². They concluded that, in general, low-grade gliomas with a relative total creatine level below 1.0 may have a longer progression-free survival and a delayed risk of malignant transformation compared to cases with higher total creatine levels.

A more recent study investigated longitudinal changes in low-grade gliomas using multiparametric MRI and applied magnetic resonance spectroscopy imaging to monitor metabolic changes, specifically the creatine-to-NAA ratio (CRNI). Notably, CRNI values were found to be higher in astrocytomas that showed progression compared to stable cases; however, this pattern was not observed in oligodendrogliomas. The authors suggest that changes in creatine levels may be specific to WHO glioma subtypes¹⁴³. Another study reported that glioblastomas had lower creatine levels than astrocytomas, WHO grade 2 or 3¹⁴⁴. In poorly perfused regions with abnormal pH, high-grade gliomas also showed reduced creatine and elevated lactate levels. Tumor areas with increased cerebral blood volume demonstrated higher creatine levels, likely due to the initial rise in energy demands associated with new blood vessel formation¹⁴³. Additionally, another study found decreased creatine in grade 3 tumors overall, although areas of higher metabolism exhibited elevated creatine. An increase in creatine may be an early indicator of cellular energy stress, preceding the shift to anaerobic respiration and subsequent lactate accumulation¹⁴³. A more recent study looked at different metabolite concentrations while combining low- and high-grade glioma MRS imaging data at 7T. Similarly to our study, by including both low- and high-grade gliomas, the authors observed an overall decrease in total creatine in the tumor regions, although a few cases showed an increase in total creatine¹⁴⁵.

CEST contrast at 2 ppm is known to have a substantial contribution from guanidinium protons⁴⁹. A recent study investigated the origins of the CEST contrast at 2 ppm in the rat brain¹¹⁷. The

authors concluded that the contribution from guanidinium protons in amino acids cannot be excluded when interpreting the CEST contrast at 2 ppm in the rat brain. Although confirmation of these results in humans still needs to follow, these results show the importance of being cautious regarding interpreting the origins of the 2 ppm CEST contrast in the brain. More recent studies in the human brain have also investigated the contribution of the guanidinium pool to the CEST contrast at 2 ppm. They concluded that CEST contrast at 2 ppm is an interesting technique for creatine mapping of the brain and showed guanidinium CEST mapping in a brain tumor patient at 3T^{146,147}. Since amide protons are known to be present in glioma and guanidinium protons from proteins contribute to the contrast at 2 ppm, it would be interesting to explore how much of the 2 ppm CEST contrast in tumors comes from guanidinium in proteins versus guanidinium in creatine.

Given CEST's limited specificity, the environmental conditions surrounding the metabolite or protein of interest are critical in determining the optimal parameters for accurate detection. CEST contrast is influenced not only by temperature but also by pH³³. For instance, the extravascular extracellular tumor microenvironment is often acidic due to lactate efflux, while the intracellular environment has a high basic pH¹⁴⁸. In such a high pH environment, guanidinium protons at 2 ppm undergo rapid exchange. To maximize sensitivity, the CEST sequence used in our study was designed with a high saturation power. Since guanidinium protons under the same acidic conditions are known to exchange at an intermediate rate⁹⁸ (compared to amines), we hypothesize that the CEST contrast we observed is primarily driven by guanidinium protons.

While further experiments are needed to confirm the exact origin of the contrast, our results highlight the possibilities of using the 2 ppm CEST pool in differentiating tumor components. Although we did not correct for pH in our analysis, the distinct contrasts observed across various tumor regions suggest that the pH of the tumor microenvironment may play a significant role in these findings. Previous studies have explored pH-weighted imaging of the 3 ppm amine pool using CEST in glioblastomas¹⁴⁹. One key finding was that an increase in the amine CEST effect occurred only in low pH environments, demonstrating its potential as a non-invasive tool for detecting acidic regions. This increase in contrast was predominantly observed in the more active and malignant tumor areas. Similarly, we observed an increase in CEST contrast in the enhancing regions of the tumors we studied, with a comparable MTR asymmetry.

In our study, we incorporated various CEST metrics to evaluate how the results might vary across them. Lorentzian fitting is theoretically more accurate as it accounts for relaxation effects. AREX further improves reliability by incorporating correction for T_1 -effects, allowing for more precise quantification. However, its accuracy depends on precise T_1 mapping and sufficient SNR for robust spectral analysis. Similarly, Lorentzian line shape fitting allows the separation of different CEST effects, including direct water saturation and MT. The main challenge, however, is acquiring high-quality data to effectively distinguish the various exchange pools. Contrarily, MTR asymmetry is the most widespread used quantification metric due to its simplicity which includes a straightforward reporting on the different CEST pools.

However, it is prone to contamination from competing effects, including MT and direct water saturation. Figure 1 illustrates that our findings remained largely consistent, although it should be kept in mind that the markers of Figures 1C and 1D representing an inverse metric compared to Figures 1A and 1B. The primary difference observed was that enhancing lesions exhibited higher values than non-enhancing lesions for MTR Asymmetry and Lorentzian Difference metrics compared to REX and AREX. The difference may be attributed to the fact that both REX and AREX metrics correct for MT and spillover effects. MTR asymmetry and the Lorentzian difference do not. Consequently, eliminating these confounding effects could provide a more accurate representation of the CEST contrast at 2 ppm. Similarly, we observed a larger standard deviation in the Lorentzian difference, REX and AREX results, specifically for the CL NAWM. These differences could be present due to partial volume effects in the chosen ROIs due to the voxel size, despite our efforts to minimize the partial volume effects while drawing the ROIs. Secondly, the CL NAWM ROIs were drawn on the same slice as the tumor. Since some tumors were located in lower brain regions, where magnetic field inhomogeneities are more pronounced, this may have affected T_1 mapping. Lastly, and perhaps most importantly, the concentration of guanidinium protons in white matter is relatively lower compared to tumors. Due to this lower concentration, detecting a sufficient signal becomes more challenging, making the fitting process more susceptible to noise.

However, due to our limited patient sample, these findings need to be validated in a larger cohort to potentially attenuate outliers and in some cases large standard deviations, which could have impacted our statistical conclusions. Our results suggest that the 2 ppm CEST contrast differs between enhancing, non-enhancing lesions, and normal-appearing tissue. Determining the optimal metric for this purpose lies beyond the scope of our study, as the primary aim was to explore whether the results would vary depending on the metric used to quantify the CEST contrast of interest.

Our study has several strengths, including a relatively large cohort of glioma patients with prospectively acquired CEST data at 7T MRI. Given the prospective nature we were able to optimize and implement a CEST protocol specific for fast exchanging amines (ie. higher B_1 rms) which is different from the protocol used for slow exchanging CEST pools such as APT and NOE. Additionally, clinical MR scans were available, serving as the gold standard for imaging comparison. Another key strength is the use of different CEST metrics to measure CEST contrast in this patient group for the first time.

However, there are also some limitations to consider. First, we included a somewhat heterogeneous group of glioma patients, both pre- and post-treatment. As a result, we cannot entirely rule out the potential influence of treatment procedures on the observed CEST contrast. Furthermore, because of this broad patient group, the differences in 2 ppm CEST contrast between high- and low-grade tumors remain unexplored. Second, we used a linear B_1 correction method. While other correction methods have demonstrated superior performance, they were not feasible for this study due to their time-consuming nature during data acquisition.

Thirdly, our saturation pulses were interleaved with 50 ms gaps. The interpulse delays are included to adhere to specific absorption rate (SAR) limits and the RF amplifier requirements of the MR scanner used¹³⁹. Ideally we would have employed shorter interpulse delays and longer or more saturation pulses, which would be more desirable to enhance the contrast between intermediate and fast exchanging pools. Due to these limitations it could be that there could be some contamination from slow exchanging amides in our signals. Lastly, despite optimizing our protocol for the CEST pool at 2 ppm, we cannot definitively determine the precise origin of the CEST contrast, as MRS measurements were not included.

These preliminary results indicate promising applications for 2 ppm CEST in glioma imaging. Future research could focus on expanding this methodology to different glioma subgroups, including patients with different clinical symptoms (e.g. epilepsy) allowing for a deeper understanding of how the CEST pool at 2 ppm contrast varies across disease stages. Additionally, studying groups exclusively pre- or post-treatment could help clarify the impact of treatment on the 2 ppm CEST contrast. Finally, increasing the sample size would enable a more robust evaluation of potential statistical differences between groups.

In conclusion, our study demonstrated a significantly distinctive 2 ppm CEST contrast between normal-appearing white matter, enhancing, and non-enhancing tumor lesions in glioma patients. These findings suggest that the CEST pool at 2 ppm may provide valuable non-invasive contrast for glioma evaluation, though further confirmation in a larger cohort is necessary.

5.6 Acknowledgments

This study (project no. 16862) was financed by the Dutch Research Council (NWO) Talent Programme Veni and by the Medical Delta Cancer Diagnostics 3.0 program.

This work was also made possible by all the members of the consortium listed below:

7T MRI Neuro-Oncology consortium members listed in alphabetical order based on last name

Monique Baas-Thijssen¹, Christa Benit², Jeroen de Bresser³, Marike Broekman¹, Linda Dirven^{1,4}, Daniëlle van Dorth³, Lara Fritz⁴, Melissa Kerkhof⁴, Johan A.F. Koekkoek^{1,4}, Rishi Nandoe-Tewarie⁴, Matthias J.P. van Osch^{3,5}, Bárbara Schmitz-Abecassis^{3,5}, Martin J.B. Taphoorn^{1,4}, Maaïke Vos⁴

¹Department of Neurology, Leiden University Medical Center, Leiden, the Netherlands

²Department of Neurology, Alrijne Hospital, Leiden, the Netherlands

³Department of Radiology, Leiden University Medical Center, Leiden, the Netherlands

⁴Department of Neurology, Haaglanden Medical Center, The Hague, the Netherlands

⁵Medical Delta, South-Holland, The Netherlands

5.7 Conflict of interest

Ece Ercan is a full-time employee at Philips Healthcare, Best, The Netherlands.

5.8 Abbreviations

Chemical Exchange Saturation Transfer	CEST
Non-Enhancing	NE
Contrast-Enhancing	CE
Gadolinium contrast-enhancing	Gd CE
Contralateral normal appearing white matter	CL NAWM
Magnetization transfer ratio	MTR
Exchange-dependent relaxation	REX
Apparent exchange-dependent relaxation	AREX
Amide proton transfer, APT; Nuclear overhauser effect	NOE
Part per million	ppm
Isocitrate dehydrogenase	IDH
Fluid-attenuated inversion recovery	FLAIR
Total saturation	t_{sat}
B_1 root mean squared	$B_{1,\text{rms}}$
Dual refocusing echo acquisition mode	DREAM
Water saturation shift reference	WASSR
Field of view	FOV
World Health Organization	WHO

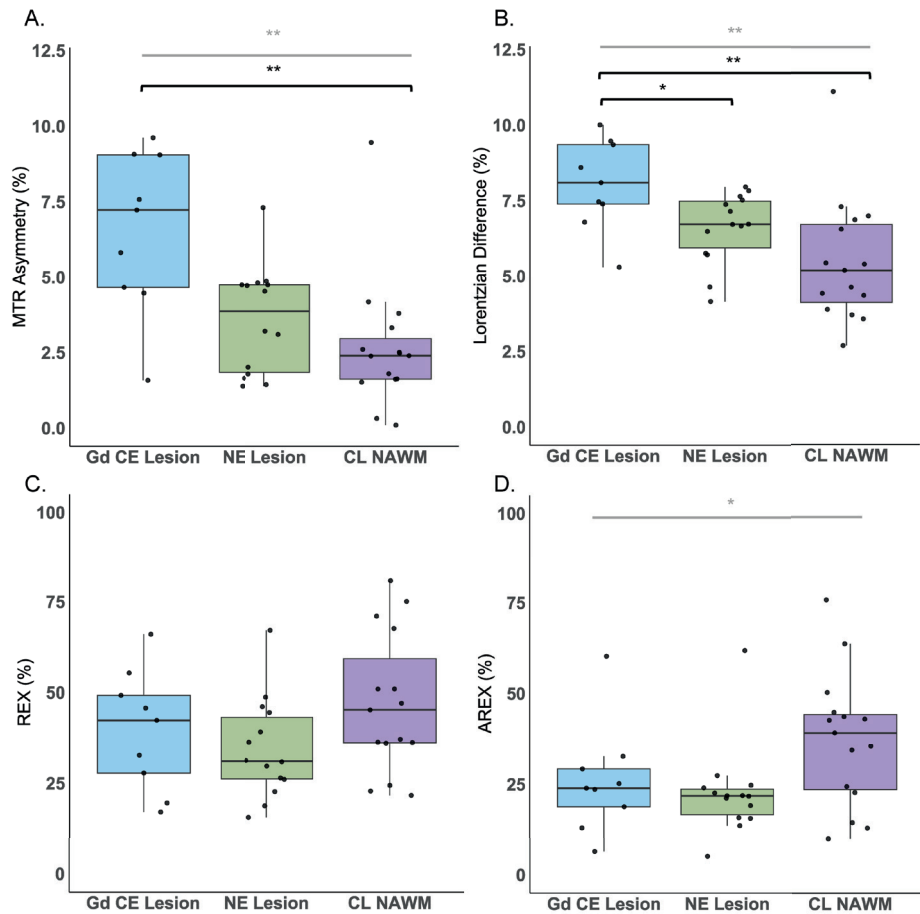
5.9 Supplementary material

Supplementary Table S1. Fitting parameters used for Lorentzian fittings.

Pool	Start	Lower	Upper
Amplitude: Water	0.9	0.02	1
Width: Water	1.4	0.3	10
Frequency: Water	0	-0.5	0.5
Amplitude: MT	0.1	0	1
Width: MT	25	0	150
Frequency: MT	0	-4	-2
Amplitude: NOE	0.02	0	0.4
Width: NOE	3	1	5
Frequency: NOE	-3.5	-3.5	-3.5
Amplitude: APT	0.025	0	0.2
Width: APT	0.5	0.4	3
Frequency: APT	3.5	3.5	3.5
Amplitude: CEST at 2 ppm	0.01	0	0.2
Width: CEST at 2 ppm	1.5	1	3.5
Frequency: CEST at 2 ppm	2	2	2

Supplementary Table S2. CEST (%) values per quantification metric from each tumor lesion. Values are displayed for all patients and respective diagnosis.

Patients	Diagnosis	WHO grading	MTR asymmetry (%)				Lorentzian Difference (%)				REX (%)				AREX (%)			
			Gd CE Lesion	NE Lesion	CL NAWM	Gd CE Lesion	NE Lesion	CL NAWM	Gd CE Lesion	NE Lesion	CL NAWM	Gd CE Lesion	NE Lesion	CL NAWM	Gd CE Lesion	NE Lesion	CL NAWM	
1	Glioblastoma, IDH-wildtype	Grade 4	9.1	1.4	4.2	9.4	7.6	4.6	55.4	44.5	75.1	32.7	27.4	50.5				
2	Glioblastoma, IDH-wildtype	Grade 4	9.1	1.4	1.6	7.5	7.5	4.4	45.7	39.1	71.0	23.6	24.0	76.1				
3	Glioblastoma, IDH-wildtype	Grade 4		1.7	1.8		4.2	3.6		18.8	36.2		21.9	39.4				
4	Glioblastoma, IDH-wildtype	Grade 4		4.8	1.6		6.7	5.2		48.7	36.0		22.6	22.6				
5	Glioblastoma, IDH-wildtype	Grade 4	4.5		2.5	7.4		5.4	32.7		67.6	18.8		42.9				
6	Glioblastoma, IDH-wildtype	Grade 4	9.6	7.3	-0.3	8.1	6.5	7.0	19.6	22.7	36.3	13.0	15.8	34.3				
7	Glioblastoma, IDH-wildtype	Grade 4		3.2	-0.1		5.7	3.9		30.9	21.7		13.6	14.3				
8	Glioblastoma, IDH-wildtype	Grade 4	4.7	4.7	3.3	5.3	5.8	4.4	66.0	67.1	45.2	60.3	61.8	45.0				
9	Glioblastoma, IDH-wildtype	Grade 4	7.2	4.5	3.8	8.6	7.8	7.3	42.3	26.5	37.1	25.2	15.6	24.3				
10	Glioblastoma, IDH-wildtype	Grade 4	5.8	4.7	1.5	10.0	8.0	2.7	27.8	29.7	51.0	29.3	21.9	43.9				
11	Anaplastic astrocytoma, IDH-mutant	Grade 3		2.1	2.3		7.5	4.6		21.5	49.9		19.4	42.6				
12	Oligodendroglioma (suspected)	Grade 2		3.5	2.5		6.0	3.6		41.3	72.4		17.2	41.7				
13	Glioblastoma, IDH-wildtype	Grade 4		3.1	2.4		6.7	5.4		26.1	51.0		21.2	43.2				
14	Glioblastoma, IDH-wildtype	Grade 4		4.9	2.5		6.7	6.9		46.1	22.9		21.7	12.9				
15	Glioblastoma, IDH-wildtype	Grade 4	7.6	4.7	2.6	9.5	7.4	3.7	49.2	36.3	80.8	23.9	24.7	63.9				
16	Diffuse Astrocytoma, IDH mutant	Grade 2		1.4	2.0		4.1	4.2		12.4	29.5		7.4	21.6				
17	Diffuse Astrocytoma, IDH mutant	Grade 2		4.4	3.4		7.5	6.0		32.8	47.6		16.8	30.3				
18	Glioblastoma, IDH-wildtype	Grade 4		2.0	9.5		4.6	11.1		31.3	47.0		19.1	35.4				
19	Anaplastic astrocytoma, IDH-mutant	Grade 3		4.8	0.7		7.9	3.8		16.1	47.7		4.4	27.3				
20	Oligodendroglioma, IDH-mutant and 1p/19q co deleted	Grade 2		6.0	4.4		5.8	5.1		29.7	98.7		20.3	71.5				
21	Glioblastoma, IDH-wildtype	Grade 4	1.6	1.8	2.4	6.8	7.2	6.6	17.1	15.6	24.4	6.4	5.1	9.9				



Supplementary Figure S1. Scatter and box plots showing the 2 ppm pool values for the Glioblastoma IDH-wildtype patients and respective mean and standard deviations of the calculated A. MTR asymmetry, B. Lorentzian difference, C. REX and D. AREX of the voxels included in the contralateral normal appearing white matter (CL NAWM), non-enhancing lesion (NE lesion) and gadolinium contrast enhanced lesion (Gd CE lesion) regions of interest. The significantly different results are illustrated with * and ** for ≤ 0.05 and ≤ 0.01 , respectively; marked in grey and black for the Kruskal Wallis test and post-hoc test, respectively.

6 Extension of T_2 hyperintense areas in patients with a glioma: a comparison between high-quality 7T MRI and clinical scans

Bárbara Schmitz-Abecassis
Ivo Cornelissen
Robin Jacobs
Jasmin A. Kuhn-Keller
Linda Dirven
Martin J. B. Taphoorn
Matthias J. P. van Osch
Johan A. F. Koekkoek
Jeroen de Bresser

NMR in Biomedicine (2025). DOI: 10.1002/nbm.5316

6.1 Abstract

Gliomas are highly heterogeneous and often include a non-enhancing component that is hyperintense on T_2 weighted MRI. This can often not be distinguished from secondary gliosis and surrounding edema. We hypothesized that the extent of these T_2 hyperintense areas can more accurately be determined on high-quality 7T MRI scans. We investigated the extension, volume and complexity (shape) of T_2 hyperintense areas in patients with glioma on high-quality 7T MRI scans compared to clinical MRI scans.

T_2 hyperintense areas of 28 patients were visually compared and manually segmented on 7T MRI and corresponding clinical (1.5T/3T) MRI scans, and the volume and shape markers were calculated and subsequently compared between scans.

We showed extension of the T_2 hyperintense areas via the corpus callosum to the opposite hemisphere in 4 patients on the 7T scans that was not visible on the clinical scan. Furthermore, we found a significantly larger volume of the T_2 hyperintense areas on the 7T scans compared to the clinical scans [7T scans: 28 ml (12.5-59.1); clinical scans: 11.9 ml (11.8–56.6); $p=0.01$]. We also found a higher complexity of the T_2 hyperintense areas on the 7T scans compared to the clinical scans (convexity, solidity, concavity index and fractal dimension ($p<0.001$)).

Our study suggests that high-quality 7T MRI scans may show more detail on the exact extension, size and complexity of the T_2 hyperintense areas in patients with a glioma. This information could aid in more accurate planning of treatment, such as surgery and radiotherapy.

6.2 Introduction

Gliomas are the most common primary malignant brain tumor and are diffuse and heterogeneous in their morphology¹⁵⁰. They are known to grow along white matter tracts and usually include non-enhancing components as well as possible secondary gliosis (related to treatment effects and secondary ischemia) and the usual surrounding edema^{151–153}. Patients with glioma often undergo MRI scans for the purpose of diagnosis, treatment planning and follow-up¹⁵⁴. Standard clinical practice includes the acquisition of T_2 weighted imaging (T_2 WI) and T_2 fluid attenuated inversion recovery (T_2 -FLAIR)¹⁵⁵. The T_2 WI scans allow visualization of fluid rich compartments as well as abnormal tissue, as these usually have longer T_2 relaxation times and thus will appear hyperintense. T_2 -FLAIR allows portraying abnormal tissue in a similar way, but with the difference that any free moving fluid is suppressed. Combined, these clinical images allow portrayal of important details on tumor morphology. However, distinguishing between non-enhancing tumor components and secondary changes (such as edema and gliosis), which all appear as T_2 hyperintense areas can be challenging¹⁵⁶. Information on the exact extent of these could aid in more accurate planning of tumor-directed treatment, such as surgery and radiotherapy.

Ultra-high field 7T MRI benefits from an increase in contrast and signal to noise ratio (CNR and SNR, respectively), allowing the acquisition of higher resolution images with more contrast between sub-components of tumors¹⁵⁷. The higher resolution potential is harnessed by yielding images with smaller voxel size, resulting in less partial volume effect and thus more tissue specific representation per voxel. For patients with glioma in clinical practice this could mean obtaining images with enhanced tumor visualization regarding tissue borders and extension in a reasonable clinical acquisition time¹⁵⁸. The more limited resolution of current clinical MRI scans might underestimate the tumor extension along white matter tracts, which could influence the planning of radiotherapy and surgical resection.

The value of using ultra-high field 7T MRI for patients with glioblastoma has been studied before, for example Regnery et al. have demonstrated that 7T T_2 -FLAIR images may enhance the delineation of organs at risk for radiotherapy planning, such as the hippocampus, which could help to preserve long-term cognitive function¹⁵⁹. Moreover, they found an increase of signal to noise ratio (SNR), but a decrease in contrast to noise ratio (CNR). A smaller gross tumor volume of the T_2 hyperintense area was also found in the 7T T_2 -FLAIR images. Although their sequence duration was longer than common in current clinical practice, it still proved to be clinically feasible. This study showed preliminary evidence of the benefit of higher-quality images for this patient population, specifically concerning radiotherapy planning. However, several important other features, such as tumor shape, were not considered. Shape would be a particularly interesting feature to explore, given the suggestion that gliomas may grow along white matter tracts, potentially shaping the complexity of these lesions^{152,153}. Moreover, the previous study only looked at patients with glioblastoma, whereas visualization of T_2 hyperintense areas is at least as clinically relevant in generally non-contrast enhancing lower

grade gliomas. Given that ultra-high field 7T MRI has the potential to acquire higher-quality images at reasonable scanning times, we wanted to investigate if these benefits can enhance glioma tumor visualization in general and help in estimating its extension and complexity. We therefore aimed to investigate the extension, volume and shape of T_2 hyperintense areas in patients with a glioma on high-quality 7T MRI scans compared to clinical MRI scans.

6.3 Methods

6.3.1 Patient inclusion

Patients from the Leiden University Medical Center and Haaglanden Medical Center were prospectively included for this study between March 2021 and May 2023 when there was a high suspicion of having a glioma or a confirmed histopathological diagnosis. Other inclusion criteria included a Karnofsky Performance Status score ≥ 70 and no MRI contraindications. The study was approved by the local ethics committee and all patients gave written informed consent prior to participation.

6.3.2 Data acquisition

Clinical MRI scans, obtained at either 1.5T or 3T, were collected as part of patients' standard clinical care, adhering to routine clinical guidelines. 3T T_2 WI multi slice were acquired on a Philips Ingenia 3T MRI scanner (Philips Healthcare, Best, The Netherlands) with TR = 4490ms TE = 80ms, voxel size = 0.4x0.5x3mm and FOV = 220x175x50. Total acquisition time was 01:57 minutes. 1.5T T_2 -FLAIR multi slice were acquired on a Siemens MAGNETOM Avanto 1.5T scanner (Siemens, Erlangen, Germany) with TR = 7500ms, TE = 105ms, voxel size = 0.4x0.4x5 mm and FOV = 230 x 230 x 144 mm. Total acquisition time was 02:08 minutes.

7T MRI scans were acquired on a Philips Achieva 7T MRI scanner (Philips Healthcare, Best, The Netherlands) with a dual-transmit and a 32-channel receive head coil (Nova Medical Inc, Wilmington, MA, USA). The 3D T_2 WI was acquired with TR = 3000ms, TE = 278ms, voxel size = 0.75x0.75x0.75 mm, FOV = 250x250x190 mm and the total acquisition time was 04:06 minutes. The 3D T_2 -FLAIR was acquired with TR = 8000ms, TE = 256ms, voxel size = 0.7x0.7x0.7mm, FOV = 240x209x190mm and the total acquisition time was 05:12 minutes.

High-quality 7T MRI and clinical MRI scans (1.5T or 3T) were acquired, on average, within (mean) 5 days (± 5.3 standard deviation) of each other.

6.3.3 Visual assessment of the T_2 hyperintense areas

Firstly, a systematic visual assessment of the T_2 hyperintense areas was performed by evaluating side by side the high-quality and clinical MRI scans for all 28 patients. The goal was to compare the range of extension of the T_2 hyperintense areas with a special focus on the involvement of neighboring anatomical structures. Such structures also served as anatomical landmarks for a fair comparison between the clinical and 7T images acquired. Examples of considered structures include the corpus callosum, the basal ganglia, brain stem, and white matter tracts. In cases where the tumor was located in the center of the brain (close to the brain stem), and artefacts in the high-quality MRI scans impaired proper visualization, the clinical scans were used to determine the border of the T_2 hyperintense area. The visual assessment

was performed by a radiologist in training (IC) under supervision of an experienced neuro-radiologist (JB).

6.3.4 Segmentation of the T_2 hyperintense areas

Segmentations of the T_2 hyperintense areas were performed by two investigators on T_2 WI, and when not available, on the T_2 -FLAIR. To minimize learning effects between delineations performed on the clinical images and those on the 7T images, all delineations were first completed on the clinical images, followed by the 7T images. This process was accomplished under supervision of IC and JB. Although the segmentations were done by two observers, the methodology employed and the radiological supervision was the same. This means that a methodological consensus was reached between the radiologist (in training) and the two investigators before performing the segmentations and that the segmentations were visually checked in a consensus meeting with the experienced neuro-radiologist. Areas were defined as T_2 hyperintense when there was a clear and solid hyperintense area including the tumor core, peritumoral edema and/or non-enhancing tumor components. Other T_2 hyperintense brain changes such as resection cavities, infarctions and age related white matter hyperintensities were excluded from the segmentations. Finally, in cases where the border between the T_2 hyperintense lesion and eventual white matter hyperintensities could not be clearly distinguished, we defined what would most probably be the T_2 hyperintense area and its respective border. The same strategy was used for both clinical and 7T scans to result in similar segmentation results.

6.3.5 Volume and shape of the T_2 hyperintense areas

Volume and shape markers were computed for the T_2 hyperintense areas. Shape markers, including solidity, convexity, concavity index, and fractal dimension, were calculated based on the convex hull, volume, and surface areas of the segmented lesions, similarly to a method previously used for white matter hyperintensities¹⁵⁹. In cases where patients had T_2 hyperintense areas appearing continuous on the 7T high-quality scans, but fragmented in the clinical scans (i.e., more than one area), the largest area was chosen for the shape analysis.

6.3.6 Statistical analysis

To evaluate differences in volume and shape of the T_2 hyperintense areas between the high-quality 7T MRI scans compared to the clinical MRI scans, we conducted a paired sample Wilcoxon Signed-rank test, given the non-normal distribution of the data.

As a sensitivity analysis, we repeated the same analysis after excluding areas smaller than 10 cm³. This threshold was selected to minimize potential segmentation errors, which tend to be more pronounced in smaller areas due to the lower number of voxels included and does

especially influence shape markers.

The significance level was set at $p \leq 0.05$. Statistical analysis was performed using IBM SPSS version 29 (Chicago, IL).

6.3.7 Data availability

Data will be made available upon reasonable request.

6.4 Results

6.4.1 Patient inclusion

In total, we recruited 28 patients with a glioma (Table 1) of whom the majority had a glioblastoma, Isocytate Dehydrogenase (IDH) wild type (71%), while the remaining patients had an astrocytoma, IDH mutant (18%), or (suspected) oligodendroglioma, IDH-mutant, 1p/19q codeleted (11%). Most patients had undergone some form of tumor-targeted treatment, with only 18% being included before first surgery. At the time of the MRI scans, five patients were using dexamethasone.

Table 1. Clinical characteristics of the glioma patients (n = 28).

Patient demographics		Intervention	
Age, mean ± standard deviation	58 ± 12	No intervention	5 (18%)
Female	13 (46%)	Surgery	23 (82%)
Male	15 (53%)	Partial resection	16 (57%)
Diagnosis		Total resection	1 (4%)
Glioblastoma, IDH-wildtype	20 (71%)	Biopsy	6 (2%)
Astrocytoma, IDH-mutant, grade 4	1 (4%)	Radiotherapy	15 (54%)
Astrocytoma, IDH-mutant, grade 3	1 (4%)	Photon therapy	14 (50%)
Astrocytoma, IDH-mutant, grade 2	3 (10%)	Proton therapy	1 (4%)
Oligodendroglioma, IDH-mutant, 1p/19q codeleted	2 (7%)	Total dose 30 Gy	2 (7%)
Suspected oligodendroglioma	1 (4%)	40 Gy	2 (7%)
Tumor location		60 Gy	11 (39%)
Temporal	11 (40%)	Adjuvant chemotherapy	19 (68%)
Frontal	13 (46%)	Temozolomide	17 (61%)
Parietal	2 (7%)	Temozolomide and lomustine	1 (4%)
Other	2 (7%)	PCV	1 (4%)
		Total daily use of dexamethasone	5 (18%)
		1 mg	3 (11%)
		4 mg	1 (4%)
		6 mg	1 (4%)

IDH: isocitrate dehydrogenase

PCV: Procarbazine

CCNU: (Lomustine)

Vincristine Variables represent number of patients (n) and the percentage of the total patient population (%).

6.4.2 Visual assessment of the extension of T_2 hyperintense areas

The comparison between the high-quality and clinical MRI scans yielded a few visual differences that were observed when systematically going through all cases. Namely, it was observed that in 10 patients there was involvement of the corpus callosum. In 4 of these patients, this involvement could be more clearly discerned on the high-quality 7T images. In the remaining 6, the corpus callosum involvement was equally well observed on both high-quality and clinical MRI scans. In the cases where the high-quality 7T images provided a more clear involvement, we could trace the connection of the corpus callosum hyperintensity to the primary hyperintense area (Figure 1, 2 and 3). High-quality 7T scans also allowed for enhanced tumor visualization, such as tissue boundaries, for example, between ventricles and white matter and between tumor lesions and healthy appearing tissue (Figure 4). However, we also noticed that in the deep areas of the brain, the clinical 3T scans outperformed the 7T scans. This can be observed in Figure 4, where the involvement of the insular cortex is shown to be more hyperintense on the clinical image (Figure 4A). The involvement of fiber tracts in the T_2 hyperintense area, could be better visualized on the high-quality 7T images. An example can be seen in Figure 5, where involvement of the optical tract can be seen, just as that we could better exclude the involvement of other smaller and finer structures such as the optical chiasm. Another interesting example in Supplementary Figure S1 shows a patient with a glioblastoma where most likely Wallerian degeneration is present secondary to the tumor pathology, which was virtually invisible on the clinical scan, whereas its presence can be clearly visualized on the high-quality image. Overall these examples show that high-quality 7T MRI scans in some cases and certain areas of the brain provide improved visualization of T_2 hyperintense areas compared to standard clinical scans.

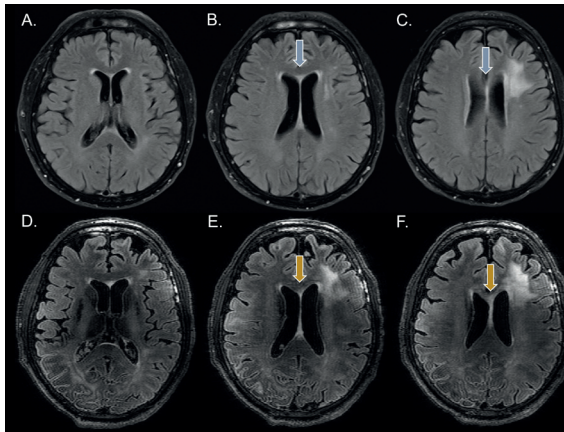


Figure 1. Visual assessment of tumor extension represented on T_2 -FLAIR images in a patient with glioblastoma, IDH wild type, showing three representative slices of the tumor in A-C for the clinical 1.5T T_2 -FLAIR and in D-F for the high-quality 7T T_2 -FLAIR. In this case the corpus callosum involvement is better observed in the high-quality 7T images. Especially, the connectivity between the T_2 hyperintense area in the corpus callosum and the lesions can be more clearly followed on the high-quality 7T image compared to the clinical scan.

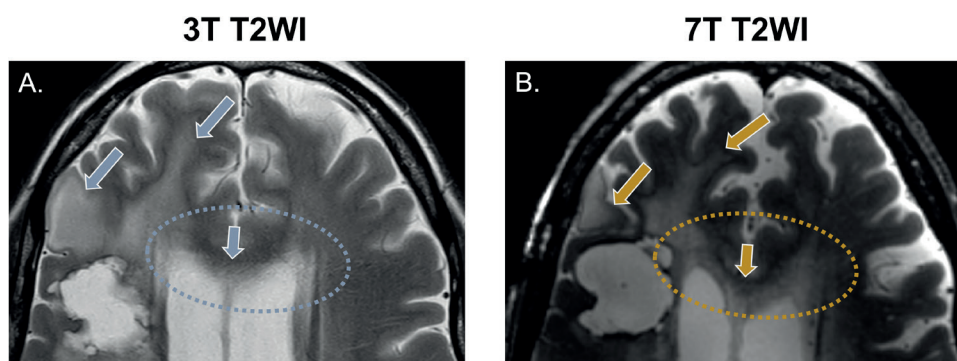


Figure 2. Visual assessment of tumor extension on T_2 weighted images. The presented case is from a patient after partial resection of a glioblastoma, IDH wild type, indicating T_2 hyperintensities in the corpus callosum. While in A, the clinical scan cannot clearly illustrate its structure due to partial volume with the ventricles, in B, the high-resolution scan shows a clear involvement of the corpus callosum, as well as how it connects to the T_2 hyperintense areas in both hemispheres.

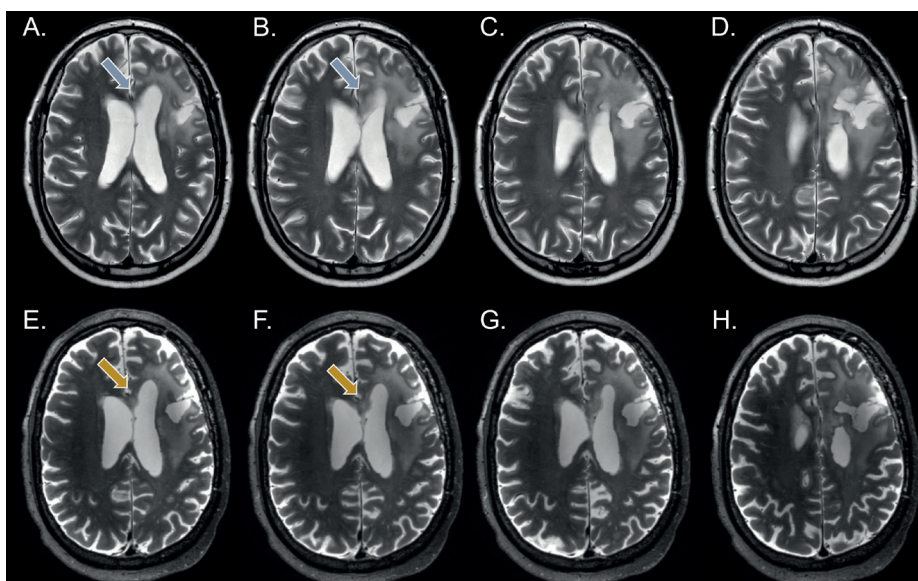


Figure 3. Visual assessment of tumor extension using T_2 -weighted images. The example presented is from a patient after partial resection of a diffuse astrocytoma, IDH mutant WHO grade 2. In A and B it is challenging to determine whether the T_2 hyperintensities indicated by the blue arrow are due to the partial volume effects from the ventricles or whether they suggest the involvement of the corpus callosum, despite the T_2 hyperintense tumor area appearing to connect with that region in C and D. The high-resolution 7T images in the bottom row, E and F, provide a clear view of the T_2 hyperintense areas in this region, indicated by the yellow arrows, where the hyperintense area can be distinctly seen as a shape of its own. In G, a distinct connection of this area with the primary tumor area on the right hemisphere can be seen. In H the tumor extension to the right hemisphere is evident from the periventricular T_2 hyperintense area, which can be clearly distinguished from the ventricle. On the other hand, in D this can also be clearly observed on the clinical scan.

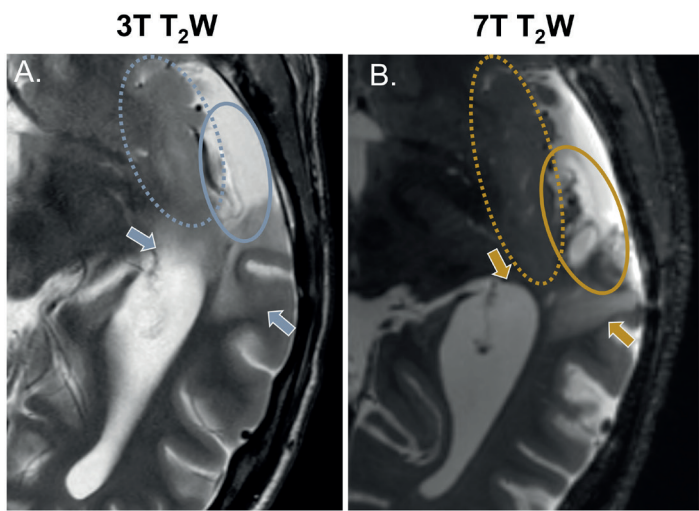


Figure 4. Visual assessment of tumor characteristics and boundaries using T_2 -weighted images. An example patient after partial resection of a diffuse astrocytoma, IDH mutant WHO grade 2 is presented. In A, the clinical image illustrates, with blue arrows, how the boundaries between tissues are blurred in this case. In contrast, in B, the high-quality 7T image clearly depicts these boundaries, indicated by the yellow arrows. Differences in how characteristics within the resection cavity can be visualized are also noticeable, indicated by the full-line ellipses in blue and yellow. The dotted ellipses in both images indicate the involvement of the insular cortex, which can actually be more clearly seen on the clinical scan. This is a result from signal drop in the deep regions of the brain that can occur with 7T imaging.

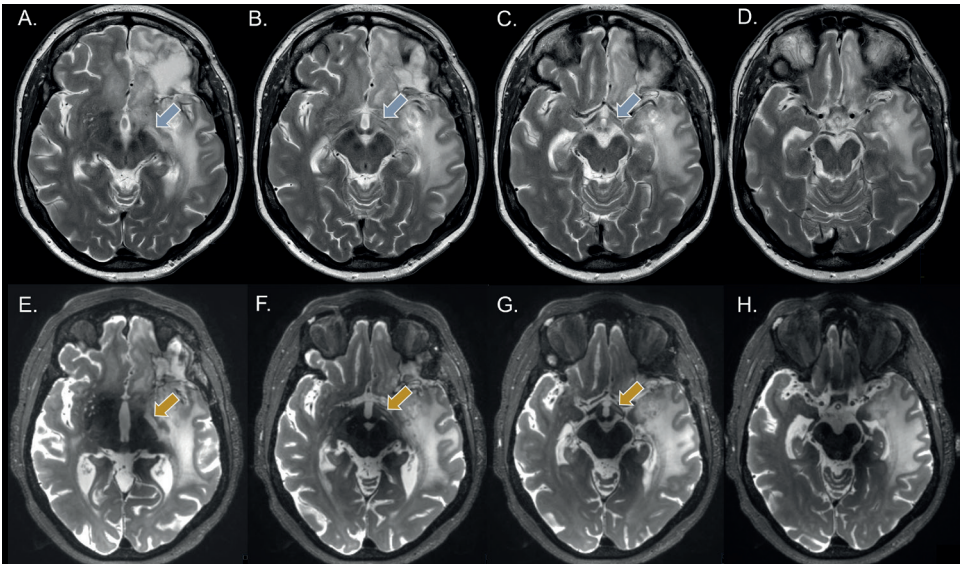


Figure 5. Visual assessment of tumor extension to the left optic tract using T_2 -weighted images. An example of a patient with a glioblastoma, IDH wild type in whom there is a suspicion of involvement of the left optic tract in the tumor pathology. Whereas a T_2 hyperintense area can be seen on the clinical scans, the connection between the left optic tract and the lesion can be better followed on the high-resolution 7T MRI scans.

6.4.3 Volume and shape assessment of the extension of T₂ hyperintense areas

Table 2. Difference in volume and shape markers of all patients between the high-quality 7T MRI scans and the clinical scans.

	High-quality 7T MRI scan (median (IQR - 25 th and 75 th percentiles))	Clinical MRI scan (median (IQR - 25 th and 75 th percentiles))	p-value
Volume (ml)	28 (12.51 – 59.13)	24.33 (11.84 – 56.56)	0.016
Convexity	0.55 (0.48 – 0.61)	0.68 (0.60 – 0.77)	< 0.001
Solidity	0.36 (0.31 – 0.49)	0.43 (0.34 – 0.55)	< 0.001
Concavity Index	1.59 (1.53 – 1.64)	1.41 (1.34 – 1.51)	< 0.001
Fractal Dimension	2.10 (2.06 – 2.15)	1.90 (1.81 – 1.96)	< 0.001

Volume and shape markers are expressed as medians and the respective interquartile ranges are displayed. All parameters differed significantly between the high-quality 7T MRI scans and clinical scans. IQR: interquartile range

Volume and shape markers were compared between the high-quality 7T MRI scans and the clinical scans in order to quantitatively compare differences in the T₂ hyperintense area extension. A significantly higher volume of the T₂ hyperintense area was shown for the high-quality 7T MRI scans (Median: 28.00 ml, IQR - 25th and 75th percentiles: 12.51 – 59.13) compared to the clinical MRI scans (24.33 ml, 11.84 – 56.56; p=0.016), as shown in Table 2. The Bland-Altman plot also showed that the mean differences was above 0 (Figure 6).

We also identified a statistically significant more complex shape of the T₂ hyperintense areas on the high-quality 7T MRI scans compared to the clinical scans (all p < 0.001). These results are depicted in figure 7, where the T₂ hyperintense areas in the high-quality 7T MRI scans show a significantly lower convexity and solidity (Figure 7A and 7B, p < 0.001), as well as a higher fractal dimension and concavity index (Figure 7C and 7D, p < 0.001), all indicating a more complex shape. In the supplementary material (Supplementary Figure S3) Bland-Altman plots are shown that support these findings. In sensitivity analyses we observed that excluding lesions <10 cm³ did not impact our results and the results obtained remained very similar to when all the patients were included in our analysis (Supplementary Table 1).

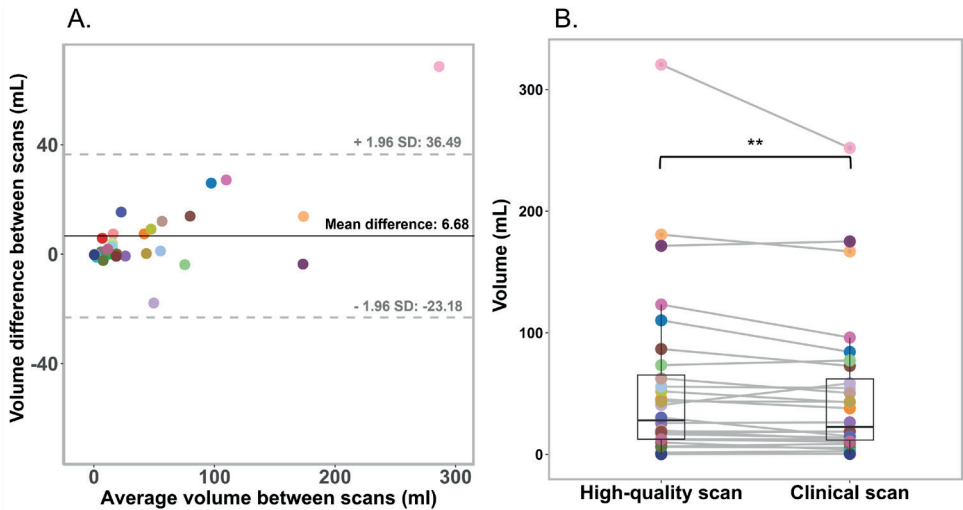


Figure 6. A. Bland-Altman plot illustrating the differences in the volume measurements between the high-quality 7T MRI scans and clinical MRI scans. Each individual data point represents the result from an individual patient. The limits of agreement (indicated by the grey dotted lines) illustrate the range which most differences fall into (± 1.96 of the standard deviation), while the black central line depicts the mean difference. B. Box plot depicting the volume measurements per patient for both the high-quality 7T MRI scans and clinical MRI scans. Data points per scan correspond to the values of an individual patient, and in B the corresponding values of a patient are connected with a line.

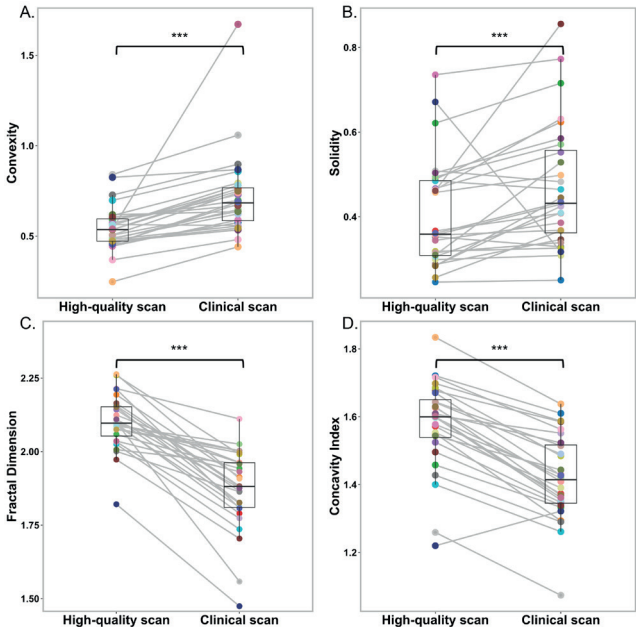


Figure 7. Box plots illustrating A. convexity, B. solidity, C. fractal dimension and D. concavity index shape marker values for both the high-quality 7T MRI scans and the clinical scans. Data points per scan are connected between the high-quality 7T MRI and clinical MRI scans and correspond to the values of an individual patient. All markers differed significantly between scans ($p > 0.001$).

6.5 Discussion

In the current study we show that high-quality 7T MRI scans may provide more detail on the extension, size and complexity of the T_2 hyperintense areas in patients with a glioma. We showed extension of the T_2 hyperintense areas via the corpus callosum to the opposite hemisphere in 4 patients on the high-quality 7T scans that was not visible on the clinical scan. Furthermore, we found a significantly larger volume of the T_2 hyperintense areas on the high-quality scans compared to the clinical scans. We also found a higher complexity of the T_2 hyperintense areas on the high-quality 7T MRI scans compared to the clinical scans.

We wanted to exploit the higher resolution that can be obtained with T_2 WI hypothesizing that this would allow for increased visualization of details on 7T MRI. Although this study was focused on T_2 hyperintensities in glioma patients, other modalities such as SWI and contrast enhanced MRI have their own role in diagnosis and follow-up of glioma, albeit beyond our current focus. When T_2 WI scans at clinical field strengths were not available, we used T_2 -FLAIR scans instead. Despite the lower resolution of the T_2 -FLAIR scans compared to T_2 WI (in our case due to increased slice thickness), it is commonly used in clinical practice given the advantage of free fluid suppression. We have also assessed the shape of the T_2 hyperintense areas in glioma patients and investigated whether there is a difference in determining lesion complexity between 7T MRI scans and conventional MRI scans. To the best of our knowledge, this study is the first to study the shape of T_2 hyperintense areas in gliomas. This shape has, however, been previously studied in other pathologies with a similar methodology^{158,159}.

Our study shows that there is an improvement in T_2 hyperintense area visualization with 7T high-quality MR images. More specifically tissue boundaries could be better discerned and the involvement of brain structures such as the corpus callosum and the optical tract could be more clearly identified. For instance, the clinical scan of the patient in Figure 5 did not clearly show whether the optical tract was connected to the tumor T_2 -hyperintense area (due to partial volume effects), but this was clearly visible on the 7T high-quality scan. These findings are in line with previous studies where high-quality 7T MRI T_2 WI, allowed for improved visualization of disease specific changes, as well as improved visualization of different anatomical brain structures. For example, in the case of multiple sclerosis, the T_2 WI 7T scan has been shown to allow improved visualization of gray and white matter lesions and other structural abnormalities¹⁶⁰. Similarly, in patients with tuberous sclerosis complex, 7T MRI facilitated the visualization of microtubers and radial glial abnormalities providing improved characterization of the lesion margins. The enhanced visualization of subtle margins could support pathological findings that had only been observed in animal-models before¹⁶¹. Another interesting finding has been that different segments of the globus pallidus in the brain could be more clearly depicted. Specifically, whereas the 3T T_2 WI could hardly show the medial medullary lamina and accessory medullary lamina, in the 7T T_2 WI both structures could be clearly distinguished¹⁶². In gliomas only few previous studies were performed with 7T MRI brain scans. Our results showed that with the 7T high-quality T_2 WI images, T_2 hyperintense areas extension were significantly larger and their

shape was significantly more complex compared to conventional MRI scans. Our findings are surprisingly not in line with the previous study of Regnery et al. which concluded that the gross tumor volume measured at 7T was significantly smaller than at 3T. In their investigation T_2 hyperintense area measurements were compared between 3T and 7T T_2 -FLAIR images, which are known to be more sensitive to signal loss near the skull base and in the center of the brain (i.e. near the brainstem)¹⁶³. The visualization and consequent measurement of tumor lesions close to those areas might become compromised using 7T T_2 -FLAIR. The fact that our study mostly used T_2 WI instead could explain the contradicting results. However, we observed that at least in one case (Supplementary Figure S2A) the clinical T_2 WI was more robust in the lower brain regions, despite the fact that the T_2 TSE sequence does suffer from signal loss as severely as the T_2 -FLAIR does. In our study in some cases where a T_2 WI was not available we also resorted to T_2 -FLAIR images. However, when leaving those cases out we did not reach different results (results not shown). We also showed that the T_2 hyperintense areas were more complex when measured on the 7T high-quality scans compared to the clinical scans. This could be explained by the fact that we are able to capture more fine details of the tumor boundaries due to the smaller voxels. Enhancing the portrait of tumor boundaries may aid in understanding, for instance, its growth pattern in the brain. High-quality imaging might possibly also aid in distinguishing non-enhancing tumor tissue from gliosis, despite both having long T_2 relaxation times. Visual features might help in some way to further differentiate. Gliosis typically mostly shows a more homogeneous and smoother T_2 signal compared to tumor tissue. In contrast, non-enhancing tumor parts may present with a more heterogeneous signal due to most likely variations in cellular density, as well as possible influences of neighboring edema and necrosis. Furthermore, non-enhancing tumor parts may present with mass effect especially in the cortico-subcortical region and might involve tracts, resulting in a more irregular shape. High-resolution T_2 -weighted imaging helps to capture these borders more accurately and thus could help in further differentiation. On the other hand, an inherent limitation of these technique includes the inability to distinguish solid T_2 enhancing tumor components and inflammation derived edema. The latter often results from treatment induced abnormalities. While higher quality T_2 WI or T_2 -FLAIR images may not entirely resolve this challenge, they do afford us a clearer understanding of tumor shape and the extent of their growth. Enhanced detailed visualization is believed to be crucial in tracking the growth of gliomas along white matter tracts, offering a more definitive indication as to whether the visualized lesion is indeed a component of solid tumor progression. Better visualization of tumor growth extension pattern could also be of added clinical value for treatment planning for radiotherapy and resection. For example, in cases where glioma T_2 hyperintense areas are more diffuse, it could be of added value to include 7T high-quality T_2 WI for radiotherapy planning. Additionally, these scans could also help to determine exact tumor boundaries for surgical resection. Specifically for non-enhancing lower gliomas, where maximally safe resection is oftentimes aimed for, the improved visualization could have a significant impact on patient's prognosis, but this needs to be proven in a prospective clinical trial. Perhaps better planned radiotherapy and surgery could be less detrimental for patient's cognitive functioning and improve their quality of life. It is

already known that the extent of resection significantly increases the overall survival of patients with a low-grade glioma¹⁶⁴. Lastly, the 7T T_2 TSE scan has a slightly longer scan duration relative to the clinical scan. However, considering its absolute total acquisition time duration of 05:12 minutes, it remains feasible for scanning this in a clinical setting.

The strengths of our study include a larger sample size compared to a previous study done on this topic. Additionally, our protocol included the acquisition of both T_2 WI and T_2 -FLAIR, which could be consulted during the tumor segmentation process. On the other hand, our study also had a few limitations. The patient population that was included was heterogeneous, and consisted mostly of patients with glioblastoma and only few patients with lower grade glioma. High grade gliomas appear more diffuse whereas lower grade glioma usually have more circumscribed lesions. Our results show that lesion borders become better defined on the high-quality scans, which can be of greater advantage for diffuse tumors. Lower grade tumors, because of their more circumscribed nature, might, relatively to the higher grade tumors, show less difference in defining the T_2 hyperintense areas between the clinical and the high quality scans. However, since the number of lower grade tumor included is limited, we cannot conclude what the overall benefit would be specifically for this group of patients. Moreover, patients were included at different time points during their diagnostic and treatment workup. Although most were included at 3 months follow-up, few were also treatment naïve or were further along in their treatment course. For example, patients who have received radiotherapy may have edema which cannot be distinguished from solid tumor, both appearing T_2 hyperintense, contributing to a possible overestimation of tumor size. Additionally, for a few patients there was no T_2 WI available and we had to utilize the T_2 -FLAIR instead. Although these two imaging techniques are not exactly the same we expect that the differences between high-quality and clinical scans remain comparable between these two techniques. Moreover, the imaging acquisition parameters from both clinical (1.5T/3T) and 7T scans were not similar. The clinical scans were established through clinical consensus and were primarily utilized for patient's clinical care. Thus these thus could not be modified for our research. On the other hand we optimized the 7T T_2 WI to achieve the most optimal images to establish especially how much of the extent of T_2 hyperintense areas might be missed on clinical MRI scans. We acknowledge that future studies could explore optimized parameters in clinical field strengths that maximize resolution to assess how closely they can approximate 7T images. Note that this is also the reason why we refer to the 7T scans as 'high quality' to avoid the impression that this is a 3T vs 7T comparison. With the increase in field strength, there is a greater susceptibility to magnetic field inhomogeneities. Supplementary Figure S2 illustrates cases where B_1 or B_0 inhomogeneities could have contributed to shading artifacts, primarily in the lower brain regions, which impaired visualization in these areas. Non-uniform RF results in variations in the flip angle across the image, which can both lower signal intensities as well as affect contrast. At the same time, variations in B_0 may cause local field inhomogeneities resulting in signal loss. Lastly, more artefacts as well as the inherent increased tissue contrast present on the high-quality 7T images may have impacted the quantitative geometric measurements. Notably, we consider the increase in contrast in tissue contrast an inherent part of the higher-quality

images which was the basis of this investigation, i.e. a wanted influence. We believe these points represents a current limitation of our 7T imaging setup (two channel transmit head-coil) that should be carefully considered, particularly when imaging tumors located in lower brain regions. Techniques like multi-transmit can resolve most of the inhomogeneity issues.

In conclusion, our study suggests that high-quality 7T MRI scans may show more detail on the exact extension, size and complexity of T₂ hyperintense areas in patients with a glioma. This information could aid in more accurate planning of treatment, such as surgery and radiotherapy, but this needs to be proven in a prospective trial.

6.6 Acknowledgments

This research was funded by the Medical Delta foundation and is inserted within the 3.0 Cancer diagnostics program.

This work was also made possible by all the members of the consortium listed below:

7T MRI Neuro-Oncology consortium members listed in alphabetical order based on last name

Monique Baas-Thijssen¹, Christa Benit², Jeroen de Bresser³, Marike Broekman¹, Linda Dirven^{1,4}, Daniëlle van Dorth³, Lara Fritz⁴, Melissa Kerkhof⁴, Johan A.F. Koekkoek^{1,4}, Rishi Nandoe-Tewarie⁴, Matthias J.P van Osch^{3,5}, Bárbara Schmitz-Abecassis^{3,5}, Martin J.B. Taphoorn^{1,4}, Maaïke Vos⁴

¹Department of Neurology, Leiden University Medical Center, Leiden, the Netherlands

²Department of Neurology, Alrijne Hospital, Leiden, the Netherlands

³Department of Radiology, Leiden University Medical Center, Leiden, the Netherlands

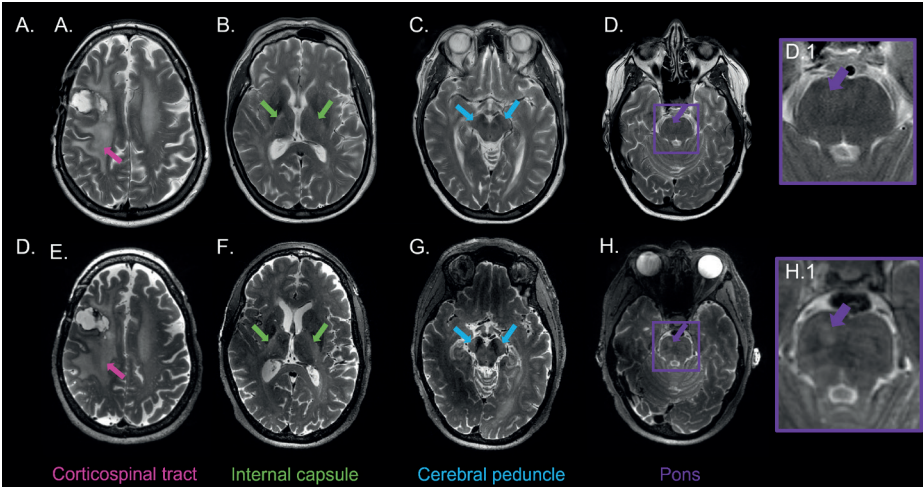
⁴Department of Neurology, Haaglanden Medical Center, The Hague, the Netherlands

⁵Medical Delta, South-Holland, The Netherlands

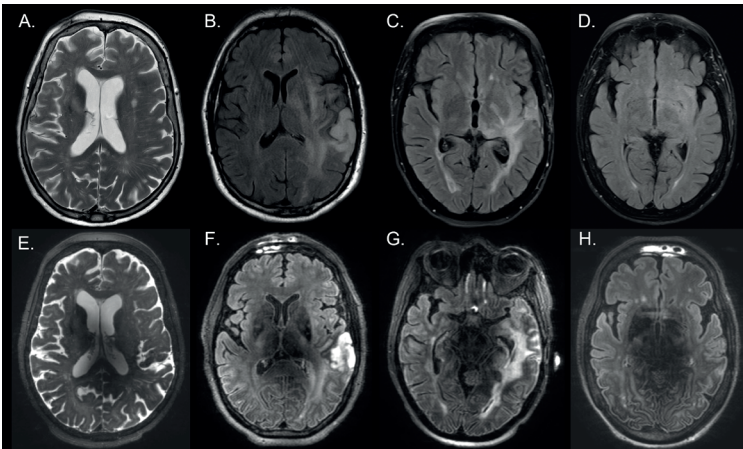
6.7 Abbreviations

Magnetic Resonance Imaging	MRI
Signal to noise ratio	SNR
Contrast to noise ratio	CNR
T ₂ weighted imaging	(T ₂ WI)
Isocytate Dehydrogenase	IDH
Gray	Gy
Procarbazine + CCNU (Lomustine) + Vincristine	PCV
Interquartile range	IQR

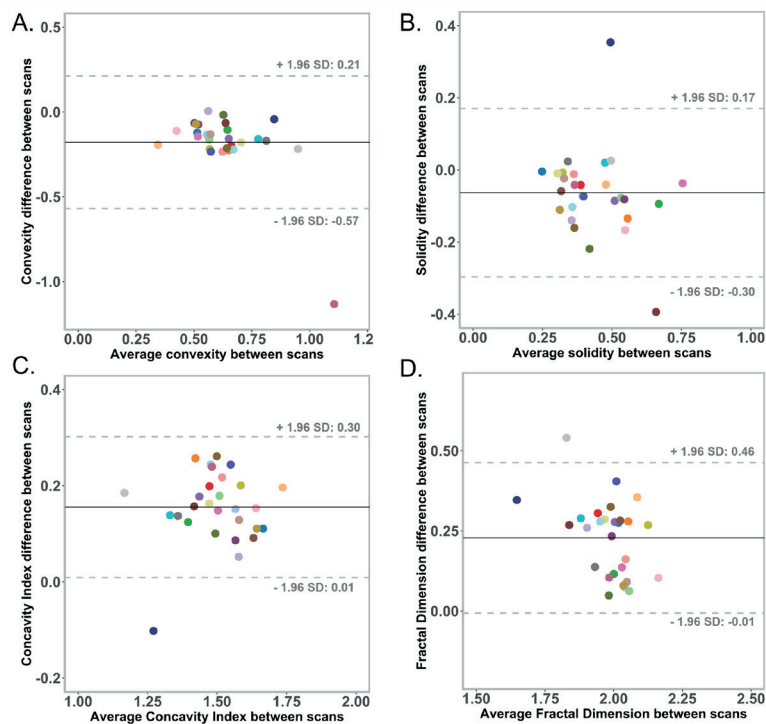
6.8 Supplementary material



Supplementary Figure S1. Visual assessment of T_2 hyperintensities in the corticospinal tract using T_2 -weighted images on A-D the clinical MRI scans and on E-H the high-quality 7T MRI scans. An example of a patient with a glioblastoma where most likely Wallerian degeneration is present due to the tumor pathology. This example illustrates how the T_2 hyperintensities on the high-quality images (on the bottom row) are more clearly visible, especially the lesion in D and H, which is virtually invisible on the clinical scan, whereas its presence can be clearly visualized on the high-quality image (D.1 and H.1, respectively). Compared to the clinical scans, the high-quality scans show a clearer connection of the primary tumor lesion (A & E) and the Wallerian degeneration along the corticospinal tract.



Supplementary Figure S2. Four different example patients, In A. clinical and E. high-quality T_2 weighted scans from a glioblastoma patient who has had partial tumor resection, chemo- and radiotherapy. In B. – D. clinical and F. – H. high-quality T_2 -FLAIR scans, where each column represents one patient with a glioblastoma, anaplastic astrocytoma and a glioblastoma, respectively. Regarding treatment, these patients have had a biopsy, partial tumor resection with chemo- and radiotherapy and a biopsy, respectively. These examples illustrate cases where the clinical scans shows to be superior than the 7T high-quality ones. In the lower row we can see a drop in signal around the center of the brain. The hypointense regions make it challenging to visualize and correctly assess the involvement and extension of T_2 hyperintense areas in those areas.



Supplementary Figure S3. Bland-Altman plots that illustrate the difference between the shape marker measurements calculated from the high-quality 7T MRI scans and the clinical MRI scans. Each individual data point represents the result from one individual patient. The limits of agreement (indicated by the grey dotted lines) illustrate the range that most differences fall into (± 1.96 of the standard deviation), while the black central line depicts the mean difference. Most data points lie between the limits of agreement.

Supplementary Table 1. Difference in volume and shape markers of patients (n= 22) with lesions >10 cm³ between the high-quality 7T MRI scans and the clinical scans.

	High-quality 7T MRI scan (median (IQR - 25 th and 75 th percentiles))	Clinical MRI scan (median (IQR - 25 th and 75 th percentiles))	p-value
Volume (ml)	44.48 (18.46 – 73.43)	11.92 (15.88 – 72.80)	0.013
Convexity	0.50 (0.46 – 0.56)	0.69 (0.57 – 0.73)	< 0.001
Solidity	0.36 (0.30 – 0.47)	0.43 (0.34 – 0.58)	< 0.001
Concavity Index	1.62 (1.57 – 1.68)	1.46 (1.38 – 1.55)	< 0.001
Fractal Dimension	2.12 (2.09 – 2.17)	1.93 (1.88 – 1.99)	< 0.001

Volume and shape markers are expressed as medians and the respective interquartile ranges are displayed. All parameters differed significantly between the high-quality 7T MRI scans and clinical scans. IQR: interquartile range

7 MRI phenotypes of glioblastomas early after treatment are suggestive of overall patient survival

Bárbara Schmitz-Abecassis

Linda Dirven

Janey Jiang

Jasmin A. Keller

Robert J. I. Croese

Daniëlle van Dorth

Rashid Ghaznawi

Ilse M. J. Kant

Martin J. B. Taphoorn

Matthias J. P. van Osch

Johan A. F. Koekkoek

Jeroen de Bresser

Neuro-Oncology Advances (2023). DOI:10.1093/noajnl/vdad133

7.1 Abstract

Distinguishing true tumor progression (TP) from treatment induced abnormalities (e.g. pseudo-progression (PP) after radiotherapy) on conventional MRI scans remains challenging in patients with a glioblastoma. We aimed to establish brain MRI phenotypes of glioblastomas early after treatment by combined analysis of structural and perfusion tumor characteristics, and assessed the relation with recurrence rate and overall survival time.

Structural and perfusion MR images of 67 patients at 3 months post-radiotherapy were visually scored by a neuroradiologist. In total 23 parameters were predefined and used for hierarchical clustering analysis. Progression status was assessed based on the clinical course of each patient 9 months after radiotherapy (or latest available). Multivariable Cox regression models were used to determine the association between the phenotypes, recurrence rate and overall survival.

We established 4 subgroups with significantly different tumor MRI characteristics, representing distinct MRI phenotypes of glioblastomas: TP and PP rates did not differ significantly between subgroups. Regression analysis showed that patients in subgroup 1 (characterized by having mostly small and ellipsoid nodular enhancing lesions with some hyper-perfusion) had a significant association with increased mortality at 9 months (HR:2.6 (CI:1.1–6.3); $p=0.03$) with a median survival time of 13 months (compared to 22 months of subgroup 2).

Our study suggests that distinct MRI phenotypes of glioblastomas at 3 months post-radiotherapy can be indicative of overall survival, but does not aid in differentiating TP from PP. The early prognostic information our method provides might in the future be informative for prognostication of glioblastoma patients.

7.2 Importance of the study

Determining brain MRI phenotypes of glioblastomas early after treatment can help in showing which combination of MRI markers is driving a lower survival chance 9 months after treatment. These distinct MRI phenotypes of glioblastomas could in the future guide complex clinical decision making based on patient prognosis early after treatment assessment.

7.3 Key points

Distinct MRI phenotypes of glioblastomas at 3 months post-radiotherapy are significantly associated with overall survival.

The same MRI phenotypes at 3 months post-radiotherapy do not seem to aid in differentiating between true- and pseudo-progression at 9 months after radiotherapy.

7.4 Introduction

Glioblastoma is the most common and severe type of primary malignant brain tumor¹⁶⁵. Current multimodal treatment after surgical resection includes radiotherapy and concomitant and adjuvant chemotherapy with temozolomide¹⁶⁶. Despite this treatment, a high local recurrence rate is observed during the disease course (90%)¹⁶⁶. MRI is the cornerstone for brain tumor surveillance, and aids clinicians in guiding management decisions. However, a challenge is that high dose radiotherapy may cause treatment induced abnormalities in the early stages after treatment (i.e. pseudo-progression (PP)), which can look similar to tumor progression on conventional MRI scans^{166,167}. Therefore, distinguishing between true tumor progression (TP) and PP early after treatment can be challenging. Early differentiation could aid clinicians in accurately identifying patients who require an alternative treatment strategy to delay further disease progression, and at the same time spare responding patients the burden of additional tumor-targeted treatment.

Structural MRI markers have shown some added value for identifying TP, specifically when assessing the size and the morphology of the enhancing lesion on post contrast 3DT₁ images^{168–171}. Furthermore, several studies have shown that perfusion MRI (with dynamic susceptibility contrast (DSC) and/or arterial spin labeling (ASL)) have added value in distinguishing between TP and PP in glioblastomas^{30,172–177}. However, despite perfusion MRI techniques being promising in differentiating between TP and PP, individual MRI markers showed at best only a modest association with tumor progression and overall survival. This indicates the need to combine MRI markers to get a more reliable early assessment of TP in glioblastomas¹⁷⁷.

More recently, a number of studies have focused on the use of radiomics in glioblastomas to analyze MRI markers in a combined way. One previous study found that structural MRI markers

(gray level texture markers) were associated with TP¹⁷⁸. Few previous studies have specifically applied radiomics models on perfusion MRI with the aim of developing models that could accurately predict TP^{179–181}. Moreover, radiomics approaches such as deep learning models rely on MRI markers of higher order that are not directly clinically translatable, and it is not always completely clear how these markers drive the algorithms decision making (i.e., which combination of MRI markers). With this in mind we set out to explore an alternative approach, which includes grouping of patients with glioblastoma based on clinically scored structural and both ASL and DSC perfusion MRI markers^{182,183}. We subsequently studied how these subgroups progressed over time. We have previously developed a method that was able to identify brain MRI phenotypes based on hierarchical clustering, which resulted in clinical meaningful sub-categories in other disease conditions. For example, we identified brain MRI phenotypes related to predisposition to post operative delirium (in preoperative patients) and brain MRI phenotypes related to an increased risk of stroke and mortality (in patients with manifest arterial disease)¹⁸⁴. To date, it is unknown what specific MRI phenotypes exist in patients with a glioblastoma.

We hypothesize that MRI phenotypes of glioblastomas based on both structural and perfusion tumor characteristics early after treatment could help in the risk assessment of glioblastoma recurrence rate and overall survival time. We therefore aimed to establish brain MRI phenotypes of glioblastomas early after treatment by combined analysis of radiological scores of structural and perfusion tumor characteristics, and to assess the relation of these phenotypes with tumor recurrence rate and overall survival time.

7.5 Materials and methods

7.5.1 Patient population

Patient clinical data were retrospectively retrieved from the clinical archive of the Leiden University Medical Center between the period of January 2015 and February 2022 following local IRB regulations. The study population consisted of adult patients with a histologically confirmed grade IV glioblastoma IDH wild-type or diffuse astrocytoma IDH-mutant, following the most recent WHO guidelines at the time of diagnosis. Consecutive patients who received postoperative treatment consisting of radiotherapy (in combination with concomitant and adjuvant chemotherapy), with at least a 3 months post-radiotherapy follow-up MRI scan with both ASL and DSC scans, and confirmation of TP or PP were included.

7.5.2 Tumor progression and survival assessment

The diagnosis of TP or PP was based on the patients' medical charts including clinical and radiological findings discussed in the multidisciplinary team meetings at either 3, 6 and/or 9 months after radiotherapy. The diagnosis at each of the time points was scored on a 5-point Likert scale: 1) Definite PP; 2) probable PP; 3) no preference ; 4) probable TP; 5) definite TP. The conversion to a binary scale was done by assessing scores 1 and 2 as tumor progression and 4 and 5 as no progression. In this way, the binary score agrees with clinical practice, i.e., if there was doubt about the progression status (score of 3), treatment was continued (and assumed there was no progression). Updated molecular and pathological findings were leading regarding the diagnosis in case of a re-resection. At the latest timepoint available (maximum of 9 months after radiotherapy), patients were only considered to have tumor progression if this was suggested by the clinical and radiological assessment, if the anti-tumor treatment regimen was changed or if the patient was deceased.

Patient survival was calculated as the time between the start of tumor-targeted therapy (i.e. the day of tumor surgical resection or biopsy) and the date of death.

7.5.3 Type of surgical resection

All patients underwent surgery for either maximally safe tumor removal (i.e., total or partial resection of the enhancing part of the tumor) or a biopsy to obtain a histopathological diagnosis. Patients were considered to have had a total resection of the enhancing parts if no enhancing lesion was observed on the directly postoperative MRI scan (performed within 48 hours after tumor resection). In contrast, if residual tumor enhancement was found on the directly postoperative MRI scan, it was considered a partial resection.

7.5.4 MRI scans

Patients were scanned at approximately 3 months post-radiotherapy on a 3T MR scanner (Philips Ingenia or Achieva, Philips Healthcare, Best, The Netherlands). The MRI scans acquired followed the routine clinical guidelines for all scans collected, thus all imaging acquisition parameters reported are based on standard clinical practice. These included a post gadolinium contrast enhanced 3D T₁ scan with 3D-TFE readout and T₂-FLAIR scan, acquired with the following parameters: 3D T₁: TR = 9.91ms, TE = 4.67ms, resolution = 1x1x1mm, field of view (FOV) = 220x175x156mm, 0.3 mL per kg bodyweight of gadolinium-based contrast agent (gadoterate meglumine) and T₂-FLAIR: TR = 11000 ms, TE = 125ms, resolution = 0.4x0.4x5.5mm, FOV = 220x175mm. During the period of data collection, changes to the ASL protocol were made, including transitioning from a 2D to 3D pCASL having changed the label duration (LD) and post-label duration (PLD). For 2D pCASL, LD = 1650ms and PLD = 1525ms (first slice) & 2120ms (last slice). Whereas for the 3D pCASL both LD and PLD were 1800ms. The remainder of parameters included resolution (2D/3D) = 3x3mm/4x4mm, slice thickness (2D/3D) = 7mm/6mm, FOV = 240x240mm. Finally the DSC scans were acquired with a SE-EPI sequence with the following parameters, TE = 75ms, TR = 1600ms, resolution = 2.6x2.3x5mm, FOV = 240x210mm; a third of the contrast agent was injected as pre-bolus.

7.5.5 Radiological scoring of the brain MRI scans

An independent neuroradiologist scored the structural brain scans, i.e. the contrast enhanced 3D T₁ and the T₂-FLAIR scans of the 3 months post-radiotherapy visit (and in doubt consulted a second experienced neuroradiologist for consensus), to determine 1) whether the tumor contrast enhancing lesions were either nodular or patchy on the contrast enhanced 3D T₁, 2) the presence of T₂ hyperintense areas surrounding the enhancing lesion on the T₂-FLAIR and 3) the size of the tumor contrast enhancing and T₂ hyperintense area in 3 orthogonal directions. The T₂ hyperintense area was defined as the confluent hyperintense signal surrounding the contrast enhancing lesion, excluding any resection cavities. The measurements in 3 orthogonal directions were used to estimate the tumor volume for the contrast enhancing lesions and T₂ hyperintense areas individually, as well as to calculate the shape as the eccentricity factor (EF). The volume was calculated using an ellipse formula, as this has been shown to correlate well with the absolute tumor volume, using the following formula¹⁸⁵:

$$\frac{4}{3} \pi D1 D2 D3$$

Where D1, D2 and D3 correspond to the sagittal, coronal and axial measurements, respectively. The resulting volume was afterwards converted to milliliters for the final volume calculation. The EF was calculated according to the following formula:

$$EF = \sqrt{1 - \left(\frac{PPD}{MD}\right)^2}$$

Where MD is the maximal diameter (highest value in all 3 directions) and PPD is the largest perpendicular diameter, i.e. the largest diameter in the other two directions¹⁸⁶.

Tumor lesion perfusion was scored qualitatively using the contrast enhanced 3DT₁ and the T₂-FLAIR as anatomical references. On the DSC relative cerebral blood volume (rCBV) maps were scored as either increased (hyper-perfusion), decreased (hypoperfusion) or no change (isoperfusion) compared to contralateral normal tissue. The ASL was scored as hyperperfusion or isoperfusion compared to the contralateral side, since hypoperfusion on ASL scans is especially difficult to identify¹⁸⁷. Perfusion scores for both contrast enhancing lesions and T₂ hyperintense areas were separately determined. For the clustering analysis, if there was more than one lesion in a patient, the most aggressive tumor contrast enhancing lesion and related T₂ hyperintense area were included per patient. The lesion with the largest volume, increased perfusion and most nodularity was considered to be the most aggressive. In total, 23 radiological tumor markers were included (see the supplementary methods). These markers were rigorously selected to be the most representative to avoid overfitting and selection bias of the model.

7.5.6 Statistical analysis

7.5.6.1 Hierarchical clustering analysis

To identify different brain MRI phenotypes at 3 months post-radiotherapy, hierarchical clustering was performed on the available patient data consisting of the radiological structural and perfusion tumor characteristics. The visually scored markers were included in the model as either binary, categorical or continuous variables. Continuous markers that did not have a normal distribution, including the volume and eccentricity, were normalized by multiplying by 100 and natural log-transforming, and thereafter normalized into z-scores. The normalization step allowed all markers to be equally scaled and then weighted by the analysis model.

Hierarchical clustering was performed using the Ward's method, Nbclust¹⁸⁸, factoextra¹⁸⁹, cluster¹⁹⁰ and dendextend¹⁹¹ in R version 4.1.2 (R Core-Team 2021). Initially the model considers each patient as an individual cluster after which it tries to iteratively merge the two closest clusters while equally weighing each marker (i.e., merge the clusters that share the highest number of markers in common; the agglomerative approach). In this way the clustering analysis is performed in a hierarchical manner. Each time sub-clusters are merged into one cluster, the distance between the remaining clusters is subsequently updated in the model, and the next iteration starts. Ultimately, when all clusters have been merged only one cluster will remain. To determine the optimal number of clusters from the hierarchical clustering analysis, we used the heatmap and Dunn index. The Dunn index calculates the ratio of the smallest distance between markers within each cluster over the maximum distance between the clusters.

7.5.6.2 Differences between the subgroups with a different MRI phenotype of glioblastomas

Descriptive statistics were used to describe the patient population. Clinical characteristics between the subgroups identified with the hierarchical cluster analysis were compared as

follows: for categorical and binary variables, a chi-square test was used; continuous variables were compared using a one-way ANOVA or Kruskal Wallis test, depending on the distribution of the tested variable. In order to assess how the subgroups differed from each other considering the different variables, Bonferroni post-hoc analyses were performed for continuous variables and Bonferroni chi-square residual analyses for categorical variables.

7.5.6.3 Differences between the overall survival time of the subgroups

A log-rank test was performed to determine whether the median overall survival times were significantly different between the different subgroups. For this we compared the median overall survival times between subgroups 1, 3 and 4 and compared to the reference one, subgroup 2.

7.5.6.4 Association between different MRI phenotypes of glioblastomas and progression and survival

First, a multivariable logistic regression analysis was performed to assess the association between MRI phenotype subgroups and TP. The model was corrected for age, KPS score and surgical resection type. Whereas the first two variables were continuous, surgical resection type was categorized into three different groups (ie. biopsy, partial resection and total resection).

Secondly, an adjusted Cox proportional hazard model was used to determine the association between the MRI phenotype subgroups and overall survival time. The model was corrected for age, KPS score and surgical resection type. For sensitivity analysis, an unadjusted multivariable Cox proportional hazard model was performed to assess the influence of correcting for clinical variables on our results and thus to get more insight into the data. The subgroup chosen as reference for the regression analysis had the least aggressive MRI markers (i.e., subgroup 2). This subgroup with the least aggressive radiological markers was identified by an experienced neuroradiologist who assessed the structural and perfusion radiological markers of all subgroups (e.g. hyper-perfusion and increased nodular enhancement were considered aggressive markers).

The threshold for significance was $p \leq 0.05$. All statistical analyses were performed using IBM SPSS version 25 (Chicago-IL).

7.5.7 Data availability

Data will be made available upon reasonable request.

7.6 Results

7.6.1 Patient population

In total, 67 patients with a glioblastoma were eligible according to our inclusion criteria and were included in the analysis (Table 1). The majority (72%) had an Isocitrate Dehydrogenase (IDH)-wildtype tumor and most (61%) patients were male, with a mean age of 60 years (standard deviation 13 years). Most patients (79%) had undergone total or partial resection, radiotherapy as well as concomitant and adjuvant chemotherapy, and a small group of patients were only treated with radiotherapy (21%). See Table 1 for all sociodemographic and clinical variables.

Representative examples of the scored MRI markers can be found in Figure 1, which includes perfusion markers characterized in ASL and rCBV maps as well as structural markers such as enhancing lesion patterns on contrast enhanced 3DT₁ and T₂ hyperintense areas on T₂-FLAIR.

7.6.2 Identification of subgroups with a different MRI phenotype of glioblastomas

The hierarchical clustering analysis resulted in the heatmap displayed in Figure 2. Establishing the optimal number of subgroups was a multistep process. First, we considered that with our number of patients included, the number of subgroups should be relatively low. Second, we inspected the heatmap (Figure 2) and found a good between-subgroup separation with four subgroups. Lastly, we considered the Dunn index (DI), which also showed a relatively high value at four subgroups. The number of subgroups of patients with a different MRI phenotype of glioblastomas was therefore determined at four (with n= 12, 13, 17 and 25 patients in the subgroups respectively).

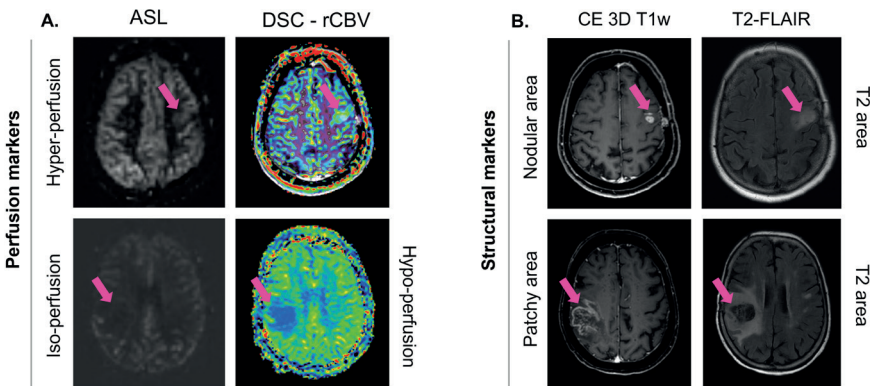


Figure 1. Examples of some of the MRI markers scored by a neuroradiologist. A. Perfusion MRI markers retrieved from corresponding images, namely ASL and DSC-rCBV maps. On the upper and lower row examples of patients with increased and no change/decreased perfusion, for ASL and DSC respectively. In B. contrast enhanced (CE) 3DT₁ and T₂-FLAIR MRI scans from which the structural markers were assessed; it shows examples of nodular and patchy contrast enhancing areas, as well as T₂ hyperintense areas. The scans on each row correspond to one patient.

Table 1. Baseline clinical characteristics of the patients with a glioblastoma.

Total number of patients included		Surgery type	
Age	60 ± 13	Total Resection	31 (46%)
Female	26 (39%)	Partial Resection	22 (33%)
Male	41 (61%)	Biopsy	14 (21%)
IDH status		Radiotherapy (total dose)	
Wild-type: glioblastoma	48 (72%)	40 Gy	10 (15%)
Mutant: diffuse astrocytoma grade IV	5 (7%)	45 Gy	10 (15%)
Unknown / not determined*	14 (21%)	60 Gy	47 (70%)
MGMT status		Temozolomide chemotherapy	
Methylated	18 (27%)	53 (79%)	
Unmethylated	49 (73%)		
KPS median (range)	90 (60 - 100)		

*Cases diagnosed prior to WHO 2016 classification. IDH: Isocitrate dehydrogenase; MGMT: O6-methylguanine-DNA methyltransferase; KPS: Karnofsky Performance Scale.

7.6.3 Differences between the subgroups with a different MRI phenotype of glioblastomas

A summary of the clinical characteristics of these patient subgroups can be found in Supplementary Material Table S1. There were no significant differences between subgroups regarding KPS score, radiotherapy dose received, gender, IDH status, MGMT promotor status and receiving combined chemoradiotherapy (all $p > 0.05$). However, there was a significant difference in age and type of surgery between the 4 subgroups ($p = 0.013$ and $p = 0.001$ respectively). From the Bonferroni post-hoc analyses it was evident that the overall significant difference in age was particularly observed because patients in subgroup 3 were significantly older than in subgroup 1 (68 versus 54 years, respectively, $p = 0.02$). For surgery type, subgroup 1 had significantly more total resections compared to subgroup 3 (75% versus 12%, respectively, $p = 0.003$) and subgroup 4 (75% versus 12%, respectively, $p = 0.001$), explaining the overall significant difference. Supplementary Table S2 shows the distribution of the MRI markers present in each subgroup. Regarding tumor location, the temporal tumor region was the only location that differed significantly between the subgroups, with more patients having a temporal lesion in subgroup 1 (50% versus 15%, 0% and 32% in groups 2, 3 and 4, $p = 0.02$). As expected, the majority of all other MRI markers were significantly different between the resulting subgroups (all $p < 0.05$) (Supplementary Table S2). The structural MRI markers that differed significantly between subgroups include the presence of a patchy enhancing lesions, the number of nodular and enhancing lesions, as well as the volume and eccentricity from both enhancing and T_2 hyperintense tumor lesions ($p < 0.05$) (Supplementary Material Table S2). Moreover, the perfusion markers differed significantly between subgroups, such as the

DSC-rCBV for both nodular and patchy enhancing lesions, and the ASL-CBF of the nodular and patchy enhancing lesions and of the T_2 hyperintense tumor areas ($p<0.05$) (Supplementary Material Table S2).

Overall, subgroup 1 was characterized by relatively few, small and mostly nodular enhancing lesions with a more ellipsoid shape and some lesions showing hyper-perfusion. Subgroup 2 was characterized by relatively few, small lesions with mostly patchy enhancing lesions, with a more ellipsoid shape and almost no lesions with hyper-perfusion. Subgroup 3 had the most lesions that also had the highest volume and highest amount of lesions with hyper-perfusion. Lastly, subgroup 4 was characterized by a relatively moderate amount of nodular and patchy enhancing lesions with a relatively high volume, ellipsoid shape and moderate amount of lesions with hyper-perfusion. A summary of the most relevant MRI markers of the MRI phenotypes of glioblastomas can be found in Figure 4.

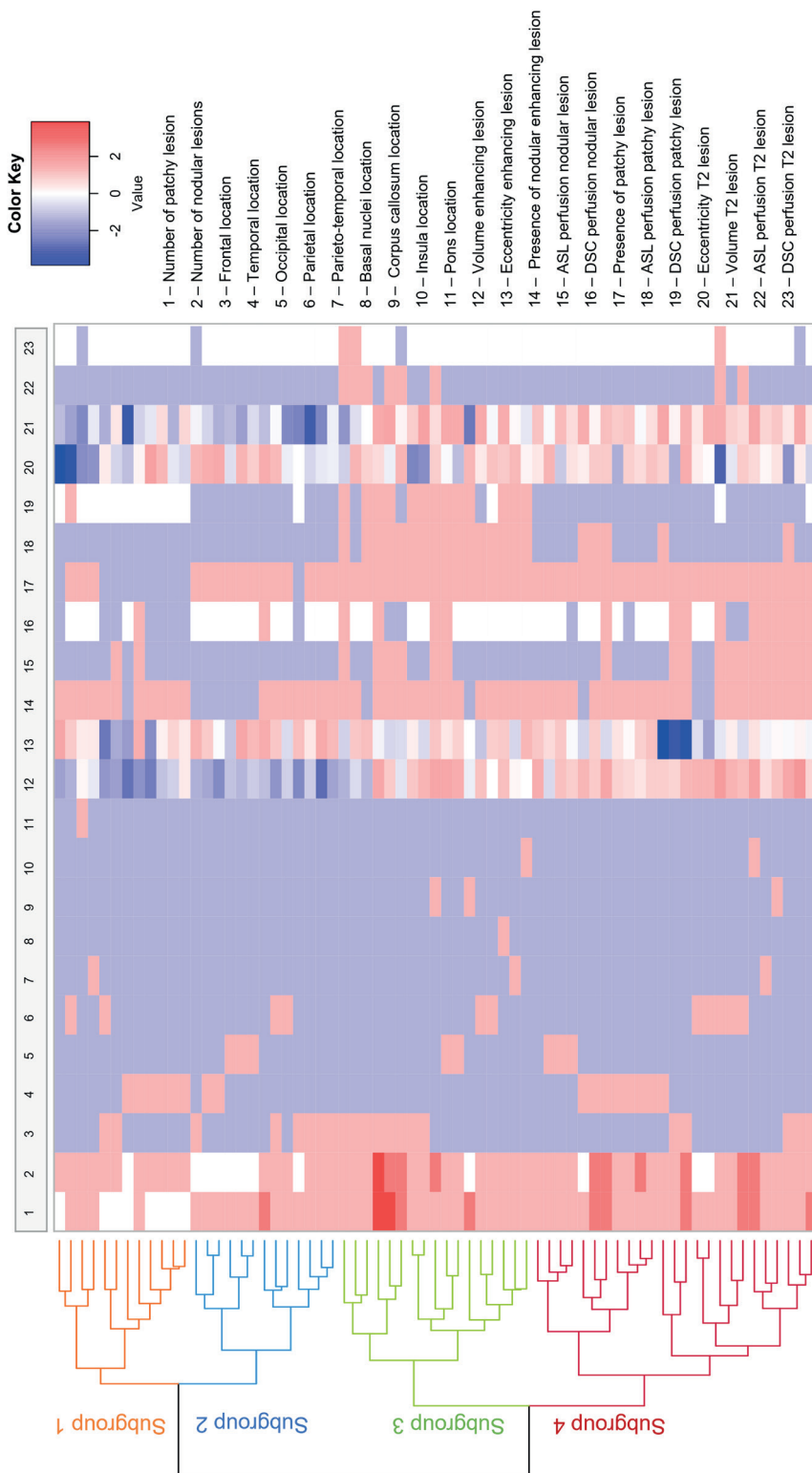


Figure 2. Heatmap results of the hierarchical clustering analysis.

The subgroups (subgroup 1 (n=12), subgroup 2 (n=13), subgroup 3 (n=17) and subgroup 4 (n=25)) are represented in different colors on the left side of the figure. Each row represents one patient and each column represents one MRI marker. In total 23 MRI markers were included. The normalized values were included, where blue represents a low value and red a high value of the MRI marker.

7.6.4 Differences between the overall survival time of the subgroups

A significant difference was found between the overall survival times of the reference subgroup (subgroup 2) and subgroup 3 ($p=0.009$), but not between the reference subgroup and subgroup 1 ($p=0.166$) and 4 ($p=0.191$) (Supplementary Table S5, Supplementary Figure S3).

7.6.5 Association between different MRI phenotypes of glioblastomas and progression and survival

Out of the 67 patients, 49 showed a final diagnosis of TP at 9 months follow-up. Per subgroup this translated in 8/12 (67%) patients having TP in subgroup 1, 9/13 (69%) in subgroup 2, 14/17 (82%) in subgroup 3 and 18/25 (72%) in subgroup 4. From the multivariable logistic regression analysis, we found that subgroups 1 (HR: 1.3 (95% CI: 0.2 – 6.8); $p = 0.772$), 3 (HR: 1.7 (95% CI: 0.3 – 10.4); $p = 0.570$) and 4 (HR: 1.6 (95% CI: 0.3 – 8.4); $p = 0.551$) were not significantly associated with TP, compared to the reference subgroup 2 (Supplementary Table S6).

In total, 65 out of the 67 (97%) patients had passed away by the time the database was locked. The median survival in months per subgroup (with respective inter-quartile ranges) was: subgroup 1 = 13 (10 – 21) months, subgroup 2 = 22 (15 – 29) months, subgroup 3 = 11 (7 – 14) months, and subgroup 4 = 10 (8 – 18) months. Figure 4 shows the results of the survival analyses where subgroup 2 was taken as the reference group. Our results show that subgroup 1 (HR: 2.6 (95% CI: 1.1 – 6.3); $p=0.03$) is significantly associated with mortality (Figure 5, Supplementary Figure S2), but not subgroups 3 and 4, when correcting for clinical variables (model 2). On the other hand, our secondary analysis included in the uncorrected logistic regression analysis, showed that subgroup 3 had a significant association with mortality (HR: 2.4 (95% CI: 1.1 – 5.0; $p = 0.03$), but not subgroups 1 and 4.

Figure 3. Illustration of the most representative structural and perfusion MRI markers as well as tumor volume and shape markers, per subgroup. These illustrative results are based on the values in Supplementary Table S2.

Structural markers					Perfusion markers						
Lesion types	Lesion dimensions			Lesion enhancing pattern		DSC perfusion		ASL perfusion			
	Volume of Enhancing Lesions	Eccentricity of Enhancing Lesion	Volume of T2 Hyperintense Lesions	Eccentricity of T2 Hyperintense Lesions	Presence of Nodular Enhancing Lesions	Presence of Patchy Enhancing Lesions	Number of Nodular Enhancing Lesions	Number of Patchy Enhancing Lesions	Perfusion in Nodular Enhancing Lesions	Perfusion in Patchy Enhancing Lesions	Perfusion in T2 Hyperintense Lesions
Subgroup 1											
Subgroup 2											
Subgroup 3											
Subgroup 4											
Legend	<div><div></div><div>Circle</div></div> <div><div></div><div>Ellipsoid</div></div> <div><div></div><div>Small</div></div> <div><div></div><div>Large</div></div> <div>Legend for the anatomical features: Yes in dark gray & No in light gray. No lesion in light gray, one lesion in yellow, two lesions in orange and three lesions in red.</div> <div>Legend for the perfusion scans: hyperperfusion in red, isoperfusion in white & hypoperfusion in blue.</div>										

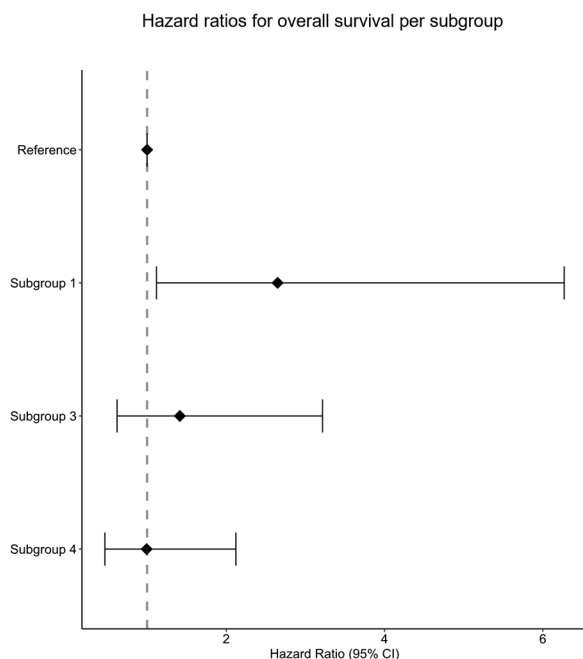


Figure 4. Forrest plot of the hazard ratios (95%-CI) per subgroup for survival. Illustrated results of the cox proportional hazards survival analysis are shown (adjusted for age, KPS and surgery type). Subgroup 2 has been set as a reference and marked with the striped line in red. Hazard ratios are shown with a 95% confidence interval.

7.7 Discussion

We identified distinct brain MRI phenotypes of glioblastomas in patients early after radiotherapy (at 3 months). Based on these brain MRI phenotypes we were able to define 4 distinct subgroups that also differed in their overall median survival times, but showed no differences in TP and PP rates.

In our current study, to establish different brain MRI phenotypes of glioblastomas, our clustering model hierarchically stratified the different patients based on the similarities between radiological MRI markers. Furthermore, we independently assessed the clinical outcomes. This approach, contrarily to most traditional machine learning models, is seen as a form of unsupervised learning. One of the advantages of our method includes the possibility of independently establishing new MRI marker combinations that in machine learning methods could otherwise not be determined.

The radiological MRI markers utilized in our study were based on radiological scoring of structural and perfusion images, and when combined, resulted in phenotypes of glioblastomas. Most of the MRI markers differed significantly between the 4 subgroups, and we identified subgroup 1 to have a significant association with mortality at 9 months. This subgroup's MRI phenotype of glioblastomas was characterized by relatively few, small and mostly nodular enhancing lesions with a more ellipsoid shape and some lesions showing hyper-perfusion, especially on ASL images, and the T_2 hyperintense area on the DSC scans showed mainly hypo-perfusion.

Some individual MRI markers that drive the model and that could influence the lower chance of overall survival in subgroup 1 can be identified. For example, the morphology of the nodular enhancing lesions are thought to reflect a more malignant phenotype¹⁹². Furthermore, the more ellipsoid shape of the lesions in subgroup 1 could indicate a more aggressive pattern of tumor infiltration in the neighboring healthy brain tissue¹⁹³. Given the complexity of glioblastomas, and the uncertainty of what exact combination of MRI markers drives its severe prognosis, MRI phenotypes of glioblastomas can give more prognostically meaningful information and maybe in the future could help in treatment decisions.

Previous machine learning approaches have studied diagnostic performance using radiomics markers in brain gliomas^{182,183}. For instance, a previous study utilized higher order texture and gray level intensity markers from ASL and DSC perfusion-weighted images and compared their quantitative patterns between high-grade and low-grade gliomas to assess diagnostic performance¹⁸². Radiomics in ASL and DSC was shown to be valuable, providing quantitative patterns to classify low and high grade gliomas with an area under the curve of 0.888 and 0.962, respectively¹⁸². Similarly, another previous study also investigated if, among others, grey level intensity and texture markers retrieved from DSC perfusion images, could identify glioma grades and IDH status. This study demonstrated stratification of glioma grades and IDH mutations status based on the DSC perfusion markers in a radiomics model performed correctly in 71% and 53% of the cases, respectively¹⁸³. Both of these previous studies showed that a machine learning approach with MRI perfusion markers showed potential to reliably classify gliomas grades and molecular genotypes. In traditional machine learning approaches, markers of interest were pre-determined and coupled to a known outcome for predictive modeling, where the markers of interest are mostly abstract and of higher-order, not directly representing clinical MRI markers. However, the main disadvantage of these machine learning approaches is that it is not always clear which exact marker (or combination of markers) is associated with a certain clinical outcome. Contrarily, in the current study we did not train a model to predict a certain outcome. Rather, we are utilizing MRI markers that are more representative of clinical radiological markers, and group the patients according to how similar these markers are. After this grouping, post-hoc analyses is performed to gain insight in which combination of these markers (MRI phenotypes of glioblastomas) are underlying specific clinical outcomes. Utilizing phenotypes (i.e. a combination of markers) instead of single markers can be more advantageous, because it allows identification of which group of characteristics could be prognostically more meaningful in a disease with a complex biology. In this way our approach is unique and also allows for a more comprehensive link between phenotype and outcome, as was also shown in previous studies of our group in other diseases^{184,194}.

Regarding recurrence and overall survival outcomes of the 4 subgroups with a distinct MRI phenotype of glioblastomas, we observed different overall median survival times and TP cases. Subgroup 2 had the longest overall median survival time (22 months) and 69% of TP incidences. We found subgroup 1 to have a significant association with mortality at 9 months, while the percentage of TP cases (67%) was similar. These results were somewhat unexpected.

The discrepancy between TP cases and overall survival time at 9 months follow-up could be explained by the large overall survival time range, a possible effect of a few outliers cases, and the small sample size for each subgroup. Moreover, subgroup 1 was shown to have a significant association with mortality at 9 months follow-up when correcting for confounding variables, including age¹⁹⁵. This suggests that such significant association observed in subgroup 1 is most likely a reflection of the tumor phenotype, not influenced by the age of the patients. When the model was not corrected for clinical variables, we found that only subgroup 3, with a considerably older median age (68 ± 11), had a significant association with mortality at 9 months. When comparing the median survival times, also not corrected for clinical confounders, a significant difference was also found for subgroup 3, as well as no significance difference for subgroups 1 and 4. The fact that clinical confounders are not weighted in most likely explains the non-significant findings, since both subgroups 1 and 4 have relatively short median survival times (compared to subgroup 2). An additional explanation for subgroup 4 could part from the crossing survival curves, which is probably due to a few outliers with longer survival times. Furthermore, we observed that patients with worse survival time in subgroups 3 and 4 (overall survival time of 11 and 10 months, respectively) not only had the lowest percentages of total resections (subgroup 3 and 4 = 12%), but also had the highest tumor volumes (subgroup 3 = enhancing lesion: 247.54 ml; T₂ lesion: 1321.70 ml and subgroup 4 = enhancing lesion: 374.45 ml; T₂ lesion: 1375.43 ml). This makes us believe that the subgroups not only reflect different tumor phenotypes, but also the differences in surgical treatment. It is known that resection type is an important prognostic factor for survival, but does not correlate with the occurrence of TP or PP (similar to what we have observed in the present study).

In clinical practice it is relevant to understand which demographic and disease specific characteristics play a role in prognosis of the patient's disease. Since glioblastomas are known to recur, early assessment of tumor characteristics could better indicate patient prognosis on a more personal level early after treatment. Contrary to traditional machine learning approaches, rather than helping predict an outcome, our study helps to understand which combination of radiological MRI markers are the imaging correlates of clinical outcomes, such as overall survival¹⁹⁶. The early prognostic information our method provides might in the future be beneficial for prognosis of patients with a glioblastoma. More specifically, when assessing a patient's perfusion and structural tumor characteristics at 3 months, stratifying patients according to their MRI phenotype of glioblastomas could inform clinicians early on after treatment about the patient's outcome at 9 months. In order to further investigate the clinical impact, a larger study would need to be conducted, but our method shows promising results to justify and power such a study.

The strengths of our study include the well characterized radiological MRI markers of glioblastomas, including DSC as well as ASL perfusion markers in combination with the extensive follow-up availability of both clinical and MRI data¹⁹⁷. This allowed us to determine the clinical outcome of all patients considering both survival and progression. Furthermore, since ASL is not widely implemented in clinical imaging guidelines of glioblastomas, this dataset is

unique for this patient population¹⁶.

Our study also has some limitations. A first limitation is that our sample size was limited to 67 patients. A reason for this was that glioblastoma patients who were certain to have died from non-tumor related causes or did not have structural and perfusion MR data available because of MRI contraindications, were not included in our study. One of the evident consequences of our sample size is visible in the survival time ranges within subgroups. Our hierarchical clustering analysis approach could differentiate subgroups with primarily different radiological markers. These subgroups also showed to have different overall survival times. However, utilizing this approach for discriminating subgroups solely based on overall survival time is challenging. It could be interesting in the future to include a larger sample size and re-evaluate these findings. Although our selection procedure narrowed our patient population, it allowed us to be certain that the clinical outcome was related to their tumor diagnosis. Despite the relatively limited sample size we were able to find clinically meaningful associations. A second limitation of our study is that the IDH status for some patients was unknown, since some of the patients were diagnosed prior to 2016. This withheld us from including this variable in the survival and progression analyses, which would have been of added value since patients with an IDH mutation are known to have an overall better prognosis¹⁹⁸. A third limitation is that over the years of data collection the parameters of the ASL MRI acquisition changed. However, these changes were only minimal (applied to only one patient), and were not expected to have affected the visual perfusion scoring by the neuroradiologist in a significant way. Since the data used was retrospectively collected, the ASL acquisition parameters were set according to clinical standards, only including one PLD. Although including more PLD could make the images less sensitive to ATT artifacts, this is not yet the standard in clinical practice. The goal of our study was to also investigate how perfusion markers in such a hierarchical clustering model could be used to establish glioblastoma phenotypes. We strived to utilize the maximum number of markers representative of clinical practice, without being redundant. However, a larger number of markers or a different selection of markers, which would also be representative of other biological processes in the tumor, could provide more complete phenotypes of this disease. This could also lead to overlapping markers and therefore pruning the model to these overlapping markers. It would be interesting to see the results of future studies which would, for instance, also include metabolic information derived from MR spectroscopy or chemical exchange saturation transfer. Lastly, the ratings of the MRI scans were performed by one experienced neuroradiologist who consulted a second experienced neuroradiologist when in doubt to obtain consensus. Using only limited raters could be perceived as a limitation. However, we chose to invest in the quality of the raters instead of the quantity of the raters to achieve high quality data.

In conclusion, we were able to establish 4 subgroups based on distinct brain MRI phenotypes of glioblastomas at 3 months post-radiotherapy. Our study suggests that these distinct MRI phenotypes of glioblastomas can be indicative of overall survival. The early prognostic information our method provides might be informative for prognosis in patients with a glioblastoma.

7.8 Acknowledgments

This research was funded by Medical Delta as part of the Cancer Diagnostic 3.0 program.

7.9 Supplementary information

7.9.1 Supplementary methods

Brain glioblastoma MRI markers were established from the visual scoring described in the methods section, resulting in the 23 markers described below. Markers 3 – 11, 14 and 17 were included in the model as binary variables; i.e. presence (1) or no presence (0) of the marker in the lesion being scored. Markers 1, 2, 15, 16, 18, 19, 22 and 23 were included as categorical variables; i.e. they were given a different number per classification (e.g. hypoperfusion -1, isoperfusion 0 and hyper-perfusion 1). The remaining markers 12, 13, 20 and 21 were used as continuous variables. Note that one representative tumor enhancing area was chosen per patient in case of multiple ones. The tumor area with the most aggressive MRI markers was chosen (e.g. hyper-perfusion) and with presentation of a T_2 hyperintense area. The latter was the case to avoid having missing values in the model for variables considering T_2 hyperintense areas. The non-normally distributed continuous variables were transformed by multiplying by 100 and natural log-transformed to approximately conform to a normal distribution, and thereafter have their values normalized with z-scores.

1. Number of patchy areas
2. Number of nodular areas
3. Frontal location
4. Temporal location
5. Occipital location
6. Parietal location
7. Parieto-temporal location
8. Basal nuclei location
9. Corpus callosum location
10. Insula location
11. Pons location
12. Volume enhancing area
13. Eccentricity enhancing area
14. Presence of nodular enhancing area
15. ASL perfusion nodular area
16. DSC perfusion nodular area
17. Presence of patchy area
18. ASL perfusion patchy area

19. DSC perfusion patchy area
20. Eccentricity T_2 hyperintense area
21. Volume T_2 hyperintense area
22. ASL perfusion T_2 hyperintense area
23. DSC perfusion T_2 hyperintense area

7.9.2 Supplementary results

As a results of the clustering analysis, we obtained 4 subgroups. Each subgroup has a unique brain MRI phenotype of glioblastomas which showed specific structural and perfusion MRI characteristics. An extended description of the subgroups shown in Figure 4 can be found below:

Subgroup 1

With regards to the structural MRI markers, subgroup 1 has the least number of patchy enhancing (PE) areas, the smallest volume of enhancing and T_2 hyperintense areas and the most round shape of the enhancing and T_2 areas.

Considering DSC perfusion markers, subgroup 1 has the least amount of hyper-perfusion in nodular enhancing (NE) areas, shows mainly iso-perfusion in PE areas, and shows mostly hypo-perfusion in T_2 hyperintense areas.

Considering ASL perfusion markers, subgroup 1 has a relatively high amount of hyper-perfusion in NE areas, and only has areas with iso-perfusion in PE areas and in T_2 hyperintense areas.

Subgroup 2

With regards to the structural markers, subgroup 2 has the least number of NE areas, a high number of PE areas, a small volume of enhancing and T_2 hyperintense area, the most ellipsoid shape of enhancing and T_2 hyperintense areas.

Considering perfusion markers, subgroup 2 has mostly hypo-perfused DSC in PE areas and T_2 areas. Considering ASL perfusion, NE and PE areas are iso-perfused.

Subgroup 3

With regards to structural markers, subgroup 3 has relatively high number of NE areas, relatively the highest number of PE areas, the largest volume of enhancing and T_2 hyperintense areas and medium sized enhancing and T_2 area and shape. Considering perfusion markers, subgroup 3 has relatively high amount of DSC hyper-perfusion in NE areas, it has the highest amount of hyper-perfusion in PE areas and shows relatively the most hyper-perfused but mostly iso-perfused T_2 areas. Considering ASL perfusion, subgroup 3 has the highest amount of PE areas with hyper-perfusion and . Lastly, relatively highest amount of hyper-perfusion in T_2 areas.

Subgroup 4

Considering structural markers, subgroup 4 has a high number of NE and PE areas, the largest volume of enhancing and T_2 hyperintense areas and the most round shape of enhancing and T_2 areas. Considering DSC perfusion markers, subgroup 4 has the highest amount of hyper-perfused NE areas, has mostly hypo-perfused PE areas and shows mostly hypo-perfused T_2 areas. Concerning ASL perfusion markers, subgroup 4 has the highest number of hyper-perfused NE areas, a relatively high amount of PE areas with hyper-perfusion and some T_2 areas with hyper-perfusion.

As part of the survival analysis we performed Cox regression analysis and looked at the model when not corrected for clinical confounding variables. This allowed us to have a better insight of what the correction would do to our results. The results represent the association between different MRI phenotypes of glioblastomas and progression and survival.

In the uncorrected model, subgroup 3 has a significantly increased mortality risk (HR: 2.4 (CI: 1.1 – 5.0); $p=0.03$) compared to subgroup 2 (Supplementary Table S3; Supplementary Figure S2).

7.9.3 Supplementary tables

Supplementary Table S1. Clinical characteristics per subgroup.

The data represents mean ± SD, n (percentage) or median (interquartile range). Statistical analyses were performed with chi-square tests.

	Subgroup 1 (n=12)	Subgroup 2 (n=13)	Subgroup 3 (n=17)	Subgroup 4 (n=25)	p-value
Age	54 ± 12	56 ± 15	68 ± 11	60 ± 12	0.013
Female	4 (33%)	4 (31%)	8 (47%)	10 (40%)	0.799
IDH					
Wild-type	10 (83%)	6 (46%)	13 (76%)	19 (76%)	0.243
Mutant	0 (0%)	3 (23%)	1 (6%)	1 (4%)	
Not otherwise specified	2 (17%)	4 (31%)	3 (18%)	5 (20%)	
MGMT status					
Positive	2 (17%)	4 (31%)	6 (35%)	7 (28%)	0.741
Negative	10 (83%)	9 (69%)	11 (65%)	18 (72%)	
KPS median	90 (30)	90 (40)	90 (30)	90 (40)	
KPS 100	5 (42%)	2 (15%)	4 (24%)	7 (28%)	0.365
KPS 90	5 (42%)	5 (38%)	5 (29%)	8 (32%)	
KPS 80	1 (8%)	3 (23%)	5 (29%)	4 (16%)	
KPS 70	1 (8%)	2 (15%)	3 (18%)	3 (12%)	
KPS ≤60	0 (0%)	1 (8%)	0 (0%)	3 (12%)	
Surgery type					
Partial resection	2 (17%)	5 (38%)	9 (53%)	15 (60%)	<0.001
Total resection	9 (75%)	8 (62%)	2 (12%)	3 (12%)	
Biopsy	1 (8%)	0 (0%)	6 (35%)	7 (28%)	
Radiotherapy (total dose (Gy))					
40	1 (8%)	1 (8%)	4 (24%)	5 (20%)	0.458
45	2 (17%)	1 (8%)	3 (18%)	3 (12%)	
60	9 (75%)	11 (84%)	9 (53%)	17 (68%)	
Temozolomide chemotherapy	11 (92%)	10 (77%)	13 (77%)	13 (77%)	0.705

Supplementary Table S2. MRI markers of the glioblastomas per subgroup.

The data represents mean \pm SD or n (percentage). Statistical analysis was performed with a chi-square test for categorical variables and a one-way ANOVA for the continuous variables. Most markers, except for most of the tumor location markers, and DSC perfusion in T₂ areas, differed significantly between subgroups ($p < 0.05$).

Ordinal variables	Subgroup 1 (n=12)	Subgroup 2 (n=13)	Subgroup 3 (n=17)	Subgroup 4 (n=25)	p-value
Frontal (N(%))	2 (17%)	6 (46%)	8 (32%)	8 (32%)	0.11
Temporal (N(%))	6 (50%)	2 (15%)	0 (0%)	0 (0%)	0.01
Occipital (N(%))	0 (0%)	3 (23%)	2 (12%)	3 (12%)	0.37
Parietal (N(%))	2 (17%)	2 (15%)	2 (12%)	5 (20%)	0.92
Parieto-temporal (N(%))	1 (8%)	0 (0%)	1 (4%)	1 (4%)	0.77
Basal-nuclei (N(%))	0 (0%)	0 (0%)	1 (4%)	0 (0%)	0.40
Corpus-callosum (N(%))	0 (0%)	0 (0%)	2 (12%)	1 (4%)	0.35
Insular (N(%))	0 (0%)	0 (0%)	1 (4%)	1 (4%)	0.72
Pons (N(%))	1 (8%)	0 (0%)	0 (0%)	0 (0%)	0.12
Presence of a nodular enhancing lesion (N(%))	11 (92%)	7 (54%)	15 (88%)	22 (88%)	0.03
Presence of a patchy enhancing lesion (N(%))	3 (25%)	12 (92%)	17 (100%)	24 (96%)	<0.001
Number of nodular lesions					
No lesions (N(%))	1 (8%)	7 (54%)	1 (6%)	3 (12%)	0.008
One lesion (N(%))	11 (92%)	6 (46%)	12 (71%)	16 (64%)	
Two lesions (N(%))	0 (0%)	0 (0%)	3 (18%)	6 (24%)	
Three lesions (N(%))	0 (0%)	0 (0%)	1 (6%)	0 (0%)	
Number of patchy lesions					
No lesions (N(%))	8 (67%)	0 (0%)	0 (0%)	0 (0%)	<0.001
One lesion (N(%))	4 (33%)	12 (92%)	13 (77%)	19 (76%)	
Two lesions (N(%))	0 (0%)	1 (8%)	2 (12%)	6 (24%)	
Three lesions (N(%))	0 (0%)	0 (0%)	2 (12%)	0 (0%)	
DSC perfusion in nodular lesions					
Hypoperfused (N(%))	7 (58%)	1 (8%)	2 (12%)	4 (16%)	0.004
Isoperfused (N(%))	4 (33%)	11 (85%)	11 (65%)	11 (44%)	
Hyperperfused (N(%))	1 (8%)	1 (8%)	4 (24%)	10 (40%)	

DSC perfusion in patchy lesions					
Hypoperfused (N(%))	0 (0%)	12 (92%)	3 (18%)	23 (92%)	<0.001
Isoperfused (N(%))	11 (92%)	1 (8%)	1 (6%)	2 (8%)	
Hyperperfused (N(%))	1 (8%)	0 (0%)	13 (77%)	0 (0%)	

DSC perfusion in T ₂ lesions					
Hypoperfused (N(%))	1 (8%)	1 (8%)	1 (6%)	1 (4%)	0.73
Isoperfused (N(%))	11 (92%)	12 (92%)	14 (82%)	23 (92%)	
Hyperperfused (N(%))	0 (0%)	0 (0%)	2 (12%)	1 (4%)	

ASL perfusion in nodular lesions					
Isoperfused (N(%))	10 (83%)	13 (100%)	11 (65%)	13 (52%)	0.01
Hyperperfused (N(%))	2 (17%)	0 (0%)	6 (35%)	12 (48%)	

ASL perfusion in patchy lesions					
Isoperfused (N(%))	12 (100%)	13 (100%)	1 (6%)	20 (80%)	<0.001
Hyperperfused (N(%))	0 (0%)	0 (0%)	16 (94%)	5 (20%)	

ASL perfusion in T ₂ lesions					
Isoperfused (N(%))	12 (100%)	13 (100%)	11 (65%)	23 (92%)	0.005
Hyperperfused (N(%))	0 (0%)	0 (0%)	6 (35%)	2 (8%)	

Continuous markers	Mean	SD	Mean	SD	Mean	SD	Mean	SD	p-value
Volume of enhancing lesions (ml)	19.49	29.37	7.14	5.21	247.54	249.60	374.45	282.52	<0.001
Volume of T2 lesions (ml)	329.44	338.37	181.19	148.76	1321.70	1094.77	1375.43	739.15	0.02
Eccentricity of enhancing lesions	0.65	0.22	0.80	0.15	0.68	0.13	0.60	0.18	<0.001
Eccentricity of T2 lesions	0.63	0.18	0.78	0.11	0.74	0.12	0.73	0.11	0.04

Supplementary Table S3. Regression analysis results for both adjusted and unadjusted models where the probability of survival of the subgroups is compared to subgroup 2, the subgroup with the least aggressive MRI markers.

		Model 1	Model 2
	Survival ^a (median (range))	Hazard ratio (95%-CI)	Hazard ratio (95%-CI)
Subgroup 1	13 (10 – 21)	1.7 (0.7 – 3.8)	2.6* (1.1 – 6.3)
Subgroup 2	22 (15 – 29)	Reference group	
Subgroup 3	11 (7 – 14)	2.4* (1.1 – 5.0)	1.4 (0.6 – 3.2)
Subgroup 4	10 (8 – 18)	1.5 (0.8 – 3.1)	0.995 (0.5 – 2.1)

^a in months, * Significant (p-value < 0.05); CI: confidence interval.

The subgroup with the least aggressive MRI markers of glioblastomas (subgroup 2) was used as reference for the models. Model 1 was unadjusted and model 2 adjusted as multivariable analysis correcting for age, KPS, and extent of tumor surgical resection.

Supplementary Table S4. Regression analysis results for both adjusted and unadjusted models where the probability of progression of the subgroups is compared to subgroup 2, one of the subgroups with the least aggressive MRI markers.

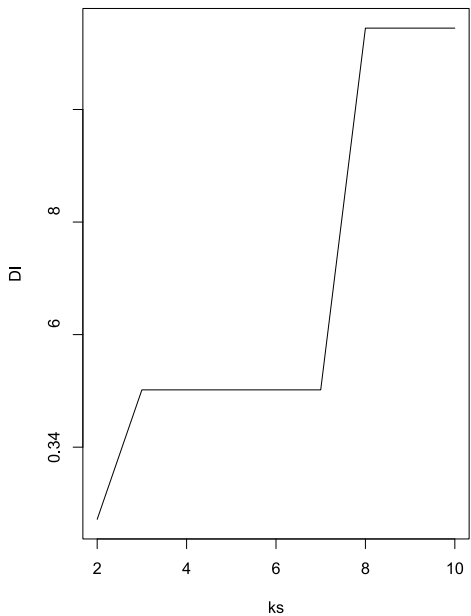
		Model 1	Model 2
	True progression (N(%))	Hazard ratio (95%-CI)	Hazard ratio (95%-CI)
Subgroup 1	67%	1.8 (0.4 – 8.3)	1.3 (0.2 – 6.8)
Subgroup 2	69%	Reference group	
Subgroup 3	82%	0.8 (0.8 – 3.4)	1.7 (0.3 – 10.4)
Subgroup 4	72%	0.9 (0.2 – 3.8)	1.7 (0.3 – 8.4)

^a in months, * Significant (p-value < 0.05); CI: confidence interval.
The subgroup with the least aggressive MRI markers of glioblastomas (subgroup 2) was used as reference for the models. Model 1 was unadjusted and model 2 adjusted as multivariate analysis correcting for age, KPS, and extent of tumor surgical resection.

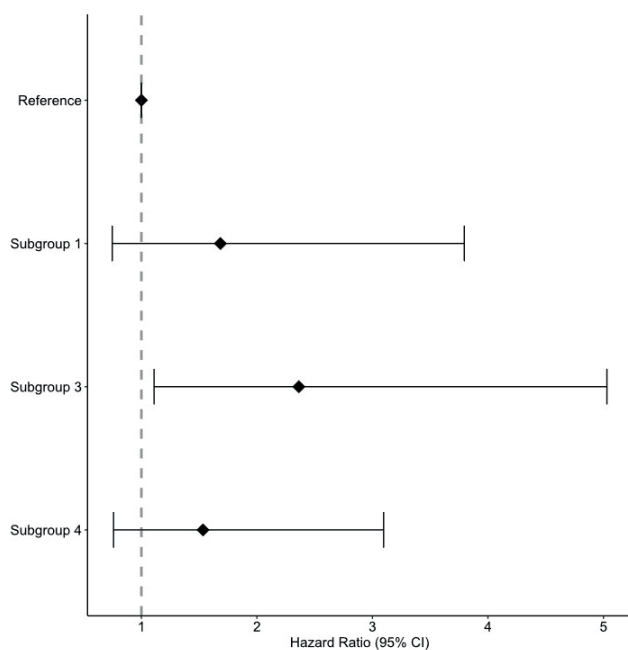
Supplementary Table S5. Log-rank test results comparing the overall survival times between subgroups and the reference group, subgroup 2, the subgroups with the least aggressive MRI markers.

Subgroups	Medial survival time in months (range)	X ²	p-value
Subgroup 1	13 (10 – 21)	1.919	0.166
Subgroup 2	11 (7 – 14)	6.906	0.009
Subgroup 3	10 (8 – 18)	1.710	0.191

7.9.4 Supplementary figures



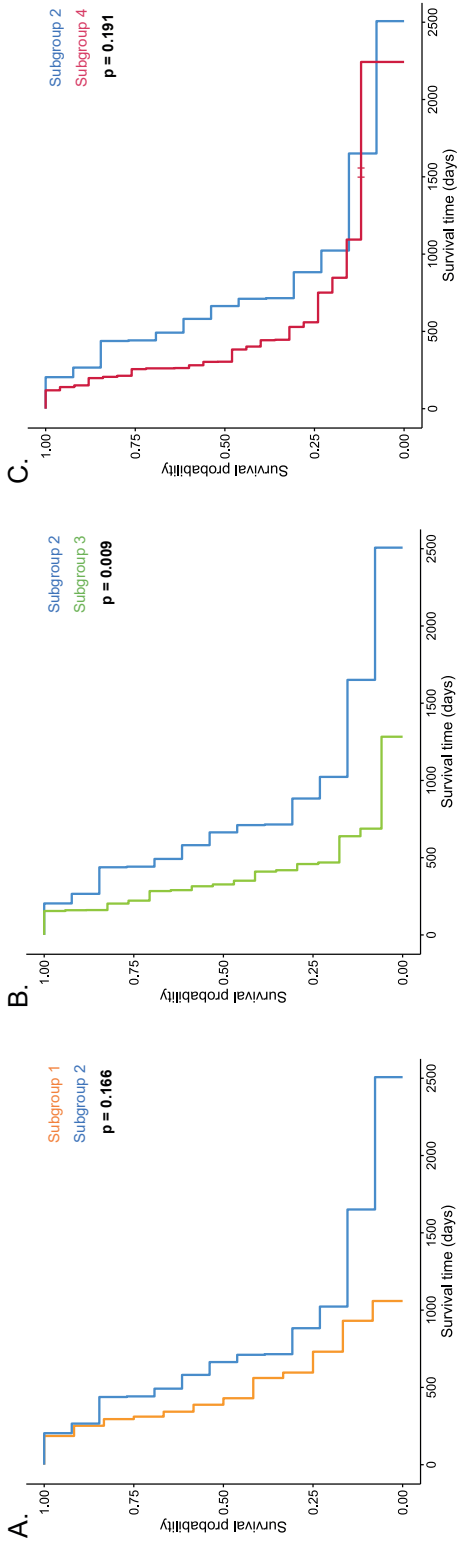
Supplementary Figure S1. The Dunn index of the hierarchical clustering model. The y-axis shows the Dunn Index (DI) and the x-axis the number of clusters (ks).



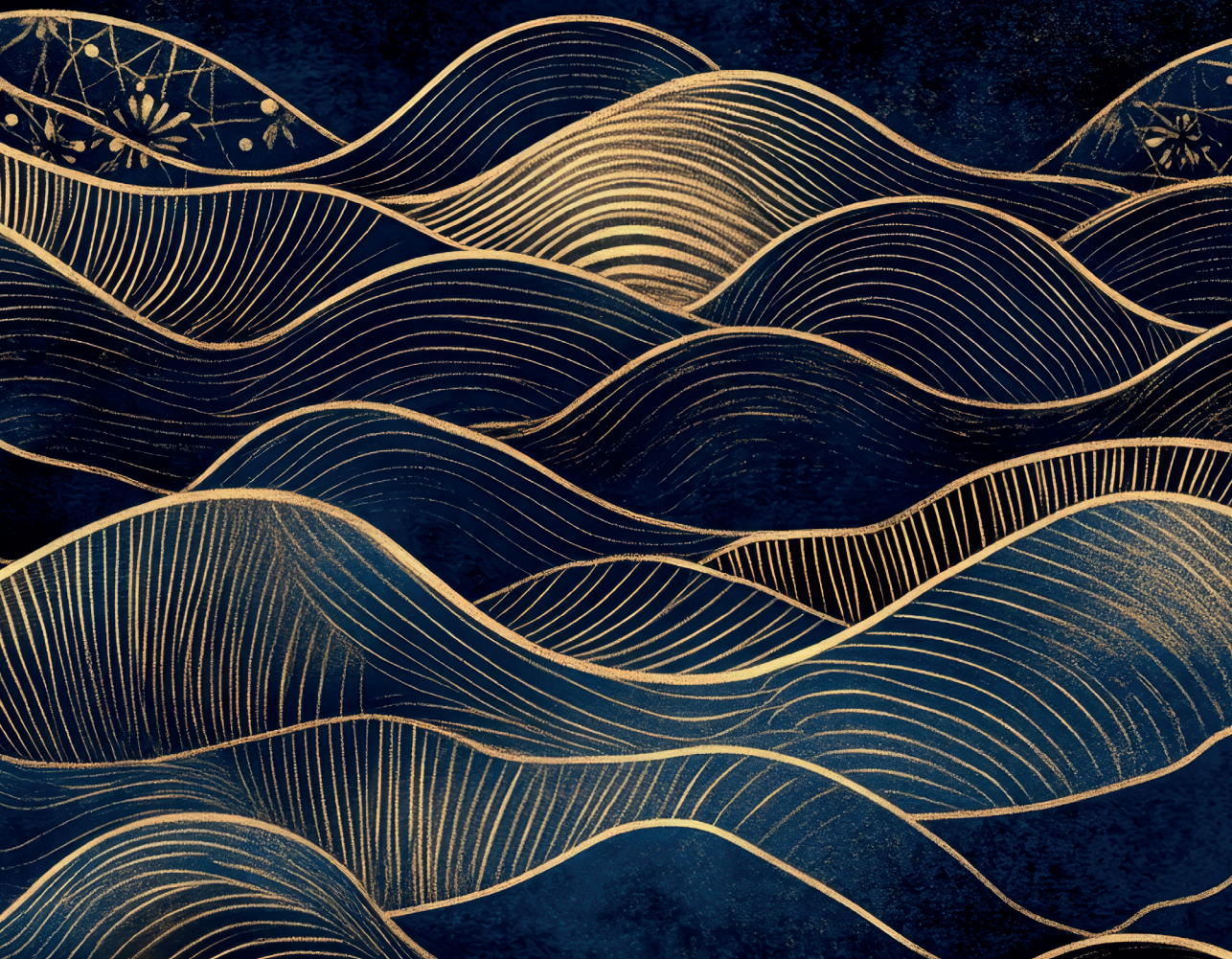
Supplementary Figure S2. Forrest plot of the hazard ratios (95%-CI) per subgroup for survival.

Illustrated results of the cox proportional hazards survival analysis are shown unadjusted for confounding clinical variables. Subgroup 2 has been set as a reference and marked with the striped line in red. Hazard ratios are shown with a 95% confidence interval.

Supplementary Figure S3. Survival curves resulting from log-rank test between subgroups. The results from a log-rank test are shown illustrating how the median overall survival time differs between the reference subgroup (subgroup 2) and subgroup 1 (A), subgroup 3 (B) and subgroup 4 (C).



8 Discussion



In this discussion key findings from the individual chapters are addressed and contextualized within the broader body of literature. The first few chapters addressed isolation of CEST pools in the brain, the contribution of different metabolites to the CEST contrast of amines at 2 and 3 ppm in the human brain, and the 2 ppm amine 7T CEST contrast in gliomas. The two latter chapters described the added value of higher-quality ultra-high field T_2 weighted images compared to their current clinical counterpart, and the use of structural and perfusion tumor characteristics to evaluate tumor recurrence and overall survival in patients with glioblastoma.

8.1 Prospects of CEST for glioma imaging at 7T

CEST's sensitivity for detecting endogenous components such as metabolites and proteins without the need of external contrast agents, has made CEST to become an attractive non-invasive technique for *in vivo* imaging of glioma. However, the biggest challenge lies upon its relatively poor specificity, given the many competing effects resulting in CEST signal changes in complex biological tissues. A first step to maximize the benefits of CEST can be to acquire the data on an ultra-high field system. This offers significant advantages namely, improved SNR, higher spectral and spatial resolution and an enhanced CEST effect¹⁹⁹. Specifically for glioma imaging, a few groups have explored APT- and NOE-CEST contrasts and studied how these imaging modalities complement existing techniques⁴⁷, as well as how it aids in tumor diagnostics and grading^{42–44}. However, until a few years ago only one group had explored amines as an alternative CEST contrast for human *in vivo* examinations, aiming to identify the epileptogenic area of lower grade gliomas⁴⁵. Given the existing pre-clinical studies^{63,64,97,200}, but the lack of studies in glioma patients at UHF¹³³, we decided to further explore this issue.

An essential step before moving to patient studies is to select the most optimal acquisition parameters to target the desired CEST pool of interest. Our initial work of Chapter 3 and 4 had therefore the primary focus on exploring different methods to optimally visualize different CEST pools of interest. Chapter 3 was inspired by previous work, where VDMP had been used as a CEST filtering technique to target the desired contrast of interest based on the exchange rate of each pool^{169,74,83,201}. Our work extended the previous simulations and the *in vivo* investigations in human subjects. Our findings showed that VDMP is a robust CEST editing technique which allows to filter MTC contrast and, based on the proposed acquisition parameters, the sequence can be sensitized to either slow or fast exchanging CEST pools. It could be interesting to apply this technique in, for instance, glioma patients to understand whether APT, NOE and amine CEST contrasts can be reliably measured without the influence of MTC. On the other hand, our practical experience demonstrated that this sophisticated technique is time consuming and requires adequate post-processing knowledge. Especially because of the time constraints we had for our clinical protocol, it was not possible to include these experiments in the protocol of our patient cohort. It is known that at higher field strengths the T_1 relaxation times are longer, which brings the benefit of enhanced contrast, but unfortunately it comes also at the cost of longer acquisition times.

In Chapter 4 we focused on optimizing the amine CEST contrast in the human brain to achieve the most sensitive possible measurements within a reasonable acquisition time. This came at the compromise of a limited offset frequency range coverage (between -1500Hz and 1500Hz) with larger step sizes of 136.4 Hz. For example, a previous study has evaluated the feasibility of imaging creatine-weighted CEST in the human brain, by acquiring data for 17.5 minutes⁸⁹. In our experience, during a multimodal MR scanning session, acquiring data for this long to yield data to image a single CEST pool, becomes unrealistic. With this in mind we managed to achieve maximum contrast sensitivity to the pool at 2 ppm with $B_1\text{rms} = 2.14\mu\text{T}$ & $t_{\text{sat}} = 1500\text{ms}$ in 03:38 minutes. Acquisition parameters were first optimized through simulations and *in vitro* experiments. By correlating our CEST results from the pools at 2 and 3 ppm with MRS quantified metabolites, we observed that glutamate had a significant contribution in both gray and white matter. Given the broad nature of the 3 ppm pool, vastly present in glutamate, we cannot entirely rule out the possibility of some contamination of the pool at 2 ppm, explaining our observations.

Our findings were viewed as controversial, particularly due to the use of the MTR asymmetry analysis method. Alternative approaches, such as AREX, which rely on Lorentzian fittings, could potentially correct for confounding factors, like T_1 and MTC¹⁰⁶. However, we observed a broad line shape of the intermediate exchanging amines at 2 ppm, which has also been previously reported¹²³. Our multimodal protocol included two CEST protocols. Given the limited total scan time, we chose to include larger step sizes for the sampling points and restrict the frequency offset. In the end a tradeoff between the number of data points (signal intensity as a function of frequency offset relative to water resonance) and acquisition time was made to allow CEST protocols specific to different CEST pools. Acquiring fewer data points can make it more challenging to then fit the acquired *in vivo* human brain data to Lorentzian line shapes. On the other hand, other studies investigating 2 ppm amines and creatine in the human muscle - where creatine concentrations are higher - have successfully used Lorentzian lines shapes to fit their data¹¹⁸. This could suggest that with greater metabolite concentrations enough signal becomes available that would superimpose any competing effects. It should be remembered that CEST is an indirect imaging method sensitive to protein and metabolites signal through the signal of water. The solute of interest needs to be present in sufficient concentrations to be sure we are not measuring noise or artefactual signals when applying sophisticated post-processing methods.

The results based on our acquisition parameters and scan duration, suggest that for the purpose of human brain CEST imaging, a fit free approach seems to be the most reliable. Interestingly, for the purposes of clinical application, a recent study that looked at how different quantitative metrics can be utilized for grading gliomas using the 3 ppm CEST pool, has reached similar conclusions²⁰². Fitting approaches can be beneficial when imaging data produce a distinct CEST signal with sufficient quality to accurately represent the pool of interest. Otherwise, fitting becomes impractical when dealing with broad signals that do not conform to a Lorentzian shape. While more sophisticated quantification methods are being developed, their application

is currently limited to research settings. To bring CEST closer to clinical use, future research should focus not only on developing robust processing methods but also on ensuring these methods remain scientifically sound, while also practical feasible for clinical application.

In Chapter 5 we explored the clinical application of measuring the intermediate exchanging 2 ppm CEST pool in different regions in glioma patients. Our research question was whether we could measure differences in the CEST contrast of the 2 ppm CEST pool in the different tumor regions of glioma patients. Our aim was not to determine which method is most advisable but to explore their outcomes given the current lack of consensus in the field. Choosing an appropriate quantitative metric was found to be challenging, as each method has inherent limitations. We quantified the CEST effect using both Lorentzian fittings and a fit free approach, i.e. the MTR asymmetry approach. Overall our results showed significantly different 2 ppm CEST pool contrast between tumor regions, also compared to normal appearing white matter. This evidence builds upon previous findings^{89,133} suggesting that this proton pool could serve as a marker for distinguishing different tumor components.

One of the prevailing hypotheses is that the CEST pool at 2 ppm contrast originates from creatine¹¹⁷. From a biological standpoint, creatine plays a critical role in cellular metabolism by providing phosphate to synthesize adenosine triphosphate (ATP) within cells during aerobic respiration¹¹³. Elevated creatine levels have been observed in grade 2-3 astrocytomas that later progressed, compared to cases that remained stable¹⁴³. In fact, glioblastomas have been shown to have lower levels of creatine compared to astrocytomas¹⁴⁴. Another study evaluated the different tumor lesions in more detail, and found reduced creatine levels in poorly perfused areas with high lactate in grade 4 gliomas¹⁴⁰. In grade 3 gliomas areas with increased CBV were seen to also have higher creatine levels. Another study in grade 3 gliomas showed that overall creatine levels decrease compared to normal appearing white matter, except in areas of elevated metabolism, where creatine levels were higher²⁰³. Increased creatine concentrations could represent the initial rise in metabolic demand, such as for new blood vessel formation, which later shifts to anaerobic respiration due to extreme energy requirements, resulting in lactate accumulation¹⁴³. This hypothesis aligns well with the physiological understanding of tumor metabolic demands. However, for CEST imaging to non-invasively reflect such processes, it is essential that the contrast correlates directly with creatine concentration.

One of the major challenges in CEST imaging is to verify the specificity of the contrast. One possible strategy is to fine-tune the acquisition parameters to maximize sensitivity to the targeted pool. For metabolite and protein protons to be specifically targeted, it is essential not only to apply the correct pulse frequency but also to use the appropriate B_1 power and saturation time. In Chapter 3, we aimed to address this challenge by implementing a CEST editing technique designed to enhance sensitivity to specific pools of interest while minimizing the competing effects of magnetization transfer. Subsequently, in Chapter 4, we attempted to correlate our CEST imaging findings with MRS metabolite measurements. This allowed us to define optimal acquisition parameters; however, we did not observe a consistent correlation

with creatine concentration in the brains of healthy subjects. It would be valuable to replicate this experiment in patients or perhaps in muscle tissue, where creatine concentrations are known to vary more widely.

Another challenge, only partially addressed in this thesis, is achieving B_1 homogeneity. Ideally, the saturation power would remain consistent throughout the field of view. To mitigate inhomogeneities, we used dielectric pads when acquiring the data for Chapters 4 and 5. Despite this, we were unable to fully counteract the observed inhomogeneities. A potential reason for this could be that the calcium-titanate in the pads may have partially dried out, and slight mechanical adjustments were necessary to fit the pads around the subject's head inside the head coil¹⁰⁴. Parallel transmit or meta-materials might be better solutions, but these were not available for our studies of this thesis.

In terms of acquisition parameters, intermediate and fast-exchanging CEST pools require high total B_1 saturation power. The B_1 should ideally be between 2 and 3 μT , with a total saturation time around 1000 to 1500 ms. However, due to SAR constraints, reaching this level of total saturation power can be challenging at 7T, if not currently unfeasible, resulting in an imperfect saturation profile and increased susceptibility to contamination from competing effects.

These technical considerations highlight the complexities of CEST imaging, despite its great potential. Outlining these challenges creates opportunities for further refinement before scaling up for broader clinical applications.

8.2 Advanced and multimodal MRI for non-invasive glioma characterization

Current clinical challenges that could be addressed by advancing imaging techniques include enhanced imaging to improve delineation of tumor borders and determine the full extent of tumor spread with improved accuracy. Additionally, the timely and accurate identification of true tumor progression could improve prognostic assessments and consequently allow timely treatment adjustments.

In Chapter 6, we addressed the first challenge by aiming to more accurately identify the volume and shape of non-enhancing tumors using high-resolution 7T imaging. Our results showed that high-quality 7T T_2 -weighted images significantly improved visualization of T_2 hyperintense lesions extent and shape compared to current clinical T_2 -weighted images acquired at 1.5 or 3T. Tissue boundaries were more clearly defined, and involvement of key brain structures, such as the corpus callosum, was more discernible. A particularly striking example was the visualization of optical tract involvement of the tumor, which was unclear in clinical images but clearly visible on the high-quality 7T scans.

The advantages we identified align with previous studies, which, for example, demonstrated improved identification of potential organs at risk using 7T T_2 -FLAIR images compared to their clinical counterpart. This could make the delineation of target volume for radiotherapy planning more precise potentially sparing healthy tissue from radiation³⁷. Also for the purpose of neurosurgery the superior tissue contrast and enhanced vessel visualization has shown to be appealing²⁰⁴. These results, and the ones from our work illustrate the potential that ultra-high field imaging has in the realm of structural imaging. Given its increase in signal to noise ratio (SNR) and improved contrast, due to a stronger net magnetic moment and longer T_1 and T_2 relaxation times of tissues, an improvement in tissue characterization is possible¹⁵⁷.

On the other hand, susceptibility to distortions and motion artifacts are typically more pronounced for ultra-high field imaging than at lower magnetic field strength MRI. In our study, we observed signal loss near the skull base and the center of the brain, which can make evaluating tumors in these regions more challenging. Another challenge of ultra-high field 7T imaging has been observed during image guided neurosurgery. In structural imaging, like magnetization-prepared T_1 -weighted images, extracranial shifts (i.e. irregularities appearing outside the skull, deriving from motion, implants, field inhomogeneities, susceptibility artefacts) have been found to introduce a certain degree of unreliability in localization of fiducial markers. The proposed solution involved fusing the 7T images with the clinical ones in the surgical image guidance system²⁰⁵. This approach is suggested as a temporary measure until the issue of extracranial shifts is fully resolved. This can serve as an interesting example of how clinical images can complement the high-quality images of 7T, while ultra-high field systems still having certain technical challenges. Translating this cooperative method to our work, the use of high-quality 7T images for tumor assessment could prove to be valuable in ambiguous cases where the extent of the tumor is unclear on clinical MR images. Conversely, in areas affected by distortion or signal loss in 7T imaging, clinical images should be leading in radiological assessment. This

interplay between clinical and ultra-high field images highlights their complementary roles in overcoming current limitations and perhaps making it more feasible to be introduced in clinical practice.

One of the biggest challenges in glioma imaging is the differentiation between true tumor progression and pseudo-progression. Unfortunately, total resection of glioblastomas is practically impossible due to their infiltrative growth, and despite adjuvant therapies, glioblastomas often quickly recur. Ideally clinicians would be able to visualize true progression in a timely manner, but often times this is not clear from conventional MR imaging, or even when more advanced modalities like perfusion imaging are added to the assessment. Gliomas are biologically heterogeneous, having different physiological processes occurring simultaneously (eg. neoangiogenesis, altered lipid metabolism, etc.)²⁰⁶. Combining different imaging data can make it interesting to understand if certain tumor characteristics are present (or absent) in tumors with similar (or different) outcomes. In Chapter 7 we explored a clustering approach to understand if perfusion imaging characteristics together with structural and enhancing pattern features, could group patients with glioblastoma and whether these groups would be predictive of progression and overall survival. Our results showed that this grouping did not differentiate patients with true from those with pseudo-progression, but the groups did exhibit different overall survival times. Our data set was limited to the images retrospectively acquired in the clinical setting and did not include other imaging modalities, such as diffusion weighted images and magnetic resonance spectroscopy. Since glioblastomas are biologically heterogeneous, it could have been interesting to have added radiological characteristics from such other MR images to the model for an even broader representation of tumor characteristics. Also, other imaging modalities such as positron emission tomography (PET) could have been interesting to add to the model as they can account for metabolic activity, which could help to differentiate between active tissue, necrosis and non-tumorous inflammation²⁰⁷. Moreover, the method we used included visual scoring which is time consuming and labor intensive. The idea behind visually scoring these images was based on including the expert opinions of radiologists when assessing these images in the clinic. Translating such expert knowledge into automatic, quantifiable features is not easily done. Currently, many studies have focused on machine learning alternatives as less labor intensive methods, where oftentimes tumor genetics' profile and high-order imaging characteristics (eg. gray-level texture) are combined. However, the downside of this approach is that the way in which the algorithms combine this information is not always clear and, importantly, do not represent how radiologists currently assess MR images. The use of machine learning, and in the broader sense, artificial intelligence, for medical purposes poses a very interesting possibility given the rise in medical data and labor time and costs. Perhaps the use of such technology is more suited for applications that are performed more frequently than glioma imaging and have very well-defined specific imaging characteristics, in this way benefiting from more data available. For example, using machine learning to detect very well defined lung cancer nodules on CT is probably more likely to benefit from machine learning applications than the reporting on glioblastoma. However, implementing these tools for clinical decision-making or even prediction of disease outcome

seems, at this day and time, still far away.

8.3 Concluding remarks

The overarching aims of this thesis were to investigate the potential of advanced methods for imaging gliomas, with a particular focus on UHF imaging and CEST.

CEST is a promising non-invasive technique for glioma imaging, benefiting from higher spectral resolution provided by UHF. However, despite the advantage of UHF providing higher spectral resolution, magnetic field inhomogeneities currently hinder CEST's sensitivity and imaging reliability. Another challenge lies in mitigating competing effects, particularly the MTC. The VDMP results demonstrated how this technique can be used to resolve this challenge, specifically by isolating specific CEST effects. Nevertheless, the major limitation of VDMP remains its long acquisition times.

Regarding CEST quantification techniques, there is currently a lack of consensus on the most optimal method. Depending on the data acquired, its acquisition parameters, and the targeted CEST pool of interest, using different quantification techniques will be most optimal.

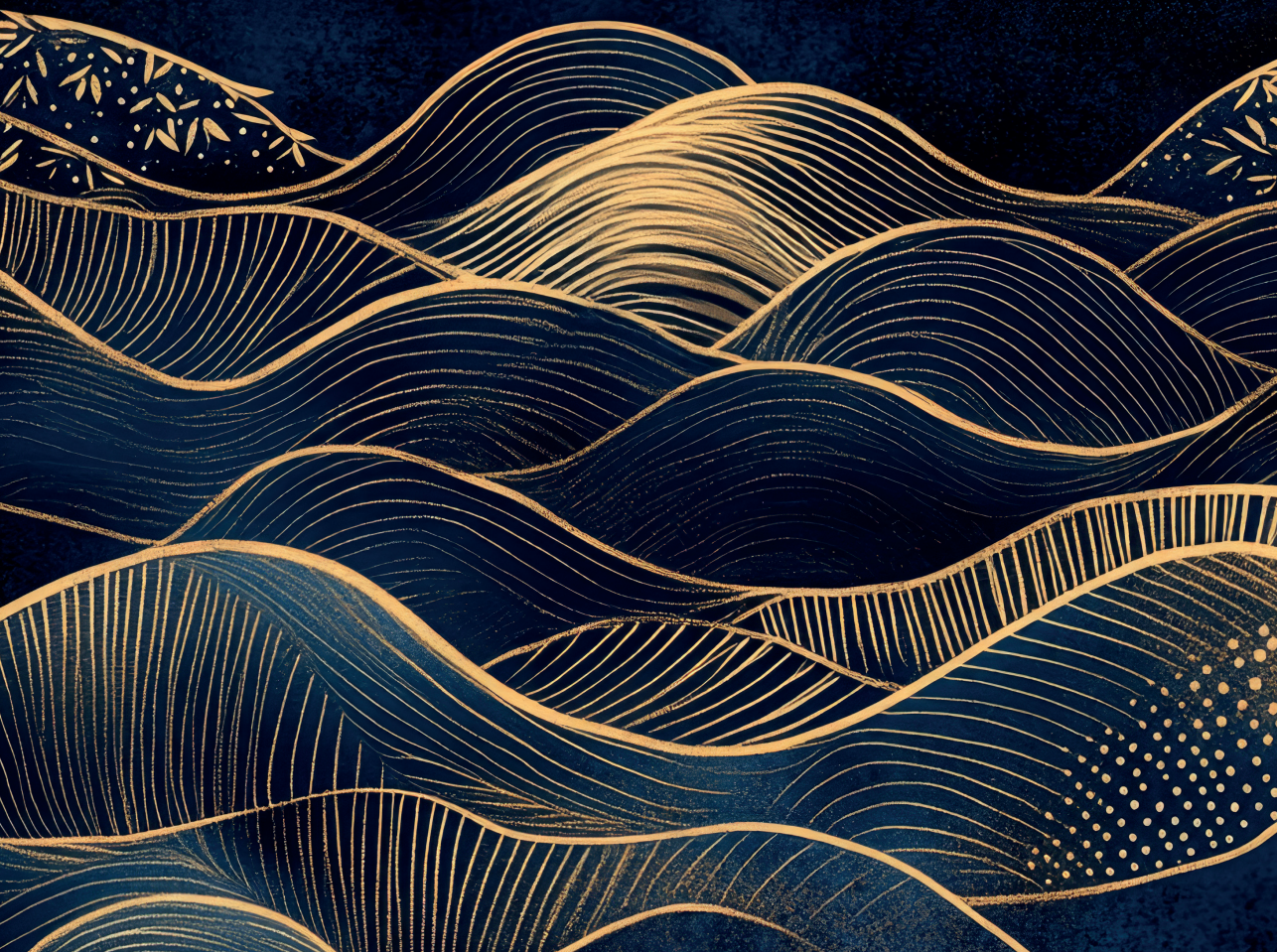
When investigating and optimizing the acquisition protocol for amines CEST we found that glutamate seems to also contribute to the pool at 2 ppm. Moreover, we showed how the 2 ppm CEST pool contrast significantly differs between tumor lesions.

This thesis has also shown how UHF could be of value for treatment planning including delineating glioma's boundaries and evaluating the presence of infiltration of critical brain structures, given its improved spatial resolution and contrast.

Lastly, this work investigated a clustering analysis model that utilized anatomical and perfusion radiological characteristics to identify MRI phenotypes in glioblastoma patients. The MRI phenotypes were shown to have different overall survival outcomes. However, the underlying technique of manually annotating images to perform clustering analysis can be very time consuming, even though it still only included limited radiological features. These efforts could be expanded and maybe automatized to cover the complex nature of glioblastoma more thoroughly.

In sum, this thesis explored several advanced techniques to improve the characterization of gliomas, which might help local treatment planning, differentiate glioma components, and identify sub-groups of patients with glioblastoma with a distinct overall survival. The clinical use of these new techniques not only needs much greater validation which goes beyond the pilot studies conducted during this thesis, but also a careful consideration of practical aspects such as standardization, accessibility and costs before they should be introduced in clinical practice.

9 Summary



9.1 Summary in English

This thesis explored advanced MRI modalities and their applications to obtain improved characterization of glioma. A substantial focus was put on optimizing CEST imaging and analysis. The optimization work presented in this thesis was performed on healthy individuals, whereas the application of it was done in a pilot study with glioma patients. The work with these patients included a broad protocol allowing to understand the added value of CEST compared to its more traditional clinical imaging counterparts.

Chapter 2 provided a comprehensive review of various Chemical Exchange Saturation Transfer (CEST) imaging modalities that were researched and applied in glioma imaging, discussing their potential clinical implications. Amide Transfer Proton (APT)-CEST emerges as the most extensively studied contrast, and the chapter highlights the promising results achieved to date. However, it also addressed significant challenges to clinical implementation, particularly the need for broader validation and consensus on acquisition parameters. The chapter further explored newer CEST modalities, such as amine and glucose CEST, in the context of pre-operative glioma imaging.

Chapter 3 presented the initial methods optimization, focusing on Variable Delay Multipulse (VDMP)-CEST for *in vivo* human brain imaging. The aim was to separate signals from different CEST pools based on their exchange rates while mitigating effects from magnetization transfer contrast (MTC). Slow-exchanging amides and relative Nuclear Overhauser Effect (rNOE) were successfully distinguished from fast-exchanging amines after Magnetization Transfer Contrast (MTC) correction. The chapter identified the optimal acquisition parameters, such as B_1 amplitude and mixing time, for effective imaging of each CEST pool.

In Chapter 4, the focus shifted to fast-exchanging amines. Both 2 and 3 parts per million (ppm) amine pools have been shown to be present in the human brain, and so the goal was to optimize acquisition parameters to maximize sensitivity to these pools. The study also sought to correlate the 2 ppm and 3 ppm amine pools with creatine and glutamate, respectively. Unexpectedly, the findings revealed that glutamate contributes significantly to the 2 ppm amine pool.

Chapter 5 investigated the application of CEST imaging in gliomas, specifically examining the value of the 2 ppm CEST pool for non-invasive characterization of enhancing and non-enhancing glioma lesions. The CEST signal was analyzed using different methods, consistently revealing differences between enhancing and non-enhancing lesions when compared to contralateral healthy tissue. These findings suggest that the 2 ppm pool could serve as a valuable non-invasive tool for distinguishing between these regions in glioma patients.

The second part of this thesis explored the use of common radiological tumor characteristics, as well as ultra-high field MR imaging, to address current challenges in clinical decision making in patients with glioma.

Chapter 6 compared the extension, volume, and shape complexity of T_2 hyperintense areas

between clinical MRI and high-resolution 7T scans. The high-quality 7T images revealed T_2 hyperintense areas that were not visible on clinical MRI. Additionally, tumor volume and shape complexity were significantly larger and more intricate on 7T scans. These results suggest that 7T imaging could provide more detailed tumor information, potentially improving clinical decision-making and treatment planning by better assessing tumor extension, size, and shape complexity.

In the final part, Chapter 7 investigated whether common radiological tumor characteristics can be utilized to group patients and whether these sub-groups show different behavior according to their progression and survival. Using structural and perfusion data scored from MR images three months post-radiotherapy, four distinct MRI phenotypes could be identified sharing similar tumor perfusion characteristics. Their recurrence rates and overall survival were assessed based on progression status at nine months post-radiotherapy. While the phenotypes appeared to be predictive of overall survival, they did not prove to be useful in differentiating between true and pseudo-tumor progression.

9.2 Summary in Dutch

In deze thesis werd onderzocht geavanceerde MRI modaliteiten en hun toepassingen om een verbeterde karakterisering van glioom te verkrijgen. Hierbij lag de focus op het optimaliseren van CEST beeldvorming en analyse. Het optimalisatiewerk dat in deze thesis wordt gepresenteerd, werd uitgevoerd bij gezonde individuen, terwijl de toepassing van CEST werd onderzocht in een pilotstudie met glioompatiënten. Het onderzoek met deze patiënten omvatte een uitgebreid protocol om de toegevoegde waarde van CEST te begrijpen in vergelijking met meer traditionele klinische beeldvormingstechnieken.

Hoofdstuk 2 gaf een uitgebreid overzicht van verschillende Chemical Exchange Saturation Transfer (CEST) beeldvormingsmodaliteiten die onderzocht en toegepast zijn bij de beeldvorming van gliomen, waarbij de mogelijke klinische implicaties werden besproken. Amide Proton Transfer (APT)-CEST komt naar voren als het meest uitgebreid bestudeerde contrast, en het hoofdstuk belicht de veelbelovende resultaten die tot nu toe zijn behaald. Er worden echter ook belangrijke uitdagingen voor klinische implementatie besproken, met name de noodzaak van bredere validatie en consensus over acquisitieparameters. Verder werden in het hoofdstuk nieuwere CEST modaliteiten, zoals amine en glucose CEST, in de context van preoperatieve beeldvorming van gliomen.

Hoofdstuk 3 presenteerde de initiële methode optimalisatie, met de focus op Variable Delay Multipulse (VDMP) CEST voor *in vivo* beeldvorming van de hersenen. Het doel was om signalen van verschillende CEST pools te scheiden op basis van hun uitwisselingsnelheden, terwijl de effecten van magnetisatie transfercontrast (MTC) werden geminimaliseerd. Langzaam uitwisselende amides en de relatieve Nuclear Overhauser Effect (rNOE) werden succesvol onderscheiden van snel uitwisselende amines na correctie voor magnetisatie-transfercontrast (MTC). In dit hoofdstuk werden de optimale acquisitieparameters, zoals B_1 amplitude en mixtijd, geïdentificeerd voor een effectieve beeldvorming van elke CEST pool.

In Hoofdstuk 4 verschoof de focus naar snel uitwisselende amines. Zowel de 2 als de 3 parts per million (ppm) amine pools bleken aanwezig te zijn in de menselijke hersenen, en daarom was het doel om acquisitieparameters te optimaliseren om de gevoeligheid voor deze pools te maximaliseren. In deze studie werd ook geprobeerd om de 2 ppm en 3 ppm amine pools te correleren met respectievelijk creatine en glutamaat. Onverwacht toonden de bevindingen aan dat glutamaat aanzienlijk bijdraagt aan de 2 ppm amine pool.

In hoofdstuk 5 werd de toepassing van CEST beeldvorming bij glioom onderzocht, specifiek door de waarde van de 2 ppm CEST pool te bestuderen voor de niet-invasieve karakterisering van aankeurend en niet aankeurend laesies. Het CEST signaal werd geanalyseerd met verschillende methoden en toonde consequent verschillen aan tussen aankeurend en niet aankeurend laesies in vergelijking met contralateraal gezond weefsel. Deze bevindingen suggereren dat de 2 ppm pool een waardevol niet-invasief hulpmiddel kan zijn om onderscheid te maken tussen deze regio's bij patiënten met een glioom.

In het tweede deel van deze thesis werd het gebruik van gangbare radiologische tumor-eigenschappen en ultra-hoge veld MRI onderzocht om huidige uitdagingen bij klinische besluitvorming bij glioompatiënten aan te pakken.

Hoofdstuk 6 vergeleek de extensie, het volume en de vormcomplexiteit van T_2 hyperintense gebieden tussen klinische MRI en hoge-resolutie 7T scans. De hoogwaardige 7T beelden onthulden T_2 hyperintense gebieden die niet zichtbaar waren op klinische MRI. Bovendien bleken tumorvolume en vormcomplexiteit significant groter en gedetailleerder op 7T scans. Deze resultaten suggereren dat 7T beeldvorming meer gedetailleerde tumorinformatie kan verschaffen, wat mogelijk kan bijdragen aan verbeterde klinische besluitvorming en behandelplanning door een betere beoordeling van tumor extensie, grootte en vormcomplexiteit.

In het laatste deel van deze thesis werd in Hoofdstuk 7 onderzocht of gangbare radiologische tumor eigenschappen kunnen worden gebruikt om patiënten te groeperen en of deze subgroepen verschillend gedrag vertonen met betrekking tot progressie en overleving. Met behulp van structurele en perfusie data, verkregen uit MRI scans drie maanden na radiotherapie, konden vier verschillende MRI fenotypen worden geïdentificeerd die vergelijkbare tumorperfusie eigenschappen deelden. De recidiepercentages en algehele overleving van deze vier groepen/fenotypen beoordeeld op basis van progressiestatus negen maanden na radiotherapie. Hoewel de fenotypen voorspellend leken voor de algehele overleving, bleken ze niet bruikbaar om onderscheid te maken tussen echte en pseudo-tumorprogressie.

9.3 Summary in Portuguese

Esta dissertação explora a aplicação de diferentes modalidades avançadas de ressonância magnética (RM) na caracterização do glioma, tendo como foco a otimização e análise de imagens obtidas por CEST. O trabalho de otimização apresentado nesta tese foi realizado em indivíduos saudáveis, enquanto a sua aplicação foi implementada num estudo piloto em pacientes com glioma. O trabalho com estes doentes incluiu um protocolo alargado, permitindo compreender o seu valor acrescentado em comparação com técnicas de imagem clínica mais tradicionais.

O Capítulo 2 fornece uma revisão abrangente de várias modalidades de imagem por Transferência de Saturação por Troca Química (CEST) utilizadas no estudo do glioma, discutindo ainda potenciais implicações clínicas. A modalidade Amide Proton Transfer (APT)-CEST surge como o contraste mais amplamente utilizado, e o capítulo destaca os resultados promissores obtidos com este contraste até à data. No entanto, a utilização de APT-CEST em contexto clínico ainda detém desafios significativos, nomeadamente a necessidade de uma validação mais abrangente e de consenso sobre os parâmetros de aquisição a utilizar. O capítulo explorou ainda novas modalidades de CEST, como CEST de aminas e glicose, no contexto de imagiologia pré-operatória do glioma.

O Capítulo 3 apresenta a optimização inicial dos métodos, com foco no CEST de Pulso Múltiplo com Atraso Variável (VDMP) para obtenção de imagens *in vivo* do cérebro humano. O objetivo foi separar sinais de diferentes reservatórios de CEST com base nas suas taxas de transferência, ao mesmo tempo que se minimizaram os efeitos do contraste por transferência de magnetização (MTC). As amidas de troca lenta e o Efeito Nuclear Overhauser Relativo (rNOE) foram distinguidos com sucesso de aminas de troca rápida após correção para MTC. O capítulo identificou os parâmetros ótimos de aquisição, como a amplitude de B_1 e o tempo de mistura, para uma imagiologia consistente dos diferentes reservatórios de CEST.

No Capítulo 4, o foco mudou para as aminas de troca rápida. Foi demonstrado que os reservatórios de amina de 2 e 3 partes por milhão (ppm) estão presentes no cérebro humano e, conseqüentemente, o objectivo do trabalho apresentado neste capítulo foi otimizar os parâmetros de aquisição para maximizar a sensibilidade a estes reservatórios. O estudo procurou ainda correlacionar os reservatórios de amina de 2 ppm e 3 ppm com creatina e glutamato, respetivamente. Surpreendentemente, os resultados revelaram que o glutamato contribui significativamente para o reservatório de amina de 2 ppm.

O Capítulo 5 investiga a aplicação da imagiologia por CEST em pacientes com glioma, examinando especificamente o valor do reservatório de 2 ppm para a caracterização não invasiva de lesões de glioma, com e sem contraste. O sinal de CEST foi analisado utilizando diferentes métodos, revelando diferenças consistentes entre lesões, com e sem contraste, quando comparadas com tecido saudável contralateral. Estes resultados sugerem que o reservatório de 2 ppm pode servir como potencial biomarcador não invasivo para distinção

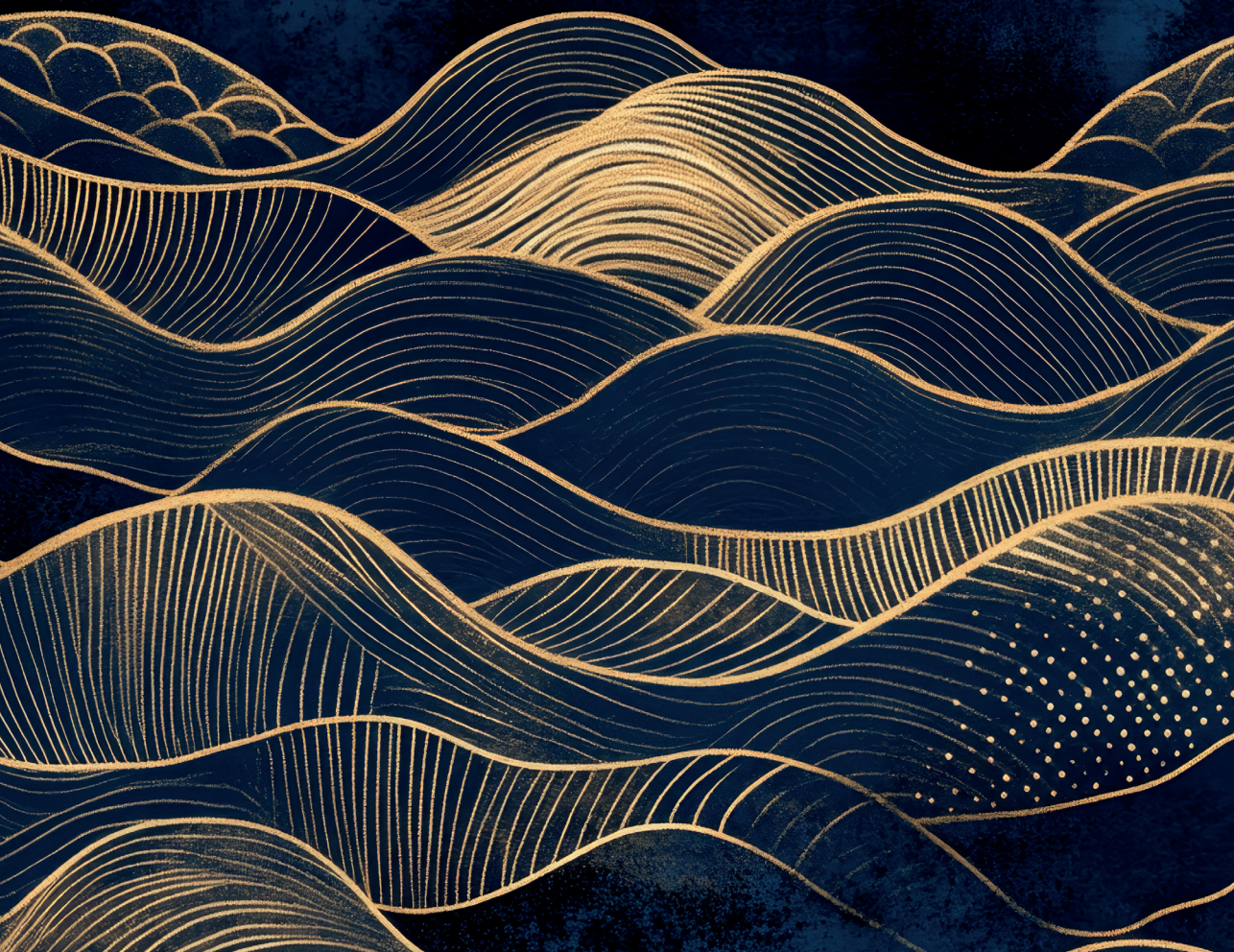
destes tecidos em doentes com glioma.

A segunda parte desta dissertação explora a utilização de características tumorais radiológicas comuns, bem como a imagiologia por RM 7T, para abordar desafios atuais na gestão clínica de doentes com glioma.

O Capítulo 6 compara a extensão, volume e complexidade de forma das áreas hiperintensas em T_2 entre a RM clínica e as imagens de alta resolução obtidas com RM 7T. As imagens de RM 7T revelaram áreas hiperintensas em T_2 que não eram visíveis na RM clínica. Além disso, o volume tumoral e a complexidade da forma foram significativamente maiores nas imagens de RM 7T. Estes resultados sugerem que a imagiologia por 7T pode fornecer informações tumorais mais detalhadas, permitindo uma melhor avaliação da extensão, tamanho e complexidade de forma do tumor, melhorando potencialmente a gestão clínica destes doentes.

Por fim, o Capítulo 7 investiga se características tumorais radiológicas comuns podem ser utilizadas para identificar subgrupos de doentes e se estes apresentam progressão de doença e sobrevivência distintos. Utilizando dados de imagem estrutural e de perfusão extraídos de imagens de RM três meses após a radioterapia, foram identificados quatro fenótipos distintos de RM que partilhavam características semelhantes de perfusão tumoral. As taxas de recidiva e sobrevivência global foram avaliadas com base no estado de progressão nove meses após a radioterapia. Embora os fenótipos tenham demonstrado ser preditivos da sobrevivência global, não se revelaram úteis para diferenciar entre progressão tumoral real e pseudoprogessão.

10 References



1. Pellerino A, Caccese M, Padovan M, Cerretti G, Lombardi G. Epidemiology, risk factors, and prognostic factors of gliomas. *Clin Transl Imaging*. 2022;10(5):467-475. doi:10.1007/s40336-022-00489-6
2. Jäkel S, Dimou L. Glial cells and their function in the adult brain: A journey through the history of their ablation. *Front Cell Neurosci*. 2017;11(February):1-17. doi:10.3389/fncel.2017.00024
3. Bachiller S, Jiménez-Ferrer I, Paulus A, et al. Microglia in neurological diseases: A road map to brain-disease dependent-inflammatory response. *Front Cell Neurosci*. 2018;12(December):1-17. doi:10.3389/fncel.2018.00488
4. Deng S, Gan L, Liu C, et al. Roles of Ependymal Cells in the Physiology and Pathology of the Central Nervous System. *Aging Dis*. 2023;14(2):468-483. doi:10.14336/AD.2022.0826-1
5. Norden AD, Drappatz J, Wen PY. Malignant gliomas in adults. *Blue Books of Neurology*. 2010;36:99-120. doi:10.1016/B978-0-7506-7516-1.00005-0
6. Teng C, Zhu Y, Li Y, et al. Recurrence- and Malignant Progression-Associated Biomarkers in Low-Grade Gliomas and Their Roles in Immunotherapy. *Front Immunol*. 2022;13(May):1-18. doi:10.3389/fimmu.2022.899710
7. Sadetzki S, Bruchim R, Oberman B, et al. Description of selected characteristics of familial glioma patients-Results from the Gliogene Consortium. *Eur J Cancer*. 2013;49(6):1335-1345. doi:10.1016/j.ejca.2012.11.009
8. Neglia JP, Robison LL, Stovall M, et al. New primary neoplasms of the central nervous system in survivors of childhood cancer: A report from the childhood cancer survivor study. *J Natl Cancer Inst*. 2006;98(21):1528-1537. doi:10.1093/jnci/djj411
9. Inskip PD, Sigurdson AJ, Veiga L, et al. Radiation-related new primary solid cancers in the childhood cancer survivor study: Comparative radiation dose response and modification of treatment effects. *Int J Radiat Oncol Biol Phys*. 2016;94(4):800-807. doi:10.1016/j.ijrobp.2015.11.046
10. Louis DN, Perry A, Wesseling P, et al. The 2021 WHO classification of tumors of the central nervous system: A summary. *Neuro Oncol*. 2021;23(8):1231-1251. doi:10.1093/neuonc/noab106
11. Lee JH, Wee CW. Treatment of Adult Gliomas: A Current Update. *Brain & Neurorehabilitation*. 2022;15(3). doi:10.12786/bn.2022.15.e24
12. van der Weide HL, Kramer MCA, Scandurra D, et al. Proton therapy for selected low grade glioma patients in the Netherlands. *Radiotherapy and Oncology*. 2021;154:283-290. doi:10.1016/j.radonc.2020.11.004
13. Thust SC, Heiland S, Falini A, et al. Glioma imaging in Europe: A survey of 220 centres and recommendations for best clinical practice. *Eur Radiol*. 2018;28(8):3306-3317. doi:10.1007/s00330-018-5314-5
14. Zhang L, Min Z, Tang M, Chen S, Lei X, Zhang X. The utility of diffusion MRI with quantitative ADC measurements for differentiating high-grade from low-grade cerebral gliomas: Evidence from a meta-analysis. *J Neurol Sci*. 2017;373:9-15. doi:10.1016/j.jns.2016.12.008
15. Smits M. MRI biomarkers in neuro-oncology. *Nat Rev Neurol*. 2021;17(8):486-500. doi:10.1038/s41582-021-00510-y
16. Hirschler L, Sollmann N, Schmitz-Abecassis B, et al. Advanced MR Techniques for Preoperative Glioma Characterization: Part 1. *Journal of Magnetic Resonance Imaging*. Published online 2023:1-21. doi:10.1002/jmri.28662
17. Hangel G, Schmitz-Abecassis B, Sollmann N, et al. Advanced MR Techniques for Preoperative Glioma Characterization: Part 2. *Journal of Magnetic Resonance Imaging*. 2023;57(6):1676-1695. doi:10.1002/jmri.28663
18. Henriksen OM, del Mar Álvarez-Torres M, Figueiredo P, et al. High-Grade Glioma Treatment Response Monitoring Biomarkers: A Position Statement on the Evidence Supporting the Use of Advanced MRI Techniques in the Clinic, and the Latest Bench-to-Bedside Developments. Part 1: Perfusion and Diffusion Techniques. *Front Oncol*. 2022;12(March):1-27. doi:10.3389/fonc.2022.810263
19. Booth TC, Wiegers EC, Warnert EAH, et al. High-Grade Glioma Treatment Response Monitoring Biomarkers: A Position Statement on the Evidence Supporting the Use of Advanced MRI Techniques in the Clinic, and the

- Latest Bench-to-Bedside Developments. Part 2: Spectroscopy, Chemical Exchange Saturation., *Front Oncol.* 2022;11(February):1-22. doi:10.3389/fonc.2021.811425
20. Hanahan D. Hallmarks of Cancer: New Dimensions. *Cancer Discov.* 2022;12(1):31-46. doi:10.1158/2159-8290.CD-21-1059
 21. Schmainda KM, Rand SD, Joseph AM, et al. Characterization of a first-pass gradient-echo spin-echo method to predict brain tumor grade and angiogenesis. *American Journal of Neuroradiology.* 2004;25(9):1524-1532.
 22. McCullough BJ, Ader V, Aguedan B, et al. Preoperative relative cerebral blood volume analysis in gliomas predicts survival and mitigates risk of biopsy sampling error. *J Neurooncol.* 2018;136(1):181-188. doi:10.1007/s11060-017-2642-2
 23. Lu J, Li X, Li H. Perfusion parameters derived from MRI for preoperative prediction of IDH mutation and MGMT promoter methylation status in glioblastomas. *Magn Reson Imaging.* 2021;83(April):189-195. doi:10.1016/j.mri.2021.09.005
 24. Connelly JM, Prah MA, Santos-Pinheiro F, Mueller W, Cochran E, Schmainda KM. Magnetic Resonance Imaging Mapping of Brain Tumor Burden: Clinical Implications for Neurosurgical Management: Case Report. *Neurosurgery Open.* 2021;2(4):2-5. doi:10.1093/neuopn/okab029
 25. Taylor C, Ekert JO, Sefcikova V, Fersht N, Samandouras G. Discriminators of pseudoprogression and true progression in high-grade gliomas: A systematic review and meta-analysis. *Sci Rep.* 2022;12(1):1-12. doi:10.1038/s41598-022-16726-x
 26. Soldozy S, Galindo J, Snyder H, et al. Clinical utility of arterial spin labeling imaging in disorders of the nervous system. *Neurosurg Focus.* 2019;47(6):1-10. doi:10.3171/2019.9.FOCUS19567
 27. Falk Delgado A, De Luca F, Van Westen D, Falk Delgado A. Arterial spin labeling MR imaging for differentiation between high- and low-grade glioma - A meta-analysis. *Neuro Oncol.* 2018;20(11):1450-1461. doi:10.1093/neuonc/noy095
 28. Abdel Razek AAK, Talaat M, El-Serougy L, Gaballa G, Abdelsalam M. Clinical Applications of Arterial Spin Labeling in Brain Tumors. *J Comput Assist Tomogr.* 2019;43(4):525-532. doi:10.1097/RCT.0000000000000873
 29. Yoo RE, Yun TJ, Hwang I, et al. Arterial spin labeling perfusion-weighted imaging aids in prediction of molecular biomarkers and survival in glioblastomas. *Eur Radiol.* 2020;30(2):1202-1211. doi:10.1007/s00330-019-06379-2
 30. Jovanovic M, Radenkovic S, Stosic-Opincal T, et al. Differentiation between progression and pseudoprogression by arterial spin labeling MRI in patients with glioblastoma multiforme. *Journal of BUON.* 2017;22(4):1061-1067.
 31. Wang Q, Zhang H, Zhang JS, et al. The diagnostic performance of magnetic resonance spectroscopy in differentiating high-from low-grade gliomas: A systematic review and meta-analysis. *Eur Radiol.* 2016;26(8):2670-2684. doi:10.1007/s00330-015-4046-z
 32. Suh CH, Kim HS, Jung SC, Choi CG, Kim SJ. 2-Hydroxyglutarate MR spectroscopy for prediction of isocitrate dehydrogenase mutant glioma: A systemic review and meta-analysis using individual patient data. *Neuro Oncol.* 2018;20(12):1573-1583. doi:10.1093/neuonc/noy113
 33. Vinogradov E, Sherry AD, Lenkinski RE. CEST: From basic principles to applications, challenges and opportunities. *Journal of Magnetic Resonance.* 2013;229:155-172. doi:10.1016/j.jmr.2012.11.024
 34. Ugurbil K. Magnetic resonance imaging at ultrahigh fields. *IEEE Trans Biomed Eng.* 2014;61(5):1364-1379. doi:10.1109/TBME.2014.2313619
 35. Shaffer A, Kwok SS, Naik A, et al. Ultra-High-Field MRI in the Diagnosis and Management of Gliomas: A Systematic Review. *Front Neurol.* 2022;13(April):1-11. doi:10.3389/fneur.2022.857825
 36. Tractnig S, Springer E, Bogner W, et al. Key clinical benefits of neuroimaging at 7 T Europe PMC Funders Group. *Neuroimage.* 2018;168:477-489. doi:10.1016/j.neuroimage.2016.11.031.Key
 37. Regnery S, Knowles BR, Paech D, et al. High-resolution FLAIR MRI at 7 Tesla for treatment planning in

- glioblastoma patients. *Radiotherapy and Oncology*. 2019;130:180-184. doi:10.1016/j.radonc.2018.08.002
38. Radbruch A, Eidel O, Wiestler B, et al. Quantification of tumor vessels in glioblastoma patients using time-of-flight angiography at 7 Tesla: A feasibility study. *PLoS One*. 2014;9(11):1-13. doi:10.1371/journal.pone.0110727
 39. Zhou J, Zijl PCM van. Chemical exchange saturation transfer imaging and spectroscopy. *Prog Nucl Magn Reson Spectrosc*. 2006;48(2-3):109-136. doi:10.1016/j.pnmrs.2006.01.001
 40. Paech D, Zaiss M, Meissner JE, et al. Nuclear overhauser enhancement mediated chemical exchange saturation transfer imaging at 7 tesla in glioblastoma patients. *PLoS One*. 2014;9(8):3-9. doi:10.1371/journal.pone.0104181
 41. Zaiss M, Windschuh J, Goerke S, et al. Downfield-NOE-suppressed amide-CEST-MRI at 7 Tesla provides a unique contrast in human glioblastoma. *Magn Reson Med*. 2017;77(1):196-208. doi:10.1002/mrm.26100
 42. Paech D, Windschuh J, Oberhollenzer J, et al. Assessing the predictability of IDH mutation and MGMT methylation status in glioma patients using relaxation-compensated multipool CEST MRI at 7.0 T. *Neuro Oncol*. 2018;20(12):1661-1671. doi:10.1093/neuonc/now073
 43. Heo HY, Jones CK, Hua J, et al. Whole-brain amide proton transfer (APT) and nuclear overhauser enhancement (NOE) imaging in glioma patients using low-power steady-state pulsed chemical exchange saturation transfer (CEST) imaging at 7T. *Journal of Magnetic Resonance Imaging*. 2016;44(1):41-50. doi:10.1002/jmri.25108
 44. Dreher C, Oberhollenzer J, Meissner JE, et al. Chemical exchange saturation transfer (CEST) signal intensity at 7T MRI of WHO IV° gliomas is dependent on the anatomic location. *Journal of Magnetic Resonance Imaging*. 2019;49(3):777-785. doi:10.1002/jmri.26215
 45. Neal A, Moffat BA, Stein JM, et al. Glutamate weighted imaging contrast in gliomas with 7 Tesla magnetic resonance imaging. *Neuroimage Clin*. 2019;22(June 2018):101694. doi:10.1016/j.nicl.2019.101694
 46. Meissner JE, Korzowski A, Regnery S, et al. Early response assessment of glioma patients to definitive chemoradiotherapy using chemical exchange saturation transfer imaging at 7 T. *Journal of Magnetic Resonance Imaging*. 2019;50(4):1268-1277. doi:10.1002/jmri.26702
 47. Paech D, Burth S, Windschuh J, et al. Nuclear overhauser enhancement imaging of glioblastoma at 7 Tesla: Region specific correlation with apparent diffusion coefficient and histology. *PLoS One*. 2015;10(3):1-16. doi:10.1371/journal.pone.0121220
 48. Van Zijl PCM, Yadav NN. Chemical exchange saturation transfer (CEST): What is in a name and what isn't? *Magn Reson Med*. 2011;65(4):927-948. doi:10.1002/mrm.22761
 49. van Zijl PCM, Lam WW, Xu J, Knutsson L, Stanisz GJ. Magnetization Transfer Contrast and Chemical Exchange Saturation Transfer MRI. Features and analysis of the field-dependent saturation spectrum. *Neuroimage*. 2018;168(April 2017):222-241. doi:10.1016/j.neuroimage.2017.04.045
 50. Zu Z, Louie EA, Lin EC, et al. Chemical exchange rotation transfer imaging of intermediate-exchanging amines at 2 ppm. *NMR Biomed*. 2017;30(10):1-12. doi:10.1002/nbm.3756
 51. Xu X, Sehgal AA, Yadav NN, et al. d-glucose weighted chemical exchange saturation transfer (glucoCEST)-based dynamic glucose enhanced (DGE) MRI at 3T: early experience in healthy volunteers and brain tumor patients. *Magn Reson Med*. 2020;84(1):247-262. doi:10.1002/mrm.28124
 52. Goldenberg JM, Pagel MD. Assessments of tumor metabolism with CEST MRI. *NMR Biomed*. 2019;32(10):1-12. doi:10.1002/nbm.3943
 53. Togao O, Yoshiura T, Keupp J, et al. Amide proton transfer imaging of adult diffuse gliomas: Correlation with histopathological grades. *Neuro Oncol*. 2014;16(3):441-448. doi:10.1093/neuonc/not158
 54. Zhang J, Zhu W, Tain R, Zhou XJ, Cai K. Improved Differentiation of Low-Grade and High-Grade Gliomas and Detection of Tumor Proliferation Using APT Contrast Fitted from Z-Spectrum. *Mol Imaging Biol*. 2018;20(4):623-631. doi:10.1007/s11307-017-1154-y
 55. Jiang S, Wen Z, Ahn SS, et al. Applications of chemical exchange saturation transfer magnetic resonance imaging

- in identifying genetic markers in gliomas. *NMR Biomed.* 2023;36(6):1-15. doi:10.1002/nbm.4731
56. Su C, Xu S, Lin D, et al. Multi-parametric Z-spectral MRI may have a good performance for glioma stratification in clinical patients. *Eur Radiol.* Published online 2021. doi:10.1007/s00330-021-08175-3
 57. Warnert EAH, Wood TC, Incekara F, et al. Mapping tumour heterogeneity with pulsed 3D CEST MRI in non-enhancing glioma at 3 T. *Magnetic Resonance Materials in Physics, Biology and Medicine.* 2021;(0123456789). doi:10.1007/s10334-021-00911-6
 58. Jiang S, Eberhart CG, Lim M, et al. Identifying recurrent malignant glioma after treatment using amide proton transfer-weighted MR imaging: A validation study with image-guided stereotactic biopsy. *Clinical Cancer Research.* 2019;25(2):552-561. doi:10.1158/1078-0432.CCR-18-1233
 59. Zhou J, Zaiss M, Knutsson L, et al. Review and consensus recommendations on clinical APT-weighted imaging approaches at 3T: Application to brain tumors. *Magn Reson Med.* 2022;88(2):546-574. doi:10.1002/mrm.29241
 60. Herz K, Lindig T, Deshmane A, et al. T1 ρ -based dynamic glucose-enhanced (DGE ρ) MRI at 3 T: method development and early clinical experience in the human brain. *Magn Reson Med.* 2019;82(5):1832-1847. doi:10.1002/mrm.27857
 61. Mccicar N, Li AX, Meakin SO, Bartha R. Imaging chemical exchange saturation transfer (CEST) effects following tumor-selective acidification using Iodidamine. *NMR Biomed.* 2015;28(5):566-575. doi:10.1002/nbm.3287
 62. Yao J, Tan CHP, Schlossman J, et al. pH-weighted amine chemical exchange saturation transfer echoplanar imaging (CEST-EPI) as a potential early biomarker for bevacizumab failure in recurrent glioblastoma. *J Neurooncol.* 2019;142(3):587-595. doi:10.1007/s11060-019-03132-z
 63. Cai K, Singh A, Poptani H, et al. CEST signal at 2ppm (CEST at 2ppm) from Z-spectral fitting correlates with creatine distribution in brain tumor. *NMR Biomed.* 2015;28(1):1-8. doi:10.1002/nbm.3216
 64. Cai K, Tain RW, Zhou XJ, et al. Creatine CEST MRI for Differentiating Gliomas with Different Degrees of Aggressiveness. *Mol Imaging Biol.* 2017;19(2):225-232. doi:10.1007/s11307-016-0995-0
 65. Dou W, Lin CYE, Ding H, et al. Chemical exchange saturation transfer magnetic resonance imaging and its main and potential applications in pre-clinical and clinical studies. *Quant Imaging Med Surg.* 2019;9(10):1747-1766. doi:10.21037/qims.2019.10.03
 66. Khlebnikov V, van der Kemp WJM, Hoogduin H, Klomp DWJ, Prompers JJ. Analysis of chemical exchange saturation transfer contributions from brain metabolites to the Z-spectra at various field strengths and pH. *Sci Rep.* 2019;9(1):1-11. doi:10.1038/s41598-018-37295-y
 67. Zhou J. Amide Proton Transfer Imaging of the Human Brain. *Methods Mol Biol.* 2011;711(711):227-237. doi:10.1007/978-1-61737-992-5_10
 68. Xu X, Yadav NN, Zeng H, et al. Magnetization transfer contrast-suppressed imaging of amide proton transfer and relayed nuclear overhauser enhancement chemical exchange saturation transfer effects in the human brain at 7T. *Magn Reson Med.* 2016;75(1):88-96. doi:10.1002/mrm.25990
 69. Xu J, Yadav NN, Bar-Shir A, et al. Variable delay multi-pulse train for fast chemical exchange saturation transfer and relayed-nuclear overhauser enhancement MRI. *Magn Reson Med.* 2014;71(5):1798-1812. doi:10.1002/mrm.24850
 70. Haris M, Nanga RPR, Singh A, et al. Exchange rates of creatine kinase metabolites: Feasibility of imaging creatine by chemical exchange saturation transfer MRI. *NMR Biomed.* 2012;25(11):1305-1309. doi:10.1002/nbm.2792
 71. Zhou J, Payen JF, Wilson DA, Traystman RJ, Van Zijl PCM. Using the amide proton signals of intracellular proteins and peptides to detect pH effects in MRI. *Nat Med.* 2003;9(8):1085-1090. doi:10.1038/nm907
 72. Heo HY, Han Z, Jiang S, Schär M, van Zijl PCM, Zhou J. Quantifying amide proton exchange rate and concentration in chemical exchange saturation transfer imaging of the human brain. *Neuroimage.* 2019;189(December 2017):202-213. doi:10.1016/j.neuroimage.2019.01.034

73. Xu J, Chan K W Y, Xu X, Yadav N, Liu G, van Zijl P C M. On-resonance variable delay multipulse scheme for imaging of fast-exchanging protons and semisolid macromolecules. *Magn Reson Med*. 2017;77(2):730-739. doi:10.1002/mrm.26165
74. Chen L, Xu X, Zeng H, et al. Separating fast and slow exchange transfer and magnetization transfer using off-resonance variable-delay multiple-pulse (VDMP) MRI. *Magn Reson Med*. 2018;80(4):1568-1576. doi:10.1002/mrm.27111
75. Dortch R D, Moore J, Li K, et al. Quantitative magnetization transfer imaging of human brain at 7T. *Neuroimage*. 2013;64(1):640-649. doi:10.1016/j.neuroimage.2012.08.047
76. Nehrke K, Börnert P. DREAM-a novel approach for robust, ultrafast, multislice B1 mapping. *Magn Reson Med*. 2012;68(5):1517-1526. doi:10.1002/mrm.24158
77. Lin E C, Li H, Zu Z, et al. Chemical exchange rotation transfer (CERT) on human brain at 3 Tesla. *Magn Reson Med*. 2018;80(6):2609-2617. doi:10.1002/mrm.27365
78. Smith S M. Fast robust automated brain extraction. *Hum Brain Mapp*. 2002;17(3):143-155. doi:10.1002/hbm.10062
79. Zhang Y, Brady M, Smith S. Segmentation of brain MR images through a hidden Markov random field model and the expectation-maximization algorithm. *IEEE Trans Med Imaging*. 2001;20(1):45-57. doi:10.1109/42.906424
80. Reuter M, Schmansky N J, Rosas H D, Fischl B. Within-subject template estimation for unbiased longitudinal image analysis. *Neuroimage*. 2012;61(4):1402-1418. doi:10.1016/j.neuroimage.2012.02.084
81. Windschuh J, Zaiss M, Meissner J E, et al. Correction of B1-inhomogeneities for relaxation-compensated CEST imaging at 7T. *NMR Biomed*. 2015;28(5):529-537. doi:10.1002/nbm.3283
82. Shu Z, Xu Y, Shao Y, Pang P, Gong X. Radiomics from magnetic resonance imaging may be used to predict the progression of white matter hyperintensities and identify associated risk factors. *Eur Radiol*. 2020;30(6):3046-3058. doi:10.1007/s00330-020-06676-1
83. Chen L, Xu X, Zeng H, et al. Separating fast and slow exchange transfer and magnetization transfer using off-resonance variable-delay multiple-pulse (VDMP) MRI. *Magn Reson Med*. 2018;80(4):1568-1576. doi:10.1002/mrm.27111
84. Lee J S, Xia D, Jerschow A, Regatte R R. In vitro study of endogenous CEST agents at 3T and 7T. *Contrast Media Mol Imaging*. 2016;11(1):4-14. doi:10.1002/cmml.1652
85. Jones C K, Huang A, Xu J, et al. Nuclear Overhauser enhancement (NOE) imaging in the human brain at 7T. *Neuroimage*. 2013;77:114-124. doi:10.1016/j.neuroimage.2013.03.047
86. Khlebnikov V, Polders D, Hendrikse J, et al. Amide proton transfer (APT) imaging of brain tumors at 7 T: The role of tissue water T1-Relaxation properties. *Magn Reson Med*. 2017;77(4):1525-1532. doi:10.1002/mrm.26232
87. Paech D, Dreher C, Regnery S, et al. Relaxation-compensated amide proton transfer (APT) MRI signal intensity is associated with survival and progression in high-grade glioma patients. *Eur Radiol*. 2019;29(9):4957-4967. doi:10.1007/s00330-019-06066-2
88. Cai K, Haris M, Singh A, et al. Magnetic Resonance Imaging of Glutamate. *Nat Med*. 2012;18(2):302-306. doi:10.1038/nm.2615. Magnetic
89. Singh A, Debnath A, Cai K, et al. Evaluating the feasibility of creatine-weighted CEST MRI in human brain at 7 T using a Z-spectral fitting approach. *NMR Biomed*. 2019;32(12):1-18. doi:10.1002/nbm.4176
90. Cai K, Singh A, Roalf D R, et al. Mapping glutamate in subcortical brain structures using high-resolution GluCEST MRI. *NMR Biomed*. 2013;26(10):1278-1284. doi:10.1002/nbm.2949
91. Khlebnikov V, Windschuh J, Siero J C W, et al. On the transmit field inhomogeneity correction of relaxation-compensated amide and NOE CEST effects at 7 T. *NMR Biomed*. 2017;30(5):1-10. doi:10.1002/nbm.3687
92. Cui J, Zu Z. Towards the molecular origin of glutamate CEST (GluCEST) imaging in rat brain. *Magn Reson Med*. 2020;83(4):1405-1417. doi:10.1002/mrm.28021

93. Haris M, Nanga RPR, Singh A, et al. Exchange rates of creatine kinase metabolites: Feasibility of imaging creatine by chemical exchange saturation transfer MRI. *NMR Biomed.* 2012;25(11):1305-1309. doi:10.1002/nbm.2792
94. Kogan F, Harris M, DeBrosse C, et al. In vivo CEST imaging of Creatine (CrCEST) in Skeletal Muscle at 3T. *Journal of Magnetic Resonance Imaging.* 2014;40(3):596-602. doi:10.1002/jmri.24412.In
95. Kogan F, Haris M, Singh A, et al. Method for high-resolution imaging of creatine in vivo using chemical exchange saturation transfer. *Magn Reson Med.* 2014;71(1):164-172. doi:10.1002/mrm.24641
96. Davis KA, Nanga RPR, Das S, et al. Glutamate imaging (GluCEST) lateralizes epileptic foci in nonlesional temporal lobe epilepsy. *Sci Transl Med.* 2015;7(309):1-8. doi:10.1126/scitranslmed.aaa7095
97. Cai K, Tain R wen, Zhou XJ, et al. Degrees of Aggressiveness. 2018;19(2):225-232. doi:10.1007/s11307-016-0995-0. Creatine
98. Goerke S, Zaiss M, Bachert P. Characterization of creatine guanidinium proton exchange by water-exchange (WEX) spectroscopy for absolute-pH CEST imaging in vitro. *NMR Biomed.* 2014;27(5):507-518. doi:10.1002/nbm.3086
99. Zhang Z, Wang K, Park S, et al. The exchange rate of creatine CEST in mouse brain. *Magn Reson Med.* 2023;(March):1-12. doi:10.1002/mrm.29662
100. Zaiss, Moritz, Zu, Zhongliang, Xu, Junzhong, Schuenke, Patrick, Gochberg, Daniel F., Gore, John C., Ladd, Mark E., and Bachert P. A combined analytical solution for Chemical Exchange Saturation Transfer and semi-solid Magnetization Transfer Moritz. *NMR Biomed.* 2015;28(2):217-230. doi:10.1002/nbm.3237.A
101. Mueller S, Scheffler K, Zaiss M. On the interference from agar in chemical exchange saturation transfer MRI parameter optimization in model solutions. *NMR Biomed.* 2021;34(1):1-12. doi:10.1002/nbm.4403
102. Kim M, Gillen J, Landman BA, Zhou J, Van Zijl PCM. Water saturation shift referencing (WASSR) for chemical exchange saturation transfer (CEST) experiments. *Magn Reson Med.* 2009;61(6):1441-1450. doi:10.1002/mrm.21873
103. Teeuwisse WM, Brink WM, Webb AG. Quantitative assessment of the effects of high-permittivity pads in 7 Tesla MRI of the brain. *Magn Reson Med.* 2012;67(5):1285-1293. doi:10.1002/mrm.23108
104. O'Reilly TPA, Webb AG, Brink WM. Practical improvements in the design of high permittivity pads for dielectric shimming in neuroimaging at 7 T. *Journal of Magnetic Resonance.* 2016;270:108-114. doi:10.1016/j.jmr.2016.07.003
105. Singh A, Cai K, Haris M, Hariharan H, Reddy R. On B1 inhomogeneity correction of in vivo human brain glutamate chemical exchange saturation transfer contrast at 7T. *Magn Reson Med.* 2013;69(3):818-824. doi:10.1002/mrm.24290
106. Zaiss M, Windschuh J, Paech D, et al. Relaxation-compensated CEST-MRI of the human brain at 7T: Unbiased insight into NOE and amide signal changes in human glioblastoma. *Neuroimage.* 2015;112:180-188. doi:10.1016/j.neuroimage.2015.02.040
107. Provencher SW. Estimation of metabolite concentrations from localized in vivo proton NMR spectra. *Magn Reson Med.* 1993;30(6):672-679. doi:10.1002/mrm.1910300604
108. Simpson R, Devenyi GA, Jezzard P, Hennessy TJ, Near J. Advanced processing and simulation of MRS data using the FID appliance (FID-A)—An open source, MATLAB-based toolkit. *Magn Reson Med.* 2017;77(1):23-33. doi:10.1002/mrm.26091
109. Marjańska M, Auerbach EJ, Valabrègue R, Van de Moortele PF, Adriany G, Garwood M. Localized ¹H NMR spectroscopy in different regions of human brain in vivo at 7T: T₂ relaxation times and concentrations of cerebral metabolites. *NMR Biomed.* 2012;25(2):332-339. doi:10.1002/nbm.1754
110. Neal A, Moffat BA, Stein JM, et al. Glutamate weighted imaging contrast in gliomas with 7 Tesla magnetic resonance imaging. *Neuroimage Clin.* 2019;22(January):101694. doi:10.1016/j.nicl.2019.101694

111. Davis KA, Nanga RPR, Das S, et al. Glutamate imaging (GluCEST) lateralizes epileptic foci in nonlesional temporal lobe epilepsy. *Sci Transl Med*. 2015;7(309):1-19. doi:10.1126/scitranslmed.aaa7095
112. Lucas A, Nanga RPR, Hadar P, et al. Mapping hippocampal glutamate in mesial temporal lobe epilepsy with glutamate weighted CEST (GluCEST) imaging. *Hum Brain Mapp*. 2022;(May 2022):549-558. doi:10.1002/hbm.26083
113. W A Belitzer KSG. PHOSPHATE ACCEPTORS IN "RESPIRA- TORY PHOSPHORYLATION" IN MUSCLE TISSUE. 1940;92(2397):536-537.
114. Li X, Lu Y, Pirzkall A, McKnight T, Nelson SJ. Analysis of the spatial characteristics of metabolic abnormalities in newly diagnosed glioma patients. *Journal of Magnetic Resonance Imaging*. 2002;16(3):229-237. doi:10.1002/jmri.10147
115. Cai K, Haris M, Singh A, et al. Magnetic resonance imaging of glutamate. *Nat Med*. 2012;18(2):302-306. doi:10.1038/nm.2615
116. Schuff N, Ezekiel F, Gamst AC, et al. Region and tissue differences of metabolites in normally aged brain using multislice 1H magnetic resonance spectroscopic imaging. *Magn Reson Med*. 2001;45(5):899-907. doi:10.1002/mrm.1119
117. Zhang XY, Xie J, Wang F, et al. Assignment of the molecular origins of CEST signals at 2 ppm in rat brain. *Magn Reson Med*. 2017;78(3):881-887. doi:10.1002/mrm.26802
118. Xu J, Chung JJ, Jin T. Chemical exchange saturation transfer imaging of creatine, phosphocreatine, and protein arginine residue in tissues. *NMR Biomed*. 2023;36(6):1-37. doi:10.1002/nbm.4671
119. Duarte JMN, Lei H, Mlynárik V, Gruetter R. The neurochemical profile quantified by in vivo 1H NMR spectroscopy. *Neuroimage*. 2012;61(2):342-362. doi:10.1016/j.neuroimage.2011.12.038
120. Cai K, Singh A, Roalf DR, et al. Mapping glutamate in subcortical brain structures using high-resolution GluCEST MRI. *NMR Biomed*. 2013;26(10):1278-1284. doi:10.1002/nbm.2949
121. Zaiß M, Schmitt B, Bachert P. Quantitative separation of CEST effect from magnetization transfer and spillover effects by Lorentzian-line-fit analysis of z-spectra. *Journal of Magnetic Resonance*. 2011;211(2):149-155. doi:10.1016/j.jmr.2011.05.001
122. Schmitz-Abecassis B, Vinogradov E, Wijnen JP, et al. The use of variable delay multipulse chemical exchange saturation transfer for separately assessing different CEST pools in the human brain at 7T. *Magn Reson Med*. 2022;87(2):872-883. doi:10.1002/mrm.29005
123. Zhang XY, Wang F, Li H, et al. Accuracy in the quantification of chemical exchange saturation transfer (CEST) and relayed nuclear Overhauser enhancement (rNOE) saturation transfer effects. *NMR Biomed*. 2017;30(7):1-14. doi:10.1002/nbm.3716
124. Cember ATJ, Nanga RPR, Reddy R. Glutamate weighted CEST (gluCEST) imaging for mapping neurometabolism: An update on the state of the art and emerging findings from in vivo applications . *NMR Biomed*. 2022;(November 2021):1-21. doi:10.1002/nbm.4780
125. Chung JJ, Jin T, Lee JH, Kim SG. Chemical exchange saturation transfer imaging of phosphocreatine in the muscle. *Magn Reson Med*. 2019;81(6):3476-3487. doi:10.1002/mrm.27655
126. Chen L, Zeng H, Xu X, et al. Investigation of the contribution of total creatine to the CEST Z-spectrum of brain using a knockout mouse model. *NMR Biomed*. 2018;30(12):1-24. doi:10.1002/nbm.3834. Investigation
127. Chen L, Barker PB, Weiss RG, et al. Creatine and phosphocreatine mapping of mouse skeletal muscle by a polynomial and Lorentzian line-shape fitting CEST method. *Magn Reson Med*. 2019;81(1):69-78. doi:10.1002/mrm.27514. Creatine
128. Wermter FC, Bock C, Dreher W. Investigating GluCEST and its specificity for pH mapping at low temperatures. *NMR Biomed*. 2015;28(11):1507-1517. doi:10.1002/nbm.3416

129. Kakimoto A, Ito S, Okada H, Nishizawa S, Minoshima S, Ouchi Y. Age-related sex-specific changes in brain metabolism and morphology. *Journal of Nuclear Medicine*. 2016;57(2):221-225. doi:10.2967/jnumed.115.166439
130. Cui J, Afzal A, Zu Z. Comparative evaluation of polynomial and Lorentzian lineshape-fitted amine CEST imaging in acute ischemic stroke. *Magn Reson Med*. 2022;87(2):837-849. doi:10.1002/mrm.29030
131. Lingl JP, Wunderlich A, Goerke S, et al. The Value of APTw CEST MRI in Routine Clinical Assessment of Human Brain Tumor Patients at 3T. *Diagnostics*. 2022;12(2):1-11. doi:10.3390/diagnostics12020490
132. Zaiss M, Windschuh J, Paech D, et al. Relaxation-compensated CEST-MRI of the human brain at 7T: Unbiased insight into NOE and amide signal changes in human glioblastoma. *Neuroimage*. 2015;112:180-188. doi:10.1016/j.neuroimage.2015.02.040
133. Mancini L, Casagrande S, Gautier G, et al. CEST MRI provides amide/amine surrogate biomarkers for treatment-naïve glioma sub-typing. *Eur J Nucl Med Mol Imaging*. 2022;(0123456789). doi:10.1007/s00259-022-05676-1
134. Groothuis DR, Vick NA. Brain tumors and the blood-brain barrier. *Trends Neurosci*. 1982;5(C):232-235. doi:10.1016/0166-2236(82)90134-5
135. Kanda T, Ishii K, Kawaguchi H, Kitajima K, Takenaka D. High signal intensity in the dentate nucleus and globus pallidus on unenhanced T1-weighted MR images: Relationship with increasing cumulative dose of a gadolinium-based contrast material. *Radiology*. 2014;270(3):834-841. doi:10.1148/radiol.13131669
136. Scott JN, Brasher PMA, Sevic RJ, Newcastle NB, Forsyth PA. How often are nonenhancing supratentorial gliomas malignant? A population study. *Neurology*. 2002;59(6):947-949. doi:10.1212/WNL.59.6.947
137. 137. Dao Trong P, Kilian S, Jesser J, et al. Risk Estimation in Non-Enhancing Glioma: Introducing a Clinical Score. *Cancers (Basel)*. 2023;15(9):1-14. doi:10.3390/cancers15092503
138. Zaiss M, Xu J, Goerke S, et al. Inverse Z-spectrum analysis for spillover-, MT-, and T1-corrected steady-state pulsed CEST-MRI - application to pH-weighted MRI of acute stroke. *NMR Biomed*. 2014;27(3):240-252. doi:10.1002/nbm.3054
139. Schmitz-Abecassis B, Najac C, Plugge J, van Osch MJ, Ercan E. Investigation of metabolite correlates of CEST in the human brain at 7 T. *NMR Biomed*. 2024;37(5):1-13. doi:10.1002/nbm.5104
140. Lupo JM, Cha S, Chang SM, Nelson SJ. Analysis of metabolic indices in regions of abnormal perfusion in patients with high-grade glioma. *American Journal of Neuroradiology*. 2007;28(8):1455-1461. doi:10.3174/ajnr.A0586
141. Park S, Rintaro H, Kim SK, Park I. Characterization of distinctive in vivo metabolism between enhancing and non-enhancing gliomas using hyperpolarized carbon-13 mri. *Metabolites*. 2021;11(8). doi:10.3390/metabo11080504
142. Hattingen E, Raab P, Franz K, et al. Prognostic value of choline and creatine in WHO grade II gliomas. *Neuroradiology*. 2008;50(9):759-767. doi:10.1007/s00234-008-0409-3
143. Avalos LN, Luks TL, Gleason T, et al. Longitudinal MR spectroscopy to detect progression in patients with lower-grade glioma in the surveillance phase. *Neurooncol Adv*. 2022;4(1):1-9. doi:10.1093/noajnl/vdac175
144. Howe FA, Barton SJ, Cudlip SA, et al. Metabolic profiles of human brain tumors using quantitative in vivo ¹H magnetic resonance spectroscopy. *Magn Reson Med*. 2003;49(2):223-232. doi:10.1002/mrm.10367
145. Hangel G, Cadrien C, Lazen P, et al. High-resolution metabolic imaging of high-grade gliomas using 7T-CRT-FID-MRSI. *Neuroimage Clin*. 2020;28(May):102433. doi:10.1016/j.nicl.2020.102433
146. Wang K, Ju L, Song Y, et al. Whole-cerebrum guanidino and amide CEST mapping at 3 T by a 3D stack-of-spirals gradient echo acquisition. *Magn Reson Med*. 2024;92(4):1456-1470. doi:10.1002/mrm.30134
147. Wang K, Huang J, Ju L, et al. Creatine mapping of the brain at 3T by CEST MRI. *Magn Reson Med*. 2024;91(1):51-60. doi:10.1002/mrm.29876
148. Chen Z, Han F, Du Y, Shi H, Zhou W. Hypoxic microenvironment in cancer: molecular mechanisms and therapeutic interventions. *Signal Transduct Target Ther*. 2023;8(1). doi:10.1038/s41392-023-01332-8
149. Harris RJ, Cloughesy TF, Liau LM, et al. PH-weighted molecular imaging of gliomas using amine chemical

- exchange saturation transfer MRI. *Neuro Oncol.* 2015;17(11):1514-1524. doi:10.1093/neuonc/nov106
150. Osborn AG, Louis DN, Poussaint TY, Linscott LL, Salzman KL. The 2021 World Health Organization Classification of Tumors of the Central Nervous System: What Neuroradiologists Need to Know. *American Journal of Neuroradiology.* 2022;43(7):928-937. doi:10.3174/ajnr.A7462
 151. D'Abaco GM, Kaye AH. Integrins: Molecular determinants of glioma invasion. *Journal of Clinical Neuroscience.* 2007;14(11):1041-1048. doi:10.1016/j.jocn.2007.06.019
 152. Giese A, Kluwe L, Laube B, Meissner H, Berens ME, Westphal M. Migration of Human Glioma Cells on Myelin. *Neurosurgery.* Published online 1996:755-764. doi:10.1097/00006123-199604000-00026
 153. Ellingson BM, Bendszus M, Boxerman J, et al. Consensus recommendations for a standardized Brain Tumor Imaging Protocol in clinical trials. *Neuro Oncol.* 2015;17(9):1188-1198. doi:10.1093/neuonc/nov095
 154. Bernstock JD, Gary SE, Klinger N, et al. Standard clinical approaches and emerging modalities for glioblastoma imaging. *Neurooncol Adv.* 2022;4(1):1-19. doi:10.1093/oaajnl/vdac080
 155. Verma G, Balchandani P. Ultrahigh field MR Neuroimaging. *Topics in Magnetic Resonance Imaging.* 2019;28(3):137-144. doi:10.1097/RMR.0000000000000210
 156. Verma N, Cowperthwaite MC, Burnett MG, Markey MK. Differentiating tumor recurrence from treatment necrosis: A review of neuro-oncologic imaging strategies. *Neuro Oncol.* 2013;15(5):515-534. doi:10.1093/neuonc/nos307
 157. Morrison MA, Lupo JM. 7-T Magnetic Resonance Imaging in the Management of Brain Tumors. *Magnetic Resonance Imaging Clinics of NA.* 2021;29(1):83-102. doi:10.1016/j.mric.2020.09.007
 158. Keller JA, Sigurdsson S, Klaassen K, et al. White matter hyperintensity shape is associated with long-term dementia risk. *Alzheimer's and Dementia.* 2023;(November 2022):5632-5641. doi:10.1002/alz.13345
 159. Kant IMJ, Mutsaerts HJMM, van Montfort SJT, et al. The association between frailty and MRI features of cerebral small vessel disease. *Sci Rep.* 2019;9(1):1-9. doi:10.1038/s41598-019-47731-2
 160. Kollia K, Maderwald S, Putzki N, et al. First clinical study on ultra-high-field MR imaging in patients with multiple sclerosis: Comparison of 1.5T and 7T. *American Journal of Neuroradiology.* 2009;30(4):699-702. doi:10.3174/ajnr.A1434
 161. Chalfoux JR, Y NP, Katz JS, et al. The ability of high field strength 7-T magnetic resonance imaging to reveal previously uncharacterized brain lesions in patients with tuberous sclerosis complex. *J Neurosurg Pediatr.* 2013;11(3):268-273. doi:10.3171/2012.12.PEDS12338
 162. Maruyama S, Fukunaga M, Fautz HP, Heidemann R, Sadato N. Comparison of 3T and 7T MRI for the visualization of globus pallidus sub-segments. *Sci Rep.* 2019;9(1):1-8. doi:10.1038/s41598-019-54880-x
 163. Zwanenburg JJM, Hendrikse J, Visser F, Takahara T, Luijten PR. Fluid attenuated inversion recovery (FLAIR) MRI at 7.0 Tesla: Comparison with 1.5 and 3.0 Tesla. *Eur Radiol.* 2010;20(4):915-922. doi:10.1007/s00330-009-1620-2
 164. Xia L, Fang C, Chen G, Sun C. Relationship between the extent of resection and the survival of patients with low-grade gliomas: A systematic review and meta-analysis. *BMC Cancer.* 2018;18(1):1-10. doi:10.1186/s12885-017-3909-x
 165. Louis DN, Perry A, Wesseling P, et al. The 2021 WHO Classification of Tumors of the Central Nervous System: a summary. *Neuro Oncol.* 2021;23(8):1231-1251. doi:10.1093/neuonc/noab106
 166. Sheikh S, Radivoyevitch T, Barnholtz-Sloan JS, Vogelbaum M. Long-term trends in glioblastoma survival: Implications for historical control groups in clinical trials. *Neurooncol Pract.* 2020;7(2):158-163. doi:10.1093/nop/npz046
 167. Fatterpekar GM, Galheigo D, Narayana A, Johnson G, Knopp E. Treatment-related change versus tumor recurrence in high-grade gliomas: A diagnostic conundrum - Use of dynamic susceptibility contrast-enhanced (DSC) perfusion MRI. *American Journal of Roentgenology.* 2012;198(1):19-26. doi:10.2214/AJR.11.7417

168. Hansen MR, Pan E, Wilson A, et al. Post-gadolinium 3-dimensional spatial, surface, and structural characteristics of glioblastomas differentiate pseudoprogression from true tumor progression. *J Neurooncol.* 2018;139(3):731-738. doi:10.1007/s11060-018-2920-7
169. Gladwish A, Koh ES, Hoisak J, et al. Evaluation of early imaging response criteria in glioblastoma multiforme. *Radiation Oncology.* 2011;6(1):1-7. doi:10.1186/1748-717X-6-121
170. Abel R, Jones J, Mandelin P, Cen S, Pagnini P. Distinguishing Pseudoprogression From True Progression by FLAIR Volumetric Characteristics Compared to 45 Gy Isodose Volumes in Treated Glioblastoma Patients. *International Journal of Radiation Oncology*Biophysics.* 2012;84(3):S275. doi:10.1016/j.ijrobp.2012.07.716
171. Le Fèvre C, Constans JM, Chambrelant I, et al. Pseudoprogression versus true progression in glioblastoma patients: A multiapproach literature review. Part 2 – Radiological features and metric markers. *Crit Rev Oncol Hematol.* 2021;159(January). doi:10.1016/j.critrevonc.2021.103230
172. Wang YL, Chen S, Xiao HF, et al. Differentiation between radiation-induced brain injury and glioma recurrence using 3D pCASL and dynamic susceptibility contrast-enhanced perfusion-weighted imaging. *Radiotherapy and Oncology.* 2018;129(1):68-74. doi:10.1016/j.radonc.2018.01.009
173. Ye J, Bhagat SK, Li H, et al. Differentiation between recurrent gliomas and radiation necrosis using arterial spin labeling perfusion imaging. *Exp Ther Med.* 2016;11(6):2432-2436. doi:10.3892/etm.2016.3225
174. Choi YJ, Kim HS, Jahng GH, Kim SJ, Suh DC. Pseudoprogression in patients with glioblastoma: added value of arterial spin labeling to dynamic susceptibility contrast perfusion MR imaging. *Acta radiol.* 2013;54(4):448-454. doi:10.1177/0284185112474916
175. Rau MK, Braun C, Skardelly M, et al. Prognostic value of blood flow estimated by arterial spin labeling and dynamic susceptibility contrast-enhanced MR imaging in high-grade gliomas. *J Neurooncol.* 2014;120(3):557-566. doi:10.1007/s11060-014-1586-z
176. Ozsunar Y, Mullins ME, Kwong K, et al. Glioma Recurrence Versus Radiation Necrosis?. A Pilot Comparison of Arterial Spin-Labeled, Dynamic Susceptibility Contrast Enhanced MRI, and FDG-PET Imaging. *Acad Radiol.* 2010;17(3):282-290. doi:10.1016/j.acra.2009.10.024
177. Manning P, Daghighi S, Rajaratnam MK, et al. Differentiation of progressive disease from pseudoprogression using 3D PCASL and DSC perfusion MRI in patients with glioblastoma. *J Neurooncol.* 2020;147(3):681-690. doi:10.1007/s11060-020-03475-y
178. Chen X, Wei X, Zhang Z, Yang R, Zhu Y, Jiang X. Differentiation of true-progression from pseudoprogression in glioblastoma treated with radiation therapy and concomitant temozolomide by GLCM texture analysis of conventional MRI. *Clin Imaging.* 2015;39(5):775-780. doi:10.1016/j.clinimag.2015.04.003
179. Yan JL, Toh CH, Ko L, Wei KC, Chen PY. A neural network approach to identify glioblastoma progression phenotype from multimodal mri. *Cancers (Basel).* 2021;13(9):1-9. doi:10.3390/cancers13092006
180. Shim KY, Chung SW, Jeong JH, et al. Radiomics-based neural network predicts recurrence patterns in glioblastoma using dynamic susceptibility contrast-enhanced MRI. *Sci Rep.* 2021;11(1):1-14. doi:10.1038/s41598-021-89218-z
181. Kim JY, Yoon MJ, Park JE, Choi EJ, Lee J, Kim HS. Radiomics in peritumoral non-enhancing regions: fractional anisotropy and cerebral blood volume improve prediction of local progression and overall survival in patients with glioblastoma. *Neuroradiology.* 2019;61(11):1261-1272. doi:10.1007/s00234-019-02255-4
182. Hashido T, Saito S, Ishida T. A radiomics-based comparative study on arterial spin labeling and dynamic susceptibility contrast perfusion-weighted imaging in gliomas. *Sci Rep.* 2020;10(1):1-10. doi:10.1038/s41598-020-62658-9
183. Sudre CH, Panovska-Griffiths J, Sanverdi E, et al. Machine learning assisted DSC-MRI radiomics as a tool for glioma classification by grade and mutation status. *BMC Med Inform Decis Mak.* 2020;20(1):1-14. doi:10.1186/s12911-020-01163-5

184. Jaarsma-Coes MG, Ghaznawi R, Hendrikse J, et al. MRI phenotypes of the brain are related to future stroke and mortality in patients with manifest arterial disease: The SMART-MR study. *Journal of Cerebral Blood Flow and Metabolism*. 2020;40(2):354-364. doi:10.1177/0271678X18818918
185. Le Fèvre C, Sun R, Cebula H, et al. Ellipsoid calculations versus manual tumor delineations for glioblastoma tumor volume evaluation. *Sci Rep*. 2022;12(1):1-9. doi:10.1038/s41598-022-13739-4
186. Schwartz LH, Colville JAC, Ginsberg MS, et al. Measuring tumor response and shape change on CT: Esophageal cancer as a paradigm. *Annals of Oncology*. 2006;17(6):1018-1023. doi:10.1093/annonc/mdl058
187. Van Osch MJP, Teeuwisse WM, Van Walderveen MAA, Hendrikse J, Kies DA, Van Buchem MA. Can arterial spin labeling detect white matter perfusion signal? *Magn Reson Med*. 2009;62(1):165-173. doi:10.1002/mrm.22002
188. Charrad M, Ghazzali N, Boiteau V, Niknafs A. Nbclust: An R package for determining the relevant number of clusters in a data set. *J Stat Softw*. 2014;61(6):1-36. doi:10.18637/jss.v061.i06
189. Kassambara A. Package "factoextra": Extract and Visualize the Results of Multivariate Data Analyses for R. Published online 2020.
190. Rousseeuw P, Struyf A, Hubert M, Studer M, Roudier P. "Finding Groups in Data": Cluster Analysis Extended." Published online 2022.
191. Galili T. dendextend: An R package for visualizing, adjusting and comparing trees of hierarchical clustering. *Bioinformatics*. 2015;31(22):3718-3720. doi:10.1093/bioinformatics/btv428
192. Pallud J, Capelle L, Taillandier L, et al. Prognostic significance of imaging contrast enhancement for WHO grade II gliomas. *Neuro Oncol*. 2009;11(2):176-182. doi:10.1215/15228517-2008-066
193. Curtin L, Whitmire P, White H, et al. Shape matters: morphological metrics of glioblastoma imaging abnormalities as biomarkers of prognosis. *Sci Rep*. 2021;11(1):1-11. doi:10.1038/s41598-021-02495-6
194. Kant IMJ, Slooter AJC, Jaarsma-Coes M, et al. Preoperative MRI brain phenotypes are related to postoperative delirium in older individuals. *Neurobiol Aging*. 2021;101:247-255. doi:10.1016/j.neurobiolaging.2021.01.033
195. Shieh LT, Ho CH, Guo HR, Huang CC, Ho YC, Ho SY. Epidemiologic Features, Survival, and Prognostic Factors Among Patients With Different Histologic Variants of Glioblastoma: Analysis of a Nationwide Database. *Front Neurol*. 2021;12(November):1-9. doi:10.3389/fneur.2021.659921
196. Palpan Flores A, Vivancos Sanchez C, Roda JM, et al. Assessment of Pre-operative Measurements of Tumor Size by MRI Methods as Survival Predictors in Wild Type IDH Glioblastoma. *Front Oncol*. 2020;10(September):1-12. doi:10.3389/fonc.2020.01662
197. van Dijken BRJ, van Laar PJ, Smits M, Dankbaar JW, Enting RH, van der Hoorn A. Perfusion MRI in treatment evaluation of glioblastomas: Clinical relevance of current and future techniques. *Journal of Magnetic Resonance Imaging*. 2019;49(1):11-22. doi:10.1002/jmri.26306
198. Songtao Q, Lei Y, Si G, et al. IDH mutations predict longer survival and response to temozolomide in secondary glioblastoma. *Cancer Sci*. 2012;103(2):269-273. doi:10.1111/j.1349-7006.2011.02134.x
199. Dula, Adrienne N., Smith, Seth. GCJ. Application of Chemical Exchange Saturation Transfer (CEST) MRI for Endogenous Contrast at 7 Tesla. *Journal of Neuroimaging*. 2013;23(4):526-532. doi:10.1111/j.1552-6569.2012.00751.x. Application
200. Zhang Z, Wang K, Park S, et al. The exchange rate of creatine CEST in mouse brain. *Magn Reson Med*. 2023;(February):373-384. doi:10.1002/mrm.29662
201. Xu J, Chan K W Y, Xu X, Yadav N, Liu G, Van Zijl PCM. On-resonance Variable Delay Multi Pulse Scheme for Imaging of Fast-exchanging Protons and semi-solid Macromolecules HHS Public Access. *Magn Reson Med*. 2017;77(2):730-739. doi:10.1002/mrm.26165
202. Liu R, Wang X, Zhao Z, et al. A comparative study of quantitative metrics in chemical exchange saturation transfer imaging for grading gliomas in adults. *Magn Reson Imaging*. 2023;96(May 2022):50-59. doi:10.1016/j.

mri.2022.11.008

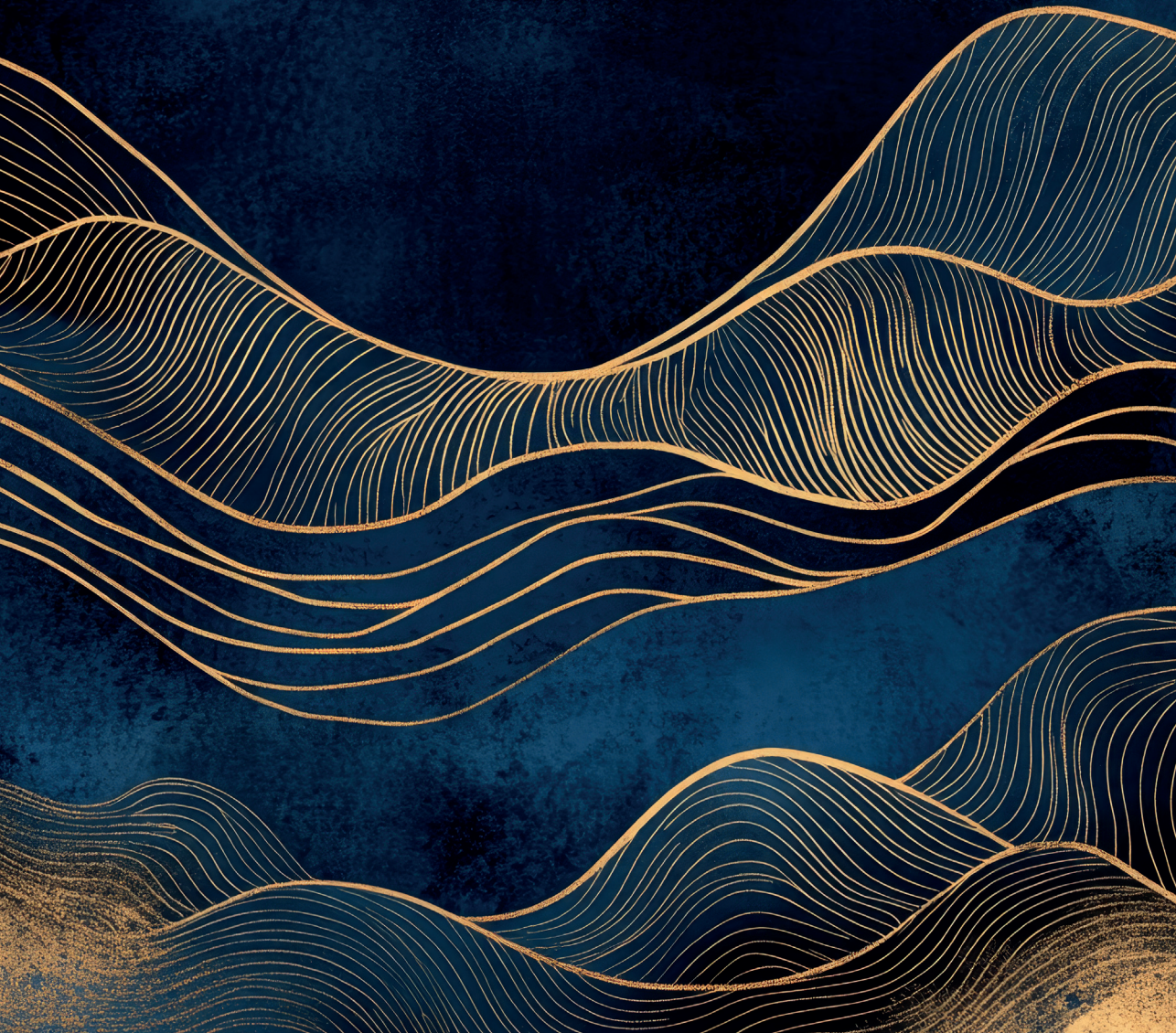
203. Ozturk-Isik E, Pirzkall A, Lamborn KR, Cha S, Chang SM, Nelson SJ. Spatial characteristics of newly diagnosed grade 3 glioma assessed by magnetic resonance metabolic and diffusion tensor imaging. *Transl Oncol.* 2012;5(1):10-18. doi:10.1593/tlo.11208
204. Perera Molligoda Arachchige AS, Meuli S, Centini FR, Stomeo N, Catapano F, Politi LS. Evaluating the role of 7-Tesla magnetic resonance imaging in neurosurgery: Trends in literature since clinical approval. *World J Radiol.* 2024;16(7):274-293. doi:10.4329/wjr.v16.i7.274
205. Voormolen EH, Diederens SJH, Woerdeman P, et al. Implications of Extracranial Distortion in Ultra-High-Field Magnetic Resonance Imaging for Image-Guided Cranial Neurosurgery. *World Neurosurg.* 2019;126:e250-e258. doi:10.1016/j.wneu.2019.02.028
206. Verdugo E, Puerto I, Medina MÁ. An update on the molecular biology of glioblastoma, with clinical implications and progress in its treatment. *Cancer Commun.* 2022;42(11):1083-1111. doi:10.1002/cac2.12361
207. Quartuccio N, Laudicella R, Vento A, et al. The additional value of 18F-FDG PET and MRI in patients with glioma: A review of the literature from 2015 to 2020. *Diagnostics.* 2020;10(6). doi:10.3390/diagnostics10060357

11 List of publications

First author presentations at
international conferences

Acknowledgments

Curriculum Vitae



11.1 List of publications

Schmitz-Abecassis B, Vinogradov E, Wijnen JP, van Harten T, Wiegers EC, Hoogduin H, van Osch MJP, Ercan E. The use of variable delay multipulse chemical exchange saturation transfer for separately assessing different CEST pools in the human brain at 7T. *Magn Reson Med*. 2022;87(2):872-883. doi:10.1002/mrm.29005

Schmitz-Abecassis B, Dirven L, Jiang J, Keller JA, Croese RJL, van Dorth D, Ghaznawi R, Kant IMJ, Taphoorn MJB, van Osch MJP, Koekkoek JAF, de Bresser J. MRI phenotypes of glioblastomas early after treatment are suggestive of overall patient survival. *Neurooncol Adv*. 2023;5(October):1-11. doi:10.1093/noajnl/vdad133

Hangel G, **Schmitz-Abecassis B**, Sollmann N, Pinto J, Arzanforoosh F, Barkhof F, Booth T, Calvo-Imirizaldu M, Cassia G, Chmelik M, Clement P, Ercan E, Fernández-Seara MA, Furtner J, Fuster-Garcia E, Grech-Sollars M, Tugay Guven N, Hale Hatay G, Karami G, Keil VC, Kim M, Koekkoek JA, Kuhran S, Mancini L, Nechifor RE, Özcan A, Ozturk-Isik E, Piskin S, Schmainda KM, Svensson SF, Tseng CH, Unnikrishnan S, Vos F, Warnert E, Zhao MY, Jancalek R, Nunes T, Hirschler L, Smits M, Petr J, Emblem KY. Advanced MR Techniques for Preoperative Glioma Characterization: Part 2. *Journal of Magnetic Resonance Imaging*. Published online 2023. doi:10.1002/jmri.28663 – Only part of this publication is included in the thesis, more specifically the section on Chemical Exchange Saturation Transfer (CEST)

Hirschler L, Sollmann N, **Schmitz-Abecassis B**, Pinto J, Arzanforoosh F, Barkhof F, Booth T, Calvo-Imirizaldu M, Cassia G, Chmelik M, Clement P, Ercan E, Fernández-Seara MA, Furtner J, Guster-Garcia E, Grech-Sollars M, Tugay Guven N, Hale Hatay G, Karami G, Keil VC, Kim M, Koekkoek JAF, Kukran S, Mancini L, Nechifor RE, Özcan A, Ozturk-Isik E. Advanced MR Techniques for Preoperative Glioma Characterization: Part 1. *Journal of Magnetic Resonance Imaging*. Published online 2023:1-21. doi:10.1002/jmri.28662

van Dorth D, Jiang FY, **Schmitz-Abecassis B**, et al. Influence of arterial transit time delays on the differentiation between tumor progression and pseudoprogession in glioblastoma by arterial spin labeling magnetic resonance imaging. *NMR Biomed*. 2024;37(9):1-11. doi:10.1002/nbm.5166

van Dorth D, Croese RJL, Jiang FY, **Schmitz-Abecassis B**, Taphoorn MJB, Smits M, Dirven L, van Osch MJP, de Bresser J, Koekkoek JAF. Perfusion MRI-based differentiation between early tumor progression and pseudoprogession in glioblastoma and its use in clinical practice. *Neuro-Oncology Practice*. 2024;(October):1-10.

Keller JA, Sigurdsson S, **Schmitz Abecassis B**, Kant IMJ, van Buchem MA, Launer LJ, van Osch MJP, Gudnason V, de Bresser J. Identification of Distinct Brain MRI Phenotypes and Their Association With Long-Term Dementia Risk in Community-Dwelling Older Adults. *Neurology*. 2024;102(7):e209176. doi:10.1212/WNL.0000000000209176

Schmitz-Abecassis B, Najac C, Plugge J, van Osch MJP, Ercan E. Investigation of metabolite correlates of CEST in the human brain at 7 T. *NMR Biomed*. 2024;37(5):1-13. doi:10.1002/nbm.5104

Schmitz-Abecassis B, Cornelissen I, Jacobs R, Kuhn-Keller JA, Dirven L, Taphoorn M, van Osch MJP, Koekkoek JA, de Bresser J. Extension of T2 Hyperintense Areas in Patients With a Glioma : A Comparison Between High-Quality 7 T MRI and Clinical Scans. *NMR Biomed*. Published online 2025:1-10. doi:10.1002/nbm.5316

Schmitz-Abecassis B, de Bresser J, Dirven L, Taphoorn MJB, van Osch MJP, Koekkoek JAF, Ercan E. Insights into CEST contrast at 2 ppm in enhancing and non-enhancing lesions from glioma patients scanned at 7T. 2025. *Submitted to NMR in Biomedicine*

11.2 First author presentations at international conferences

Schmitz-Abecassis B, Sakai K, Toyotsuji T, Ota Y, Yamada K. Experience counts! Comparisons of ROI placement strategies for radiomics analysis of gliomas. Poster presentation. 29th Annual Meeting of the International Society for Magnetic Resonance in Medicine, 2020, Online.

Schmitz-Abecassis B, Vinogradov E, Wijnen JP, Hoogduin H, van Osch MJP, Ercan, Ece. Investigating variable delay multi-pulse chemical exchange saturation transfer (VDMP-CEST) effects from phantom and in vivo human brain at 7T. Poster presentation. 12th Annual Meeting of the International Society for Magnetic Resonance in Medicine Benelux chapter, 2020, Arnhem, the Netherlands.

Schmitz-Abecassis B, Vinogradov E, Wijnen JP, van Harten TW, Wiegers E, Hoogduin H, van Osch MJP, Ercan, Ece. Magnetization transfer (MT) removed Variable Delay Multi-Pulse Chemical Exchange Saturation Transfer (VDMP-CEST) imaging of the human brain at 7T. Poster presentation. 37th Annual Meeting of the European Society for Magnetic Resonance in Medicine and Biology, 2020, Online.

Schmitz-Abecassis B, Vinogradov E, Wijnen JP, van Harten TW, Wiegers E, Hoogduin H, van Osch MJP, Ercan, Ece. Magnetization transfer (MT) removed Variable Delay Multi-Pulse Chemical Exchange Saturation Transfer (VDMP-CEST) imaging of the human brain at 7T. Oral presentation. CEST 2020 meeting, 2020, Online.

Schmitz-Abecassis B, Vinogradov E, Wijnen JP, van Harten TW, Wiegers E, Hoogduin H, van Osch MJP, Ercan, Ece. MTC removed and exchange rate differentiated CEST using Variable Delay Multi-Pulse in the human brain at 7T. Poster presentation. 13th Annual Meeting of the International Society for Magnetic Resonance in Medicine Benelux chapter, 2021, Online.

Schmitz-Abecassis B, Vinogradov E, Wijnen JP, van Harten TW, Wiegers E, Hoogduin H, van Osch MJP, Ercan, Ece. Variable Delay Multi-Pulse CEST to evaluate MTC removed CEST pools in the human brain at 7T. Poster presentation. 30th Annual Meeting of the International Society for Magnetic Resonance in Medicine, 2021, Online.

Schmitz-Abecassis B, van Osch MJP, Dirven L, Taphoorn MJB, Koekkoek JAF, de Bresser J. T2 hyperintense regions on MRI in gliomas: a comparison between routine clinical MRI and 7T MRI. Poster presentation, 16th Annual meeting of the European Association of Neuro-Oncology, 2021, Online.

Schmitz-Abecassis B, Koekkoek JAF, de Bresser J, Dirven L, Taphoorn MJB, van Osch MJP, Ercan E. Preliminary investigation of APT- and Glutamate-weighted CEST at 7T for gadolinium-free imaging of high-grade gliomas. Oral presentation. 38th annual meeting of the European Society of Magnetic Resonance in Medicine and Biology, 2021, Online.

Schmitz-Abecassis B, Najac C, de Bresser J, Dirven L, Taphoorn MJB, van Osch MJP, Koekkoek JAF, Ercan E. A preliminary investigation into the contribution of Amines to the CEST contrast at 2 ppm and 3 ppm in glioblastomas at 7T. Poster presentation. 14th Annual Meeting of the International Society for Magnetic Resonance in Medicine Benelux chapter, 2022, Maastricht, the Netherlands.

Schmitz-Abecassis B, Najac C, de Bresser J, Dirven L, Taphoorn MJB, van Osch MJP, Koekkoek JAF, Ercan E. A preliminary investigation into the contribution of Amines to the CEST contrast at 2 ppm and 3 ppm in glioblastomas at 7T. Poster presentation. 31st Annual Meeting of the International Society for Magnetic Resonance in Medicine, 2022, London, United Kingdom.

Schmitz-Abecassis B, Ercan E, de Bresser J, Dirven L, Taphoorn MJB, van Osch MJP, Koekkoek JAF. Amine CEST contrast in gliomas to measure metabolic treatment effect at 7T. Poster presentation. 17th Annual meeting of the European Association of Neuro-Oncology, 2022, Vienna, Austria.

Schmitz-Abecassis B, Najac C, Plugge J, van Osch MJP, Ercan E. Optimization and validation of Creatine- and Glutamate-CEST weighted imaging in the human brain at 7T. Poster presentation. 15th Annual Meeting of the International Society for Magnetic Resonance in Medicine Benelux chapter, 2023, Brussels, Belgium.

Schmitz-Abecassis B, Dirven L, Jiang J, Keller JA, Croese RJJ, van Dorth D, Kant IMJ, Taphoorn MJB, van Osch MJP, Koekkoek JAF, de Bresser B. Brain MRI phenotypes of glioblastomas are suggestive of overall patient survival. Poster presentation. 32nd Annual Meeting of the International Society for Magnetic Resonance in Medicine, 2023, Toronto, Canada.

Schmitz-Abecassis B, Najac C, Plugge J, van Osch MJP, Ercan E. Optimization and validation of metabolite weighted CEST contrast at 7T. Poster presentation. 32nd Annual Meeting of the International Society for Magnetic Resonance in Medicine, 2023, Toronto, Canada.

Schmitz-Abecassis B, Dirven L, Jiang J, Keller JA, Croese RJJ, van Dorth D, Kant IMJ, Taphoorn MJB, van Osch MJP, Koekkoek JAF, de Bresser B. Brain MRI phenotypes of glioblastomas early after treatment are suggestive of overall patient survival. Poster presentation. 18th Annual meeting of the European Association of Neuro-Oncology, 2023, Rotterdam, the Netherlands.

11.3 Acknowledgments

This thesis is the result of the hard work and dedication of many people. I feel very fortunate to have pursued my PhD at the Gorter Center at LUMC. First, I want to thank Thijs, Johan, and Martin for their trust and support throughout these years. A special thanks to Thijs for being a patient, open-minded, and attentive daily supervisor.

Just weeks into my PhD, I began working with Ece on CEST. Ece, thank you for your guidance and dedication, even after joining Philips. I was also eager to include MRS in the glioma protocol, and I am grateful to Chloé for her patience, collaboration, and invaluable help with data acquisition and analysis, as well as our 2HG collaboration with Utrecht. After I began scanning patients, I quickly realized the importance of radiological assessments; Jeroen, thank you for your help with the 7T project and our MRI phenotypes project. I would also like to thank Linda's crucial role in the 7T project and her insightful feedback on our work and manuscripts.

The PhD journey is demanding, but I was lucky to be part of Thijs's group, which balanced hard work with a fun and supportive environment. A big thank you to the MR physiology group: Suzanne, Thijs van Harten, Merlijn, Sophie, Thom, Leonie, Manon, Lydiane, Emiel, Balazs, Ingmar, Martijn, Jasmin, Lena, Helena, Eva, and Daniëlle. Jasmin, I appreciate our conversations and brainstorming sessions on the phenotypes project, career prospects, and everything in between. Daniëlle, thank you for being my paranymph and for our fun talks about work, experiences at the EANO conferences, but also about sports, nutrition, and more - it was great to bond over our shared enthusiasm.

A big thank you to my first office mates, Kevin, Lena, Francesca, and Aashley, for making the start of my PhD fun and enjoyable. Later, thank you to Chloé, Sahar, Manon, Ernst, Nadieh, and Fieke for the fun times in our office. A big thanks to Ivana, Özge, Mathieu, Bea, Lisa, and Bart for insightful conversations about work careers, sports, and more. Also, to Yiming and Javad for the great discussions and restaurant recommendations during ISMRM conferences.

The Gorter Center has been a warm, hardworking group that made the beginning of my professional journey a very positive experience. I would also like to thank Robert Croese and Ivo Cornelissen for their valuable clinical input. Thank you also to Robin Jacobs for allowing me to be her daily supervisor during her bachelor thesis and for her enthusiasm in the T_2 hyperintensities project. On the technical side, a big thank you to Wouter Teeuwisse for teaching me about the 7T scanner and troubleshooting when needed. Thanks also to Wyger Brink for helping with B_1 inhomogeneities during CEST scanning and providing the dielectric pads, as well as Jaimy Plugge for working on the CEST simulations during his master thesis.

A special thank you to all the patients and volunteers who were willing to undergo an (extra) MRI scan and contribute to our research.

Outside of the LUMC I would also like to thank collaborators at UMCU, including Jannie Wijnen and Zahra Shams for their work on MRS, and Evita Wiegers, Sarah Jacobs, and Iris Obdeijn on

CEST. A special thanks to the GLiMR workgroup. It was wonderful to start my PhD alongside this group, allowing me to connect with experts in the field and network in Malta and Turkey. A special thank you to Esther Warnert, Patricia Clement, Patricia Figueiredo, Rita Nunes, Teresa Nunes, Lydiane Hirschler, Joana Pinto, Jan Petr, Esin Ozturk-Isik, Gilbert Hangel and Fatemehsadat Arzanforoosh.

Finally, I would not have reached this milestone without the support of my family and friends. To my parents and brothers - thank you for always standing by my decisions. To my extended family and in laws for the support, including my aunt Marielle, for being my paranymp and support away from home.

To my friends, despite the distance, your support and care have meant a lot. A special thanks to Francisco Viana for helping me translating the thesis summary into Portuguese.

And last but certainly not least, Luc, thank you for helping with assembling the cover and layout of the thesis, and of course, for your unconditional support, patience, and advice. Our endless conversations have been invaluable.

11.4 Curriculum Vitae

Bárbara Schmitz Abecassis was born in Lisbon, Portugal, on the 20th of April 1995. She attended Escola Secundária de Cascais for secondary school, following the Sciences and Technology curriculum, and graduated in 2013. That same year, she moved to Maastricht, the Netherlands, to pursue a bachelor's degree at the Maastricht Science Programme, graduating in 2016 with a concentration in human biology and neuroscience.

After a gap year, Bárbara followed a master's in Biomedical Sciences with a focus on Imaging Techniques. In her second year she participated in a double-degree program at Kyoto Prefectural University of Medicine, living in Kyoto, Japan, and interning at the university hospital's Department of Radiology under the supervision of Dr. Koji Sakai and Dr. Kei Yamada.

In September 2019, she began her PhD under the supervision of Dr. Ir. Matthias J. P. van Osch, Dr. Johan A.F. Koekkoek, and Dr. Martin J.B. Taphoorn, researching advanced imaging of gliomas. She also collaborated with Dr. Ir. Ece Ercan on optimizing and implementing CEST imaging.

During her PhD, her passion for sports, balanced nutrition and a healthy lifestyle grew, dedicating significant time to sports, in particular running. Bárbara has since decided to switch careers and recently started studying to become a dietitian, with the goal to combine it with scientific research.

